DEVELOPMENT OF NANOSTRUCTURED WEAR RESISTANT SURFACES THROUGH MICROWAVE CLADDING

Ph.D. THESIS

by

SUNNY ZAFAR

DEPARTMENT OF MECHANICAL AND INDUSTRIAL ENGINEERING
INDIAN INSTITUTE OF TECHNOLOGY ROORKEE
ROORKEE – 247667, INDIA
MAY, 2016

DEVELOPMENT OF NANOSTRUCTURED WEAR RESISTANT SURFACES THROUGH MICROWAVE CLADDING

A THESIS

Submitted in partial fulfilment of the requirements for the award of the degree of

DOCTOR OF PHILOSOPHY

in

MECHANICAL ENGINEERING

by

SUNNY ZAFAR

DEPARTMENT OF MECHANICAL AND INDUSTRIAL ENGINEERING
INDIAN INSTITUTE OF TECHNOLOGY ROORKEE
ROORKEE – 247667, INDIA
MAY, 2016

INDIAN INSTITUTE OF TECHNOLOGY ROORKEE
ROORKEE

CANDIDATE'S DECLARATION

I hereby certify that the work which is being presented in the thesis entitled **"DEVELOPMENT OF NANOSTRUCTURED WEAR RESISTANT SURFACES THROUGH MICROWAVE CLADDING"** in partial fulfilment of the requirements for the award of the degree of Doctor of Philosophy and submitted in the Department of Mechanical and Industrial Engineering, Indian Institute of Technology Roorkee, Roorkee is an authentic record of my own work carried out during the period from July 2013 to May 2016 under the supervision of Dr. Apurbba Kumar Sharma, Associate Professor, Department of Mechanical and Industrial Engineering, Indian Institute of Technology Roorkee, Roorkee.

The matter presented in this thesis has not been submitted by me for the award of any other degree of this or any other institute.

(**SUNNY ZAFAR**)

This is to certify that the above statement made by the candidate is correct to the best of my knowledge.

Dated:

(Apurbba Kumar Sharma)
Supervisor

ABSTRACT

Environmental sustainability and reduced life cycle costs are important considerations in industry today. The material selection for engineering components, their design and processing are, therefore, often influenced by combination of engineering as well as business criteria. The performance of the components, on the other hand, is greatly dependent on its surface and the environment in which they are operating. Therefore, tailoring the functional surfaces of the engineering components for improved performance with a composite design approach appears to be a pragmatic solution.

Microwave heating is well known for uniform and volumetric heating of materials at the molecular level. This volumetric and uniform nature of heating reduces processing time significantly and results in better microstructure and properties of the materials compared to conventionally processed materials. Stainless steels are known for their excellent strength and corrosion resistance. However, in wear conditions they undergo surface and subsurface plastic deformation making them candidates for possible surface modification. Microwave cladding, as a technique for surface modification, has proven its potential for various materials. The present work, therefore, was aimed at developing engineered surfaces on austenitic stainless steel through 'Microwave Cladding' for wear resistant applications. The clad layer was developed using popular wear resistant material 'WC-12Co' in two size ranges – micrometric (MM) and nanometric (NM). The MM and NM clads of thickness of approximately 1 mm were developed on stainless steel substrate using the clad powders in the range of 30-45 μm and 100-200 nm. The cladding parameters were optimised through trial and error using exhaustive experimental trials and simulations using COMSOL Multiphysics tool. The simulation studies were carried out in order to determine the electric field distribution, temperature profile, temperature gradient, resistive losses in the clad layer during the microwave exposure. The simulation results largely agreed with the confirmatory experimental data.

The MM and NM clads were evaluated for their metallurgical, mechanical and tribological characteristics through various techniques. The metallurgical characterisation of the MM and MM clads was carried out in terms of phase analysis, microstructure, porosity analysis, elemental distribution and distribution of carbide volume. The X-ray phase analyses of the MM and NM clad layers reveal the presence of various intermetallic carbides such as WC, W_2C, Co_6W_6C, Co_7W_6 and $Co_3W_9C_4$. The normalised intensity ratio (NIR) results indicate that presence of the beneficial Co_6W_6C phase was higher in the NM clad as compared to the MM clad. The microstructure of the MM WC–12Co microwave

clads consists of skeleton structured carbides distributed in the metallic matrix, while the NM WC–12Co consists of uniformly distributed clusters of nanocarbides in the clad layer. The carbide volume fraction in the NM clads was about 48% higher as compared to the MM clad. It was further observed that the WC–12Co MM and NM clads were free from interfacial cracks owing to uniform heating associated with microwave hybrid heating; the average porosity in the clads was less than 1%.

The mechanical aspects of the developed clads were analysed in terms of microhardness, flexural strength and residual stresses. The average Vickers's microhardness of the NM clad (1564±53 HV) was about 1.37 times the microhardness of the MM clad (1138±90 HV). The higher microhardness of the NM WC–12Co microwave clad is attributed to the presence of uniformly distributed nanocarbides and increased carbide volume fraction in the clad layer. The flexural strength of the MM and NM clads was evaluated using a three-point bend test. The average flexural strength of the MM clad was of 587±22 MPa, while the flexural strength of the NM clad is approximately 1.14 times higher (671±28 MPa) than the MM clad. The NM clad exhibited more ductile deformation during flexural loading. The deformation index (DI) of the NM clad is nearly six times higher than the MM clad indicating the fact that the clad DI is a good indicator of the flexural properties; higher DI indicates more ductile-like deformation characteristics. The residual stresses were found compressive in both, MM and NM clads. The magnitude of residual stresses in NM clad was observed to be approximately 1.68 times higher than the MM clads. The presence of higher residual compressive stresses influences the flexural properties of the microwave clads. The flexural strength increases with the magnitude of the residual stresses in the clad layer.

The tribological aspects of the MM and NM clads were evaluated in three different conditions, viz. dry sliding, rolling abrasion (three-body abrasion) and solid particle erosion. In dry sliding conditions, the NM WC–12Co microwave clad exhibits higher wear resistance than its MM counterpart. The average weight loss for the NM microwave clad is reduced by 54% as compared to the MM microwave clad. The enhanced sliding wear resistance of the NM microwave clads is attributed to the uniform distribution of the nanocarbides and enhanced microhardness of the clad layer. The abrasive wear of NM clad was reduced by approximately 1.6 times as compared to the MM clad. Uniformly distributed nanocarbides increase the flow stress in the clad structure, which enhances the wear resistance of the NM clads. Material loss due to erosive wear was reduced to approximately to one third for the NM clad compared to the MM clad. This is attributed to the low mean binder path and higher carbide volume fraction in the NM clads. At low

impact angles, material was removed by microcutting of the relatively soft binder, followed by the loosening and carbide pullout. However, at high impact angles, material loss took place due to fatigue induced carbide fracture as a result of repetitive impacts of the erodents. Removal of the matrix through flaking, carbide fracture and pullout were the main wear mechanisms during erosive wear. However, the presence of clusters of nanocarbides having a low mean free path effectively arrests cracking.

A mathematical (regression) model was developed to estimate the wear (cumulative weight loss) based on the erosion wear data. The wear prediction was also carried out through an artificial neural network model. The model was developed using three significant in using a three-layered configuration. It was found that both the models were reasonable in estimating the wear for the respective cases.

Overall, the work demonstrates the capability of the microwave cladding process for engineering stainless steel surfaces with NM materials. The superiority of the nanostructured surfaces with respect to different wear resistance characteristics has been established with evidences and explanations of the mechanisms. The work also creates opportunities for further research in terms of economic analyses, investigations in different material systems and different wear regimes.

ACKNOWLEDGEMENT

I take this opportunity to express special appreciation and gratitude to my thesis supervisor, **Dr. Apurbba Kumar Sharma**, for his continuous support (both technical and moral), motivation and knowledge during the course of my Ph.D. work. I would specially thank him for encouraging my research that allowed me to grow as an independent Researcher. His advice on my research and career has been invaluable. I feel privileged to work with him for my Ph.D. thesis.

I would also like to extend my sincere gratitude to the members of my Research Committee, **Prof. B.K. Mishra**, **Dr. Inderdeep Singh** and **Prof. S.K. Nath** for their valuable inputs, insightful comments, suggestions and questions that have encouraged me to widen my research from various perspectives. Inputs from **Prof. Navneet Arora** and **Dr. T.S. Sudarshan,** CEO Materials and Modification Inc. are also gratefully acknowledged.

The financial scholarship received during my Ph.D. from Ministry for Human Resource Development, Government of India is gratefully acknowledged. I would also like to acknowledge the financial support in the form of International Travel Grant from SERB, Department of Science and Technology, Government of India and Alumni Association, IIT Roorkee for the visit to the Technical University of Denmark to attend an International conference.

Further, I would also like to acknowledge the support of the laboratory staff in the department, especially, Mr. D.K. Kapil, Mr. S.M. Mishra, Mr. Subodh Kumar, Mr. Pradeep Kumar, Mr. Jasbir and others also, who have directly and indirectly assisted me in my research work. I also thankfully acknowledge the characterisation facilities and support of the staff at the Institute Instrumentation Centre, especially, Mr. S.D. Sharma and Mr. Shiv Kumar for helping in the SEM analysis.

I feel privileged to have Dr. Amit Bansal, my colleague and a good friend, whose inputs and everlasting support have been incredible during my Ph.D. work and stay at IIT Roorkee. It was really a pleasure to work with him in the laboratory; those moments are going to last a life time with me.

My time at IIT Roorkee was made enjoyable and memorable due many friends that gradually became a part of life. I am grateful to the time and memories spend with all of you, especially, Sunil, Tarlochan, Vidyarthy, Gaurav, Pandey Ji, Singla Sir, Shiv Raman, Mishra Ji, Goud Sir, Anup, Sandeep, Nitin, Dheerendra, Ravinder, Naveen, Brij Kishor Ji and Pushpendra. I would also like to thank Dr. Dheeraj Gupta, Dr. Lalit Thakur

and Dr. G. Venkatesh for their support and discussions. I am heartily grateful to Manika for the unconditional support, which will always be cherished and never forgotten.

I finish with the basic source of energy in my life, my family. What I have achieved today is due to the determination and the sacrifices made by my parents in their lives. The lessons of virtue, truth and hard work taught by my parents have remained my guiding light. I would like to give special thanks to my father, who has been the best teacher to me since my childhood and instilled in me the curiosity of Science and Nature; my mother, who raised me and taught me by her unconditional love and care; my brother, who with all love and care supported me in my accomplishments.

Thank you all!

Sunny Zafar
IIT Roorkee
May 2016

TABLE OF CONTENTS

LIST OF FIGURES

CHAPTER 5

CHAPTER 6

LIST OF TABLES

NOMENCLATURE AND ACRONYMS

NOMENCLATURE

NOTATION	DESCRIPTION	UNITS
ω	Angular frequency	rad/s
v_c	Cut off frequency	Hz
μ'	Magnetic permeability	H/m
μ''	Magnetic loss vector	H/m
2θ	Diffraction angle	degrees
β	Propagation constant	---
ε	Dielectric constant; Erosion coefficient	---
ε''	Dielectric loss factor	---
ε^*	Complex permittivity	F/m
ε_o	Permittivity of free space	---
ε_r	Relative permittivity	---
λ	Wavelength	m
λ_o	Incident wavelength	m
μ	Coefficient of friction	---
σ	Electrical conductivity; Bending strength	S/m; MPa
σ_r	Residual stress	MPa
υ	Poisson's ratio	---
c	Speed of light	m/s
C_p	Specific heat	J/kg.K
d	Grain size	µm
d_s	Skin depth	µm
E	Electric field vector; Total input energy; Young's modulus	V/m; J; MPa
f	Frequency	Hz
F_f	Friction force	N
F_n	Normal force	N
H	Magnetic field vector	H/m
i	Imaginary unit	---
k	Thermal conductivity	W/m.K
L	Distance between the support pins	mm
m	Slope	---
n	Mode component	---
P	Power absorbed per unit volume	W/m^3
R_a	Arithmetic average of surface roughness	µm
T	Temperature	°C
t	Time; Thickness	s; mm
T_c	Critical temperature	°C

ACCRONYMS

ACCRONYM	DESCRIPTION
AISI	American Iron and Steel Institute
AJE	Air Jet Erosion
ANN	Artificial Neural Network
ASM	American Society of Metals
ASS	Austenitic Stainless Steels
ASTM	American Society of Testing Materials
CNC	Computer Numerically Controlled
CTE	Coefficient of Thermal Expansion
CWL	Cumulative Wear Loss
DIN	Deutsches Institut für Normung
DSRW	Dry Sand Rubber Wheel
EDS	Energy Dispersive Spectroscopy
EPMA	Electron Probe Micro Analyser
FD	Finite Difference
FDTD	Finite Difference Time Domain
FEM	Finite Element Method
FE-SEM	Field emission scanning electron microscope
FVTD	Finite Volume Time Difference
FWHM	Full Width at Half Maximum
GTAW	Gas Tungsten Arc Welding
HAZ	Heat Affected Zone
HRTEM	High Resolution Transmission Electron Microscopy
HVOF	High Velocity Oxy Fuel
INR	Indian National Rupees
JCPDS	Joint Committee on Powder Diffraction Standards
LIHRC	Laser Induced Hybrid Rapid Cladding
MHH	Microwave Hybrid Heating
MSE	Mean Square Error
MS	Mild Steel
MSS	Martensitic Stainless Steel
NIR	Normalised Intensity Ratio
NISP	Non-Intrusive Spectral Projection
OM	Optical Microscopy
PH	Precipitation Hardening
PTAW	Plasma Transferred Arc Welding

PWHT	Post-Weld Heat Treatment
SEM	Scanning electron microscopy
TE	Transverse Electric
TEM	Transmission Electron Microscopy
TIG	Tungsten Inert Gas
TLM	Transmission Line Matrix
TM	Transverse Magnetic
UTM	Universal Testing Machine
XRD	X-Ray Diffraction

CHAPTER 1

INTRODUCTION AND OVERVIEW

1.1. INTRODUCTION

The concept of "engineering" the surface to protect the engineering components against the environment degradation has gained importance as part of an effort to conserve the natural resources. Modern equipment is highly sophisticated, mostly automated, and expensive. Engineering the surface extends the working life and process of recycling through reconditioning leads to conservation of material and energy. Thus the equipment parts are designed to sustain high production rates for a reasonable period while working in hostile environment. Therefore, it is imperative that the components are protected against environmental degradation in order to ensure satisfactory and reliable performance over a prolonged service life.

Since the mid-90s, the market for several thin film technology has expanded, including photovoltaic, energy conversion, energy efficiency, biomedical and pharmaceutical etc. The demand for tribological and corrosion resistant coatings has also increased and the global market for such coatings exceeded $7.5 billion in 2010. Progressive deterioration of metallic surfaces in use, because of wear and corrosion, ultimately leads to loss of operating efficiency and at worst, a breakdown. Advanced wear and corrosion resistant coatings have also being developed for combustion and gas turbine engines, medical implants. Surface engineered products increase and improve performance, add functionality, reduce costs, improve materials usage efficiently and provide performance not possible with bulk materials. Advanced materials and surface engineering processes are used in manufacturing the equipment in order to minimise wear. Engineering components with longer product life are desirable for uninterrupted and economic service life of a system. Surface degradation, wear in particular, of engineering components is very common, which leads to reduction in-service performance and the life of the components. A cause and effect diagram for surface degradation is illustrated in Fig.1.1. The most commonly encountered causes of degradation of engineering surfaces are shown, however, there are other reasons that cause deviation in the manufacturing attributes of the engineered surfaces. Arresting all of the causes, however, may not be critical for extending the life of an engineering component.

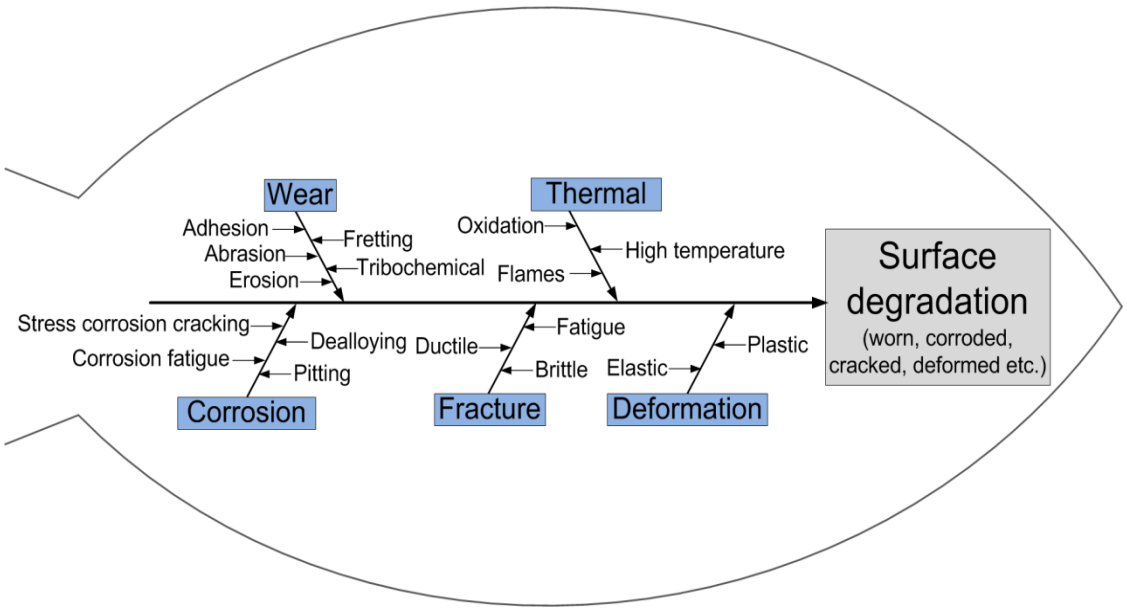

Fig. 1.1- Cause and effect diagram of surface degradation

Better environmental sustainability and reduced life cycle costs are important drivers in industry today. Engineering components with longer product life are desirable for uninterrupted service of the system. However, engineering components not only rely on their bulk material properties but also on the design and characterstics of their surfaces. The functional surfaces of engineering components, on the other hand, are subjected to various loads (Fig. 1.1) during their service life. One or more combination of these loads causes the surfaces to degrade and eventually fail. Hence the behaviour of a component is critically dependent on its surface and the environment in which it is operating. Surface engineering is a valuable tool in facilitating optimal materials selection and innovative product design. Surface engineering encompasses the total field of research and technical activity aimed at the design, manufacture, investigation and utilization of surface layers, both technological and for end use, with properties better than those of the core, such as mainly anti-corrosion, anti-fatigue, anti-wear and decorative. The ASM Metals Handbook describes surface engineering as "treatment of the surface and near-surface regions of a material to allow the surface to perform functions that are distinct from those functions demanded from the bulk of the material" (Reidenbach, 1994). Surface engineering is also conceptualised as the design and modification of a surface and substrate of an engineering material together as a system to give a cost effective performance, which neither is capable

alone (Martin, 2011). Surface engineering encompasses the total field of research and technical activity aimed at the design, manufacture and investigation and utilisation of surface layers, both technological and for end use, with properties better than that of the core, such as mainly anti-wear, anti-corrosion and anti-fatigue. The desired properties of the surface engineered components include:

- Improved corrosion resistance
- Improved oxidation/sulfidation resistance
- Improved wear resistance
- Reduced friction energy losses
- Improved mechanical properties (for example fatigue and toughness)
- Improved electrical/electronic properties
- Improved thermal insulation
- Improved aesthetic appeal

An American study concluded that the cost of friction and wear in the US is almost $5 billion annually. Table 1.1 presents the annual cost of friction and wear in the US. This figure was broken down into the following primary categories, frictional losses, wear, lubricant costs and electrical contact wear. The reasons given for the losses of material components are further broken down into the three categories of obsolescence, breakage and surface deterioration. Obsolescence and breakage each account for 15% of the material losses by industry while surface deterioration by wear and corrosion consumes 70% of the lost industrial equipment. Further, expenditure of reclaiming and repairing damage to the environment caused by poor design, maintenance and lubrication practices is becoming more significant. Stricter regulations governing the release of lubricants into the environment and their subsequent clean up are pushing the costs higher.

Table 1.1- Annual cost of friction and wear in the US

	Friction Losses ($ Million/Year)	**Wear Losses ($ Million/Year)**	**Total Losses ($ Million/Year)**
Agriculture	321	940	1,261
Electric Utilities	54	189	243
Forestry	111	158	269
Mining	211	728	940
Pulp and Paper	105	382	487
Rail Transportation	284	467	750
Trucks & Buses	126	860	986
Wood Industries	14	189	203
TOTAL	**1226 (INR 80,916)**	**3913 (INR 2,58,916)**	**5139 (INR 3,39,174)**

Source:www.maryngroup.com/pdf/RealCostOfLubrication.pdf (accessed on 11 April 2016)

Market of surface engineering in the UK in 1995 exceeded £ 10 billion (approximately INR 96 crores), of which 45% of the amount was spent on enhancement of surface properties against wear and corrosion. This market grew to £ 23.1 billion (approximately INR 220 crores) in 2005, and around £ 14.3 billion (approximately INR 130 crores) were spent on developing surfaces for enhanced wear and corrosion resistance. Data for other countries is not available; it may be assumed that it will be of the same order. Reconditioning by appropriate systems/materials during maintenance provides an opportunity to extend the life of the equipment beyond the stipulations made in the original design. In order to provide viable solutions to the critical wear problems of modern equipment, either at the design or reconditioning stage, specialized knowledge in the area of wear prognosis is essential.

The use of coatings and surface treatments has been found extremely useful for minimising friction and wear. This has fuelled the growth of a new discipline 'surface engineering'. The growth of surface engineering has been mostly due to two reasons. Firstly, development of new surface coating and treatment methods; secondly recognition of significance of the surface of the engineering components. The new surface coating and treatments provide coating characterstics and tribochemical properties that were previously unachievable. Fig. 1.2 illustrates various industrial applications of surface engineering.

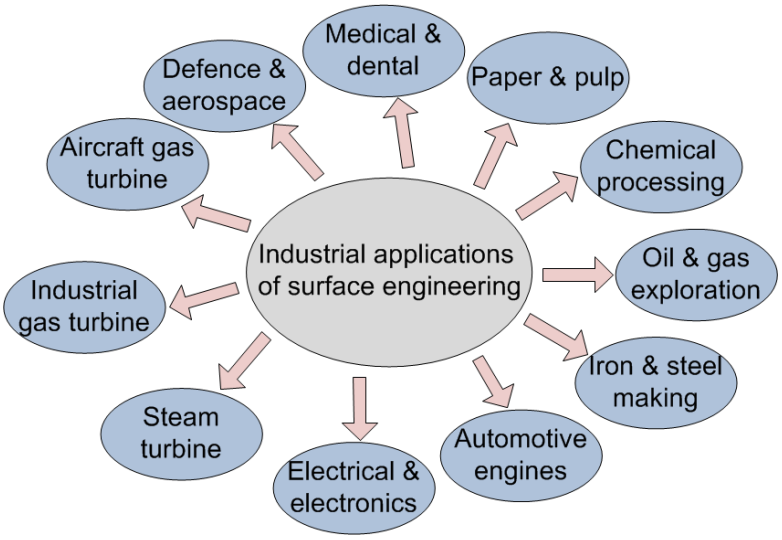

Fig. 1.2- Various industrial applications of surface engineering

The surface has a dominant influence on lifetime cost and performance of a product, including maintenance. Surface also possesses other important attributes not confined only to mechanical or chemical properties but thermal, magnetic and optical characterstics also, which influence the choice of the surface material. Retention of these surface properties is

essential throughout the life of the product. Therefore, enhancement of surface durability by appropriate coating method is critical for any components effectiveness and service life of engineering components. Typical causes of failure of the components in different fields of application and possible surface engineering based solutions are illustrated in Table 1.2.

Table 1.2- Typical causes of failures of components and applications of surface engineering (Burnell-Gray and Datta, 1996)

Failure	Applications
Electronics • Contamination by certain impurities • Diffusion/segregation of constituent materials in semiconductors	• Ion implantation in semiconductor devices • Metal-silicide layer of interconnection strips • Thermo-junctions • Superconducting films
Mechanical • Wear, seizure, fusion of surfaces in contact • Hydrogen diffusion, embrittlement • Phase change, precipitation, diffusion of constituents elements, amorphous crystalline transitions	• Hard layers for cutting tool/drills • Low friction layer for bearings
Chemical • Dissolution of chemical layers • Pitting • Segregation/diffusion of constituent materials • Oxidation and other reactions • Contamination by active species	• Corrosion resistant layer • Catalytic layers • Electrodes for gas sensors
Physical • Adhesion failure, flaking • Blistering • Phase change • Contamination-formation of impurities on optical devices	• Magnetic layers for recording tapes/discs • Diffusion barrier to protect food • Coating for optical lenses

There are number of techniques, being developed to realise high performance coatings as per the requirements of the existing materials and/or the systems. A wide variety of processes are used to deposit the metal ceramic, organic coatings or a combination of these in the form of composite coatings.

1.2. SURFACE ENGINEERING AND VARIOUS TECHNIQUES

Surface Engineering (SE) is a generic term applied to large field of technologies, often diverse in nature; seek to confer improvements of one kind or another to an engineering component during service. The SE as an area of active research and engineering applications has evolved a lot over the years. Today, it has become an interdisciplinary area for researchers to seek a viable solution for an engineering problem.

There are various aspects of surface engineering are shown in Fig. 1.3. Surface engineering involves simultaneous designing and building of substrate as a system, through promoting their efficiency in economic view point. Main objective of surface engineering is to achieve desired surface features for a particular application in a convenient cost and quality. Coatings and treatment of existing surface layer of the components are considered vital in achieving the objectives. Coatings are used to enhance resistance against different environmental agents such as various types of corrosion, create new compatibility in surfaces (e.g. in optical layers), increase hardness, and improve some physical features such as magnetic and electrical properties (Aliofkhazraei, 2011).Various techniques used for developing the coatings are illustrated in Fig. 1.4.

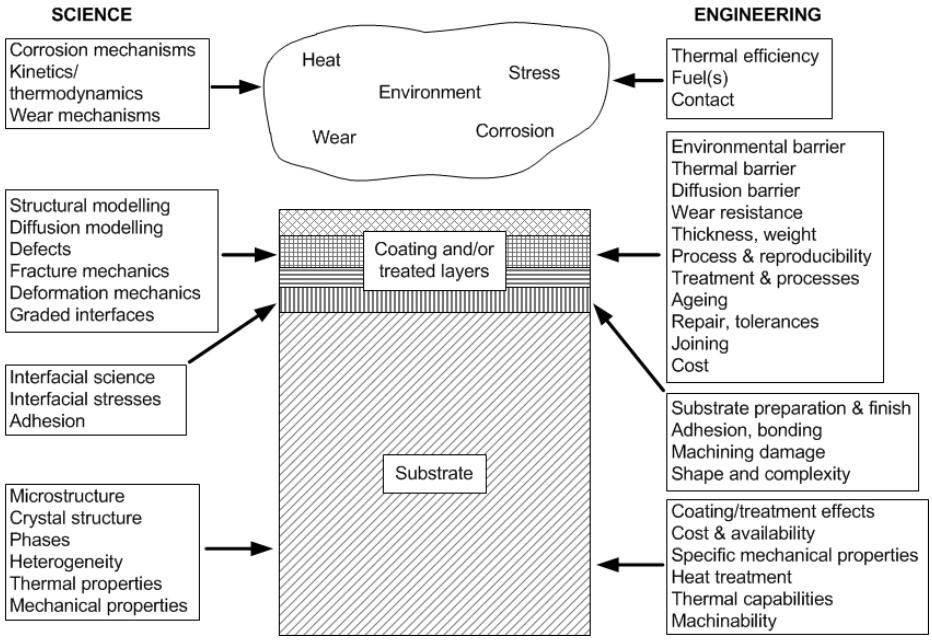

Fig 1.3- Aspects of surface engineering (after Burnell-Gray and Datta, 1996)

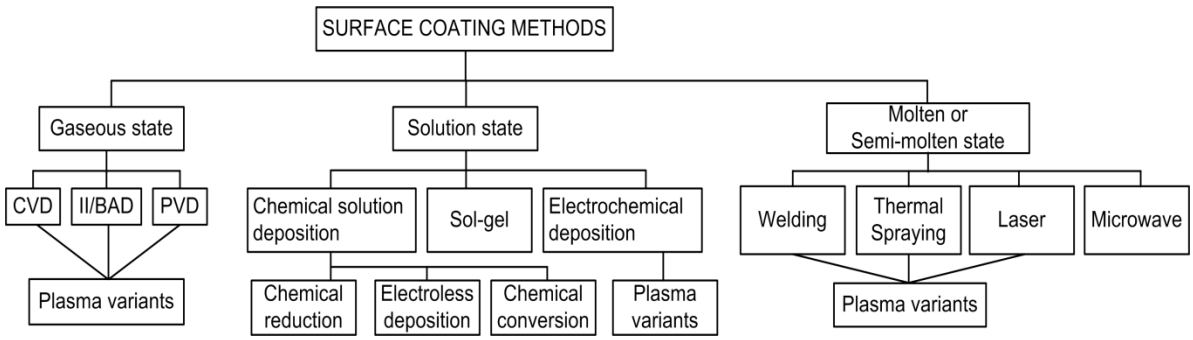

Fig. 1.4- Various techniques in surface engineering (adapted from Holmberg and Matthews, 2009)

The techniques illustrated in Fig. 1.4 involve intentional build up or addition of a new layer on the metal substrate. These techniques include a wide group of surface coating methods, where a material different from the bulk is laid upon the surface (Grewal et al., 2013a,b,c; Chaudhry and Kailas, 2015). There exists a clear boundary at the coating/substrate interface and the adhesion of the coating is a primary issue. The cladding, on the other hand, is a widely used surface engineering technique to develop an overlay of suitable materials on substrates of desired properties by partial melting of substrate along with complete melting of the target powder on to the substrate. The basic characteristic of the cladding process is to provide good metallurgical bonding with minimal dilution of the base material.

1.3. IMPORTANCE OF NANOMATERIALS IN SURFACE ENGINEERING

Surface coating is today an important industrial activity with a wide range of applications. Nanomaterials today dominate the surface coating industry. They present great promise and opportunities for a new generation of materials with improved and tailorable properties for several applications. Nanostructured materials have very large surface area per unit mass, high reactivity, and exceptional mechanical, electrical and optical properties. Nanostructured coatings are one of the most effectively used applications of nanomaterials. The goal to attain higher performance levels than those tribological layers having similar chemical and phase composition, lead to the widespread applications of nanomaterials in order to enhance wear resistance of the engineering components. The rationale behind this approach lies in the potential improvements arising from changes associated with decreasing grain size. As the grain size of the material reaches nanoscale, the fraction of the atoms at the grain boundaries becomes significant (Marple and Lima, 2005). For multiconstituent or two phase materials, finer particles allow a possibility of having a uniform distribution of components within the structure. A high level of homogeneity is often advantageous for several applications where consistent properties are required with material of the component. Further, according to the Griffith relation for crack propagation, the stress required to initiate crack propagation increases with decrease in the grain size. The yield strength, hardness and toughness of the coatings improve with decreasing grain size according to well-known Hall-Petch relation (He and Schoenung, 2002). These unique mechanical properties motivate the world to synthesize the nanostructured tribological layer(s) on functional surfaces of the engineering components. The mechanical properties of nanostructured tribological layers are dominated by the interfacial properties and it was established that nanometric scale

materials are stronger. It is generally accepted that increase in the hardness is similar to the Hall-Petch that means that the flow stress of the material is inversely proportional to the square root of the average grain size (Takadoum, 2010). This mechanism is based on the difficulty to plastically deform the material due to the effect of dislocation. There are numerous applications of nanocomposite tribological layers due to their specific characterstics, among which turbine blades, internal cylinder sleeves, valve stems, piston heads, bores, guide slots, moulds for injection of plastics and rubber. For these and other reasons, the level of research activity in the application of nanomaterials in surface engineering has increased dramatically in the recent years.

1.4. MOTIVATION

The economic impact of friction and wear on the society is huge. Improved coatings and selection procedures lead to decreased friction and wear. This will enable improved efficiency over a longer lifetime and provide considerable reduction in energy consumption and cost caused by in-service failure or maintenance or downtime cost. The objective of tribological coatings should be to achieve extended and predictable lives, and ideally non-catastrophic modes of failures.

Austenitic stainless steels (ASS) represent today in more than 2/3 of the total stainless steel production worldwide production (Plaut et al., 2007). They exhibit high corrosion and oxidation resistance and excellent weldability (Liljas, 1995). They are widely used in petrochemical and fertilizer industries, food processing industries, cryogenic vessels, pump impellers, mining and quarry equipment. However stainless steel suffers severe metallic wear due to formation of adhesive junctions, hence are not recommended to be used in potential wear applications (Sun and Bell, 2002). Superior properties of stainless steel can be exploited by tailoring the functional surface by suitable materials. Moreover, surface hardening of stainless steels for improved wear resistance while maintaining corrosion resistance and ductility has been very difficult. It is thus natural to select a bulk material of the engineering component for overlay that meets the demands of stiffness, strength, formability and cost. Application of tribological coatings is a very efficient way to deposit the material and improve the friction and wear resistance properties. Tribological coatings may fail prematurely due to detachment, delamination, cracking and/or spalling (Hogmark et al., 2000). Therefore, the tribological coating shall be selected to match the situation. Functional properties of stainless steels can also be improved through hardening, carburizing, cyaniding, welding based processes.

However, in the recent years, microwave cladding has been demonstrated as a novel surface modification technique (Sharma and Gupta, 2010) and only a very few hardfacing materials viz. Ni based (EWAC), WC10Co2Ni, EWAC+20% Composite powder, EWAC (Ni based) +20% $Cr_{23}C_6$ and Inconel 718 have been used to develop microwave clads. Development of uniform microstructure, rapid processing speeds, faster heating rates are some of the significant features of microwave energy (Clark and Sutton, 1996; Clark et al., 2000; Gupta and Sharma, 2014, 2011a, 2011b; Sharma and Gupta, 2012). Hence, development of wear resistant surfaces with different hardfacing materials on different substrates using microwave energy can be a potential alternative to the relatively matured laser cladding and other traditional hardfacing methods (e.g. weld surfacing). Nanostructured materials exhibit enhanced mechanical, physical and functional properties due to large interface and nanoscale effects associated with these materials. Further, microwave energy can also minimise the decomposition of the carbide phase. At present no work has been attempted on developing nanostructured clads using microwave hybrid heating on austenitic stainless steels. Motivated by the facts, the present work on development of micrometric and nanometric clads on austenitic stainless steel using microwave heating was taken up.

1.5. OVERVIEW OF THE THESIS

The present thesis is organised into following chapters:

Chapter 1: Introduction to understand the various modes of surface degradation have been presented. A brief introduction to surface engineering methods for engineering materials has been included. Importance of nanomaterials in surface engineering has been highlighted. Further, motivation for the present work has also been outlined.

Chapter 2: In this chapter an exhaustive description on wear, various wear mechanisms have been discussed. The importance of cladding has been highlighted with respect to surface engineering. A comprehensive literature review on surface modification through various techniques of materials has been presented. Identification of research opportunities, problem identification, objectives, scope of the work and the methodology adopted for the presented study has been discussed.

Chapter 3: Fundamentals of microwave material processing have been discussed. The characteristics of microwave heating, microwave material interactions, mechanism of microwave heating have been explained in detail with some brief discussion on types of

microwave heating. Principles of clad formation along with simulation studies have been presented. Validation of simulation results with experimental results has been presented.

Chapter 4: This chapter deals with the details of the experimental procedure carried out thrusting on the materials details, details of the experimental setup, and processing parameters. The chapter also provides information regarding details of the tribological tests carried out.

Chapter 5: This chapter presents the results of the metallurgical and mechanical characterisations of the micrometric and nanometric WC-12Co microwave clads. The metallurgical aspects of the clads are discussed in terms of phase analysis, microstructure analysis, elemental study and porosity analysis. Mechanical aspects were studied through microhardness, flexural strength test and residual stresses.

Chapter 6: The chapter addresses the tribological aspects of the micrometric and nanometric WC-12Co clads. The tribological aspects were characterised using dry sliding wear, three-body abrasive wear and solid particle erosive wear. The results are discussed with suitable illustrations.

Chapter 7: Concludes the findings of the research work. The future directions of this research have also been highlighted. Major contributions and industrial relevance of the present work have been presented.

1.6. SUMMARY

Various modes and economical outcomes of surface degradation have been discussed. The deterioration of engineering components due to corrosion and wear in various industrial applications is a challenge to combat. Surface engineering offers wide range of technologies to enhance surface properties of the engineering components. A brief overview of various surface engineering methods has been illustrated. Significance of nanomaterials in the domain of surface engineering has been highlighted; potentials of using microwave energy for material processing have been introduced. Motivation for the present work has been stated. The organization of the thesis is presented.

CHAPTER 2

LITERATURE REVIEW AND PROBLEM FORMULATION

Different forms of wear, corrosion and their combined effects lead to degradation of surfaces of the engineering components. Surface engineering could play a key role in combating such surface degradations. This chapter presents a comprehensive review of the relevant literature on friction, wear and surface engineering techniques. Application of microwave energy to develop clad layers has also been explored.

2.1. INTRODUCTION

In modern industrialised societies, there is growing need to control friction and wear for several reasons, such as, to extend the lifetime of machinery and bio-systems, to make engines and devices more efficient, to develop new advanced products, to conserve scarce natural resources, to safe energy and improve safety. Majority of the engineering components degrade or catastrophically fail in-service through surface triggered phenomena such as wear, fatigue and corrosion. This has led to the development of the new area of research, called surface engineering. Fig. 2.1 illustrates various surface degradation phenomena. Broadly, these phenomena can be divided into two categories, the phenomena related to the in-service or application related and the phenomena inherent with the environment in the component are working. The impetus of development was simulated by growing commercial maturity of wide range of technologies like welding based techniques, laser processing, thermal spray based processes, plasma thermal based processes etc. Engineering components with longer product life are desirable for uninterrupted service of the system. However, engineering components not only rely on their bulk material properties but also on the design and characteristics of their surfaces. Degradation caused by wear, corrosion and fatigue is usually limited to the surface and subsurface zone that lead to gradual loss of the properties of materials which, eventually, may lead to failure of the component. Consequently, tailoring the functional surfaces for improved performance and retaining the bulk properties can be a pragmatic solution. Like all products, mechanical components and tools are facing higher performance requirements. The use of surface coatings opens up the possibility for a material design in which the specific properties are placed where they are needed the most. In this approach, the substrate can be designed for strength and toughness, while coating can be developed for resistance to wear, corrosion or thermal loads to achieve the required functional characteristics.

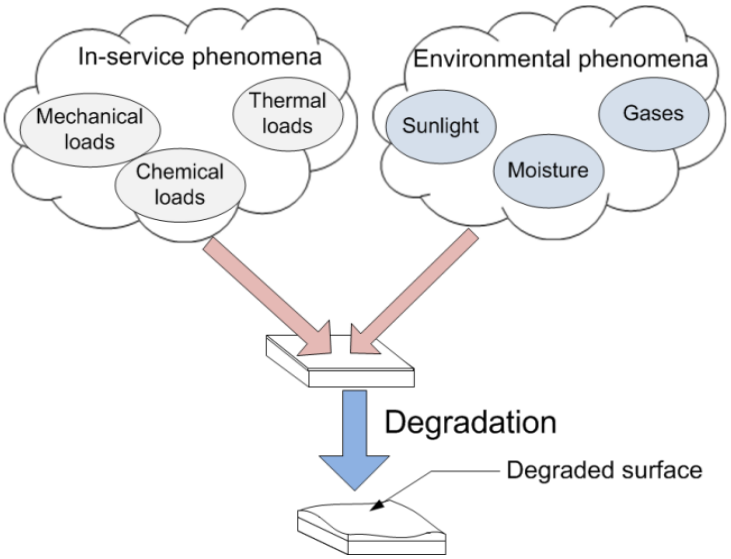

Fig. 2.1- Causes of surface degradation of materials

2.2. TRIBOLOGY

Tribology is the field of science related to contacting surfaces in relative motion which deals with phenomena related to friction, wear and lubrication. Tribology has played an important role in technological evolution of human race since ancient times. Invention of wheel in transportation and application of oil as a lubricant eventually smoothened the path for modern industrial revolution. Tribology covers many diverse disciplines including physics, chemistry, mechanical engineering and material science. Besides being an interdisciplinary field, tribology also deals with different size scale ranges, ranging from interacting atoms in contact to heavy machines. Besides the complexity of the multiscale and interdisciplinary nature of tribological problems, the challenges include selection of proper strategy and appropriate approach to understand the contact conditions and resultant wear mechanisms.

It is also important to note that all damages on the surface of the material cannot be considered as wear. The ASM handbook defines wear as surface damage as "topographical or microstructural changes, or both, in a surface layer". Surface damage can be categorised in the following four categories (Blau, 1992):

a) Structural changes- The structural changes are phase transformations, recrystallization, tempering, aging etc. Structural changes may lead to change in the shape of the material.

b) Plastic deformation- Local or global permanent deformation of the material, which may lead to change in the shape of the material.

c) Surface cracking- Surface cracking may emanate due to localised excessive thermomechanical strains or cyclic loading.

d) Surface damage involving loss or gain of materials- Different processes such as fracture (shear, brittle, ductile and fatigue), extrusion, chip formation and tearing may lead to loss of material. However, in some situations such as chemical reaction or corrosion, material may stick or get added on the surface.

2.3. WEAR

The widest definition of wear, which has been recognised only five decades ago, includes "the loss of material from a surface, transfer of material from one surface to another, or movement of material within a single surface" (Almen, 1950). Surface cracking may not be included in the definition of wear, but it could cause wear at some stages (Blau, 1997). A simple and useful statement is 'damage to a solid surface, generally involving progressive loss of materials due to relative motion between that surface and contacting substance or substances' (Reidenbach, 1994). It is quite natural that any material body in use undergoes wear. However, it is unfortunate that excessive wear can cause huge losses of resources. Various aspects of wear are presented briefly in the following sections.

2.3.1. Historical perspective of wear

Wear in association with friction is a phenomenon as old as human race. Fire was created through friction between two wood pieces or percussion of flint stones during the prehistoric ages. Wear is commonly defined as "removal of material from solid surfaces as a result of one contacting surface moving over another". Both friction and wear are simultaneously the results of same tribological contact process that takes place between two moving surfaces. Most forms of wear are events occurring at asperities in contact. But, exceptions are like erosive wear in which hard particles are collide with the surface. In view of the highly complex nature of the wear processes and scarce models to predict wear, the most common on discussions on wear start with the simplest possible relation between the wear rate volume and the applied normal load. Archard first derived a plausible relationship between the two in 1953. According to Archard's law, the total wear volume (Q) removed from the surface per unit sliding distance is directly proportional to normal load (W) applied to the surface and inversely proportional to the indentation hardness (H) of the wearing material. Mathematically

$$Q = k\frac{W}{H} \tag{2.1}$$

Here, coefficient '*k*' is a dimensionless quantity and known as the wear coefficient. The wear coefficient provides a valuable means to compare the severity of different wear processes. The constant '*k*' can be imagined as the proportion of asperities contact resulting in wear. The value of '*k'* is always less than 1, mostly 0.001. The approximate values of '*k'* for different wear processes is illustrated in Fig. 2.2. Under dry sliding conditions, the value of '*k'* ranges between 10^{-6} to 10^{-2}. The value of '*k'* at 10^{-4} is often used to distinguish the wear regimes as mild and severe, for '*k'* below and above the value, respectively. When the wear process involves hard particles, such as in abrasion (sliding and rolling) and erosion (by impact of particles), the value of '*k'* is the highest. Interactions among various wear mechanisms are illustrated in Fig. 2.3.

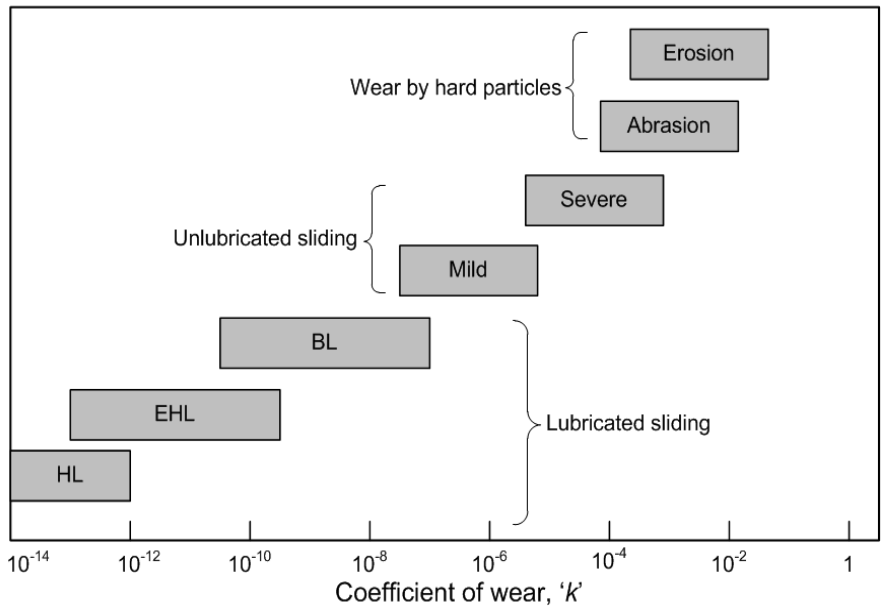

Fig. 2.2- Schematic representation of the range of wear coefficient '*k*' exhibited under different conditions of wear. HL = hydrodynamic lubrication; EHL = elastohydrodynamic lubrication (after Stachowiak, 2005)

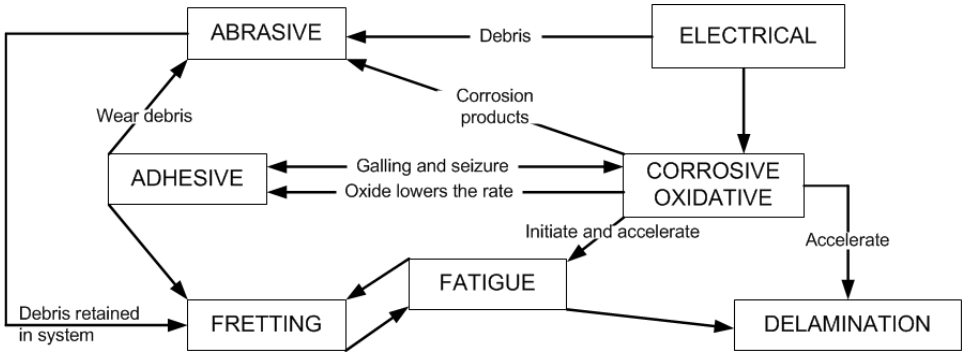

Fig. 2.3- Interactions of various modes of wear (after Holmberg and Matthews, 2009)

2.3.2. Classification of wear

There are different wear mechanisms, each characterised with specific type of movement, geometry and environment. The mechanisms of wear can be broadly classified into five categories (Zum Gahr, 1987):

1. Adhesive wear
2. Abrasive wear
3. Surface fatigue wear
4. Tribochemical reaction
5. Erosive wear

Adhesive wear

Adhesion or adhesive wear occurs when two surfaces slide against each other, and fragments are pulled off one surface to adhere to the other. During adhesion, high localised pressure results in the formation of plastic deformation, adhesion and formation of local junctions. When the two surfaces slide relatively to each other it leads to rupturing of these junctions hence metal transfer between two materials or form loose wear particles. Formation of these junctions is due to adhesion, i.e. ideally welding two similar materials leads to disappearance of the interface. With damage or increasing overloading, increasing load and velocity of slip pairs, adhesion may result in scuffing. Piston cylinders, gear contacts, cams and followers, rolling bearing elements, machine guideways are a few machine components directly affected by adhesive wear.

Abrasive wear

Abrasion or abrasive wear occurs due to displacement of material caused due to hard particles or embedding of hard particles between two surfaces moving with a relative velocity or hard pro-turbulences on one or both relatively moving surfaces. Hard particles may be product of processing, example silica, alumina or work hardened wear fragment from entry of dirt from outside. The hard particles plough a series of grooves on the surface. The material is displaced from the grooves in form of wear particles. Chutes, hydraulic presses with dirt, extruders, rock crushers etc. have surfaces embedded with hard particles may suffer wear due to abrasion. Different physical parameters may be involved depending on the wearing materials, operating conditions such as type of abrasive particles and angle of attack (Axen and Jacobson, 1994). The magnitude of abrasive wear differs depending on the ratio of hardness of the abrasive to hardness of the surface being worn. Further, abrasive wear may be classified as two-body (sliding) or three-body (rolling)

abrasion. In two-body abrasion, the surface asperities on surface cut directly into the surface of the other body. In three-body abrasion the, abrasive particles act as interfacial elements between the solid body and the counterbody. Wear is smaller by one or two magnitude in three-body abrasion than in two-body abrasion.

Surface fatigue wear

Wear due to surface fatigue is characterised by crack formation and flaking of material caused by repetitive alternative loading of solid particles. The repeated loading and unloading cycles to which the material is exposed may induce the formation of surface and subsurface cracks, which eventually lead to break-up of the surfaces. The rolling and/or sliding contacts of solids or the impacting contacts of solids and/or liquids result in cyclic stressing of surface. Localised fatigue may occur due to sliding contact of asperities on the surface of the solids in relative motion. Surface fatigue wear may lead to formation of large fragments, leaving large pits on the surface. Brittle materials tend to break up in the form of large fragments. Severe damage may occur in rail and wheel system, ball and roller bearings, gears, rollers for cold and hot rolling etc. Fatigue of materials precedes a sequence of elastic plastic deformation, work hardening crack initiation and crack propagation.

Tribochemical reaction

The tribochemical reaction can be quantified "by rubbing contact between two solid surfaces that react with the environment. The corrosive environment may be gaseous or liquid. The wear proceeds by continuously removal and formation of new reaction layers on contact surfaces. In presence of atmospheric oxygen the worn debris consists largely of oxides formed on the surfaces in rubbing contact." Tight-fit surfaces are particularly endangered example between race and shaft or race and housing on roller bearings, bevel-wheels, riveted joints, clutches, chain plates, springs seals etc. The tribochemical wear results from removal of metal and chemical reaction products from the surfaces in contact. The tribochemical wear is strongly influenced by the kinetics of the formation of surface layers and properties, which determine their resistance to removal, e.g. ductility, strength, adhesion to substrate.

Fretting is a special form of tribochemical wear, caused when surfaces in contact undergo small oscillatory tangential movements relative to each other. The amplitude of the relative motion is small (of the order of 80 μm). Larger amplitude of relative motion

may result in reciprocating sliding motion. Fretting in cyclically loaded components can be come when fatigue cracks are initiated at the fretted surfaces.

Erosive wear

Erosion or erosive wear is caused on solid particles by the sliding or impacting actions of the solids, liquids or gases or combination of these. Tribosystems suffering from erosion can be characterised as an open system in which the counterbody is continuously replaced. Blast erosion is caused by erodents carried in carrier gas (Beste et al., 2001). Blast erosion can result problems in areas of pneumatic transfer of coal dust or aero gas turbines. Flush erosion is caused by erodents being carried away in the stream of liquid. Example, pipelines in transfer of slurry. Damage due to erosive wear occurs on the blades of the gas turbine when the aircraft files through the dust clouds, wear of pump impellers in mineral processing systems etc. The mechanism leading to blast erosion originates from single particle processing. Multi particle impingement involves complex phenomena, such as wide range of simultaneous incidence angles, particle interactions, particles embedding on the surface.

Cavitation is a special form of erosion in which vapour bubbles in the fluid form in low pressure regions, implode suddenly producing a mechanical shock. Nearby solid surface is damaged by this shock, thereby creating holes and pits. Cavitation is closely akin to surface fatigue wear. Materials that are resistant to surface fatigue wear are also resistant to cavitation.

2.4. FRICTION

Friction is the resistance to motion that exists when a solid object is moved tangentially with respect to the surface of another which it touches, or when an attempt is made to produce such motion (Rabinowicz, 1995). The importance of friction may be seen in the fact that, as estimates show, a very substantial part of the total energy consumption is expended in overcoming frictional losses during sliding. Friction is not a material property; it is system response in the form of a reaction force. A sliding tribocontact undergoes through several stages of different friction mechanisms during the running-in period before a steady state is reached. The stages of friction are specific for material tested, the experimental arrangement and the environmental conditions. In the recent years, several researchers have attempted to formulate mathematical expressions for frictional force or coefficient of friction (Andersson et al., 2003; Bhushan, 1999; Dunaevsky, 1997). However, these equations are limited to certain friction mechanisms, material

combinations or contact conditions. The ratio of the tangential force (F) to the normal load (W) is known as the coefficient of friction, μ. Mathematically,

$$\mu = \frac{F}{W} \tag{2.2}$$

Basically, friction force F can be divided in two components, an adhesion force F_a, due to adhesion between two surfaces, and a deformation force F_d due to deformation forces. The relation between F, F_a and F_d is as shown in equation 2.3.

$$F = F_a + F_d \tag{2.3}$$

When the deformation force takes place on the macroscale it is called as 'ploughing force', while on the microscale it is known as the 'asperity deformation'. Several researchers have investigated and presented various theories on the phenomena of friction (Bowden and Tabor, 2001; Dowson, 1998; Hwang and Zum Gahr, 2003; Kim and Suh, 1991; Landheer and De Gee, 1991; Rabinowicz, 1967; Rigney and Hirth, 1979; Suh and Sin, 1981).

Friction and wear results in different industrial situations and results in high cost due to equipment failure, replacement of worn parts and downtime during repairs. Further it may affect the quality of the products involved. Wear encountered in different industrial situations can be grouped as: abrasive wear (50%), adhesive wear (15%), erosive wear (8%), fretting wear (surface fatigue wear) (8%) and chemical wear (tribochemical wear) (5%) (Eyre, 1976). The cost of friction and wear was close to billions of dollars throughout the world. The reasons given for material loss were broken down further into three categories of obsolescence, breakage and surface deterioration. Obsolescence and breakage each accounted for 15% material loss, while surface deterioration by friction, wear and corrosion accounted for 70% of the material loss in the industry.

Hence, there is growing need to minimise and control friction and wear for extending the life of machinery and bio-systems, to enhance the efficiency of engines and devices, to develop advanced materials, conserve the scarce material resources, to save energy and improve safety. Historically, controlling friction and wear was carried out by selecting improved bulk materials and by utilising lubrication techniques such application of liquid or solid lubricants. In the recent years, application of surface treatment and coatings have been utilised to control friction and wear. This has led to growth of a new interdisciplinary branch of engineering known as "surface engineering".

Surface engineering plays a key role in combating mechanical and chemical surface degradation of various engineering components. Surface degradation of

engineering components can be minimised through a wide variety of surface modification techniques such as surface treatments, alloying and coatings etc. Surface modification is a pragmatic approach to enhance the properties of functional surfaces of the engineering components. There are two common objectives in the use of surface engineering for tribological applications: to increase the wear resistance of the surface material and to modify its frictional behaviour (Hutchings, 1992). The microstructure of the surface material may be modified selectively without changing its composition, as in surface treatment techniques. Alternatively, both composition and microstructure may be changed like adding a layer of chemically different material such as in surface coatings methods.

2.5. DEVELOPMENTS IN COATING/CLADDING PROCESSES

Surface engineering of steels for improved wear resistance while maintaining its corrosion resistance and ductility has been a difficult task. Traditionally, tribological coatings are commonly developed through thermal spraying, weld surfacing (such as gas tungsten arc welding (GTAW), plasma transferred arc welding (PTAW)) and laser cladding. These are the molten or semi molten state processes. A number of researchers have suggested the use of protective coating/cladding with desirable properties such as hardness (at-least equal to or more than the abrasives), toughness, homogenous microstructures, low defects (pores, cracks, voids), good adhesion with the substrate for protection against wear (Carton et al., 1995; Hogmark et al., 2000).

Cladding is widely used to develop an overlay of suitable materials with desired properties on the substrate by partial melting of the substrate along with complete melting of the target powder on to the substrate. The significant characteristic of the cladding process is that it provides good metallurgical bonding with minimal dilution of the base material. In general, cladding is carried out to protect the in-service components from degradation by enhancing hardness and wear resistance of the functional surfaces while retaining the toughness and ductility of the bulk component. Cladding based techniques are characterised by an interface layer between the overlay material and the substrate. Among the various methods of developing clads, GTAW, PTAW and laser cladding are popular (Arabi Jeshvaghani et al., 2011; Dinda et al., 2009; Gupta et al., 2008; St-Georges, 2007; Xu et al., 2006b; Yakovlev et al., 2004; Zhou et al., 2008a). These techniques are gaining popularity in terms of research and technological developments.

2.5.1. Weld Surfacing

The GTAW and PTAW processes are popular weld surfacing processes used for deposition of wear resistant coatings on metallic surfaces by feeding powder in the melt pool. In PTAW process, a high frequency non-transferred arc is initiated between a tungsten cathode and a water cooled anode. Argon gas is passed through the inner annulus between the cathode and anode is ionised, thus forming a constricted plasma arc column. The shielding gas is flooded around the weld pool to protect it from oxidation. The powder consumables are blown into the arc periphery using a mechanical and powder carrier gas feeding system and enter the plasma just above the substrate (Deuis and Subramanian, 2000). A typical schematic of the PTAW process used for depositing wear resistant overlays is shown in Fig. 2.4. The overlays can be customised for specific in-service condition with the desired composition. This is due to use of powder as the deposit material which allows free mixing of the powders as long as the powder sizes are consistent (Mendez et al., 2014).

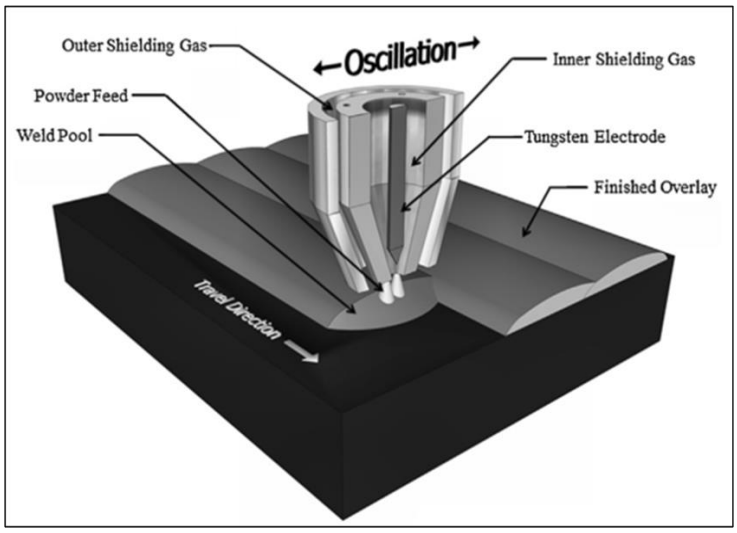

Fig. 2.4- Schematic of PTAW process for depositing wear resistant overlays (Mendez et al., 2014)

The GTAW is another popular weld surfacing technique in which the arc is formed between a tungsten electrode and base material. The shielding gas flows around the melt pool to protect it from contamination (like oxidation etc.). The GTAW can rapidly melt various alloys onto metal substrates to form strong metallurgically clad layers. The characteristic of GTAW is rapid solidification, which produces extremely fine microstructures (Peng and Kang, 2015). The PTAW is an extension of GTAW process as both utilize a gas shielding produced around the non-consumable tungsten electrode. However, PTAW offers high arc density by virtue of the collimated nature of the plasma

beam. The stiff plasma beam is not deflected by external magnetic and high energy concentrations can be produced with higher arc temperature.

Deuis et al. reported the development of metal-matrix composite coatings to enhance the tribological properties of ferrous and non-ferrous substrates (Deuis et al., 1998). Composite coatings exhibit higher wear resistance as the load is transferred from the soft matrix to hard reinforcing particles. The load transfer is possible by virtue of the existence of the bond between the particulate and reinforcement. The investigation highlights the research on PTAW surfacing to develop wear resistant surfaces for various industrial applications. The comparison in terms of process characteristics of PTAW with laser cladding and thermal spraying is also presented. The PTAW surfacing technique outweighs laser cladding in terms of process efficiency.

High temperature performance of plasma transferred arc coatings was studied by D'Oliveira et al. (D'Oliveira et al., 2002). They further compared the performance of the plasma transferred arc coatings with laser coatings. Co-based coatings were deposited on stainless steel (grade 304) and were then subjected to temperature cycling at 1050 °C. It was observed at that ambient temperature, laser coatings exhibited enhanced performance; however, at elevated temperature PTAW coatings exhibited enhanced performance. This was attributed to high stability of the carbides in PTAW coatings which were not affected by the temperature cycling.

Investigations to enhance the cavitation erosion resistance of AISI 316 stainless steel were attempted through TIG cladding (Cheng et al., 2003). A few mm thick NiTi layer was deposited on to 316 stainless steel substrate with strong metallurgical bonding between the deposit and substrate. A dilution of approximately 14% and small pores (size less than 20 μm) was reported in the clad layer. However, the average microhardness of the clad layer (700 HV) was approximately three times higher than the substrate (200 HV). Further, the local cavitation erosion resistance of the clad layer was nine times higher than the substrate. This can be attributed to the partial retention of the superelasticity and higher hardness of the clad layer. The secondary phases and pores were the erosion initiation sites in the clad layer.

Wear behaviour of ceramic powder cladding on S50C steel was studied by Lin and Wang (Lin and Wang, 2003). The SiC based clad layer was deposited on the medium carbon steel substrate using GTAW surfacing. Wear behaviour of the clad layer was analysed using Taguchi parameter design. It was observed that uniform distribution of the hard ceramic particles in the martensite matrix present in the clad layer improved its wear resistance.

Lin and Wang investigated the microstructure of the TiC-W GTAW cladding on S50C steel (Lin and Wang, 2004). The microstructural examination of the clad layer was carried out using electron microscopy (SEM, TEM and HRTEM) to investigate the interface between the TiC and the matrix. Results indicate good bonding between the unmelted TiC particles and the matrix. In addition, the primary ferrite precipitated around the TiC particles by heterogeneous nucleation.

Tungsten carbide (WC) is preferred for enhancing the wear resistance of machine components. Buytoz et al. presented an investigation on dry sliding wear behaviour of TIG clad WC composite coatings (Buytoz et al., 2005). The WC powders were melted on AISI 4340 steel substrate to achieve a clad layer. Presence of eutectic and dendrite solidification was evidenced in the clad layer. The hardness of the clad layer varied between 950 and 1200 HV. The clad layers were produced with different heat inputs. Specimen with low process speed, high heat input produced a systematic solidification and hence recorded a minimum mass loss during the dry sliding wear test.

Molleda et al. studied the microstructural features of weld deposited Stellite 6 hardfacing on stainless steel through TIG cladding (Molleda et al., 2006). It was reported that diffusion of carbon from the liquid stellite to austenitic stainless steel takes place along the grain boundaries resulting in formation of arm like structures of chromium carbide (Fig. 2.5). While, the Co and Ni were observed to be uniformly distributed in austenitic matrix, the carbon from the weld fusion zone was reported to be diffused along the austenitic grain boundaries.

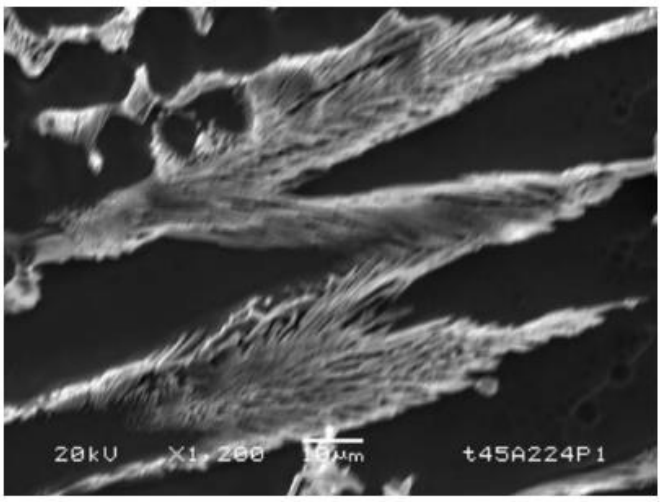

Fig. 2.5- Stellite liquid arms that penetrated the austenitic stainless steel (Molleda et al., 2006)

Wang et al. fabricated TiC particles reinforced Fe-based composite coatings through GTAW surfacing process (Wang et al., 2006). A mixture of graphite and ferrotitanium (FeTi) in the form of powder was deposited on AISI 1045 stainless steel using GTAW heat source. Microstructure of the coatings revealed presence of cubic TiC carbides and fine needle-shaped eutectic in the ternary Fe-Ti-C eutectic. The uniformly distributed TiC particles in the coatings enhanced the hardness and wear resistance of the coated AISI 1045 stainless steel substrate. It was further reported that the sliding wear resistance of the coatings improved with increasing sliding distance.

Sudha et al. studied the microchemical and microstructural properties of Ni-Cr-Si-B PTA weld overlay (Sudha et al., 2008). Overlays of thickness of the order of 7 mm were deposited in SS304L substrates. The overlays exhibited a heterogeneous microstructure consisting of three regions: γ-Ni+Cr_2B eutectic, Cr_7C_3, Cr_3C_2 and Cr_2B phases in the γ-Ni matrix and needle shaped chromium carbides. It was reported that the thickness of the inter diffusion zone was of the order of 760 μm, which is much less than as obtained in GTAW overlays (diffusion zone of the order of 2.5 mm).

Lin and Cho investigated the microstructure and tribological behaviour of NiCrAlCoCu and NiCrAlCoMo multicomponent alloy system (Lin and Cho, 2009). The alloy system was synthesised in-situ on AISI 1050 medium carbon steel using GTAW process. The results indicated that the NiCrAlCoMo clad layer consists of phases such as $AlFe_{0.23}Ni_{0.77}$, $Co_6Mo_6C_2$, and $Fe_{63}Mo_{37}$, while the NiCrAlCoCu clad layer consisted only of bcc and fcc solid solution phases. In the NiCrAlCoMo clad layer, the complex geometry of vein-shaped reinforcement results in strong mechanical interlocking. As a result, the hardness of the NiCrAlCoMo layer was four times high as compared to that of the NiCrAlCoCu layer. Hence, this prevents detachment of the clad layer therefore improves the wear performance of the NiCrAlCoMo clads.

Liyanage et al. presented investigation on the influence of alloy chemistry on the microstructure and properties of NiCrBSi PTAW overlays (Liyanage et al., 2010). Overlay powders with similar chromium content were deposited in order to determine the influence of alloying components. The coatings consisted of a γ-Ni primary interdendritic matrix, in which the harder Ni+Ni_3B, Ni+Ni_3Si eutectics and Cr-based phases (CrB, Cr_3C_2 and Cr_7C_3) were observed. It was observed that volume fraction of the relatively soft interdendritic phase decreased drastically, while the proportion of chromium boride and carbides increased with increase in the C, B, Si and Cr content. Increased volume fraction of the hard eutectics and Cr-particles contribute to increase in the hardness and wear resistance.

Deng et al. studied the influence of the coatings thickness and temperature of Co-based hardfacing alloys deposited on DIN X45CrSi9-3 heat-resistant steel through PTAW surfacing technique (Deng et al., 2010). The extent of mechanical degradation of the Stellite-12 coatings by decreasing the coating thickness and increasing temperature was examined through Vicker's hardness test and three-point bending tests. The tests were performed at room temperature and at 500 °C. The microstructure of the coating consisted of Co-rich α dendritic phase with a network of chromium carbides (Cr_7C_3 and $Cr_{23}C_6$) in the interdendritic regions. The Vicker's hardness decreased by 6%, while the bending strength decreased by 10% by reducing the coating thickness from 2.5 mm to 1 mm. However, at elevated temperature (500 °C), a decrease of 25% in the bending strength was observed. This may be attributed to the decrease in the strength of materials at elevated temperatures.

Microstructure and wear behaviour of high C-Cr based alloy cladding developed through GTAW process was examined by Lin et al. (Lin et al., 2010). The coatings were developed using pure Cr and CrC alloy powders. The microstructural examination of the coatings indicates the formation of hypoeutectic, near-eutectic, hyper eutectic and proeutectic of Cr-Fe phases, $(Cr,Fe)_{23}C_6$ and $(Cr,Fe)_7C_3$ depending on the carbon content. The wear performance of the cladding is a function of the volume fraction of pro-eutectic phases and matrix microstructure. Cladding with 5.9% C exhibited the highest wear resistance, which can be attributed to high volume fraction of relatively hard pro-eutectic $(Cr,Fe)_7C_3$ carbides uniformly distributed in the eutectic colonies [$\alpha + (Cr,Fe)_7C_3$].

Madadi et al. studied the effect of pulse current on the microstructure and wear behaviour of Stellite6/tungsten carbide composite claddings produced through TIG surfacing process (Madadi et al., 2011). The properties of the pulsed current claddings were compared with that of the constant current properties. The microstructure examination reveals that pulsed current claddings exhibited finer microstructure and higher hardness (Fig. 2.6). The presence of faceted dendrites caused improvement in the wear resistance as more WC content was introduced in the faceted dendrites. In constant current, higher heat input resulted in higher dilution and lower hardness.

Gholipour et al. investigated microstructure and wear behaviour of Stellite 6 clads deposited on 17-4 PH stainless steel through GTAW method (Gholipour et al., 2011). The microstructure of the clad layer reveals presence of carbides embedded in Co-rich solid solution with dendritic structure (Fig. 2.6). The microhardness profile indicates increase in the hardness value from interface to the top layer. This is attributed to the presence of finer grain at the top surface as compared to the interface. Delamination was the main wear

mechanism in the clad layer, hence application of an interlayer was suggested to minimise dilution and hence improve the wear resistance of the clad layer.

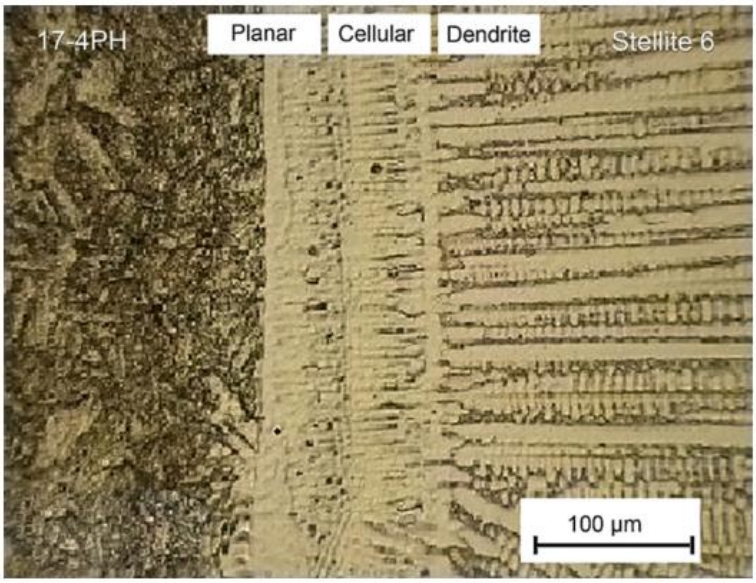

Fig. 2.6- Optical micrograph of Stellite 6 cladding on 17-4 PH stainless steel (Gholipour et al., 2011)

Liyanage et al. investigated the microstructure and abrasive wear behaviour of PTAW deposited Ni-WC overlays using different Ni-alloy chemistries (Liyanage et al., 2012). The matrix alloys chemistry of the overlays differed as Cr-free, Cr-low and Cr-high. The wear performance of the composite coatings with different matrix chemistries was compared. The Cr-free chemistry resulted in minimum WC dissolution, while the Cr-high chemistry leads to formation of the brittle carbides in the clad layer. Hence, increased volume fraction of retained WC and reduced volume fraction of brittle secondary brittle carbides enhanced the wear performance of the clads.

In another study, microstructure and wear behaviour of PTAW deposited Ni-alloy on AISI 304L stainless steel was examined (Guoqing et al., 2013). The wear behaviour of the deposited Ni-alloy was compared to the 304L substrate on block-on-ring wear testing machine. The microstructure of the as-deposited alloy consists of various phase such as: Ni-rich γ phase, Cr_7C_3, CrB, Cr_3C_2, Ni_3Si, Ni_3B and $M_{23}C_6$. The wear mechanism differs with the magnitude of the applied load and duration of wear test. For short duration, the mechanism of wear was abrasion for low load, while it was adhesive wear at high loads. During long duration, the mechanism of wear at low loads was adhesion and oxidation. At high loads it was reported to be fatigue wear.

Composite cladding consisting of hard carbide particles uniformly distributed in the tough matrix is ideally suited to counter abrasive wear. investigated the TiC-BN based cladding deposited on a AISI 1020 stainless steel substrate through GTAW surfacing process Peng and Kang (Peng and Kang, 2015). The boron nitride (BN) acts as a solid lubricant in the clad layer, which reduces the coefficient of friction and hence reduces wear. The hardness of the clad layer was observed to be about nine times higher as compared with the AISI 1020 substrate. The depth of wear in the TiC-BN specimens was reported to be one tenth of the substrate.

Heidary et al. studied the microstructure and abrasive wear characteristics of Mo-Fe-C hardfacing overlays deposited through GTAW process on DIN St-52 substrate (Heidary et al., 2015). The overlay powders were designed such that the hypoeutectic, eutectic and hypereutectic microstructures were obtained in the clad layer. The results indicate the presence of two types of carbides, Mo_2C and $(Mo,Fe)_6C$ in the deposited layer. The findings indicate that by increasing the amount of carbides in the hypereutectic structure would improve the abrasive wear behaviour of the overlays.

The available literature indicates that weld surfacing has been used to develop a variety of overlays over different substrates for imparting resistance against various forms of wear. The popularity of weld surfacing techniques is attributed to the low set-up and equipment cost and ability to deposit of small and large surfaces. However, high dilution, substrate distortion, irregular penetration in the substrate and high heat affected zone (HAZ) are the major limitations of the process (Gholipour et al., 2011; Lin and Wang, 2003; Madadi et al., 2011). Laser surface processing or laser cladding was attempted as one of the effective technique to overcome the limitations of weld surfacing techniques.

2.5.2. Laser Cladding

Laser has become the catch word for precision quality and speed. Laser processing of engineering materials enlightened the manufacturing industries in the late 1980s. Laser processing is a flexible technique, which uses a beam of light in the wavelength 700-900 nm with unique properties. Laser radiation can be controlled accurately, provides an intense source of energy, can be focused to small spot, spread to the requirement that is ideal for penetrating materials, spread into a diffused heating pattern to treat the surfaces (Ion, 2005).

Laser cladding is one of the most popular surface engineering techniques used to impart wear resistance to a number of industrial components. Laser cladding is a melting process in which a laser beam is used to fuse an alloy (powder) addition on to a surface.

The power may be introduced into the beam-material interaction zone either during the processing or prior to the processing. As very little substrate gets melted, the nominal composition of the powder is generally achieved in the clad layer. The molten clad gets solidified rapidly, forming a strong metallurgical bond with the substrate. Surface properties of the substrates can be tailored with by selecting an alloy for wear, erosion, corrosion and oxidation properties. In laser cladding, a thin layer of the substrate is melted along with complete melting of the clad powder. During melting of the substrate and clad powder, steep temperature gradient is developed between the leading edge of the melt pool and its centre. The temperature dependent surface tension drives the fluid flow, which stirs the weld pool and homogenises the composition of the clad layer (Ion, 2005). Laser cladding is schematically illustrated in Fig 2.7.

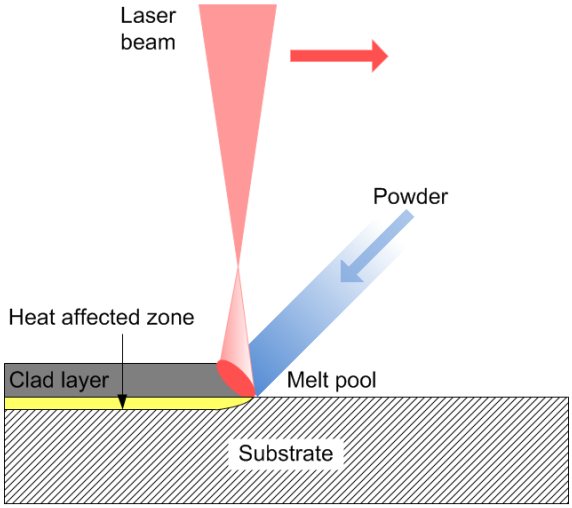

Fig. 2.7- Schematic of laser cladding process

The metallurgical bond between the clad and the substrate facilitates rapid heat transfer to the substrate, which acts an effective heat sink. High solidification and cooling rates results in fine clad microstructure, which endow superior wear and corrosion properties. Lower heat input causes little distortion to the components; therefore, the requirement of post-processing is significantly reduced. Close control of dilution from the substrate ensures the desired coating composition. A number of researchers have investigated laser cladding to develop wear resistant surfaces on various substrates. A brief review of some significant relevant investigations is presented in the following sections.

Frenk and Kurz investigated the solidification behaviour of Stellite 6 laser cladding on DIN X2CrNiMo1814 stainless steel (Frenk and Kurz, 1993). The cladding was carried out through 1.5 kW CO_2 laser with scanning speeds in the range of 1.67 m/s to 167

m/s. The microstructure of the clad specimens revealed the presence primary Co-based dendrites in the eutectic network of M_7C_3. Increased scanning speeds lead to considerable refinement of the microstructure of the clad layer for a constant laser power.

So et al. studied the wear behaviour of laser clad Stellite 6 alloy (So et al., 1996). The Stellite clads were deposited on mild steel and medium carbon steel coupons through a continuous wave 3.3 kW CO_2 gas laser. The wear behaviour was studied under load values ranging from 9.8 N to 156.8 N between sliding speeds of 1 m/s to 4 m/s. The wear mechanism in the clad layer was observed to be oxidative in nature. However, fatigue behaviour of the test led to spalling of the oxide layer formed on the clad specimens. Severe wear conditions had prevailed under the load of 156.8 N and sliding speed of 4 m/s, which led to delamination of the clad layer due to crack growth.

Zhenda et al. reported a study on microstructure of the Ni-WC composite laser clads (Zhenda et al., 1996). The AISI 1020 mild steel was used as the substrate for the Ni-WC clads developed through a 3 kW CO_2 laser. The WC particles were observed to be distributed in the tough Ni-based matrix in the microstructure of the clad layer. However, during the cladding, a thin layer of the substrate got melted, diluted and formed a metallurgical bonding with a reported dilution of 3-5%. The wear resistance of the composite clad layer was superior compared to the substrate due to uniform distribution of the hard WC particles in the clad layer.

Yang and Man studied the microstructural evolution of the W-C-Co laser clad powders through a 2 kW CO_2 laser (Yang and Man, 2000). The clad layer consisted of large WC particles in the eutectic matrix. Phases like WC, Co3W3C, α'-(Fe, Co) were observed to be present in the clad layer.

Kathuria presented a study on effect of power density and beam interaction time on the solidification and microstructure of the clad layer (Kathuria, 2000). The Stellite 6 clads were developed on Cr-12Ni steel substrate through a 5 kW continuous wave CO_2 laser. It was demonstrated that short interaction time produces fine microstructures, while long interaction time produces a relatively coarse microstructure. Finer microstructure results in higher hardness (621 HV) compared to the coarse microstructure (606 HV) in the clad layer.

Zhong et al. investigated the microstructural evolution of Stellite 6+WC laser clad layers (Zhong et al., 2002). The volume fraction of the WC was varied between 0 to 72% in steps of 9% by dual powder feeding method in 45 kW industrial CO_2 laser powder feeder. Presence of dendritic and interdendritic eutectics of α-Co, σ-CoCr and various M_7C_3 carbides was observed in the microstructure with WC content between 0-36%. When

the WC content was varied between 45-72%, the presence of faceted dendrites was observed in block, butterfly and star shapes.

Bendeich et al. investigated the residual stresses in the laser clad repaired turbine blades (Bendeich et al., 2006). Laser cladding of the blades resulted in generation of residual stresses in the parent material due to contraction during cooling and difference in thermal expansion coefficient of the clad material (Stellite 6) and substrate (SS420). Presence of tensile stresses was observed on the surface of the clad layer, which could aid in crack initiation. Hence post-weld heat treatment (PWHT) was carried out to minimise the magnitude of the residual stresses and reduce the possibility of crack initiation.

Xu et al. examined the characteristics of multi-layer laser cladding of Stellite-6 and WC powder mixtures (Xu et al. 2006a). The clad layers were deposited in constant chemical and functionally graded composition. The wear resistance of the constant chemical and functionally graded clad layers were more or less the same. However, it was observed that the crack sensitivity of the functionally graded composition was less than the constant composition clad layer.

Investigation on pulsed laser cladding of WC-12Co on low carbon steel was reported by Paul et al. (Paul et al., 2007). The study was aimed to overcome the limitations of continuous wave CO_2 laser clads of WC-Co. Presence of cracks, porosity, poor adhesion, partial melting WC in Co resulted in decreased performance of the clads. The pulsed laser cladding offers benefits such as lower average heat input, lower heat affected zone, lower dilution and low tendency to crack. Melting of WC particles was also controlled by modulating the pulse during laser cladding. The interfacial strength of the clad specimens was observed to 60 MPa, while the microhardness of the clad was in the range of 1270 to 1700 HV.

Zhou et al. investigated the crack behaviour of Ni-based WC composite coatings deposited through a 5 kW continuous wave CO_2 laser (Zhou et al. 2008a). The as-deposited specimens exhibited the presence of cracks that originated from the interface of the coatings. Hence, laser induced hybrid rapid cladding (LIHRC) was utilised to minimise the cracks in the clad layer. Further, as the temperature gradient was reduced in the clad it resulted in reduced dissolution of the WC particles in the clad layer. Consequently, the hardness of the LIHRC clad layer was higher than the non-LIHRC clad layer.

Zhang et al. reported on laser cladding of Colmonoy 6 on AISI 316 stainless steel substrate (Zhang et al., 2010). It was reported that preheating at about 450 °C was necessitated to develop crack-free clads. The microstructure of the clad exhibited the

presence of Ni-rich γ solid solution, borides and carbides. The wear resistance of the laser clad specimens was observed to be 53 times higher compared to the AISI 316 substrate.

Guo et al. studied the effect of Ni-WC content on the microstructure and wear resistance of NiCrBSi laser clads (Guo et al., 2011). It was observed that microhardness and wear resistance of the clad layer was greatly increased after adding the Ni-WC particles in the clad layer. However, it was reported that by increasing the WC content the crack susceptibility of the clad layer increased. The crack susceptibility was minimised by increasing the preheat temperature. Increased wear resistance was attributed to the formation hard WC-based phases and partial dissolution of the WC particles in the matrix.

Singh et al. examined the erosion and corrosion behaviour of laser cladded tungsten carbide on AISI 316 and 13Cr-4Ni steel substrates (Singh et al., 2012). The 83WC-17Co powder was deposited on the substrates through a diode laser. The hardness of the clad layer was observed to be 3 times and 2.5 times compared to the AISI 316 and 13Cr-4Ni substrates, respectively. The erosion and corrosion resistance of the laser cladded specimens was increased compared to the untreated substrates.

Paul et al. investigated the solid particle erosion behaviour of the WC/Ni composite laser clad layers with different WC content (Paul et al., 2013). The dissolution of the WC particles was not observed in the microstructure of the laser clad layers. Dendrites perpendicular to the clad-substrate interface were observed. The hardness of the clad layer was in the range of 900-2400 HV. The erosion resistance of the WC/Ni composite clads was observed to be four times higher compared to the clads without WC.

Laser cladding assisted by induction heating of Ni-WC composite was studied by Farahmand et al. (Farahmand et al., 2014). Laser clads with high weight fraction of WC results in issues like cracking, susceptibility, non-homogeneity and WC particle dissolution etc. (Fig. 2.8). The study investigated the Ni-60%WC laser clads with and without induction heating. It was observed that laser cladding assisted with induction heating resulted in smooth and homogenous microstructure without cracks or porosity. Further, addition of nano-WC particles and La_2O_3 enhanced the coating homogeneity, microstructure refinement and microhardness.

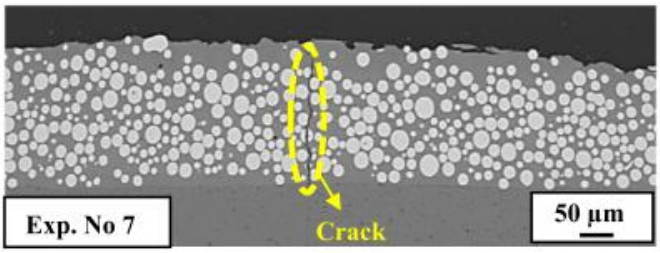

Fig. 2.8- SEM micrograph of Ni/WC laser clad without preheating (Farahmand et al., 2014)

Bartkowski et al. looked into the microstructure, microhardness and corrosion resistance of Stellite-6 coatings reinforced with WC particles using laser cladding (Bartkowski et al., 2015). Two coatings with 30% and 60% WC content were deposited using three laser power levels. Increasing the WC content led increased microhardness of the clad layer. However, increased laser power leads to reduced WC content in the coating. It was observed that the WC particles were well bonded in the Stellite 6 matrix.

A summary of the work carried out in the area of laser cladding is presented in Table 2.1. It is observed that laser cladding is popular attributed to better control over dilution level as well as higher cooling rate that enables to develop fine microstructure. However, laser cladding has some limitations like high set up cost, high operating and maintenance cost and low deposition efficiency. The development of high thermal stresses also cause clad cracking and distortion in laser cladding (Zhou et al. 2008b; Zhou et al. 2011; Farahmand et al. 2014). Further, porosity, lack of fusion and distortion are some other limitations associated with laser cladding (Ion, 2005; Zhong and Liu, 2010; Gupta et al., 2008). Conventional surface modification methods involve absorption of thermal energy on the surface of the workpiece and then the heat energy transferred inside through thermal conduction (Acierno et al., 2004). The authors reported that the kinetics of heat transfer mainly depends on physical properties (thermal conductivity, thermal diffusivity, specific heat, convective heat transfer coefficient etc.) of materials, which govern the quality of the engineered surface.

Table 2.1- Summary of laser cladding literature

Clad Material	Author (Year)	Processing conditions	Remarks
Stellite 6	Frenk and Kurz (1993)	• CO_2 laser • Power: 1.5 kW • Scanning speed: 1.67 to 167 mm/s	Increased scanning speed leads to refinement of the microstructure
	So et al. (1996)	• CO_2 laser • Power: 3.3 kW • Scanning speed: 300 mm/s	• At low loads, wear took place due to oxidation. • Delamination of the

		• Powder feed rate: 15 g/s	clad layer occurred at higher loads.
	Kathuria (2000)	• CO_2 laser • Power: 5 kW • Powder feed rate: 24 g/min	Shorter interaction times results in finer microstructure
	Bendeich et al. (2006)	• CO_2 laser • Power: 1.5 kW	• Tensile residual stresses observed in the clad layer • Post processing minimised the residual stresses
Stellite 6 + WC	Zhong et al. (2002)	• CO_2 laser • Power: 8 kW • Beam diameter: 1.2 mm • Scanning speed: 0.4 m/min • Powder feed rate: 57 g/min	WC content between 45-72% resulted in dendrites of various shapes
	Xu et al. (2006a)	• Diode laser • Power: 2.5 kW • Beam diameter: 1 mm • Travel speed: 0.4 m/min • Powder feed rate: 11.86 g/min	Crack susceptibility of the functionally graded clads was less compared to constant composition clads
	Bartkowski et al. (2015)	• Yb-YAG laser • Power: 1 kW • Beam diameter: 1.64 mm • Overlapping: 40% • Power: 1.5 kW	• Increased WC content increased microhardness • Increased laser power reduced WC content
Ni-WC	Zhou et al. (2008b)	• CO_2 laser • Power: 5 kW • Induction heater power: 20-30 kW • Induction heater frequency: 30 kHz • Powder feed rate: 52-82 g/min	• Laser induced hybrid rapid cladding minimised the cracks • Low temperature gradient resulted in low dissolution of WC
	Zhenda et al. (1996)	• CO_2 laser • Power: 3.0 kW	• Dilution of 3-5% • WC particles distributed uniformly
	Paul et al. (2013)	• CO_2 laser • Power: 1 to 1.5 kW • Beam diameter: 1.2 mm • Scanning speed: 0.2 to 0.5 m/min • Powder feed rate: 5-8 g/min	• No dissolution of WC particles • Hardness between 900-2400 HV
Ni-WC + nano WC and La_2O_3	Farahmand et al. (2014)	• High power diode laser • Power: 2.7 to 3.5 kW • Preheating temperature:	• Higher WC weight fraction leads to cracking.

		150 to 300 °C • Scanning speed: 5-9 mm/s • Powder feed rate: 0.6 to 1.2 g/min	• Induction heating causes results in smooth and homogenous microstructure
WC-Co	Yang and Man (2000)	• CO_2 laser • Power: 0.6 to 1.2 kW • Beam diameter: 3 mm • Powder feed rate: 7 g/min • Traverse velocity: 5 mm/s	Large WC particles present in the eutectic
WC-12Co	Paul et al. (2007)	• Nd-YAG pulsed laser • Power: 1.0 kW • Scanning speed: 1 to 10 mm/s • Powder feed rate: 3-8 g/min	• Pulsed laser improved the microstructure of the clads • Interfacial strength was in the range of 60 MPa
WC-17Co	Singh et al. (2012)	• CO_2 laser • Power density: 114 to 182 kW/mm^2 • Scanning speed: 600 mm/s • Powder feed rate: 16 g/s • Overlapping 25%	Hardness increased by 3 times
Colmonoy 6	Zhang et al. (2010)	• CO_2 laser • Power: 2.0 kW • Powder feed rate: 17.5 g/min • Travel speed: 700 mm/min	• Preheating at 450 °C required for crack-free clads • Wear resistance enhanced by 53 times
NiCrBSi+Ni/WC	Guo et al. (2011)	• CO_2 laser • Power: 2.0 kW • Scanning speed: 1000 mm/s • Beam diameter: 3 mm • Overlapping: 50%	• Increasing WC content increased cracking • Cracking minimised by preheating

2.5.3. Nanostructured Coatings

In the recent years, nanostructured coatings are used on surface of different parts to enhance their tribological and corrosion resistance properties. Today with development and expansion of nanotechnology, nanostructured coatings are being widely used in aerospace, military, power generation, electronics industry due to their unique properties such as corrosion resistance, high hardness and wear resistance etc. (Gleiter, 2000, 1995, 1989; Siegel, 1993). The scale of nanomaterials is classified from 1-100 nm, which is cluster or nuclear pellet with less than 100 nm size. Nanomaterials show specific properties, which they do not show in the micrometric size range. These effects come from the 'size effects' of the nanomaterials (Aliofkhazraei, 2011).

Surface coatings are used to enhance the resistance of the engineering components against various environmental agents such as corrosion, wear, improving physical properties such as electrical and magnetic. Application of nanomaterials in surface engineering is of great interest and the main objectives are as follows:

a) Promoting coating quality
b) Increasing lifetime of the products
c) Lowering cost of production, repairs and maintenance
d) Adapting the environment

Considering the developments in the field of nanotechnology, its application in surface engineering can be considered as one of the active areas. Increased strength, hardness, ductility and toughness could provide a new generation of structural nanostructured coatings (Gell, 1995). Research in the nanomaterials has opened up a wide range of potential benefits as shown in Fig. 2.9.

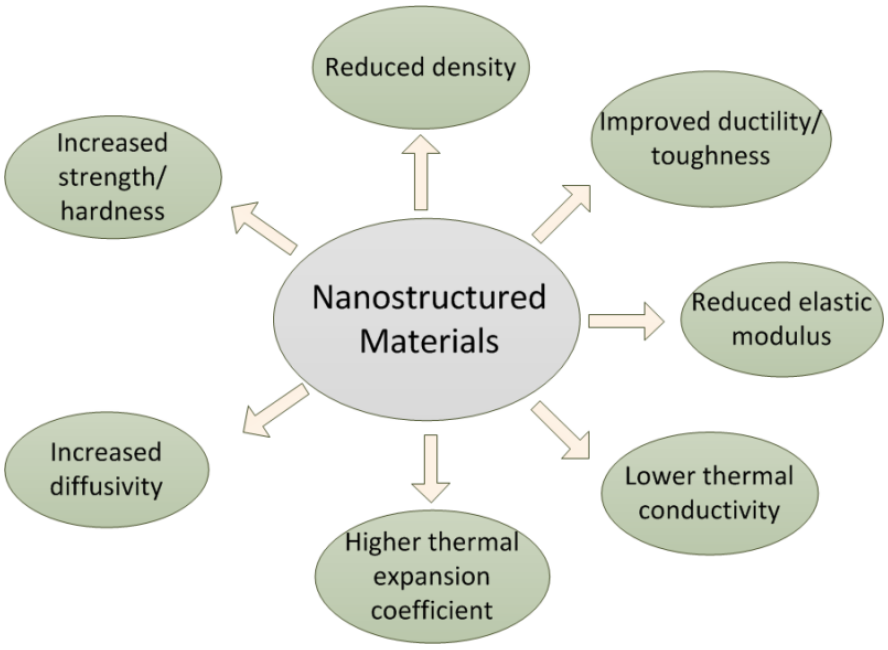

Fig. 2.9- Changes in properties associated with nanostructured materials (Gell, 1995)

The plastic deformation of the nanocrystalline materials is strongly dependent on the grain size. The coating/cladding have increased demand of optimum combination of various mechanical and metallurgical properties. It has been learnt that composite coatings commonly consisting of hard reinforcing phase embedded in a tougher matrix could provide such properties. These coatings consist of extremely hard reinforcing phases of carbides, nitrides and oxides of aluminium, tungsten, titanium and chromium (Hasan et al,

2008; Stokes and Looney, 2004; Stokes and Looney, 2009; Rajakumar et al., 2010; Karthikeyan et al., 2016). In this context, nanostructured coatings have recently attracted increasing interest because of the possibilities of synthesizing materials with unique physical-chemical properties (Holubar et al., 2000; Musil, 2000; Zhang et al., 2003). In bulk materials, grain boundary hardening is one of the possibilities for hardness improvement. With decrease in grain size, the multiplication and mobility of the dislocations are hindered, and the hardness of materials increases according to the 'Hall–Petch' relationship: $H(d)=H_0+Kd^{-1/2}$. This effect is especially prominent for grain size down to tens of nanometers. However, beyond 10 nm grain size the grain boundary sliding starts, which causes softening of the grains under stress.

Thermal spraying has been traditionally a popular route to deposit the nanostructured coatings. A lot of research has been focused on development of WC-Co based nanostructured coatings through variants of thermal spray processes. It has been reported that the wear resistance of the WC-Co composites increases significantly as the carbide grain size is reduced (Jia and Fischer, 1997, 1996; O'Quigley et al., 1997; Stewart et al., 1996). These properties are improved due to the fact that as the carbide grain size is decreased (for a given binder content), the mean free path of the matrix is reduced resulting in greater constraint, increased hardness and a reduced tendency for binder phase extrusion (Qiao et al., 2003). Zhu et al. compared the tribological properties of conventional and nanostructured WC-Co plasma sprayed coatings. Improved hardness and toughness of the nanostructured coatings enables them to exhibit improved wear performance compared to the conventional coatings (Zhu et al., 2001). However, it was reported that decomposition of the carbide phase in the nanostructured coatings during spaying tends to reduce their wear performance. He and Schoenung presented an extensive review on nanostructured WC-Co coatings (He and Schoenung, 2002). They reported how the decomposition of the WC phase during spraying can be minimised. Controlling the initial powder composition, spraying parameters such oxygen-fuel ratio, fuel chemistry can reasonably control the decomposition of the essential WC phase in the coatings. Yang et al. examined the effect of carbide size on microstructure and wear behaviour of WC-12Co coatings (Yang et al., 2003). It was concluded that wear resistance of the coatings decreased with increased carbide size. Zhang et al. presented a review on superhard nanocomposite coatings (Zhang et al., 2003). They concluded that coatings for advanced engineering applications required hardness as well as toughness. Shipway et al. compared the sliding wear behaviour of conventional and nanostructured WC-Co coatings (Shipway et al., 2005). It was reported that the nanostructured coatings exhibited the higher wear resistance. However, loss

ductility of the Co phase due to decomposition during spraying lead to the subsurface fracture and generation of wear debris.

Thermal sprayed deposits often require post processing to enhance their hardness and wear resistance. However, a study presented by Chen et al. reported that laser meting decreased the hardness and wear resistance of the thermal sprayed conventional and nanostructured coating (Chen et al., 2005). This was attributed to the fracture of large carbides and reduction of the carbide size. In an another study, dry sliding wear and friction performance of nanostructured WC-12Co coating it was observed to be better than the conventional coating even at elevated temperature (400 °C) (Zhao et al., 2006). Cold spraying is another popular variant of thermal spray process in which nano size of the reinforcing carbides is retained in the coating. However, bonding between cold sprayed nanostructured WC-12Co particles was improved by post spray annealing treatment without compromising with the hardness of the coating (Li et al., 2007).

Cho et al. reported a contrasting study revealing the lower hardness in the nano sized WC-Co HVOF sprayed coating (Cho et al., 2008). They attributed it to the decomposition of the nano sized WC phase while spraying due its higher surface area to volume ratio. Further, in an another study it was concluded that the coatings with nano sized WC exhibited higher sliding wear resistance compared to the ultra-fine sized WC particles (Chen et al., 2009). It was reported that addition of appropriate amount of nano WC-12Co powder in WC-10Co-4Cr HVAF coatings improved the wear resistance of the coatings (Liu et al., 2010). In another study, different gas mixtures were utilised to minimise the decarburisation of the WC phase (Di Girolamo et al., 2013). Best results were obtained when mixture of Ar + He utilised to deposit the coatings. Al-Mutairi et al. concluded the HVOF sprayed nano WC-Co coatings were better than the plasma sprayed components in terms of hardness and wear resistance (Al-Mutairi et al., 2015). This can be attributed to the low porosity, high density, good adhesion, lower degree of decarburisation of the carbide phase.

Thermal spraying and its variants have been a popular surface engineering technique. But thermal sprayed coatings are only mechanically anchored to the surface and are not metallurgically bonded to the substrate. Thermal sprayed deposits often present issues such as exfoliation, cracking and spalling while exposed to wear conditions. Several studies were conducted on post processing of thermal sprayed coatings to improve their density, increase homogeneity and reduce porosity. Another major concern that can be observed form the literature is high ratio of surface area to volume of the nanostructured

WC–Co powder that leads to the decomposition of the carbide phase during the thermal spray process.

2.5.4. Microwave Cladding

Microwaves are electromagnetic radiations in the frequency range of 300 MHz to 300 GHz and wavelength of 1 m to 1 mm. Microwaves are coherent and polarized and can be transmitted, absorbed, or reflected depending on the material type being processed (Clark and Sutton, 1996). Originally microwaves were used for tele-communication before, radar detection, tracking, electronic warfare, medical treatment, non-destructive testing, power transmission, heating etc. However, application of material heating through microwaves was first discovered in 1946 by Percy Spencer. It was later discovered that in microwave heating, energy conversion takes place instead of energy transfer through conventional modes of heat transfer. Since then microwaves have been extensively used in material processing due its attributes such as volumetric heating, reduced processing time, low power consumption and less environmental hazards (Jones et al., 2002; Ku et al., 2002). Until the year 2000, basically ceramics, ceramic composites, polymers, polymer composite and semiconductors were processed with microwaves because they are good absorber of microwaves at room temperature (Bajpai et al., 2012; Cheng et al., 2001; Fang et al., 2008; Fisher et al., 2003; Zhu et al., 2008; Aravindan et al, 2000; Ramkumar et al., 2002, 2005). There was a misconception that all metals reflect microwaves or cause plasma formation; hence they can't be processed using microwaves. But, this observation was not valid for powdered metal or bulk metallic materials at high temperature (Leonelli et al., 2007; Mondal et al., 2010). Heating of the metallic powders depends on its skin depth (δ). Skin depth of material also determines to what depth the material will be directly heated with microwaves (Agrawal, 2010). The skin depth of metallic material increases at higher temperature due to decrease in permeability and conductivity of material. Skin depth of material also depends on the purity of material and different phases present in it.

Since then, microwave energy has been extensively used in processing ceramics, polymers, ceramics composites, metallic materials and other lossy dielectric materials through sintering, melting, surface engineering (including glazing, coating and cladding), joining, drilling (Alpert and Jerby, 1999; Aravindan and Krishnamurthy, 1999; Bansal et al., 2015, 2014; Boccaccini et al., 2001; Breval et al., 2005; Brosnan et al., 2003; Cheng et al., 2001; Dikhtyar and Jerby, 2006; Gupta and Sharma, 2011a; Gupta and Wong, 2005; Leonelli et al., 2007; Link et al., 1999; Minay et al., 2004; Mondal et al., 2010; Oghbaei and Mirzaee, 2010; Peelamedu et al., 2002; Rajkumar and Aravindan, 2011, 2009; Sharma

and Gupta, 2012; Sharma and Krishnamurthy, 2002; Sharma et al., 2001; M. Srinath M.S. et al., 2011a; Srinath M.S. et al., 2011b; Tun and Gupta, 2009; Tun et al., 2010; Vaidhyanathan et al., 2000; Veronesi et al., 2003; Vijayakumar et al., 2002; Wong et al., 2005; Zafar et al., 2014; VaradaRajan et al., 2006). Detailed investigations on mechanisms of microwave material interaction and microwave heating have been published and available elsewhere (Mishra and Sharma, 2015; Oghbaei and Mirzaee, 2010; Singh S. et al., 2015a, 2015b; Thostenson and Chou, 1999). The applications of microwaves in processing of metallic materials in different form are shown in Fig. 2.10.

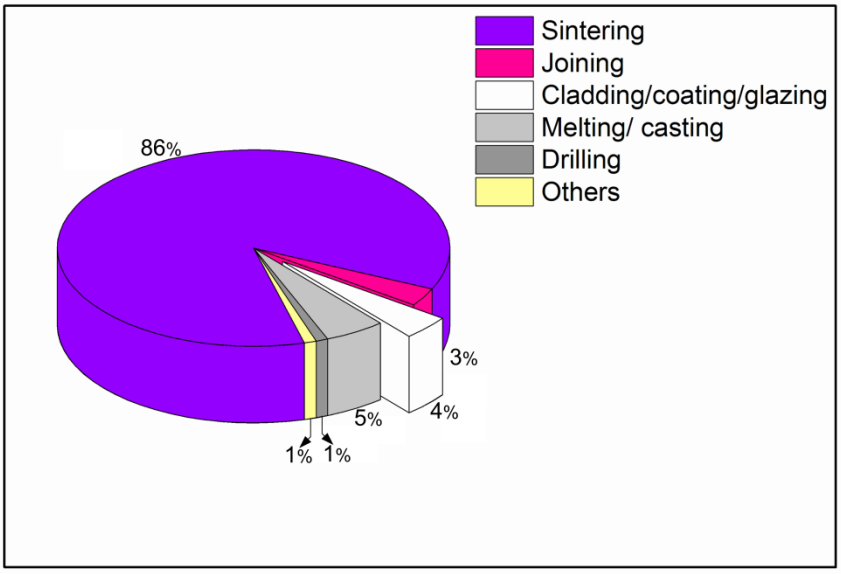

Fig. 2.10- Application of microwave energy in processing of metallic materials

The possibility of using microwaves is surface engineering was first reported in 2005 when a nickel titanium (NiTi) plate of 1.2 mm thickness was successfully clad on AISI 316L stainless steel substrate by a microwave-assisted brazing process (Chiu et al., 2005). Later Borneman and Saylor reported coating of friction reducing alloys using CuNiIn powder on Ti-6Al-4V substrate through microwave radiation (Borneman and Saylor, 2008). NiAl coatings were developed on Ti substrate through microwave energy in which ternary Ni-Al-Ti eutectic was formed that acts as an interlocking agent between the coating and substrate (Cammarota et al., 2009). Das et al. developed approximately 42 µm and 661 µm thick alumina coating on aluminium substrate by exposing to microwave radiation for 60 min and 90 min, respectively (Das et al., 2008). Glass based ceramic (MgO-Al_2O_3-TiO_2) coatings were developed on nimonic superalloy substrates through microwave and conventional heat treatment processes and results indicate that there was considerable improvement in nanohardness and Young's modulus of microwave processed

coatings that conventionally processed coatings (Das et al., 2010). Application of microwave energy was also exploited earlier for glazing of plasma sprayed surfaces. The results indicate that the microwave glazed surfaces have superior properties than conventionally processed surfaces (Sharma and Krishnamurthy, 2002; Sharma et al., 2001).

Microwave cladding is one of the recently developed and novel surface modification routes, which involves melting and deposition of the hardfacing clad powder on the substrate using microwave energy. Microwave cladding has come up as an emerging surface modification technique to resolve the limitations of laser processing (Sharma and Gupta, 2010). Microwave hybrid heating (MHH) technique is actually employed to accomplish the microwave cladding. The MHH is being employed to overcome the difficulties in heating low microwave absorbing material like metal and mostly ceramics. The technique utilises an additional material (susceptor) in the microwave cavity that readily absorbs electromagnetic energy at room temperature. The susceptor couples with microwaves at room temperature and gets heated up rapidly which, in turn, elevates the temperature of the poor microwave absorbing materials and enable them to couple with microwaves at higher temperature. The poor microwave absorbing materials is heated up through conventional mode(s) of heat transfer from the hot susceptor material initially. A schematic representation of microwave hybrid heating is shown in Fig. 2.11.

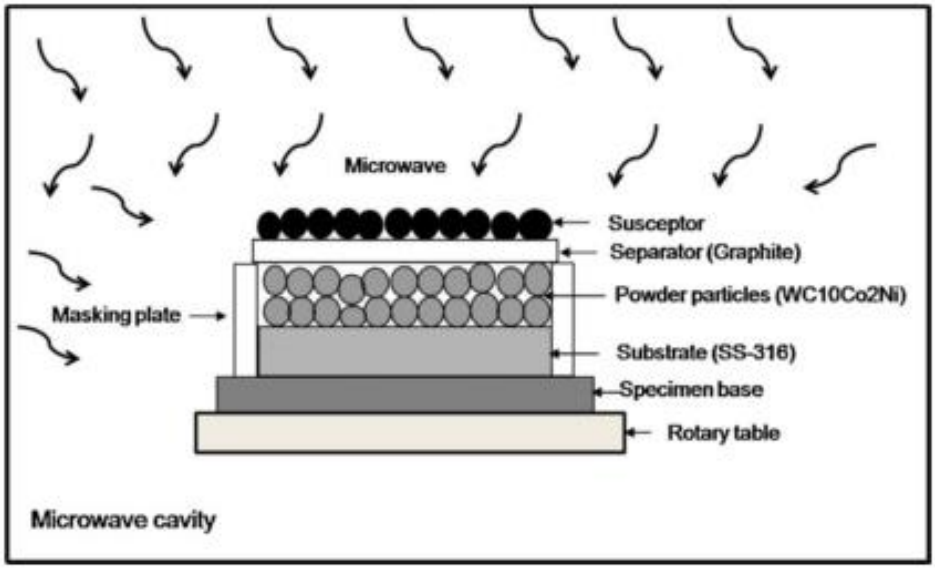

Fig. 2.11- Schematic of microwave hybrid heating setup used to develop clads (Gupta and Sharma, 2014)

In microwave processing, electromagnetic field directly supplies the energy to the material. Molecular level interaction of microwave can generate heat throughout the volume of the material. Microwave processing has some significant attributes including substantially rapid processing speed, rapid heating rates, reduced processing cycle time and development of uniform microstructures due to volumetric heating characteristic of microwave heating (Bansal et al., 2014; Breval et al., 2005; Clark and Sutton, 1996; Gupta and Sharma, 2014; Metaxas, 1991; Roy et al., 1999; Sharma et al., 2001; Sunil et al., 2010). Attributed to the volumetric heating phenomena of microwave heating, the developed clads exhibit dense microstructure and were free from interfacial and solidification cracking. In microwave cladding, only the surface layer of the substrate (approximately 10-15 μm) as reported by Gupta and Sharma (Gupta and Sharma, 2011a) is melted (due to low skin depth) and complete melting of overlaid particles does take place. This becomes possible owing to the fact that the clad powder particles couple with microwave efficiently (due to higher skin depth). The substrate gets melted to a few microns (only the skin depth approximately 10-15 μm) owing to conventional conductive heating from the molten powder layer (Gupta, 2012). The bulk of the metal-based substrate reflects the microwave due to negligible microwave interaction. This cladding has the advantage that metallic matrix exhibits better toughness while the metallic reinforcement yields increased hardness and hence enhanced wear resistance. The authors have further reported skeleton-like reinforcement (hard carbide) structure in the Co based matrix in case of cermet cladding. They have also illustrated that the hard particles are uniformly distributed in the soft matrix and the clad exhibits significantly higher wear resistance (Gupta and Sharma, 2011b). Sharma and Gupta (Sharma and Gupta, 2012) reported on development metal ceramic composite through microwave radiation. Solidification pattern of the clads exhibited cellular microstructure in the clad layer, which is an indicative of volumetric heating of microwave energy. The average flexural strength of the clad layer was reported to be 629±8 MPa. Further Zafar et al. have attempted to improve the microwave cladding process by concentrating the microwaves within the hot zone of a refractory insulating box (Zafar et al., 2013). Inconel 718 clads with approximately 1 mm thickness have been developed due to metallurgical bonding of overlay material with partial melting of the substrate surface layer. The developed clads exhibit columnar dendritic morphology. It is significant to note that microwave cladding results in considerable reduction in porosity due to uniform heating associated with MHH. Further, the usually present cracking in laser clads were reported to be absent in the microwave clads (Zafar et al., 2014). Application of microwave cladding was further extended to

develop EWAC+20%WC10Co2Ni on mild steel (MS) substrate (Pathania et al., 2015). The developed clad exhibited an average microhardness of 980±52 HV, while the wear resistance of the clads was enhanced by 128 times compared to the MS substrate. Kaushal et al. (Kaushal et al., 2015) presented investigation on development of Ni+10%SiC composite cladding on martensitic stainless steel (grade: 420) using microwave energy. Clad layer of approximately 1.25 mm exhibited a porosity of about 1.10%. The average Vicker's microhardness of the clad layer was 652±90 HV.

Further, the wear behaviour of the engineered surfaces through laser cladding, thermal spraying and microwave cladding is better understood by correlating with their mechanism of formation. The principles of formation of the three surfaces are schematically illustrated through 'single particle processing' concept in Fig. 2.12. In laser cladding, the electromagnetic radiation is absorbed by the clad powder particles according to their absorptivity. Depending on the interaction time, the electromagnetic energy causes local melting of the clad powder, which forms the engineered layer upon solidification (Fig. 2.12). Complete melting and solidification yields dense microstructure. However, in laser clads, there are a few concerns regarding development of residual stresses due to high thermal gradient, solidification cracking and the presence of porosity. Therefore, the presence of porosity and microcracks leads to spalling of the laser clad layer under severe wear conditions. In case of thermal spraying, the wear resistant layer gets built up due to combined action of rapid acceleration and intense heating. Molten/semi- molten particles, on impact with the substrate, get transformed into splats or lamellae (Fig. 2.12(inset)). The subsequent splats get deposited onto the previous splats in a layer by layer structure (Fig. 2.12). These individual splats get significantly deformed with respect to their original particle geometry; however, in most of the cases still retains the trace of a separate particle boundary as can be visualised in Fig. 2.12. Thus, the splats are mechanically anchored on the substrate and are not metallurgically bonded. This results in an inhomogeneous micro-structure with the presence of pores and cracks. Such microstructure thus, fails to exhibit superior wear performance, although wear resistance increases to certain extent owing to enhanced surface hardness. The splats also exhibit a tendency to decohere while subjected to wear conditions. In microwave processing, the heat is generated inside the powder particle due to dielectric losses which causes volumetric heating and subsequent melting. The molten particle causes the substrate temperature to rise to its melting point and get fused (Fig. 2.12). On solidification, a metallurgically bonded clad is obtained with dense and uniform microstructure, negligible porosity and the absence of solidification cracking. The properties of the developed clads, however, depends significantly on the processing

conditions. Control of the processing parameters play a key role often in tailoring the characteristics of the developed/modified surface.

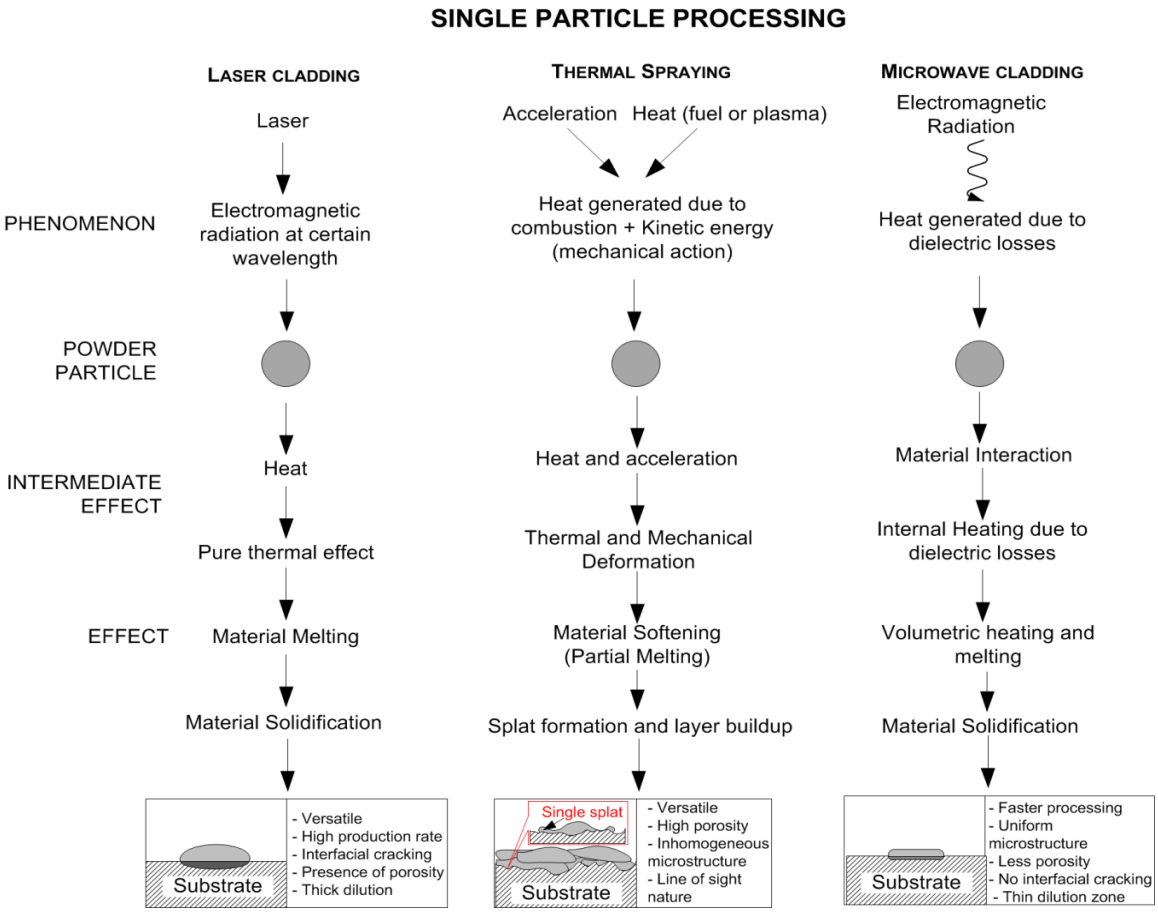

Fig. 2.12- Schematic diagram illustrating single particle processing

2.5.5. Process Parameters in Microwave Cladding

The development of clads is highly dependent on the processing parameters, such as, powder properties, powder particle size, clad thickness, microwave power, exposure time, size of the substrate etc. However, keeping other parameters fixed, microwave power and exposure time are the variables that can be changed to optimise the parameters for the different clad powders. available literature on microwave power and exposure time is presented in Table 2.2. The parametric details reveal that, while 900 W power is optimum, the exposure time required varies considerably with target material system.

It is evident that the application of microwave cladding to develop wear resistant surfaces is now growing. However, from the available literature it can be concluded that only micrometric clad powders have been used to develop the clads. Nanostructured materials exhibit high surface area per unit volume compared to the micrometric sized

materials. It is well established that material processing through microwave energy is possible based on interaction of the target material with microwaves. Higher surface area of nanomaterial could lead to better coupling with the incident microwave radiation. Therefore, the clads could be developed in less power and exposure time. Moreover, the uniform and volumetric heating characteristics of microwave processing could result in a uniform microstructure in the clad layer, which could improve the tribological performance of the nanometric clads.

Table 2.2- Parametric details of microwave cladding of various clads and substrate system

Clad Material	**Reported by**	**Microwave power (W)**	**Exposure time (s)**	**Substrate size (mm^3)**	**Substrate material**	**Powder particle size (μm)**
EWAC (Ni-based)	Gupta and Sharma, 2011a	900	360	35 × 12 × 6	ASS-316	40
WC10Co2Ni	Gupta and Sharma, 2011b	900	360	35 × 12 × 6	ASS-316	40
EWAC+20% WC10Co2Ni	Sharma and Gupta, 2012	900	420	35 × 12 × 6	ASS-316	40
EWAC (Ni based+20% $Cr_{23}C_6$	Gupta et al., 2012	900	360	35 × 12 × 6	ASS-316	40
Inconel 718	Zafar et al., 2013	900	720	25 × 25 × 8	ASS-304	30
EWAC+20% WC10Co2Ni	Pathania et al., 2015	900	360	10 × 10 × 6	MS	40
Ni+10%SiC	Khaushal et al., 2015	900	---	30 × 10 × 4	MSS-420	40

ASS: Austenitic stainless steel; MS: Mild steel; MSS: Martensitic stainless steel

2.5.6. Structure-Property Correlations in Microwave Cladding

The microstructure of the developed clad is a consequence of the processing parameters, clad powder etc. The clads developed through microwave cladding exhibit uniform microstructure, negligible interfacial cracking or solidification cracking and less porosity less than 1%). The microwave induced clads exhibit a wavy interface, attributed to the localised convective currents during microwave exposure. These convective currents lead to melting and mixing of a thin interfacing layer of the substrate (approximately 10-15 μm). A typical microstructure of the microwave WC10Co2Ni clad on austenitic stainless steel (grade 316) substrate is shown in Fig. 2.13. The reinforcement in the form of skeleton structured carbides is uniformly distributed in the metallic matrix (Fig. 2.13). Such clads have an advantage, the metallic matrix exhibits better toughness, while the metallic

reinforcement yields increased hardness and hence enhanced wear resistance. The microhardness profile of the WC10Co2Ni clad is shown in Fig. 2.14. The average microhardness of this clad layer was in the range of 1064±99 HV (Gupta and Sharma, 2012).

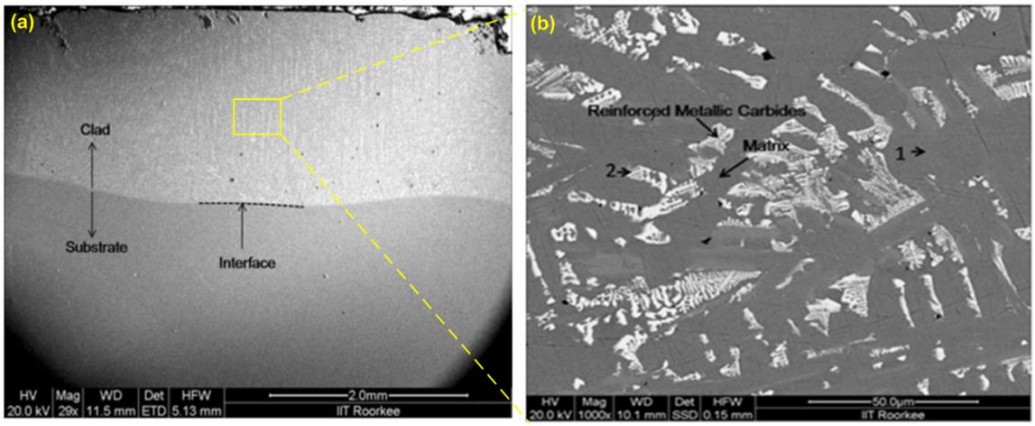

Fig. 2.13- A typical SEM micrograph of WC10Co2Ni microwave clad (a) at interface and (b) in the clad layer (Gupta and Sharma, 2012)

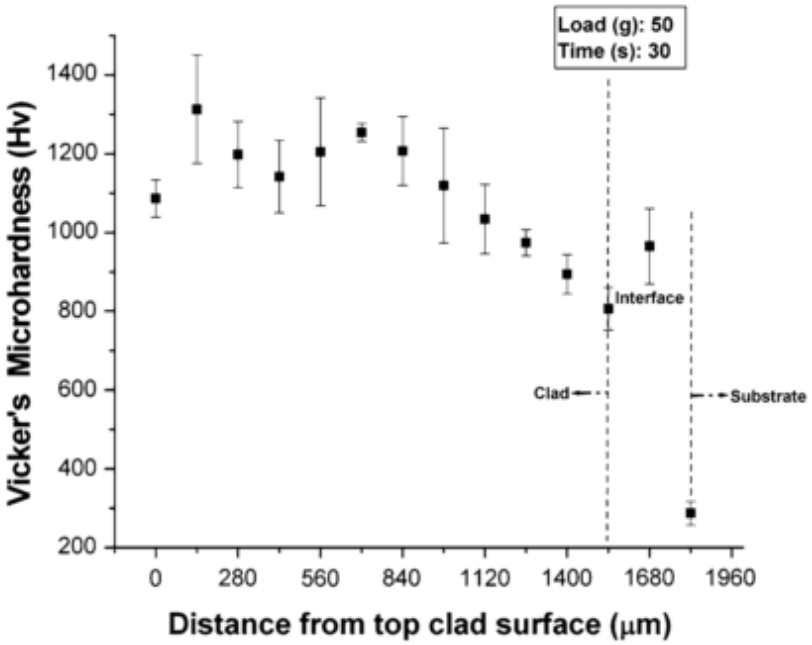

Fig. 2.14- Vicker's microhardness profile across a typical section of WC10Co2Ni microwave clad (Gupta and Sharma, 2012)

The uniform and volumetric heating nature of the microwave heating leads to the development of uniform microstructure in the clad layer. The effect of uniform microstructure affects various properties of the microwave clads. A few flexural strength values of the clads developed through laser cladding, PTAW and microwave cladding are

illustrated in Table 2.3. It can be concluded that in case of micrometric composite powders, such as WC10Co2Ni, the clad layer consists of eutectic carbides, which were uniformly distributed in the metallic matrix. However, the size of the reinforcing eutectic carbides was in the micrometric domain. Application of nanometric clad powders to develop nanometric reinforcing carbides in the clad layer could be an interesting investigation. Nanostructured clads could offer increased strength and hardness along with ductility and toughness. Based on the property improvements, the nanometric clads using microwave energy could be developed through modifications in the process parameters.

Table 2.3- Flexural strength values of a few clads

Clad material	**Technique**	**Flexural strength (MPa)**	**Reported by**
EWAC+20% WC10Co2Ni	Microwave cladding	629	Sharma and Gupta, 2012
WC-12Co	Laser cladding	60	Paul et al., 2007
Stellite 12	PTAW cladding	1089	Deng et al., 2010
Al-TiB2-TiC	Laser cladding	400	Ravnikar et al., 2013
Stellite 6	Laser cladding	69	Hjörnhede and Nylund, 2004

The microstructure of the clad layer influences the tribological properties of the clads to a great extent. In microwave cladding, the heat is generated within the target material due to dielectric losses. The uniform heating characteristics of microwave leads to development of a uniform microstructure as illustrated in Fig. 2.12. Consequently, there is excellent metallurgical bonding between the substrate and clad layer, with negligible porosity and interfacial cracking. In case of composite clads (Fig. 2.13), the uniformly distributed skeleton structured carbides provide reinforcements to the metallic matrix. Therefore, the microwave clads exhibited increased wear resistance (Table 2.4). A few results on the tribological aspects of the engineered surfaces with WC-based material through various techniques are illustrated in Table 2.4. However, it would be interesting to investigate the influence of nanostructured powders on the microstructure of the microwave induced clads. The role of microstructure in determining the tribological performance of the clads under various wear regimes are yet to be investigated exhaustively. Nanostructured clads could offer increased strength and hardness along with ductility and toughness. Based on the improvements in the properties, the nanometric clads using microwave energy could be developed, this may need suitable adjustments in the process parameters.

Table 2.4- Tribological properties of a few clads

Clad material	**Technique**	**Test Conditions**	**Cumulative weight loss (mg)**	**Reported by**
EWAC+20% WC10Co2Ni	Microwave cladding	Setup: Pin-on-disc Load: 15 N Sliding speed: 1 m/s Sliding distance: 1500 m Lubrication condition: Dry	0.6	Pathania et al., 2015
WC10Co2Ni	Microwave cladding	Setup: Pin-on-disc Load: 20 N Sliding speed: 1 m/s Sliding distance: 2000 m Lubrication condition: Dry	1.2	Gupta and Sharma, 2011b
WC	Laser cladding	Setup: Pin-on-disc Load: 19.62 N Sliding speed: 1.12 m/s Sliding distance: 300 m Lubrication condition: Dry	2	Gupta et al., 2008
WC-Ni	Laser cladding	Setup: Block-on-ring Load: 25 N Sliding speed: 1.67 m/s Sliding distance: 6100 m Lubrication condition: Dry	2.106	Zhenda et al., 1996
Ni-WC	Laser cladding	Setup: Block-on-ring Load: 400 N Sliding speed: 0.5 m/s Sliding distance: 2500 m Lubrication condition: Dry	4	Chen et al., 2005

2.5.7. Simulation Studies on Microwave Processing of Materials

Microwave energy has been used widely to process different types of materials. The dielectric properties of the material play a critical role in microwave processing of materials. The heat generated in the material is a consequence of the interaction of the electric field and magnetic field with irradiated material. Ferromagnetic materials are generally affected by the magnetic field distribution in the applicator cavity (Ayappa et al., 1991). The microwave applicator cavities are broadly classified as single-mode and multi-mode. Single-mode cavities support a single resonant mode at a given frequency, making the field distribution throughout the cavity relatively non-uniform. As a result, formation of hot spots occurs in regions of high electric field intensity, thus requiring careful sizing and placement of materials (Clemens and Saltielt, 1996). Hence, multi-mode cavities are preferred to avoid this problem by over-sizing the cavity and/or increasing the frequency of

the excitation source so that a number of high-order modes are supported simultaneously. While the fields within an empty cavity will be more uniform, the electromagnetic field intensity can be highly distorted if an absorbing material is placed in the cavity. Field distortion for high loss materials, such as ceramics, will generally be much greater than for low loss materials, e.g. polymers. Achieving uniform temperatures within the processed sample will be difficult unless the electromagnetic field distribution can be well characterized. In situations where materials absorb microwave radiation more efficiently at higher temperatures due to dramatic increase in electrical conductivity, locally temperature can rise exponentially and can lead to 'thermal runaway' (Oghbaei and Mirzaee, 2010). Thermal runaway phenomenon has been displayed by a variety of materials, including zirconia, alumina, glass ceramic, nickel zinc ferrite and nylon (Clemens and Saltielt, 1996). Poor product quality and sample cracking are often exhibited if temperature levels and distributions cannot be controlled. Therefore, understanding, predicting and preventing or controlling thermal runaway presents a major challenge to the development of microwave processing. Very limited work has been carried out in the field of simulation studies microwave processing of materials. In the following sections, relevant available reports on simulation of microwave material processing have been briefly reviewed.

The heat energy is of utmost importance while processing materials with microwave energy. A few factors that influence the uniform heating in microwave field are dielectric properties, volume, shape, and mixture ratio (Ayappa et al., 1991). The operating parameters of the microwave system are turntable speed, operating frequency, position placement inside the oven, oven size, waveguide size and position and specimen geometry (Ayappa et al., 1991; Rattanadecho and Klinbun, 2011). Knowledge of several parameters such as distribution of electromagnetic field, power absorbed, temperature and velocity field, is required for a detailed understanding of all phenomena that occur while microwave heating. The importance of experimental studies and qualitative theoretical analysis cannot be overlooked, but numerical simulations are indispensable for further to understand, predict and control the complex microwave heating process.

Numerical simulation of microwave heating process requires coupling the partial differential equation of electromagnetic field and heat transfer equations (Hill and Jennings, 1993). The interaction between the two is provided by the heat generated in the irradiated material due to dissipated microwave power, while the varying dielectric properties with temperature affect the distribution of the electromagnetic field. To solve and obtain accurate solutions of the multiphysics equations, numerical methods are widely used to simulate the microwave heating process. Various numerical methods used are finite

difference (FD) methods (e.g. Finite Differential Time Domain (FDTD) method), finite element method (FEM), moment of method (MoM), transmission line matrix (TLM) method and finite-volume time-domain (FVTD). Iskander et al. developed a FDTD code that was used to model some of the factors that influence a realistic microwave sintering process in multimode cavities (Iskander et al., 1994). The factors included the conductivity of the insulation surrounding the sample and the role of the SiC rods in modifying the EM field distribution pattern in the sample. In an another work, a numerical model for predicting the electromagnetic field in the waveguide and cavity, power absorption and temperature distribution on the processed materials was reported by Clemens and Saltielt (Clemens and Saltielt, 1996). Finite difference discretisation technique and electromagnetic field equations were used to characterise the energy deposition and physical changes that take place during microwave. Results indicated that the power absorbed by the exposed material increases with increase in the electrical conductivity. Tada et al. utilised two-dimensional finite difference time domain method to investigate the power distribution in an electromagnetic field of the microwave applicator filled partially with a dielectric material (Tada et al., 1998). Gupta et al. analysed the steady-state behaviour of a ceramic slab under microwave heating by transverse magnetic illumination (Gupta et al., 1999). It was reported that for a certain set of parameters, there are periodically recurring ranges of slab thickness for which thermal runaway may be avoided. Luo et al. (2004) developed and validated an interaction model of microwave heating of powdered pure metal alloy Fe-Cr18-10Ni with the experimental results. The results indicated good agreement between the theoretical predication and experimental values for the heating rate of the sample. However, beyond 2-3 minutes, the simulated values differed from the experimental values as the heat conduction within the metallic rod is not considered in the model. A new approach for analysing the electric field distribution inside materials in multimode cavities with mode stirrers was proposed by Plaza- González et al. (Plaza-González et al., 2004). The method was based on the linear averaging of the absorbed power in the material for different positions of some laminate mode stirrer, where for each spatial position, the wave equation is solved providing an instantaneous electric field distribution in both the cavity and sample. The electric field in the dielectric material was calculated by a two-dimensional modeling of a typical multimode microwave applicator with some mobile metallic sheets. Riedel and Svoboda modelled the microwave sintering process using the Maxwell's equations and the heat conduction equation (Riedel and Svoboda, 2006). The sintering model evaluated the density and the grain size, so as to predict runaway instabilities and to find the optimum process parameters leading to a

homogeneously sintered product with a uniform and fine grain structure. In 2006, Duan et al. reported a finite element simulation approach for microwave sintering of oxide materials using the Comsol Multiphysics Simulation Tool (Duan et al., 2006). Simulation studies were carried out considering both *E* and *H* fields or with isolated *E* and *H* field for sintering of Fe_3O_4, Al_2O_3 and ZnO oxides. The authors considered separate electromagnetic propagation and heat transfer modules with different boundary conditions. They reported that the material's dielectric constant, magnetic permeability and electric conductivity properties are dependant parameters for microwave coupling; while material thermal properties are important for heat transfer simulation. Liu and Sheen solved the Maxwell's equations using the FDTD approach and coupled it with a heat transfer equation using FD approach to obtain the temperature variation in a ceramic slab during microwave heating (Liu and Sheen, 2008).

Buchelnikov et al. provided sufficient evidences to prove that bulk metallic samples reflect microwaves while powdered samples can absorb such a radiation and be heated efficiently (Buchelnikov et al., 2008). They investigated theoretically the mechanisms of penetration of a layer of metallic powder by microwave radiation and microwave heating of such a system. Xie et al. investigated the finite element method using a JMAG-Studio program (Xie et al., 2009). The results indicated occurrence of disturbance in the magnetic field as well as in electric field by the insertion of the alumina loading pressure system due to reflection effect of alumina. Shukla et al. studied the effect of the sample dimension and its physical properties on the temporal temperature evolution during microwave and conventional heating (Shukla et al., 2010). A 2-D finite difference approach was used for investigation of the temperature distribution in cylindrical samples of different radii and thermal conductivities. The result revealed that occurrence of inverse thermal gradient increases with heating time and is higher for large sizes and lower conductivity samples. Effect of varying dielectric properties and varying magnetron frequency on the electromagnetic field distribution was studied by Santos et al. (Santos et al., 2010). The microwave heating simulation was carried out using COMSOL Multiphysics Software Tool on a ceramic specimen. It has observed that at 2.20 GHz (lowest frequency) lower number of maxima was observed, while for 2.70 GHz (highest frequency) maximum number of maxima was observed. This is attributed to the fact that with increase in the magnetron frequency, there is increase in oscillation of electric field due to decrease in the wavelength. Thermal runaway phenomena for a ceramic specimen was simulated by Santos et al. in a 2D microwave model developed using COMSOL Multiphysics software tool (Santos et al., 2011). The results indicated that due to the temperature dependence of

the real and imaginary parts of the permittivity the electromagnetic field pattern changes during the heating. It was also concluded that high temperatures, the skin depth appreciably decreases, and consequently the microwave energy is mainly absorbed at the surface of the sample. Farag et al. studied the transient temperature profiles of pinewood, carbon, Pyrex while microwave heating (Farag et al., 2012). It was concluded that heating leads to non-uniform temperature distribution, which is strongly dependent on the penetration depth of the material. Simulation also helps for placing of the specimens relevant to significant temperature distribution at specific locations in the applicator cavity. Srinath et al. carried out simulation studies on microwave heating of while joining bulk copper plates in a microwave applicator (Srinath et al., 2012). The modelling was carried out in a multimode applicator at 1 kW, 2.45 GHz microwave source through a rectangular waveguide operating in the TE_{10} mode. The magnitude of the electric field (Z component) was observed to be 1.244×10^4 V/m, while the temperature at the joint zone was observed to be 1019 ^oC after a exposure for a duration of 300 s. Rybakov et al. reviewed fundamentals of microwave sintering in light of numerical modelling of the process (Rybakov et al., 2013). They concluded that that multiphysics simulations help in predicting the densification, shrinkage, grain structure. Further, uncertainty quantification in high temperature microwave heating was simulated and reported by Vaz et al. (Vaz et al., 2014). The variability in the operating frequency and dielectric properties of the material caused the uncertainty in the temperature quantification. The uncertainty was analysed through Non-Intrusive Spectral Projection (NISP) methods based on Polynomial Chaos expansion. Yi-du et al. performed three dimensional simulation microwave heating of a coal specimen (Yi-du et al., 2016). They investigated the effect of microwave frequency, microwave power and specimen position in the applicator cavity. The maximum and minimum frequency of the coal sample change with incident microwave frequency. The effect of power was not very significant on the maximum and minimum temperature of the specimen. Lower power microwave treatment requires more energy than the higher power microwave treatment. However, the effect of specimen positioning in the cavity was remarkable.

2.6. ANALYSIS OF RESEARCH GAP

Development of wear resistant surfaces using conventional surface engineering techniques such as weld surfacing and laser cladding have their own limitations like high dilution rates, distortion of substrate, high cost and interfacial cracking etc. Several authors have reported presence of un-melted and un-dissolved reinforcing carbide particles that are present locally in regions close to the interface attributed to heat loss to the substrate through conduction (Taha-al et al., 2009; Vreeling et al., 2002). These un-melted particles tend to deteriorate the properties of the clad. Thermal spraying is a popular route to develop wear resistant surfaces, but thermal spray deposits are mechanically anchored to the surface. Thermal spray deposits often present issues like low strength, exfoliation, cracking and spalling while exposed to wear conditions. Thermal sprayed deposits also require post processing improve their density, increase homogeneity and reduce porosity. Further, nanostructured coatings developed through thermal spraying route are popular to combat wear in engineering components attributed to their enhanced mechanical, physical and functional properties. These enhanced properties are due to large interface and nanoscale effects associated with these materials. In these materials a large volume fraction of atoms are located in the interface where their behaviour is different from the bulk**.** However, the degradation of the essential carbide phase during the thermal spraying leads to poor tribo-mechanical properties of the coatings.

On the other hand, the potentially promising microwave cladding has not been explored well. No literature is available on development of nanostructured wear resistant surfaces through microwave cladding. The available results favour the application of microwave energy to process nanostructured materials (Breval et al., 2005; Sunil et al., 2010); however, there are no data available in the domain. Further, detailed data on the structure-property correlations of nanometric microwave clads could provide new solutions to combat wear and would open up a new research domain.

2.7. OBJECTIVES AND SCOPE OF THE WORK

Microwave cladding offers an array of advantages compared to the conventional processing techniques. Accordingly, the present work has been aimed at exploring development of wear resistant surfaces in the micro and nano regime through microwave cladding. The specific objectives and the scopes of the present work are stated in the following sections.

2.7.1. Objectives of the Work

Based on the analysis of the research gap, the major objectives of the current work have been formulated as:

a) To develop wear resistant surfaces using micrometric and nanometric WC-12Co clad powders on austenitic stainless steel (SS-304) through microwave cladding process.

b) To characterise and compare the micrometric and nanometric WC-12Co clads using different metallurgical, mechanical and tribological techniques.

2.7.2. Scope of the Work

a) Explore the possibility to develop nanostructured wear resistant surfaces through microwave cladding.

b) Simulation studies on microwave cladding process to assess heat transfer, electromagnetic field distribution and temperature distribution.

c) Development of micrometric and nanometric clads using WC-12Co clad material on austenitic stainless steel (SS-304) substrate.

d) Metallurgical characterisation of the WC-12Co clads in terms of phase analysis, microstructure, elemental analysis and assessment of porosity etc. The techniques to be used for these characterisations will be X-ray diffraction (XRD), electron probe micro analyser (EPMA) scanning electron microscopy (SEM) and energy dispersive X-ray spectroscopy (EDS) and assessment of porosity (using image analysis).

e) Mechanical characterisation of the clads in terms of microhardness assessment (using Vicker's microhardness tester), flexural strength (using three-point bend test) and evaluation of residual stresses (using $\sin^2\psi$ method).

f) Assessment of tribological performance of the micrometric and nanometric WC-12Co clads in terms of wear rate, cumulative wear rate, friction coefficient and analysis of wear mechanisms.

2.8. PLAN OF THE PRESENT WORK

The methodology of the proposed work is illustrated in the flow chart shown in Fig. 2.15.

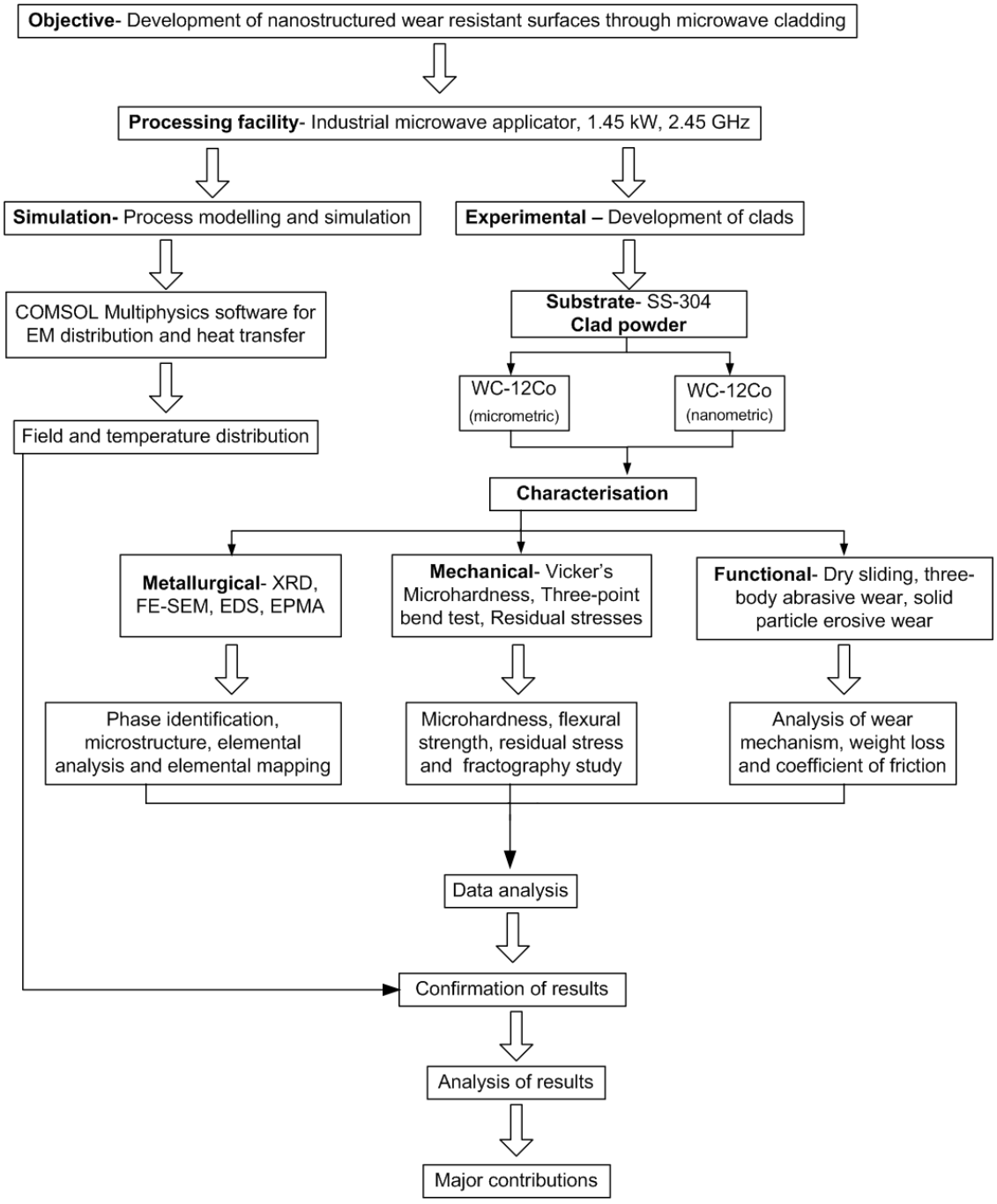

Fig. 2.15- Flow diagram illustrating the plan of the present work

2.9. SUMMARY

Surface degradation reduces the life and performance of engineering components. Wear, corrosion and fatigue have been identified as the main causes of surface degradation of engineering components. A brief discussion on the wear and friction of engineering materials has also been presented. The economic losses pertaining to friction and wear of

engineering components have been highlighted. A comprehensive review on the existing surface engineering techniques, such as, weld surfacing, laser cladding and thermal spraying has been presented. The limitations in these techniques have been highlighted. The issues with developing nanostructured coatings with thermal spraying have also been discussed. Existing literature on microwave cladding have been reviewed. The gaps observed in the literature indicate that the promising microwave cladding technique has not been explored well particularly in developing nanostructured clad layers. Hence, in the present work the possibility of developing nanostructured clad layers through microwave cladding has been explored. Accordingly, the objectives and scopes for the present study have been formulated. The methodology to be adopted to accomplish the objectives has been presented in the form of a flow chart.

CHAPTER 3

PRINCIPLES AND SIMULATION OF MICROWAVE CLADDING

The ability of microwave radiation to penetrate and couple with selected materials for instantaneous volumetric heating has made it a popular heating choice in material processing. Microwave heating for material processing at high temperature is currently an active research domain, with prospects of extensive industrial use. The approach has displayed a competitive advantage compared to the conventional heating methods. The present chapter illustrates the principles of microwave cladding process. COMSOL Multiphysics finite element software (version: 5.0) was used to carry out the simulation studies. Principles of microwave cladding were developed using the dielectric heating equations coupled with the basic heat transfer equations. The analyses are the correlated with the simulation studies of the cladding process. Results of the finite element simulation are discussed with suitable illustrations.

3.1. PRINCIPLES OF MICROWAVE CLADDING

Microwaves consist of electric and magnetic field orthogonal to each other. The dominant mechanism of microwave-induced heating at 2.45 GHz involves the agitation of molecular dipoles due to presence of an oscillating electric field (for non-magnetic materials). In the presence of an oscillating field, molecular dipoles reorient themselves in order to be in phase with the alternating field. These orientations are restricted by molecular interaction forces, which increase the molecular kinetic energy. As kinetic energy increases, system temperature increases within a short time. This time period depends on the electrical, magnetic and physical properties of the heated material (Farag et al., 2012).

The bulk metallic materials tend to reflect microwaves at 2.45 GHz when processed at room temperature owing to their low 'skin depth (d_s)'. Skin depth in microwave material processing is defined as the distance from the surface at which the magnitude of the field strength drops by a factor of 1/e (36.8%) (Mondal et al., 2010). The skin depth is calculated using equation 3.1:

$$d_s = \frac{1}{\sqrt{\pi \mu f \sigma}} = 0.029(\rho\lambda_0)^{0.5} \quad (3.1)$$

where, σ is the electrical conductivity (S/m), ρ is the electrical resistivity (Ω m) and λ_o is the incident wavelength (mm). Hence, it is imperative that absorption of microwave power depends on the dielectric properties of the materials. The microwave power absorbed per unit volume of the material exposed can be estimated using equation 3.2:

$$P = \omega [\varepsilon_o \varepsilon'' E_{RMS}^2 + \mu_o \mu'' H_{RMS}^2] \quad (3.2)$$

where, μ_o is magnetic permeability of air (H/m), μ'' is the imaginary component of the magnetic permeability (H/m), E_{rms} is the root mean square of the electric field (V/m) and H_{rms} is the root mean square of the magnetic field (A/m). In case of non-magnetic materials, μ'' is negligible, and hence contribution of magnetic field in power absorption can be neglected and equation 3.2 reduces to single term, $P = \omega[\varepsilon_o \varepsilon'' E_{RMS}^2]$. During microwave exposure, the electromagnetic energy penetrates into the target material. Ideally, volumetric heating should take place in the target material and the amount of energy added to the target material is given by equation 3.3 (Roger, 1998):

$$E = \int_0^T p.\partial t \quad (3.3)$$

where, E is the total energy added to the target (J), p is the applied power (W) and T is the time (s) for which total power is applied. Microwave hybrid heating (MHH) technique is utilised for materials that are poor absorbers of microwave radiation at low temperature. In this technique, a susceptor material is used to initiate heating. The susceptor couples with microwaves at room temperature and gets heated rapidly, which raises the temperature of the poor microwave absorbing materials. The poor absorbing materials are heated beyond their critical temperature (T_c) through conventional modes of heat transfer, such as conduction, convection and radiation.

In the cladding trials, the WC-12Co cermet powder was used to develop the clads in the present work. The WC exhibits low loss tangent at ambient temperatures, but as the temperature increases beyond the critical temperature (T_c), the loss tangent increases significantly (Rödiger et al., 1998; Demirskyi et al., 2011; Sharma and Krishnamurthy, 2002). Therefore, the MHH technique has proved to be viable to process such materials by utilising a susceptor material (Gupta and Sharma, 2014; Sharma and Gupta, 2012; Sharma et al., 2001; Wong and Gupta, 2007; Wong et al., 2005).

During the experiments, online temperature was monitored inside the hot zone of the specimen covered with the susceptor using an infrared pyrometer mounted on the industrial microwave applicator. The process temperature was recorded at an interval of 30 s, while the powder layer was irradiated for duration of 600 s. Fig. 3.1 illustrates the time–temperature plot for a typical experimental trial. Significant events during the microwave exposure are illustrated schematically in Fig. 3.2. It is observed from Fig. 3.1 that for the given volume of material load, i.e. the clad powder, it takes around 60 s of exposure for the susceptor to couple with the microwave radiation. This phase can be termed as the 'preheating phase', during which the microwave interacts with the susceptor (Fig. 3.2). The susceptor absorbs microwave energy and consequently gets heated up; it then transfers heat to the powder particles through conventional modes of heat transfer. Ideally, volumetric heating nature of microwaves tends to dissipate energy uniformly throughout the material load. Once the temperature of the powder particles reaches a critical value (approximately 410 °C, in this case), it starts absorbing microwaves and there is a steady increase in temperature till around 500 s of exposure; the corresponding rise in temperature is almost linear as can be seen in Fig. 3.1. This phase can be termed as 'interaction-cum-heating phase' and during this phase microwaves interact with clad powder particles. The microwave–material interaction causes heating of the clad powder. Beyond this point, the temperature remains steady as indicated by the characteristics of the monitored temperature profile in Fig. 3.1 and accordingly this phase can be termed as 'melting-cum-dilution phase'. The programmed set temperature (1415 °C), which was obtained from extensive trials on the material, tunes the applied power of the applicator to maintain an apparently steady temperature at this phase. However, the temperature of the core of the clad layer remains higher due to negligible thermal loss and continued exposure. As the exposure continues, melting of the clad powder starts and a melt pool is formed. Owing to continued exposure of microwaves, localised convective currents are setup in the melt-pool and this facilitates dilution of a thin layer of the substrate (Fig. 3.2). Owing to the poor thermal conductivity of the SS-304 substrate, its melting remains confined to a thin interfacing layer, which also facilitates mutual diffusion of the elements between the substrate and the clad material. This helps in formation of metallurgical bond between the clad material and the substrate.

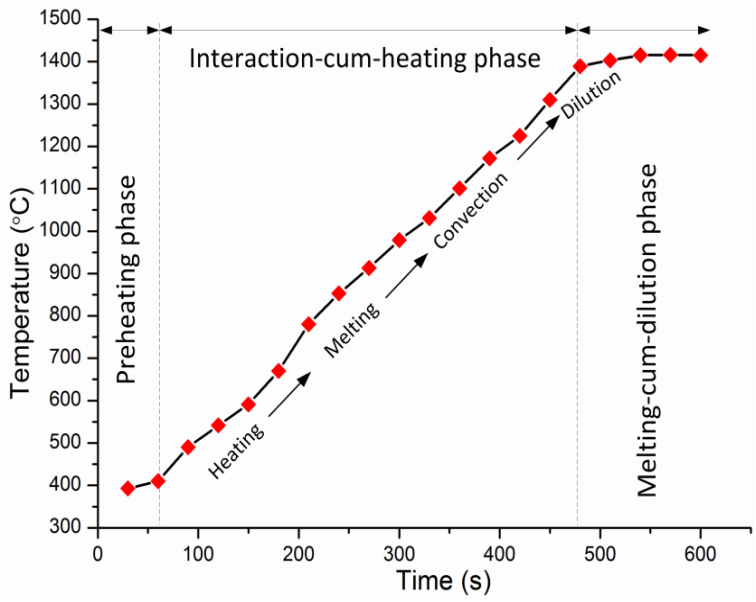

Fig. 3.1- Time–temperature plot during WC–12Co microwave cladding

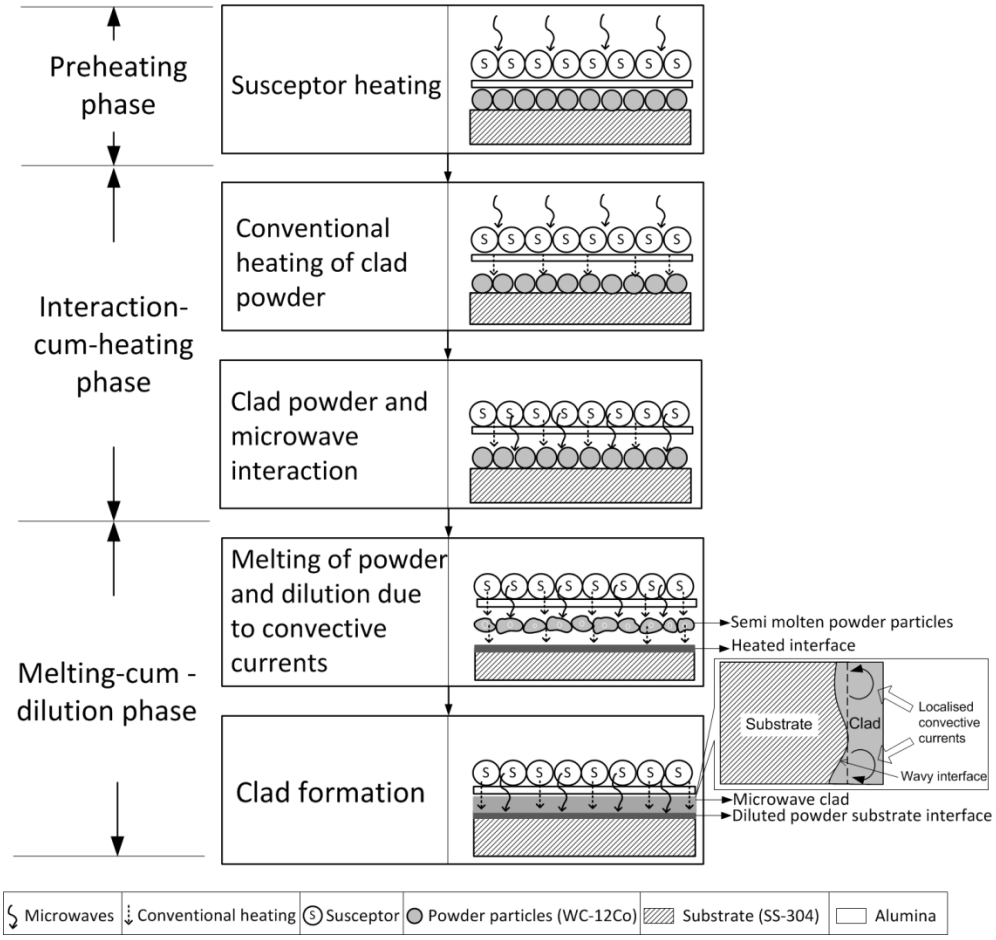

Fig. 3.2- Different events during microwave irradiation and clad formation, Inset: schematic illustration of the localised convective currents and waviness phenomenon

3.2. GEOMETRIC MODELLING OF THE MICROWAVE CLADDING SETUP

Microwave cladding of powders on metallic substrates through MHH technique has been reported by many authors (Gupta and Sharma, 2014; Kaushal et al., 2015; Pathania et al., 2015; Sharma and Gupta, 2012). The 'skin depth' of the clad powder is an important parameter that influences the microwave heating phenomena. Hybrid heating technique is popularly used to process material having low skin depth at room temperature (Gupta and Wong, 2005). The hybrid heating arrangement helps to enhance the skin depth of the clad powder by raising its temperature beyond the critical temperature. Once the temperature of the powder particles reaches beyond its critical temperature, it directly couples with the microwaves, gets heated and melted (Gupta and Sharma, 2011a). The hybrid heating arrangement consists of the substrate, clad powder, separator and susceptor.

The geometric model of the industrial multimode microwave applicator was developed in COMSOL Multiphysics software (version: 5.0) as shown in Fig. 3.3(a). The applicator cavity was assumed to be filled with air, whose ε^* and μ_r are assumed to be unity. The microwaves enter the cavity through a rectangular waveguide as shown in Fig. 3.3(a). The hybrid heating arrangement was placed at the centre of the cavity in an alumina wool envelope (Fig. 3.3(b)). The microwaves pass through the alumina wool without any attenuation due to its negligible dielectric loss of the alumina wool envelope. The alumina wool envelope also insulates the heat generated in the hybrid heating arrangement (ε^* and μ_r = 1). In the present model, heat loss from the hybrid heating arrangement to inside the walls of the alumina envelope was not assumed. The geometrical parameters to develop the model are presented in Table 3.1. The port is operating in either transverse magnetic (TM_{01}) mode or transverse electric (TE_{10}) mode depending upon the type of material and application. The developed model is as per the experimental setup used to develop the clads. The front view of the model is shown in Fig. 3.4.

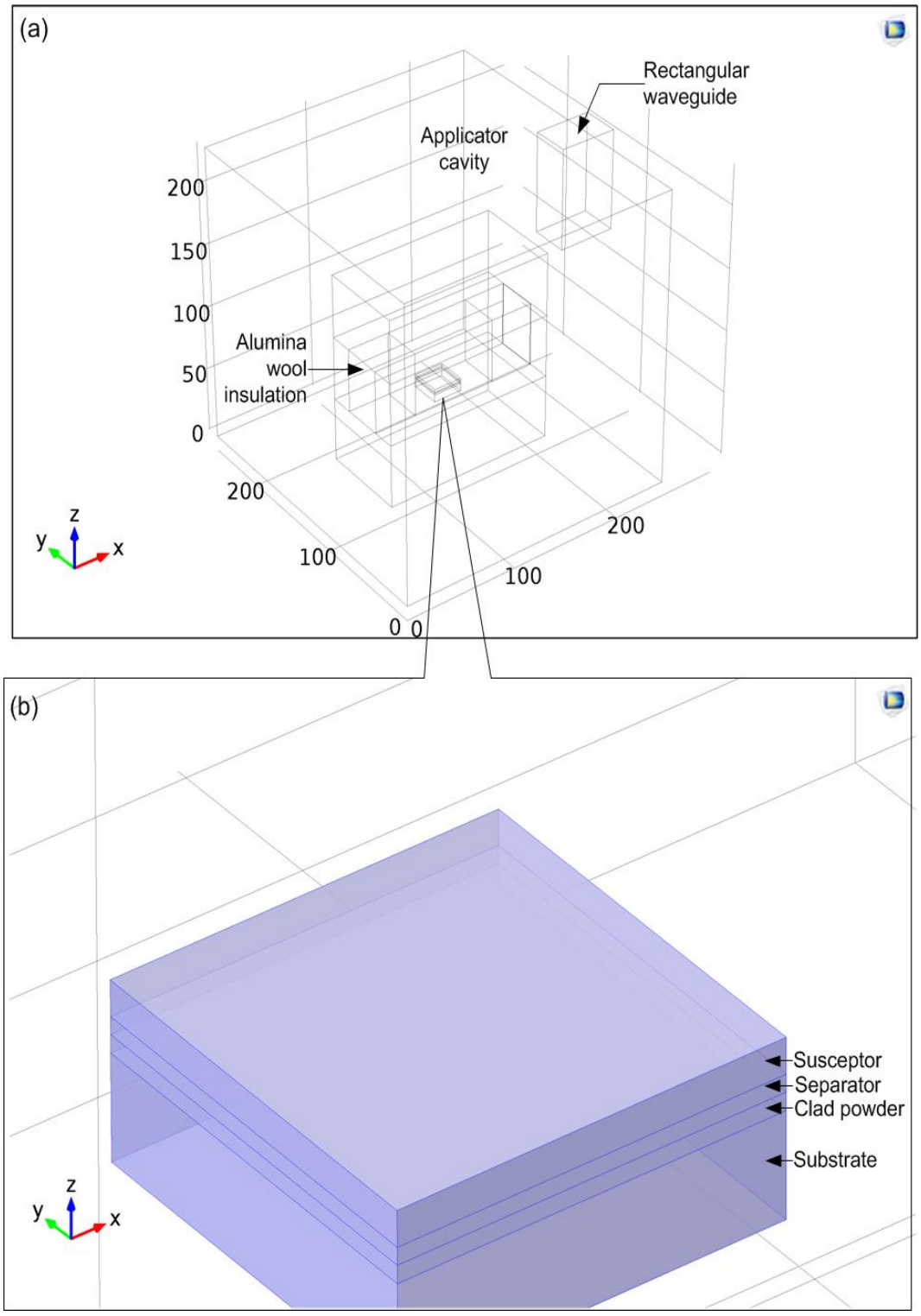

Fig. 3.3- Three-dimensional view of (a) microwave cladding setup and (b) zoomed view of the hybrid heating arrangement

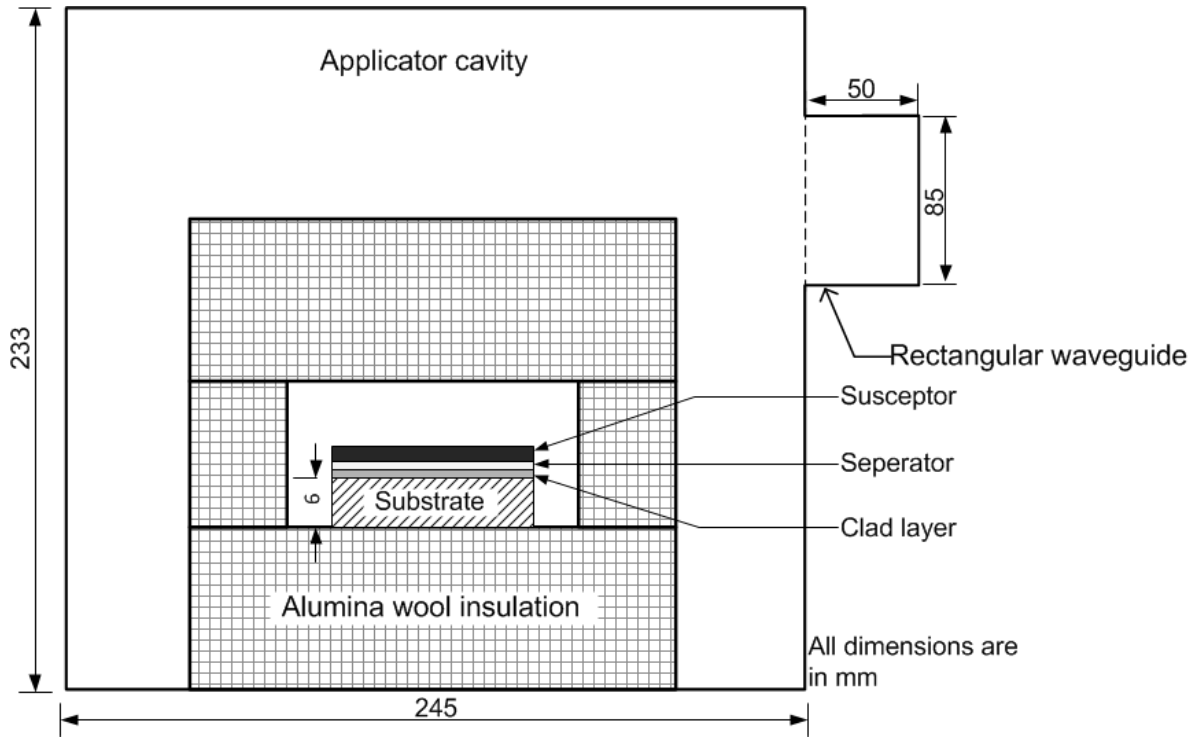

Fig. 3.4- Front view of the microwave cladding model

Table 3.1- Geometrical parameters of the model

Description	**Symbol**	**Value (mm)**
Applicator width	wo	245
Applicator depth	do	257
Applicator height	ho	233
Waveguide width	wg	50
Waveguide depth	dg	65
Waveguide height	hg	85
Substrate width	ws	25
Substrate depth	ds	25
Substrate height	hs	6
Clad width	ws	25
Clad depth	dsep	25
Clad height	hsep	1
Separator width	wsep	25
Separator depth	dsep	25
Separator height	hsep	1
Susceptor width	wsus	25
Susceptor depth	dsus	25
Susceptor height	hsus	3
Initial temperature (°C)	Ti	25

3.3. GOVERNING EQUATIONS AND BOUNDARY CONDITIONS

3.3.1. Governing equations

In order to confirm the experimental results and to obtain a better understanding of the principles of microwave cladding process, a model coupling the electromagnetic wave propagation and resulting heat transfer was constructed using COMSOL Multiphysics software (version: 5.0). The simulation studies were carried out using a Hewlett-Packard (HP) workstation (Model: HP Z420) powered with a 3.3 GHz Xeon processor. The Maxwell's equations were solved for conditions inside the applicator cavity, while the hybrid heating arrangement was coupled with the heat transfer to obtain the three dimensional temperature distribution in the hybrid heating arrangement.

The following assumptions were followed in order to reduce the computation time and simplify the model:

a) The substrate, clad powder, separator and susceptor were considered to be homogenous and isotropic.
b) The dielectric and thermomechanical properties of the components of the hybrid heating arrangement were considered as constant.
c) Mass transfer within the applicator cavity was negligible.
d) Chemical reactions were not considered within the applicator cavity.
e) The applicator cavity was filled with air, whose dielectric losses were considered as zero.
f) The dielectric losses of the refractory insulation box were considered as zero.
g) Heat transfer calculations were performed only in the hybrid heating arrangement.
h) Convective and radiative heat losses were not considered.
i) Contributions of the heating from the magnetic field were not considered as below 1138 °C the Co acts as ferroelectric (Breval et al., 2005). Moreover, the WC was dominant phase in the clad powder.
j) The waveguide port was excited by the electric field in Z direction.
k) Various physical and dielectric properties were assumed to be constant with increasing temperature.

The simulation of microwave hybrid heating was accomplished by solving the Maxwell’s equations to determine the electric field distribution within the computational domain. The Maxwell’s equation is given in equation 3.4:

$$\nabla \times \left(\frac{1}{\mu_r}\nabla \times E\right) - \frac{\omega^2}{c}\left(\varepsilon' - i\varepsilon''\right)E = 0 \quad (3.4)$$

here, E is the electric field intensity (V/m), c is the speed of light (3×10^8 m/s), ω is the angular wave frequency (rad/s), μ_r is the relative permittivity of the material, ε_r is the dielectric constant of the material and ε'' is the dielectric loss factor of the material. The amount of heat generated within a non-magnetic microwave absorbing materials depends on the complex permittivity, ε^* as represented in equation 3.5 (Farag et al., 2012).

$$\varepsilon^* = \varepsilon' - i\varepsilon'' \quad (3.5)$$

The real part of the complex permittivity (ε') is known as the dielectric constant that is the amount of electric energy that can be stored in the material. The imaginary part (ε'') is known as dielectric loss factor, which is the ability of the heated material to dissipate the microwave energy. The ratio between the real and imaginary part is the loss tangent ($tan\ \delta$). The value of loss tangent ($tan\ \delta$) indicates the conversion of the microwave energy into thermal energy within the material (Clark et al., 2000; Oghbaei and Mirzaee, 2010). The power dissipated inside the applicator cavity is represented as the heat generated within the heated material through equation 3.6:

$$P = \omega\left[\varepsilon_o\varepsilon'' E_{RMS}^2 + \mu_o\mu'' H_{RMS}^2\right] \quad (3.6)$$

here, $\omega = 2\pi f$ is the angular frequency (rad/s), E_{RMS} is the root mean square value of the electric field (V/m), H_{RMS} is the root mean square value of the magnetic field (A/m), ε_o is permittivity of free space (8.854×10^{-12} F/m), μ_o is the permeability of free space ($4\pi \times 10^{-7}$ N/A^2) and P is the power absorbed per unit volume (W/m^3). For non-magnetic materials, equation 3.6 is modified as shown in equation 3.7.

$$P = \omega\left[\varepsilon_o\varepsilon'' E_{RMS}^2\right] \quad (3.7)$$

Or

$$P = 2\pi f\left[\varepsilon' tan\delta\ E_{RMS}^2\right] \quad (3.8)$$

The dissipation of the absorbed electromagnetic energy as thermal energy within the material is governed by the Fourier's heat transfer equation as shown in 3.9 (Santos et al., 2011).

$$\rho C_P \frac{\partial T}{\partial t} = k\nabla^2 T + P \tag{3.9}$$

Where, ρ is the density (kg/m^3), C_P is the specific heat at constant pressure (J/kg °C) and k is the thermal conductivity (W/mK) of the material, T is the transient temperature (°C). The simulation strategy adopted in the present study is illustrated in Fig. 3.5.

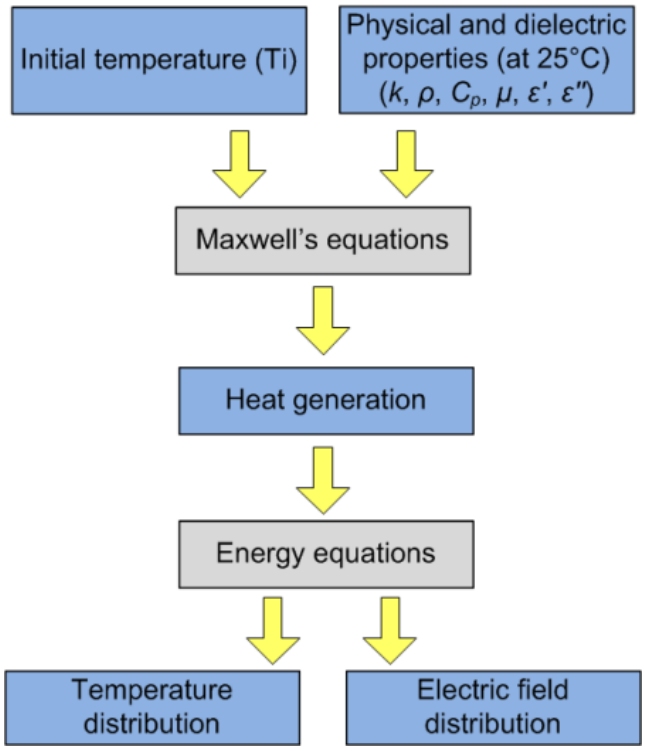

Fig. 3.5- Simulation strategy adopted in the present model

The Maxwell's equation was solved first to calculate the electric field distribution and heat generation considering the dielectric properties of the specimen material. The heat generation was then used to solve the energy balance equation based on the thermo-mechanical properties of the material. Heating of the specimen depends not only on the power absorbed but also on its thermal properties. The materials and their relevant thermal and dielectric properties are summarised in Table 3.2.

Table 3.2- Electromagnetic and thermal properties of the materials (Bonny et al., 2010; Gupta, 2012; Marland et al., 2001; Michálek et al., 2014)

Properties	**Units**	**Domain and Material**			
		Substrate (SS-304)	**Clad (WC-12Co)**	**Separator (Alumina)**	**Susceptor (Charcoal)**
Relative permittivity (ε_r)	-	1	5-0.25i	10	2.93-0.16i
Relative permeability (μ_r)	-	1	3	1	1
Electrical conductivity (σ)	S/m	1.37×10^{6}	1.88×10^{6}	1×10^{-6}	0.02
Heat capacity at constant pressure (C_p)	J/kg K	502	295	880	0.71
Density (ρ)	kg/m^3	7990	14320	3950	2260
Thermal conductivity (k)	W/mK	16.5	95	35	470

3.3.2. Boundary conditions

The metallic walls of the cavity and port were assumed to be perfect electrical conductors, represented by the boundary condition $\underset{n}{\rightarrow} \times \underset{E}{\rightarrow} = 0$ (Fig. 3.6(a)). This means that the tangential component of the electric field and normal components of the magnetic field is zero at the boundaries. The magnetron feeds the microwaves in the applicator cavity through the port boundary as shown in Fig. 3.6(b). In the present work, the microwave at 1.4 kW was fed into the applicator cavity. The rectangular port excites a frequency of 2.45 GHz and operates in the TE_{10} mode. The propagation constant of the port is given by the expression as in equation 3.10.

$$\beta = \frac{2\pi}{c}\sqrt{f^2 - f_c^2} \tag{3.10}$$

where, β is the propagation constant, f is the frequency of the microwave and f_c is the cut-off frequency.

The thermal insulation boundary condition was applied on the boundaries of the hybrid heating arrangement. This means that there was no heat flux across the boundary, i.e. temperature gradient across the boundary is zero and was defined as shown in equation 3.11. The heat transfer studies were carried out in the heat transfer domain in the model as shown in Fig. 3.6(c).

$$-n \times (-k\nabla T) = 0 \tag{3.11}$$

where, n is the mode component, k is the thermal conductivity (W/mK) and T is the temperature (°C).

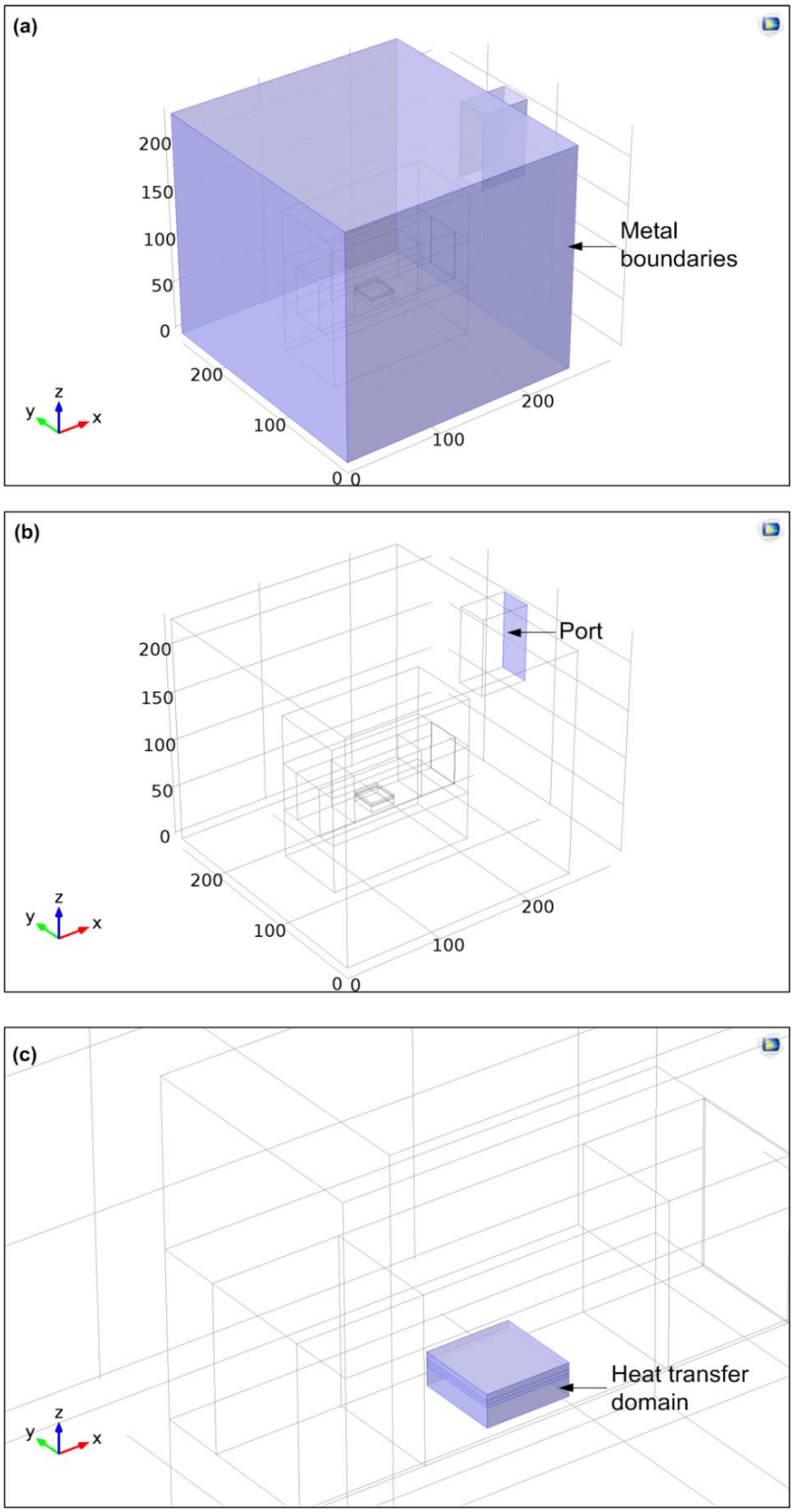

Fig. 3.6- Three-dimensional views of (a) metal boundaries, (b) port boundary and (c) heat transfer domain

3.4. MESHING SCHEME OF THE MODEL

The three dimensional computational domain of the model was discretised using hybrid mesh elements using physics controlled extra fine setting (Fig. 3.7(a) and (b)). For electromagnetic problems, the maximum element was decided as per Nyquist criterion as shown in equation (3.12) (Salvi et al., 2010).

$$S_{max} < \frac{\lambda}{2} = \frac{c}{2f\sqrt{\varepsilon'\mu'}} \tag{3.12}$$

where, λ is the wavelength (m), f is the frequency (Hz), c is the speed of light (m/s), ε' is the dielectric constant, μ' is the relative permeability. Therefore, based on the Nyquist criterion and material properties, the maximum size of the element in the air is 0.0371 and 0.025 mm, while in the heat transfer domain, it was 0.01 mm and 2.1937×10^{-3} mm, respectively. The mesh sizes in the air and heat transfer domain are shown in Fig. 3.7 (c) and (d), respectively. The parametric details of the mesh are given in Table 3.3.

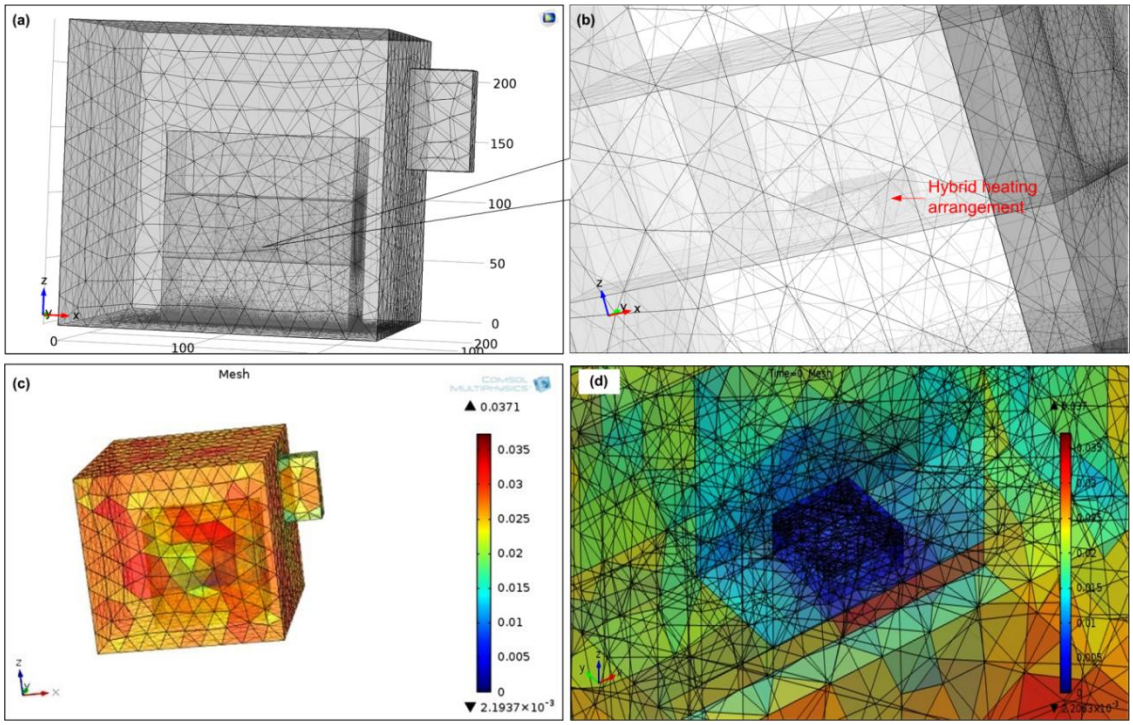

Fig. 3.7- (a) Mesh in the microwave applicator cavity, (b) mesh in the heat transfer domain, (c) quality of the mesh and (d) mesh size in heat transfer domain

Table 3.3- Mesh parameters

Description	**Value**
Tetragonal elements	437,281
Triangular elements	63,147
Edge elements	1,749
Vertex elements	72
Minimum element quality	0.02059
Average element quality	0.7202
Mesh volume	1.48×10^7 mm^3

3.5. POST PROCESSING OF RESULTS

3.5.1. Temperature distribution

The experimental and simulated temperature profiles of the top layer of the susceptor are illustrated in Fig. 3.8. The temperature profiles are in good agreement in general (Fig. 3.8(a)); however, beyond 500 s of exposure the experimental profile illustrates a flattening trend. Conversely, the simulated temperature profile exhibits an increasing trend. This attributed is to the fact that the experiments in the multimode applicator were carried out in auto cut-off mode. In the auto cut-off mode once the temperature of the susceptor layer reaches the optimum set value, the microwave power is reduced to hold the temperature constant. Condition of thermal runaway may arise if the auto cut-off mode is not used, which may lead to the melting of the substrate (Oghbaei and Mirzaee, 2010). Further, the assumptions in the present model, such as neglecting the convective and radiative losses in the alumina wool insulation lead to increased temperature at the susceptor layer beyond 500 s of exposure as shown in Fig. 3.8(a). The temperature gradient (K/m) in the z direction across the hybrid heating arrangement is shown in Fig. 3.8(b). Higher temperature at the clad layer can be confirmed from higher temperature gradient as shown in Fig. 3.8(b). Further, the inverse heating profile of the microwave heating can be visualised, as at temperature gradient is higher at the centre of the clad layer compared to its free ends. The temperature distribution on the top layer of the susceptor is shown in Fig. 3.9(a). The average value of simulated temperature on the top layer of the susceptor was observed to be 1566 °C after 510 s of exposure. The temperature at the corners of the hybrid heating arrangement was observed to be little higher as compared to the middle of the susceptor layer (Fig. 3.9(b)). This is due to the fact

that the microwave radiation tends to get concentrated at the corners and leads to formation of hot spots. However, in the experiments the substrate was selectively masked in a carbon block to avoid any reflections of microwaves in the applicator cavity. The deviation of experimental and simulated temperature profiles is also due to the dynamic variation in dielectric and thermal properties of the material in the applicator cavity. In the present model, they are assumed to be constant.

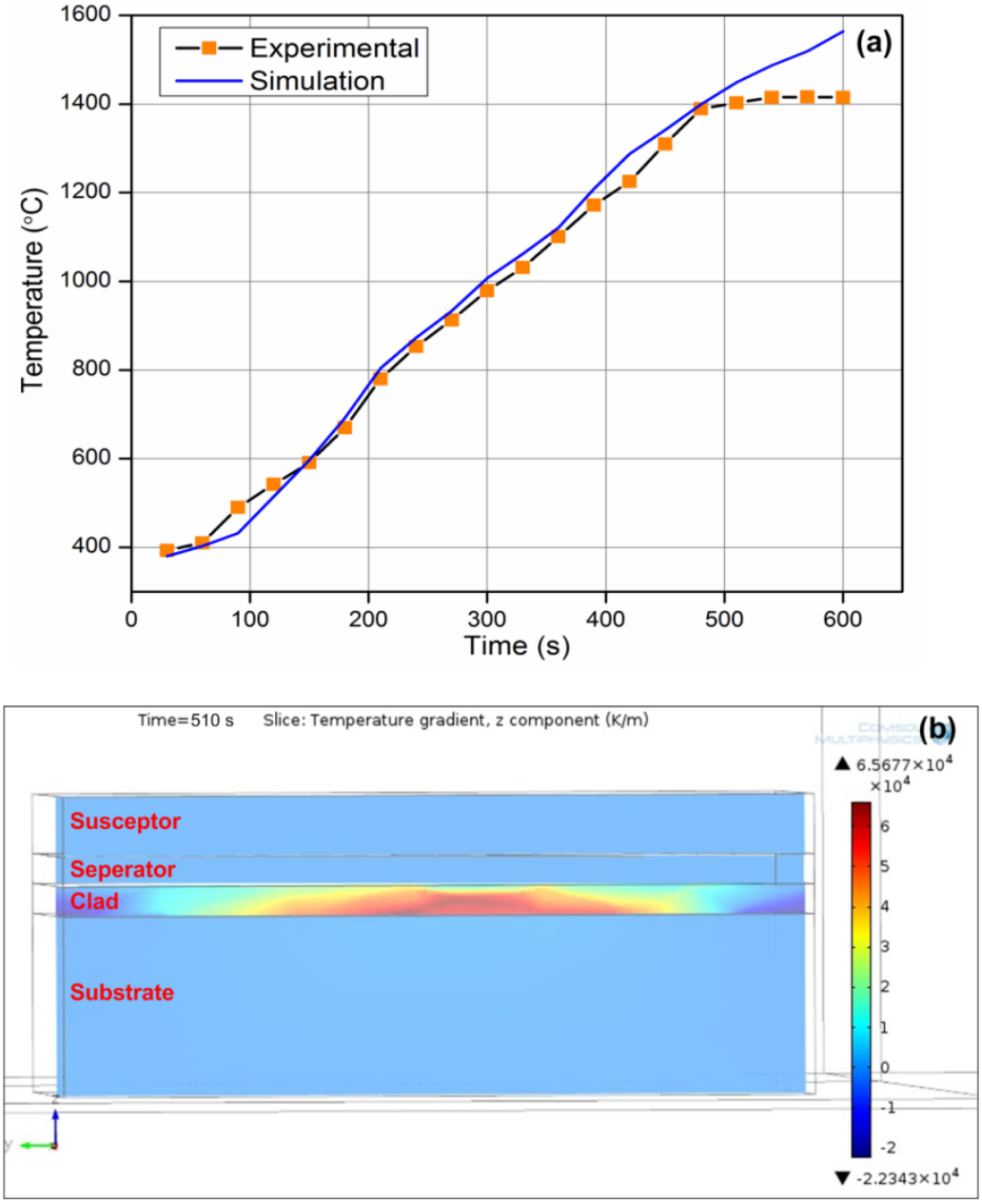

Fig. 3.8- (a) Experimental and simulated temperature profile and (b) temperature gradient across the section of the MHH arrangement

In the present hybrid heating arrangement, it is difficult to experimentally monitor the real time temperature of the clad layer as it is below the separator and susceptor. However, through the simulation it is possible to analyse the temperature distribution at the clad powder layer during exposure. The temperature distribution using slice plots at various locations within the heat transfer were analysed and are illustrated in Fig. 3.9. The temperature profiles are presented after an exposure of 510 s. It was observed that the average temperature at the top surface of the susceptor in in the range of 1560 °C, at the middle of the susceptor layer the average temperature is in the range of 1700 °C (Fig. 3.8(a) and (b)). This is a clear indicative of the inverse temperature gradient associated with microwave heating (Clark et al., 2000; Mishra and Sharma, 2015; Oghbaei and Mirzaee, 2010; Thostenson and Chou, 1999). The temperature at the middle of the separator (alumina) layer was observed to in the range of approximately 1762 °C (Fig. 3.9(c)). The temperature at the centre of the clad layer was observed to be in the range of approximately 2990 °C (Fig. 3.9(d)). In this case the WC-12Co was used as the clad powder. The temperature at the clad layer is sufficient to cause melting of the WC particle in the clad powder. Hence, the clad is formed due to complete melting and resolidification of the clad powder and the partial melting of the interfacing layer of the substrate. In the present study, SS-304 was used as the substrate, which has a low thermal conductivity (k = 16.2 W/mK (Sweet et al., 1987)). The temperature distribution near the interface reveals that the average temperature interface was in the range of approximately 960 °C (Fig. 3.9(e)). Partial diffusion of elements occurs in the face zone due to the presence of localised convective currents in the melt pool of the clad powder (Gupta and Sharma, 2014). Hence, a wavy interface is formed as illustrated in Fig. 3.2. Due to poor thermal conductivity of the substrate, much heat transfer from the molten powder layer does not take place. Therefore, the average temperature at the middle of the substrate was in the range of 122 °C (Fig. 3.9(f)).

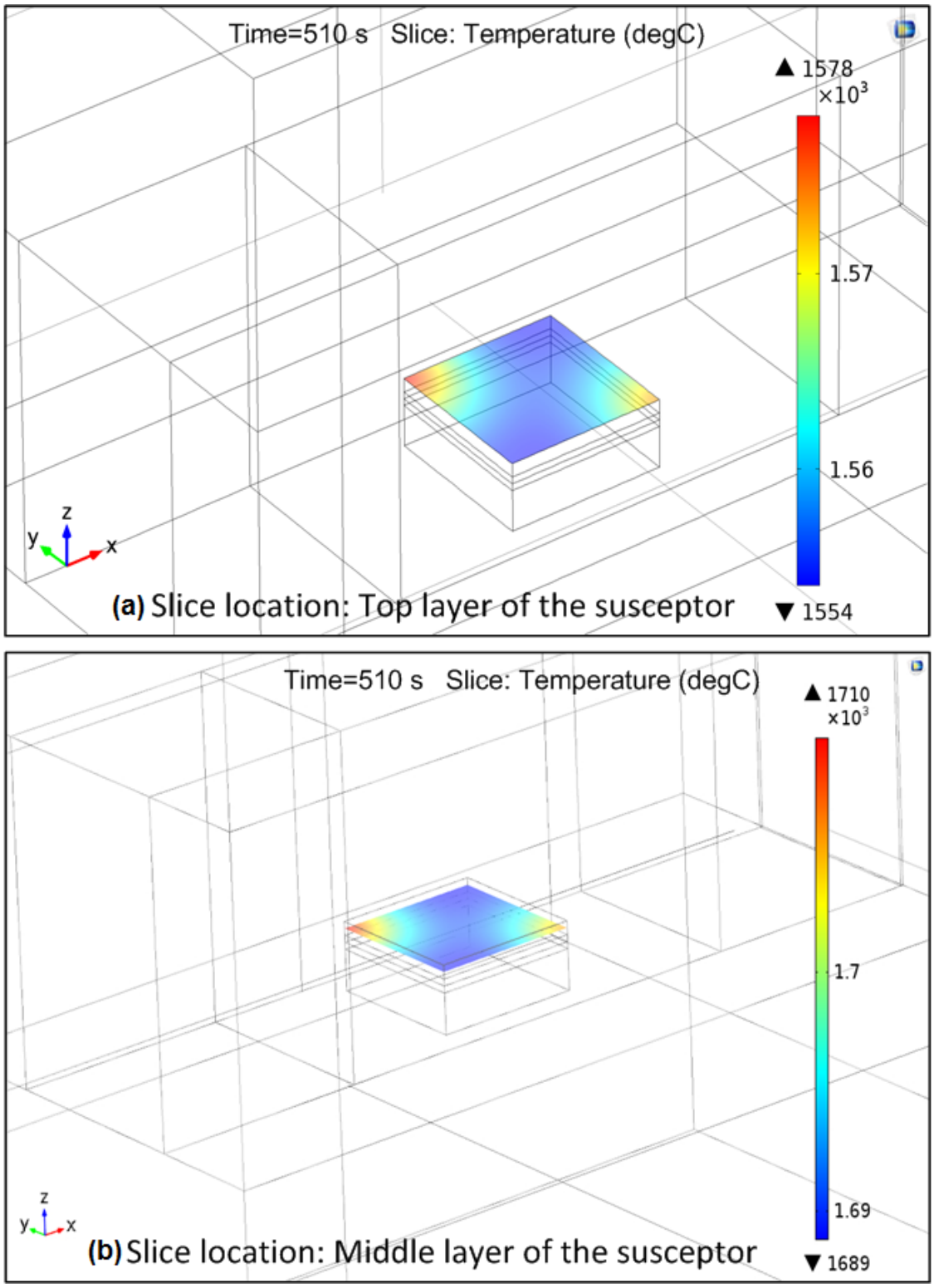

Fig. 3.9- Simulated temperature profiles at various locations after 510 s of microwave exposure

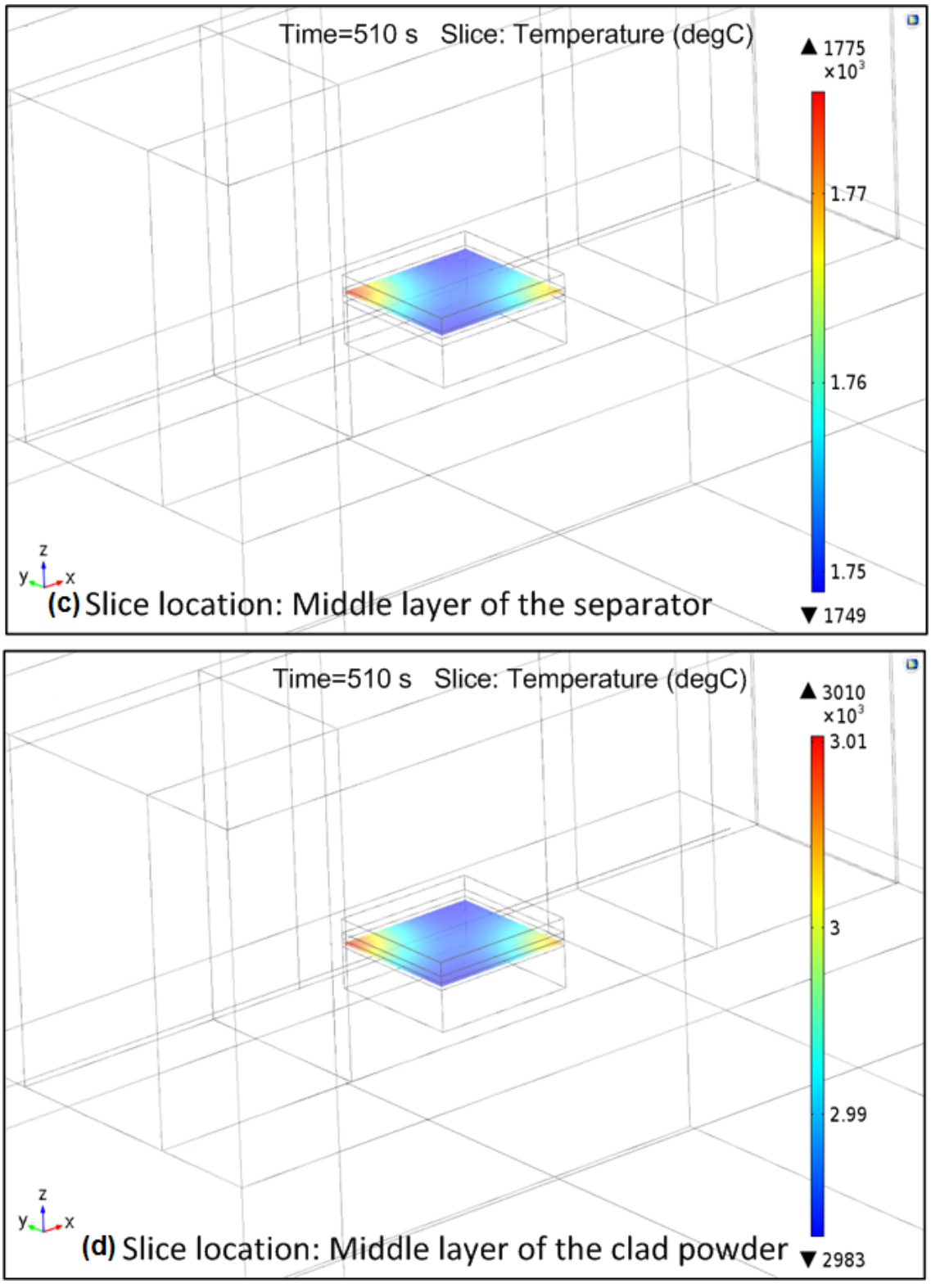

Fig. 3.9- continued

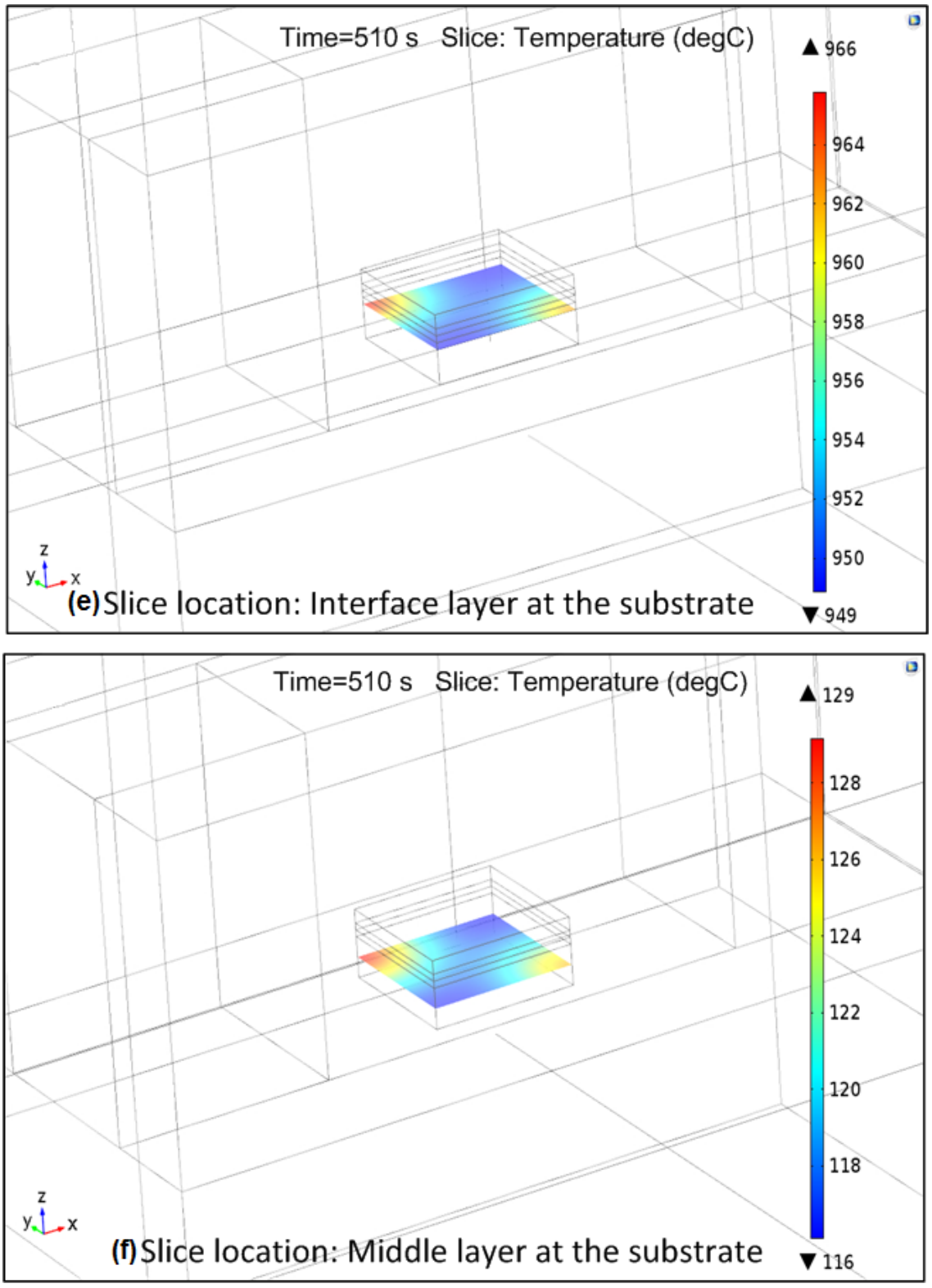

Fig. 3.9- continued

3.5.2. Electric field profile

The electric field intensity in the cavity of the microwave applicator is illustrated in Fig. 3.10. The three-dimensional multislice is shown on Fig. 3.10(a). The electric field intensity was observed to be increased at the location of the hybrid heating arrangement. The maximum value of the electric field (normal component) was observed to be 5.87×10^4 V/m. Although, the maximum intensity was observed at the port in Fig. 3.10(a), but in Fig. 3.10(b-d) the maximum electric field intensity is at the hybrid heating arrangement. It can be further observed that the electric field intensity is maximum at the middle of the clad layer ($E = 6.56 \times 10^4$ V/m). This indicates that beyond the critical temperature the clad material couples with the incident microwave radiation. Further, it is interesting to observe that the electric field intensity is more concentrated with the susceptor and clad layer as shown in Fig. 3.10(e). This indicates that the susceptor and the clad layer interact with incident microwave radiation. The charcoal powder was used as the susceptor in the present experimental trials. Once the susceptor gets heated, it transfers the heat through conventional modes to the clad powder through the separator. Beyond the critical temperature the loss tangent of the clad powder increases as it couples with microwave energy. Consequently the clad powder and a thin interfacing layer of the substrate gets melted. The electric field intensity in the clad layer after an exposure of 510 s is illustrated in Fig. 3.10(f). It can be observed that the value of the electric field is maximum (6.56×10^4 V/m) within the clad layer compared to other locations within the microwave cavity.

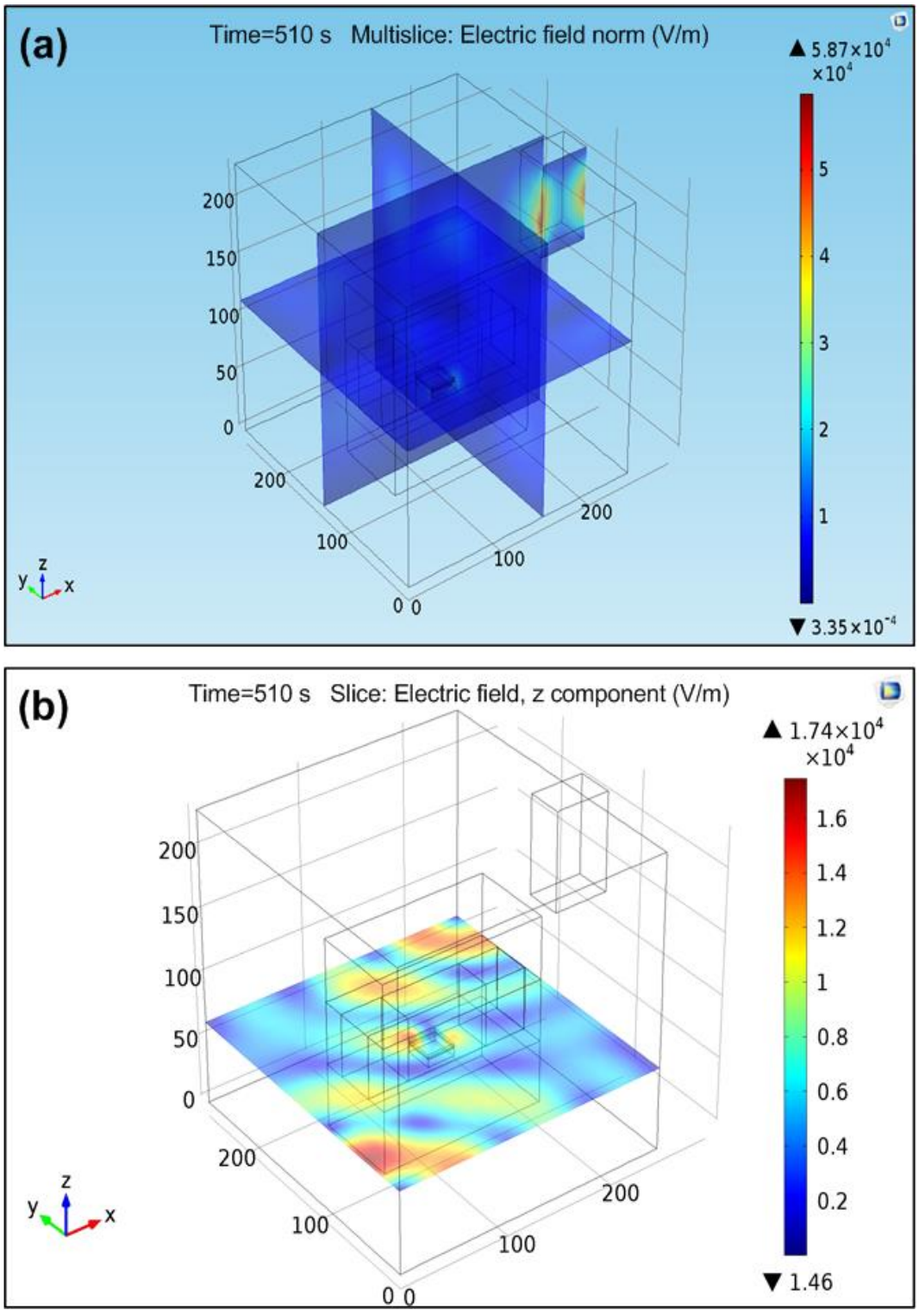

Fig. 3.10- Simulated electric field distribution (a) multislice in the applicator cavity, (b) electric filed z component, (c) electric field x component, (d) electric field y component, (e) electric field across hybrid heating arrangement and (f) electric field at middle of the clad layer

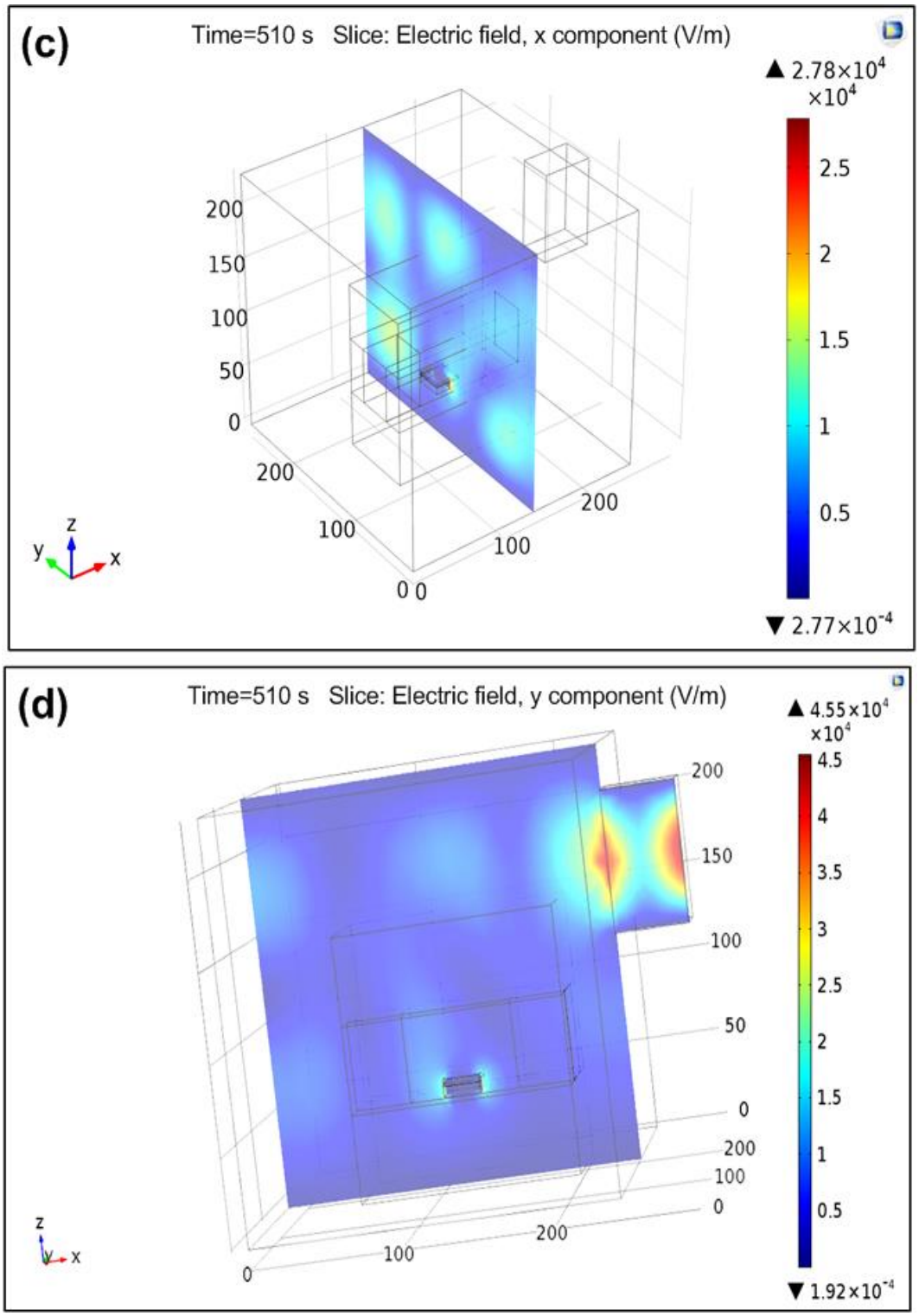

Fig. 3.10- continued

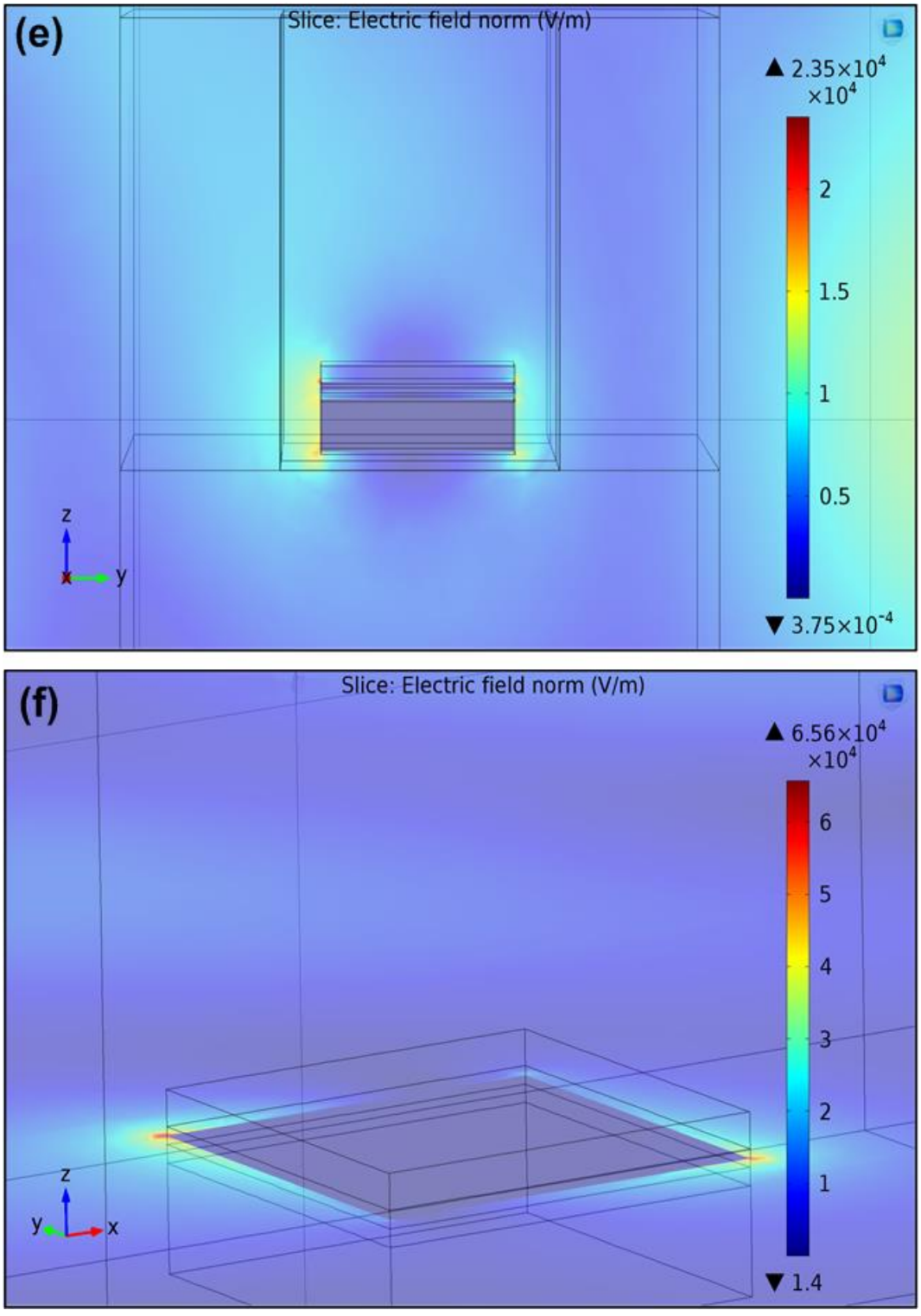

Fig. 3.10- continued

3.5.3. Resistive losses

The simulated resistive losses in applicator cavity are illustrated in Fig. 3.11. The resistive losses indicate the conversion of the microwave energy into heat energy as function of the dielectric properties of the material. It can be observed that the value of resistive losses is higher in the susceptor and clad layer as illustrated in Fig. 3.11(a). Further, it can be observed that the resistive losses were higher in the clad layer as compared to the susceptor as shown in the zoomed view in Fig. 3.11(b); further, the distribution of the resistive losses is not uniform in the clad layer. This non-uniform distribution of the resistive losses results in the formation of the localised convective currents in the molten clad layer. The occurrence of increased thermal gradient is common phenomenon observed in microwave heating (Oghbaei and Mirzaee, 2010; Thostenson and Chou, 1999). The core of the irradiated material is at higher temperature than its surface during microwave exposure. However, the material loses heat to its surroundings due to convection and radiation. The non-uniform resistive losses within the clad layer cause the formation of convective currents as illustrated in Fig. 3.11(b). This results in the formation of wavy interface in the microwave induced clads as illustrated in Fig. 3.2. The maximum value of the resistive losses is at the clad layer and is of the order of 6.1596×10^6 W/m^3. The distribution of the resistive losses in hybrid heating arrangement confirms the selective heating characteristics of microwave heating. The distribution of resistive losses and temperature distributions further confirm that the substrate is not affected by the increasing temperature of the clad layer owing to it poor thermal conductivity. The above model may be suitable to optimise the microwave cladding parameters for a non-magnetic clad powder and substrate.

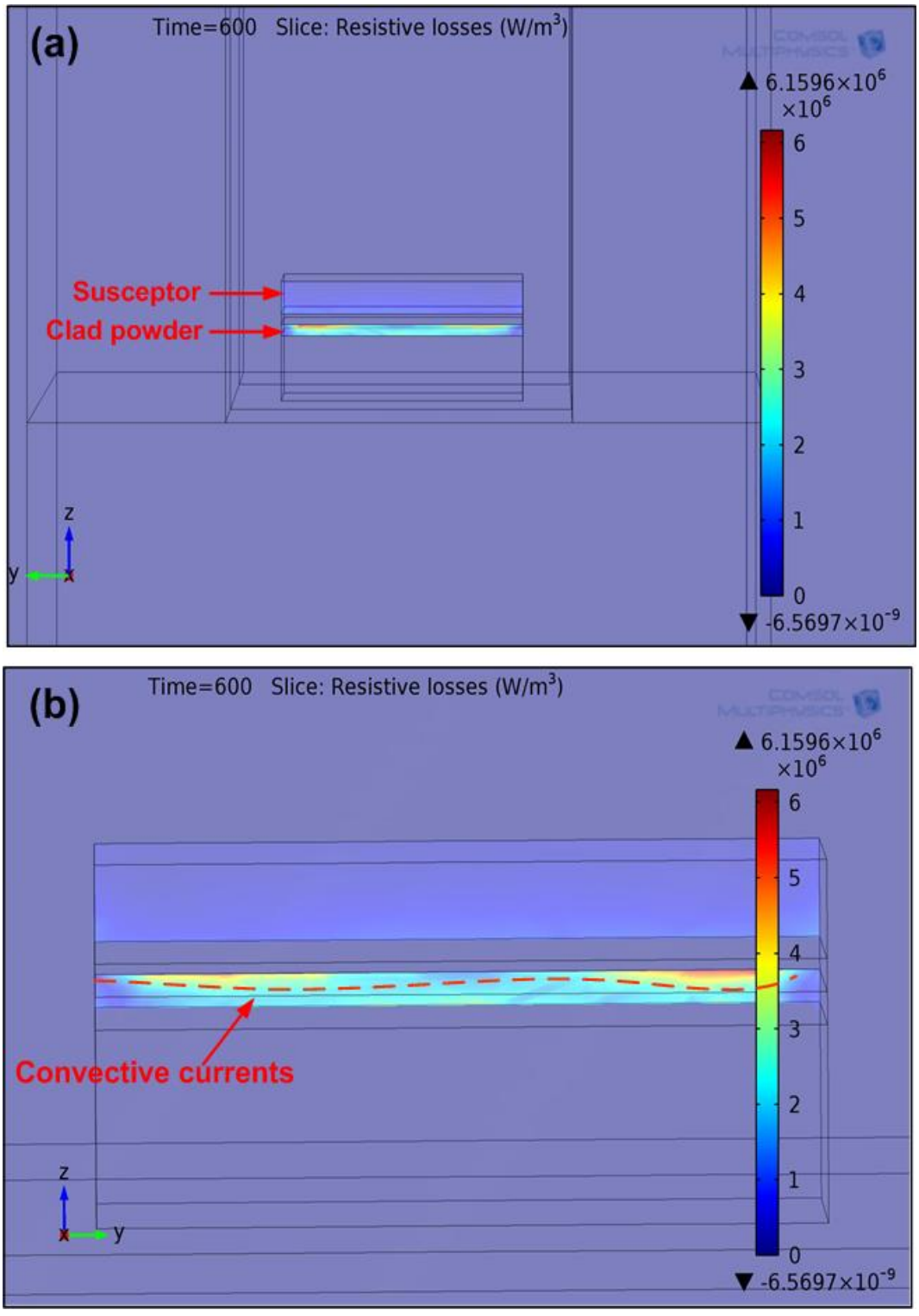

Fig. 3.11- (a) Resistive losses in the hybrid heating arrangement and (b) zoomed view of the hybrid heating arrangement (side view)

3.6. SUMMARY

The three dimensional modelling and simulation of microwave cladding process were carried out using COMSOL Multiphysics software. The simulated results include temperature distribution, electric field distribution and resistive losses within the hybrid heating arrangement. The simulated results largely agree with the experimental data, heating behaviour of the hybrid heating arrangement. The temperature of the clad layer is well higher than the temperature of the susceptor layer, which is in agreement with the inverse heating phenomenon of microwave heating. The temperature profile up to 510 s is in agreement with experimental profile. Beyond 510 s, the temperature in the simulated profile continues to increase; however, the experimental temperature profile tends to flattens as the cladding trials were carried out in auto cut-off mode. The auto cut-off mode helps in maintaining a fixed temperature of the clad layer and prevents the condition of thermal run away, which may lead to melting of the substrate as depicted by the simulated temperature profile. The microwave energy gets more concentrated at the corners of the hybrid heating arrangement due to the formation of hot spots. The electric field distribution in the applicator cavity is non-uniform, but higher electric field intensity occurs within the clad layer. This implies that the electric field component has a major influence on the heating of the WC-12Co clad powder. The distribution of the resistive losses is the maximum in the clad layer. This implies that the clad layer gets heated up due to the incident microwave radiation coupled with conventional heating from the heated susceptor. The non-uniform distribution of the resistive losses leads to inverse thermal gradient with the molten clad layer. This inverse thermal gradient leads to the occurrence of convective currents in the clad layer, which results in the formation of a wavy interface.

CHAPTER 4
EXPERIMENTAL DETAILS

In the present work, development of wear resistant surfaces was carried out bulk metallic substrate using microwave cladding technique. The following sections explain the details of the materials and experimental procedure to develop the clads. Different techniques used to characterise the metallurgical, mechanical and tribological aspects of the microwave clads have been briefly described.

4.1. MATERIAL SELECTION

The following sections describe the selection of the substrate material and clad powder.

4.1.1. Substrate material

Austenitic stainless steels (ASS) are face centred cubic structured iron based alloys. These are obtained by alloying elements that promote formation of austenite, most notably Ni in large quantities (generally over 8% wt.). Additionally C and N are also added as strong austenite promoters. Austenitic stainless steels generally exhibit good ductility, high toughness, formability and weldability and excellent corrosion resistance (Lippold and Kotecki, 2005). The 300 series of alloys are the oldest and most commonly used among a variety of austenitic stainless steels. Most of these alloys are based on the 18Cr-8Ni system, with additional alloying elements or modifications to provide unique and/or enhanced properties at reasonable cost. The 304 grade ASS exhibits poor wear characteristics including poor resistance to galling and seizure (Rigney, 1997). They suffer severe wear due to the formation of strong adhesive junctions between contact surfaces, and surface and subsurface plastic deformation (Sun and Bell, 2002). However, tribological properties of austenitic stainless steel can be improved significantly by depositing a tribological layer of suitable wear resistant material using appropriate techniques including microwave cladding process. In the present work, austenitic grade stainless steel (SS-304) was selected as the substrate material.

4.1.2. Clad powder

Hardness as well as toughness is important characteristics for enhanced tribological performance of functional surfaces of engineering components. Cermets are generally considered as wear resistant materials. Cermets are composites that consist of one or more hard material and a ductile binder that imparts certain degree of toughness. Tungsten carbide (WC) is generally known to display outstanding mechanical properties at room temperature as well as higher temperatures up to 400 °C. The exceptional combination of high hardness, strength, resistance to compressive deformation and wear resistance make WC-Co based cermets a popular wear resistant material (Upadhyaya, 1999). Further, acceptable production costs of WC-Co cermets coupled with the ability to deal with several wear mechanisms like erosion, adhesion and abrasion often make it a suitable choice as a wear resistant material. Usually, WC-Co based cermets are widely used to provide wear resistance to various industrial components such as, high speed cutting tools, material deformation tools, mining bits, rock drilling, wear resistant nozzle coatings, press moulds, bearing and mechanical face seals etc. (Bonny et al., 2010). In general, hardness and wear resistance of the WC-Co based cermets increases with the decrease of carbide particle size and increased volume fraction of the carbides. Reduced carbide particle size reduces the mean free path of the binder phase, resulting in greater constraints and higher hardness. Higher carbide volume fraction of the carbides results in less exposure of the relatively soft matrix to the counter surface material. Therefore, two types of commercially available WC-12Co powders- micrometric (MM) and nanometric (NM) were used to deposit clads on SS-304 substrate using MHH technique.

4.2. CHARACTERISATION OF THE MATERIALS

Performance and response of any material is related to its microstructure, grain size, elemental composition, hardness etc. Therefore, it is essential to characterise the material to be processed. Although several techniques for characterisation of materials are available, but the characterisations significant with respect to intended study were carried out. The materials under present investigation were characterised for their metallurgical, mechanical and tribological aspects using X-ray diffraction (XRD), field emission scanning electron microscope (FE-SEM) equipped with energy dispersive X-ray

spectrometer (EDS), optical microscope (OM), electron probe micro analyser (EPMA), microhardness tester, universal testing machine (UTM), pin-on-disc tribometer, dry sand rubber wheel test rig and solid particle erosion test rig. The relevant specifications and details of these characterisation facilities are presented in Appendix A (Fig. A-1 to A-13). The following sections briefly describe the characterisations of the substrate (SS-304) and the clad powder.

4.2.1. Characterisation of the substrate material

The characterisation of as-received austenitic stainless steel substrates (SS-304) was carried out in order to determine its microstructure, grain size, elemental composition, tensile strength, flexural strength and hardness. Fig. 4.1 illustrates the optical micrograph of the SS-304 substrate as observed using a Dewinter inverted optical microscope (Make: Dewinter, Model: LT-23B). The substrate was polished using standard metallographic procedure and was etched using Viella's etching reagent (5 cc hydrochloric acid + 2 g picric acid + 100 cc ethyl alcohol) for 15 s to reveal the microstructural features. The average grain size observed was of the order of approximately 30 µm. The elemental composition of the SS-304 substrate was determined using EPMA (Make: Cameca, Model: SX100) at an accelerating voltage of 20 kV and beam diameter of 1 µm. A Vicker's microhardness tester (Make: Chennai Metco, Model: Economet VH1-MD) was used measure the microhardness, while an UTM (Make: Instron, Model: 5982) was used to evaluate the tensile and flexural strength of the SS-304 substrate. The results of the elemental composition and mechanical properties are presented in Table 4.1.

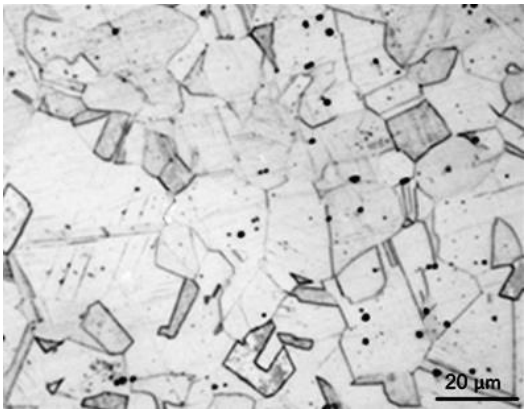

Fig. 4.1- A typical optical micrograph of SS-304 substrate

Table 4.1- Elemental composition and mechanical properties of SS-304 substrate

Elements in weight percentage							**Mechanical Properties**		
Fe	Ni	Cr	Mn	Si	C	Others	Microhardness ($HV_{0.050}$)	Tensile strength (MPa)	Flexural strength (MPa)
Bal	9.8	19.0	2.1	0.74	0.08	0.16	322±18	508±27	1198±22

4.2.2. Characterisation of the clad powder

In the present work, commercially available WC-12Co cermet powder was used as the clad powder. The clad powder used was in two sizes, MM (Product code: MEC 127; Supplier: Metallizing Equipment Company, Jodhpur, India) and NM (Product code: K512; Supplier: Hongwu International Group, Hong Kong). The clad powders were characterised using XRD, FE-SEM equipped with EDS facility. The XRD diffractograms of the MM and NM clad powders are shown in Fig. 4.2. Dominant presence of tungsten carbide (WC, JCPDS file: 005-0728) along with cobalt (Co, JCPDS file: 001-1259) were observed from the X-ray diffractograms (Fig. 4.2 (a) and (b)). The WC is responsible for imparting high hardness, while Co acts as a binder that provides toughness to the matrix through its excellent carbide wetting and adhesion properties. Peak broadening, a well-known phenomenon in XRD patterns of the nanomaterials, was observed in the XRD pattern of the NM clad powder in Fig. 4.2(b).

The morphology and elemental composition of the powder particles were evaluated using FE-SEM in secondary electron (SE) mode. The clad powder particles were sprinkled on an aluminium stub and were held in place using an adhesive carbon tab. The ensemble was then sputter coated with gold using a sputter coater (Make: EMS, Model:150R) to make the particles conductive. Typical SEM micrographs illustrating morphology along with elemental composition of the MM and NM clad powder are shown in Fig. 4.3. SEM micrograph of MM raw powder illustrates spherical agglomerated morphology (size 45±15 µm) with an average carbide size of 2-5 µm. The individual WC particles are cuboidal in shape with sharp edges and can be clearly identified in the inset (Fig. 4.3 (a)). The NM powder illustrates irregular crushed morphology with an average particle size of 100-200 nm. The inset SEM micrograph illustrates the irregular shaped WC particles in the NM clad powder (inset Fig. 4.3 (c)). The elemental composition of the MM and NM powder indicate W accounts for around 75%, while Co accounts for

approximately 12% and remaining is C (Fig. 4.3 (b) and (d)). The MM particles in Fig. 4.3 (a) appear hollow shell morphologically. A further investigation in this aspect was carried out by examining the area BB as shown in Fig. 4.4. The MM powder particles were polished from one direction keeping them fixed in an epoxy binder. The inside of a typical agglomerated particle as viewed through SEM confirms that the powder particles are not hollow (Fig. 4.4 (b)) and consisted of angular WC particles agglomerated in the Co binder (Fig. 4.4 (c)). However, this structure will not affect the clad microstructure as these particles are completely melted during the cladding process.

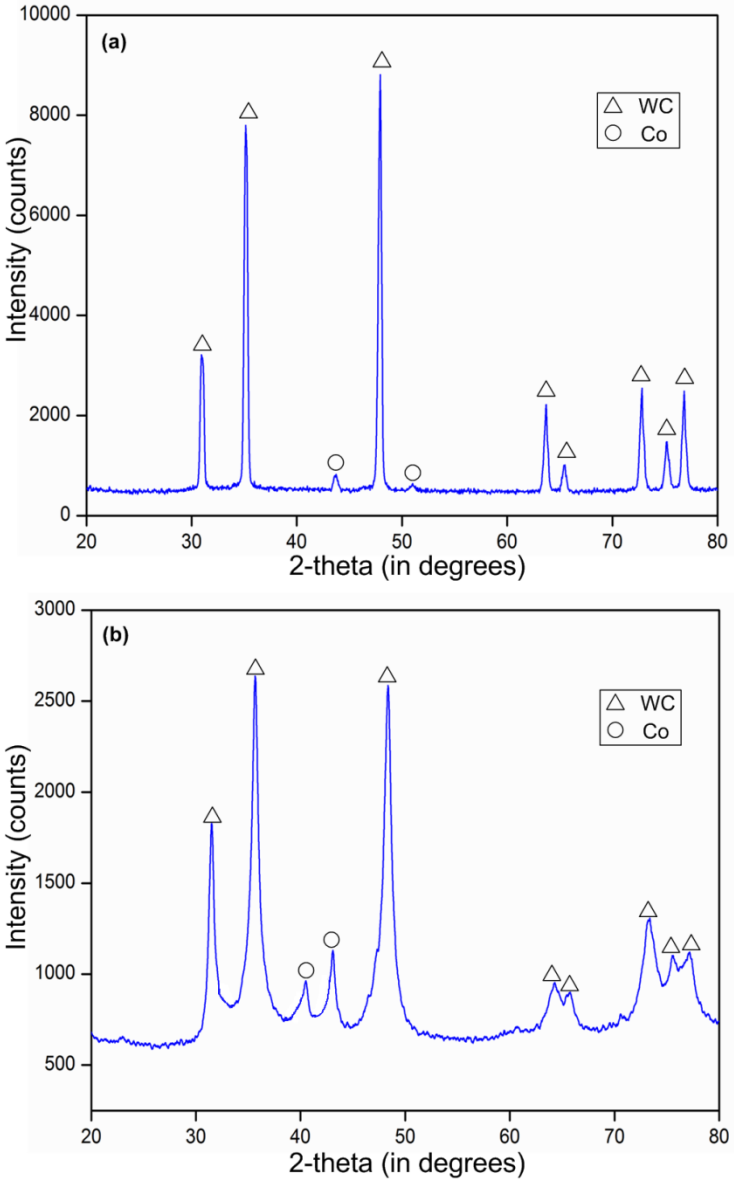

Fig. 4.2- Typical XRD diffractograms of (a) MM and (b) NM WC-12Co clad powder

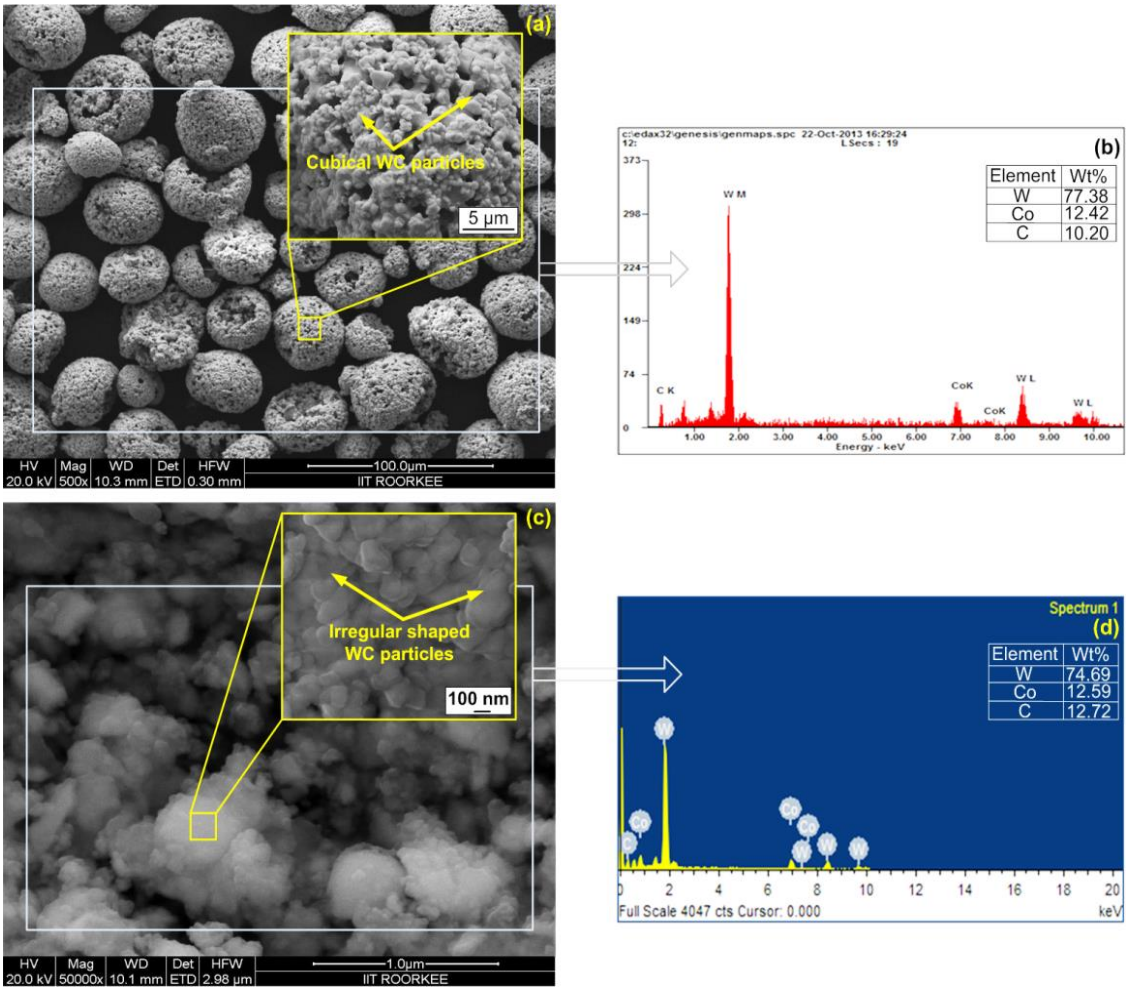

Fig. 4.3- (a) Typical SEM micrograph, (b) EDS spectrum of MM WC-12Co clad powder, (c) SEM micrograph and (d) EDS spectrum of NM WC-12Co clad powder. Inset: Magnified view of the powder particles

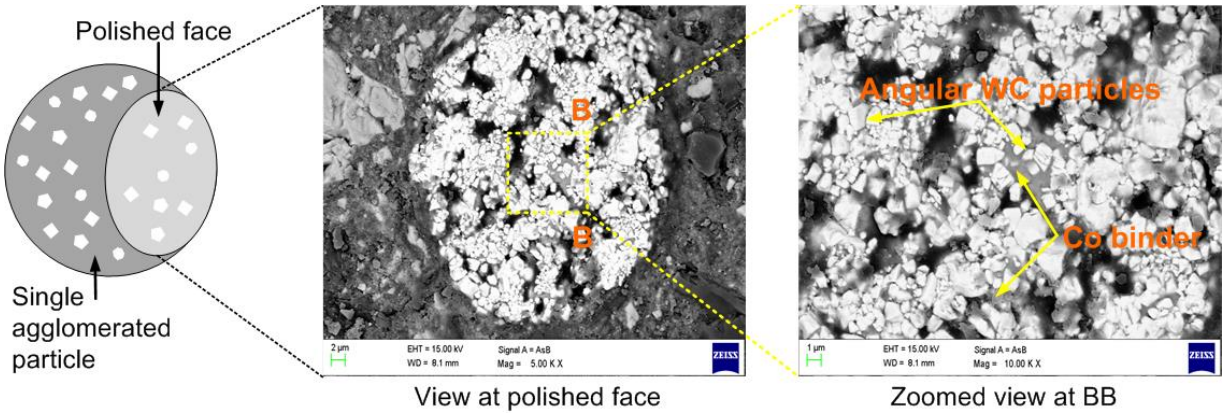

Fig. 4.4- Typical views of the cross-section of the WC-12Co MM powder particle

4.3. SUBSTRATE AND POWDER PREPERATION

Preparation of substrate and clad powder is vital to develop effective clads using microwave energy. The as-received austenitic stainless steel (SS-304) plates were machined to prepare substrate specimens of size 25 × 25 × 7 mm^3. The substrates were ground and polished up to #1500 SiC grits to achieve an initial surface roughness of R_a= 0.19 µm. Increased surface roughness offers increased surface area to from metallurgical bonding with the clad layer. A 3-D optical surface profilometer (Make: Veeco Wyko, Model: 1100NT) was used to evaluate the surface roughness of the substrates. The prepared substrates were ultrasonicated to in an ethanol bath prior to cladding. A few prepared substrate specimens are shown in Fig. 4.5. The micrometric and nanometric WC-12Co clad powders were preheated at 120 °C for 8 h in conventional muffle furnace (Make: Heraeus Electronics, Model: CD-6450) to remove any possible moisture content. The powder was then preplaced manually on the substrate maintaining an average thickness of approximately 1 mm. A CNC controlled spindle fixed with a glass slide at the tip was used to maintain uniform thickness of the preplaced powder on the substrate.

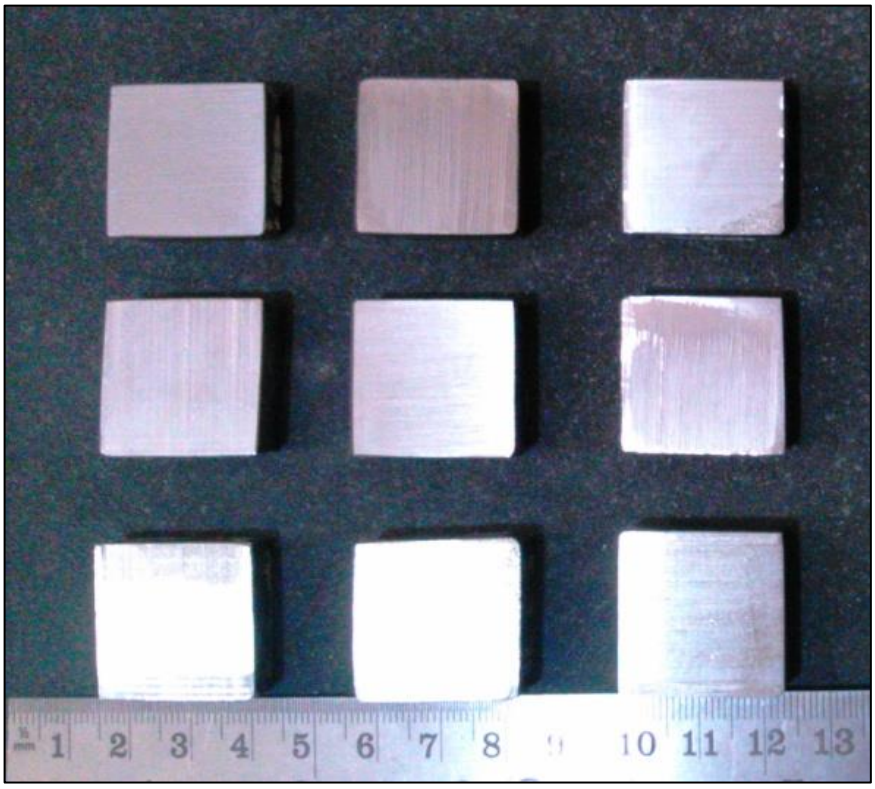

Fig. 4.5- A few prepared substrate specimens

4.4. MICROWAVE CLADDING PROCESS

Microwave cladding was accomplished in an industrial multimode microwave applicator (Make: Enerzi Microwave Systems, Model: MH-1514-101-V6) equipped with an infrared pyrometer (Range: 350 °C - 1800 °C). The microwave irradiation was carried out in auto cut-off mode at 2.45 GHz. The cladding trials were carried out in atmospheric conditions. A flow chart depicting the experimental and characterisation route adopted in the present work is shown in Fig. 4.6.

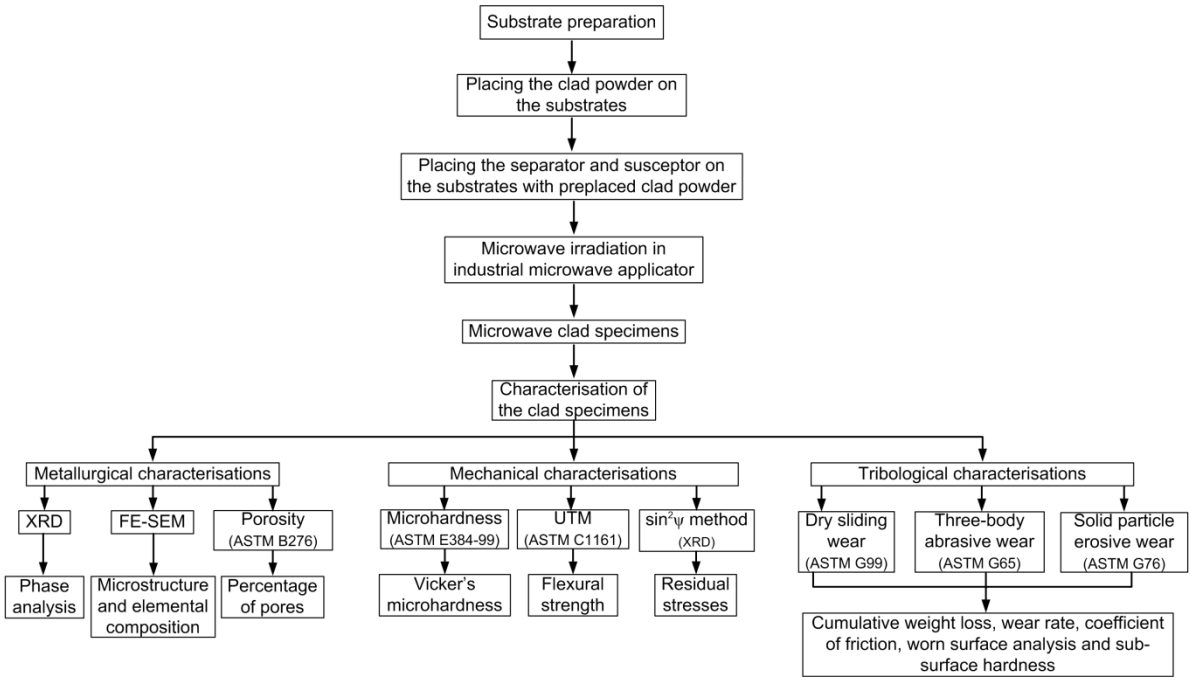

Fig. 4.6- Development and characterisations of the MM and NM WC-12Co microwave clads

Tungsten carbide is the major constituent of the WC-12Co MM and NM clad powder as indicated by the XRD spectrum of the powder in Fig. 4.2. The skin depth of tungsten carbide with respect to microwave exposure, as calculated by Rödiger et al., is approximately 4.7 μm (Rödiger et al., 1998). Skin depth is defined as 'the distance into the material at which the incident power drops to 1/e (36.8%) of the surface value' (Mondal et al., 2010). Thus, increasing the skin depth in a material body, or enhancing the penetration depth inside the material body becomes a critical issue while processing materials through microwave irradiation.

Hence, the WC-12Co cermet particles in the MM powder cannot directly absorb microwave energy instead they tend to reflect it. Further, ceramics like WC exhibit low loss tangent at ambient temperatures, but as the temperature increases beyond the critical temperature (T_c), the loss tangent increases significantly (Sharma and Krishnamurthy, 2002). The MHH technique has proved to be viable to process such materials by utilising a susceptor material (Bansal et al., 2014; Chandrakanth et al., 2009; Fida Hassan et al., 2014; Gupta and Sharma, 2014; Oghbaei and Mirzaee, 2010; Rajkumar and Aravindan, 2011, 2009; Sharma et al., 2001). The susceptor material raises the processing temperature beyond T_c, beyond which the target material effectively couples with microwave radiation.

Enhancing the skin depth of a material is an important issue in microwave processing of microwave reflecting materials. Nanostructured materials possess higher surface area. Higher surface area, coupled with reduced average particle size contributes to better absorption of microwave energy. Better microwave absorption leads to uniform and volumetric heating of the clad powder. The particle size of the NM WC-12Co clad powder is about 22 times smaller (100-200 nm) than the skin depth. Consequently, heating of the NM clad powder is possible due to interaction of the irradiated (microwave) energy with the material. However, microwave irradiation of metallic particles raises safety concerns related to electric arcing. It was further reported that as the powder particle size reduces to submicron range, arcing is significantly reduced (Bilecka and Niederberger, 2010). However, in the present work, direct microwave irradiation of the nanostructured WC-Co material resulted in differential heating. This caused arcing probably due to (i) the tiny sharp edges in the largely non-spherical particles and (ii) rapidly increasing dielectric properties that resulted in the formation of 'hot spots'. Consequently, MHH technique was used to develop the NM WC-12Co clads. In MHH, combination of both conventional heating and microwave heating leads to uniform heating of the target material.

In the present work, MHH arrangement using charcoal powder was utilised to initiate heating and minimise the thermal gradient to develop the MM and NM WC-12Co clads. Charcoal further acts as the source of carbon during the MHH that minimises possible decarburisation in the WC-Co clads (Gupta and Sharma, 2012). The hybrid heating arrangement was placed at the centre of the microwave cavity inside an alumina wool envelop, which allows microwaves to pass through and insulates the heat generated. The schematic representation of the MHH setup used to develop the WC-12Co clads is shown in Fig. 4.7. A 1 mm thick alumina plate (purity 99%) was used as a separator to

avoid any possible contamination of clad powder by the susceptor. The metallic substrate (SS-304) was selectively masked using a carbon block to avoid reflections of microwaves. A detailed description of mechanism of clad formation through MHH has been presented in Chapter 3. Several cladding trials were carried out in order to optimise the parameters through trial and error basis. The optimised cladding parameters for MM and NM powders are presented in Table 4.2.

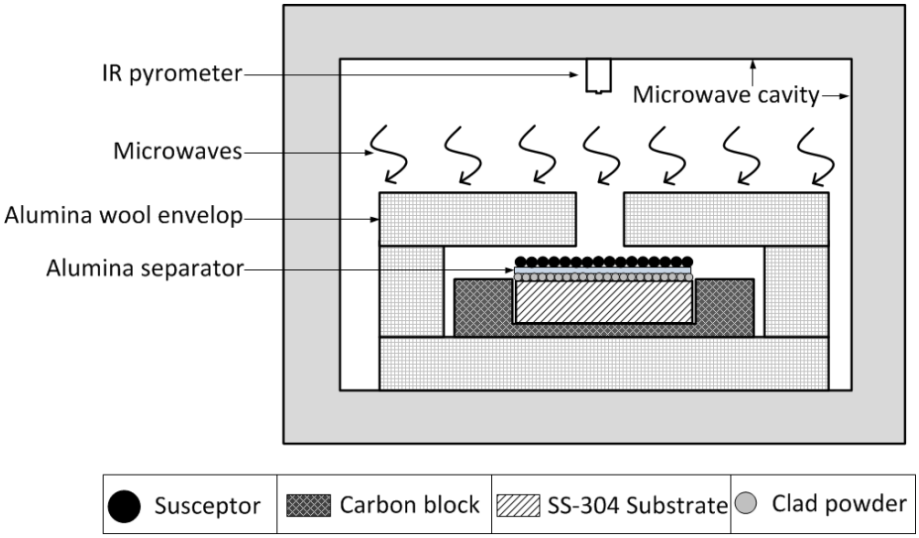

Fig. 4.7- Schematic representation of the MHH experimental setup used to develop the clads

A view of the industrial multimode microwave applicator used in the present work is illustrated in Fig. 4.8. The microwave exposure was carried out in the range of 540 to 720 s depending on the clad powder (MM or NM) and size of the substrate specimen. During the trials, the temperature at the top surface of the susceptor was monitored using a built-in non-contact infrared pyrometer through a quartz window. The optimum temperature range and other process parameters for developing the MM and NM clad are summarised in Table 4.2. In the present experimental setup, the clad powder layer was below the susceptor layer (Fig. 4.7). Therefore, it was difficult to measure the actual temperature of clad powder during microwave exposure. Hence, the temperature at the top surface of the susceptor is reported. Photographs of a few MM and NM microwave clads are shown in Fig. 4.9.

Fig. 4.8- A photograph of the industrial microwave applicator, (inset: view of the microwave cavity)

Table 4.2- Microwave processing parameters used in cladding of WC-12Co

Particulars	**MM clads**	**NM clads**
Substrate material	Commercial grade SS-304	
Clad powder	WC-12Co (MM)	WC-12Co (NM)
Powder particle size	45±15 µm	100-200 nm
Exposure time	600-720 s	540-660 s
Measured temperature	About 1400 °C	About 1400 °C
Microwave power	1.4 kW	1.1 kW
Microwave frequency	2.45 GHz	
Processing environment	Ambient	

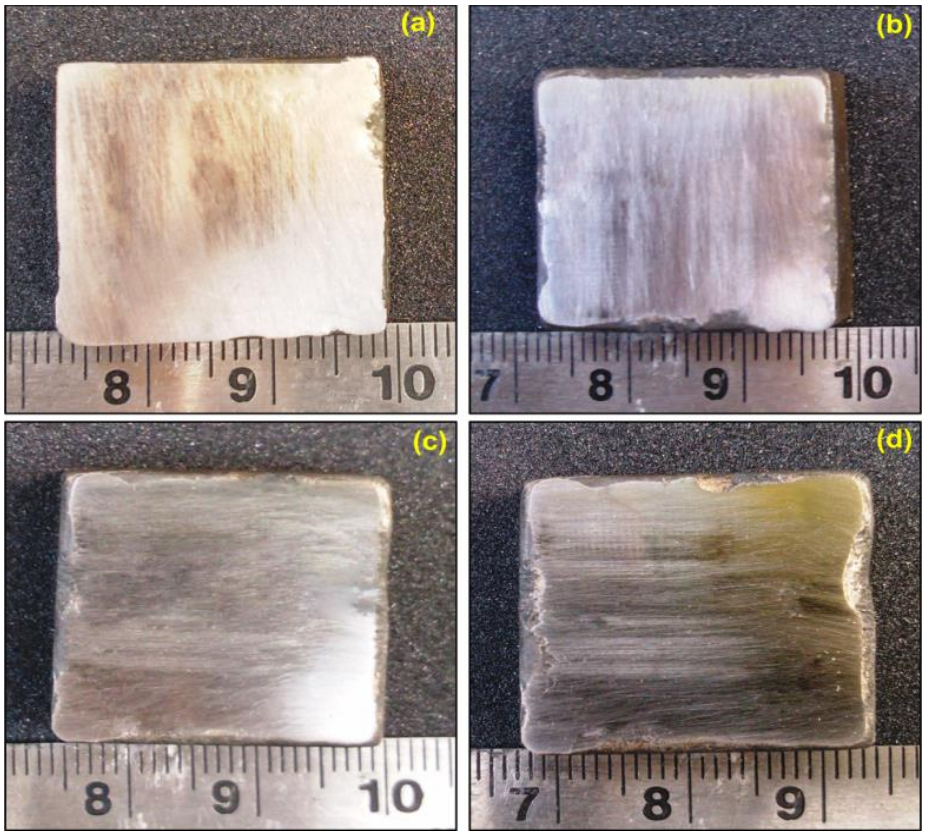

Fig. 4.9- Images of MM (a-b) and NM (c-d) WC-12Co microwave clads

4.5. METALLURGICAL CHARACTERISATION OF THE CLADS

Microwave cladding of WC-12Co MM and NM cermet powders was successfully accomplished using MHH technique in an industrial multimode microwave applicator, as discussed in section 4.4. The developed clads were sectioned across the thickness using a low speed diamond saw (Make: Chennai Metco, Model: BAINCUT LSS) and were cold mounted in an epoxy. The mounted specimens were ground and polished using different grades of emery papers, starting from 100 grit to 2000 grit, followed by velvet cloth polishing using 1 µm diamond paste (Make: Chennai Metco). Metallurgical characterisation of the microwave induced clads was carried out using X-ray diffraction (XRD), field emission scanning electron microscope (FE-SEM), electron probe micro analyser (EPMA) and optical microscope (OM). The following sections briefly explain the procedures and equipment used in the metallurgical characterisation of the WC-12Co clads.

4.5.1. X-ray diffraction (XRD)

The phase analysis of the WC-12Co MM and NM microwave clads was carried out using XRD. A Bruker AXS diffractometer (Model: D8, Make: Germany) was used to characterise the different phases present in the microwave WC-12Co clads. The details of the X-ray diffractometer are given in Fig. A-1 in Appendix A. The specimens were exposed to monochromatic Cu Kα X-ray radiation (λ=1.54056 Å) at room temperature. The voltage and current values were set at 40 kV and 30 mA, respectively. The diffraction data were collected over a sensitive 2-θ range of 30˚ to 80˚ with step size of 0.1° and 5 s dwell time per step. The value of the obtained Bragg's angle (2θ) and interplanar spacing (d) were subsequently matched with standard values of WC, Co and related phases.

4.5.2. Microstructure characterisation

Microstructural characterisation was carried out in order to determine the carbide grain size, carbide morphology, interfacial integrity between the reinforcing carbide and matrix, elemental composition of the carbide phase and matrix. The microstructural features of the microwave induced WC-12Co microwave clads was evaluated using a FE-SEM (Make: Carl Ziess, Model: Gemini Ultra Plus) equipped with EDS (Make: Oxford, Model: x-max). The FE-SEM was operated in the secondary electron (SE) mode and back scattered electron diffraction (BSE) mode to acquire the images. Back scattered electron mode was used to study to phase content, carbide grain morphology and size as difference in the atomic weight results in contrast. Detailed quantitative elemental analysis was also conducted through an EPMA (Make: Cameca, Model: SX-100) with a beam diameter of 1 µm at an accelerating voltage of 15 kV. The details of the FE-SEM and EPMA are provided in Fig. A-2 and A-3 respectively in Appendix A.

4.5.3. Porosity measurement

The porosity in the MM and NM WC-12Co microwave clads was quantified using an optical microscope (Make: Dewinter, Model: LT- 23B) having an image analysis software tool (Dewinter Material plus, version 4.2) as per ASTM B276. Details of the optical microscope are presented in Fig. A-4 in Appendix A. Images were captured from 10 different locations in the clad layer of the metallographically polished specimens at 200× to measure the porosity. The porosity was assessed by varying the threshold of the region where a small variation of threshold value generates large variations of the porosity. An average of five measurements was considered.

4.6. MECHANICAL CHARACTERISATION OF THE CLADS

The mechanical aspects of the WC-12Co MM and NM clads were assessed in terms of microhardness, residual stresses and flexural strength. The following sections briefly explain the procedures and details of mechanical characterisations of the clads.

4.6.1. Microhardness assessment

The microhardness relates to specific structure developed in the clad layer. Hardness of a material relates to its ability to resist indentation, which further influences its wear performance. In general, higher hardness indicates enhanced wear performance. The microhardness across the transverse sections of the MM and NM clads was evaluated as ASTM E384-99 using a Vickers's microhardness tester (Make: Chennai Metco, make: Economet VH1 MD) at 50 g load and 10 s dwell time. The distance between two successive indentations was kept about 100 μm starting from the top of the clad towards the substrate. Three indentations were carried out laterally and the mean was considered. The details of the microhardness tester used are presented in Fig. A-5 in Appendix A.

4.6.2. Flexural strength testing

A standard three-point bend test was carried out to evaluate the flexural strength of the microwave clads. The test were conducted on a UTM (Make: Instron, Model: 5982) as per ASTM C1161 standard at a crosshead speed set at 1 mm/min (Fig. 4.10(a)). The size of clad specimen for flexural strength test was kept as 50 × 12 × 5 mm^3. The test was conducted on flat specimens placing the cladding in tension while the span between the supporting pins was 30 mm as illustrated in Fig. 4.10(b). Prior to flexural strength testing, the samples were polished using 1 µm diamond paste to remove any oxide layer from the clad surface. Load and displacement characteristics were recorded for each sample. The flexural strength (σ) was calculated using equation 4.1.

$$\sigma = \frac{3P_y L}{2Wt^2} \tag{4.1}$$

where:
σ is the bending strength (MPa),
P_y is the maximum load (kN),
L is the distance between the support pins (mm),
W is the width of the specimen (mm), and
t is the thickness of the specimen (mm).

Average of three samples in same conditions was considered and strength values were calculated from the test data. Fractographic analysis of the fractured samples was carried out using electron microscopy. Details of UTM are presented in Fig. A-6 in Appendix A.

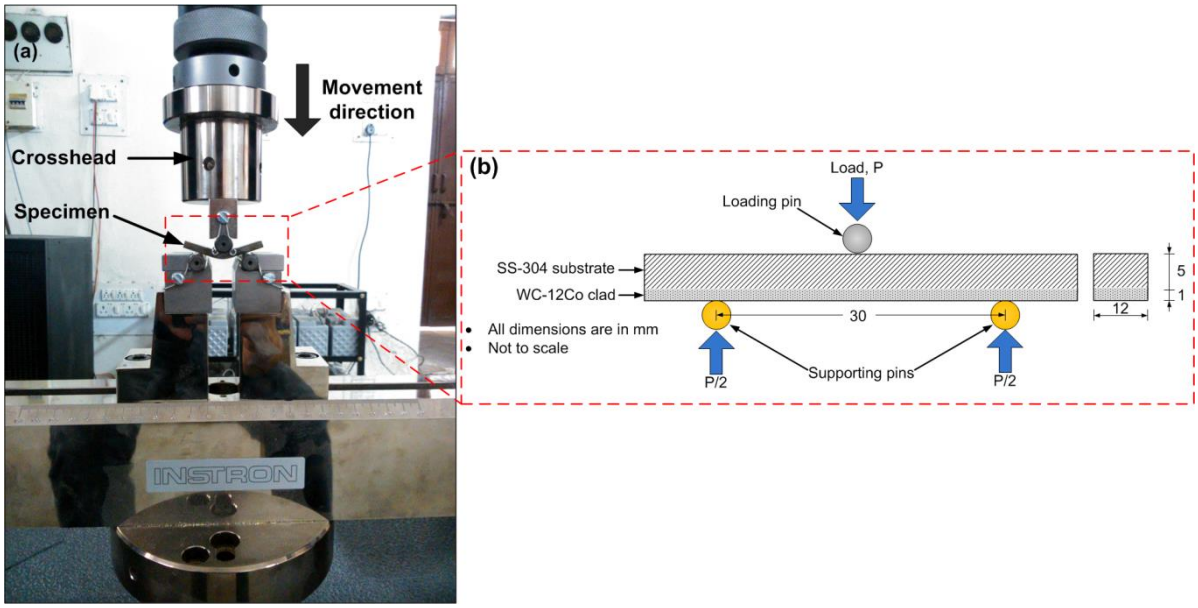

Fig. 4.10- Flexural strength test (a) photograph of the test setup and (b) schematic arrangement of test

4.6.3. Residual stress evaluation

Residual stresses play a vital role in the microstructural and functional aspects of clad layer. Non-destructive techniques, in particular the bending radius of substrate method and the X-ray diffraction, have been popular to evaluate residual stresses in thin films such as coatings/cladding (Ma et al., 2002). However, use of relatively large specimen size and poor spatial resolution in determination of localised stresses in the plan of the overlay layer make the bending radius method a less preferred choice. On the other hand, spatial resolution below 1 μm is attainable using XRD techniques. Therefore, in the present work, residual stresses in the MM and NM microwave clads were determined using XRD technique.

The residual stresses were determined using the standard '$\sin^2\psi$' method, which is based on the measurement of a diffraction peak position recorded for different 'ψ' angle. The 'ψ' is the angle between normal of the sample and normal to the diffracting plane. However, the strain is actually measured using XRD. The strains can be linked to the stress using Hooke's law. The strain is measured by comparing the unstressed lattice interplanar spacing, which is obtained by altering the tilt of the specimen within the diffractometer (Cullity and Stock, 2001). By tilting the specimen, the planes are brought in position where

it satisfies the Bragg's law. Ideally, a high 2-θ diffraction peak is chosen to ensure high sensitivity to strain. Thereafter, the residual strain was derived from the slope of a linear plot (m) between fractional change of the plane spacing and $\sin^2\psi$. Residual stress (σ_r) is calculated by the gradient of the linear plot (m) and basic knowledge of the elastic properties of the material with help of equation 4.2.

$$\sigma_r = \left(\frac{E}{1+\nu}\right) m \tag{4.2}$$

where:

E is the Young's modulus of the material, and

ν is the Poisson's ratio of the material.

Average of three samples was considered and residual stress values were calculated from the test data.

4.7. TRIBOLOGICAL EVALUATION OF THE CLADS

The tribological characterisations determine the functional performance of the microwave WC-12Co clads. Accordingly, the tribological aspects of the MM and NM clads were evaluated using dry sliding wear test, three-body abrasive wear test and solid particle erosion test. The procedures and details of tribological characterisations of the clads are briefly explained in the following sections.

4.7.1. Dry sliding wear test

In the present work, dry sliding wear behaviour of WC-12Co MM and NM microwave clads was investigated according to ASTM G99 using a pin-on-disk tribometer (Make: Ducom, Model: TR-201LE-M8). A standard oil hardened EN31 steel disc was used as the counter surface for sliding wear evaluation. The hardness of the EN31 steel disc was maintained at about 65 HRC. Prior to sliding wear tests, the mating surface of the counter disc was polished using SiC #1000 grits to maintain an initial surface roughness (R_a) of 0.2 μm. The schematic arrangement of the pin-on-disc tribometer arrangement is illustrated

in Fig. 4.11. Normal contact load was varied in order to investigate its effect on the concomitant sliding wear and friction behaviour of the WC-12Co MM and NM microwave clads.

The worn specimens were cleaned by acetone and were hot dried before measuring the weight loss. A microelectronic weight balance (Make: Mettler Toledo, Model: ML 104) with an accuracy of ± 0.1 mg was used to weigh the wear pins before and after the test. Normal load was applied on the clad surface using dead weights through a lever, pulley and string arrangement. The relevant details of the sliding wear trials and setup are given in Table 4.3. Analysis of wear was carried out in terms of wear rate, pressure-velocity-time (p-v-t) characteristics, friction coefficient and cumulative weight loss. Worn wear pins were analysed using FE-SEM for identifying the wear mechanisms. A 3-D optical surface profilometer (Make: Veeco Wyko, Model: 1100NT) was used to characterise the surface profiles of the worn surfaces. Further details of the pin-on-disc tribometer, optical surface profilometer and weight balance are given in Fig. A-9, A-12, and A-13, respectively in Appendix A.

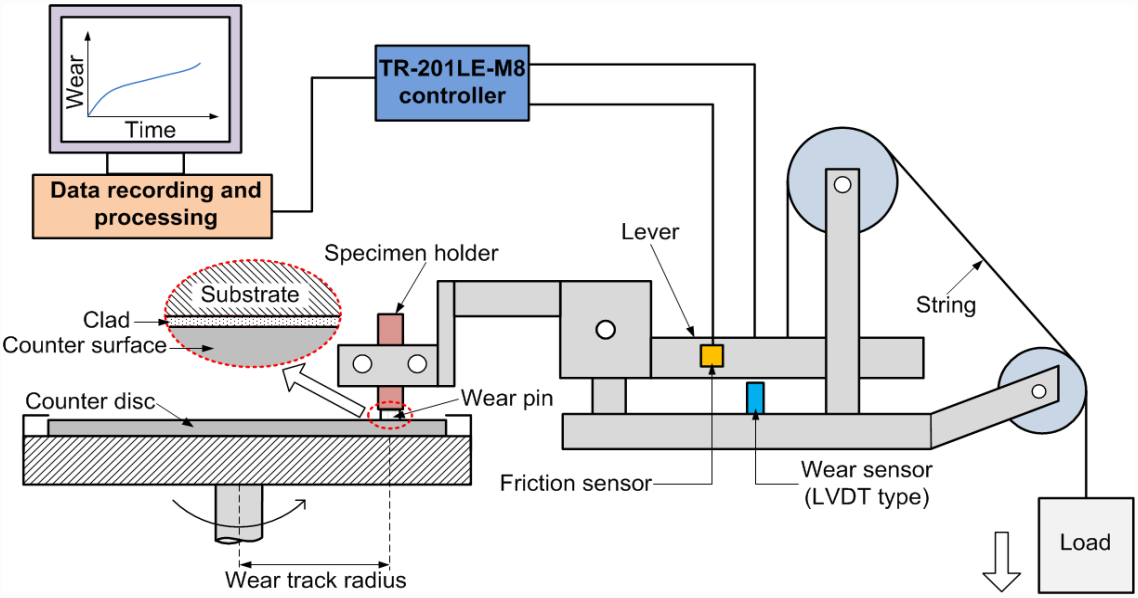

Fig. 4.11- Schematic representation of the pin-on-disc tribometer used in the dry sliding wear test

Table 4.3- Details of dry sliding wear testing

Parameters	**Values**	**Units**
Test setup	Pin-on-disc	-
Wear pin	(a) WC-12Co MM microwave clad (b) WC-12Co NM microwave clad	-
Initial roughness	R_a = 0.2	µm
Sliding distance	5000	m
Counter disc	Material: EN-31, Hardness: 65 HRC, Diameter: 60 mm	
Sliding speed	1.0	m/s
Normal load	10, 20, 30	N
Lubrication condition	Dry	-
Temperature	27±3	ºC
Relative humidity	43±4	%

4.7.2. Three-body abrasive wear test

The abrasive wear performance of the WC-12Co MM and NM microwave clads was assessed on a dry sand rubber wheel (DSRW) apparatus as per ASTM G65. Silica sand (quartz), a commonly occurring natural abrasive material, was used as the abradant in the present study. The SEM micrograph illustrates a blocky polyhedral morphology of the silica sand (Fig. 4.12(a)). A Dewinter inverted optical microscope (Model: LT-23B) equipped with an image analysis tool (Dewinter Material Plus, Version 4.3) was used to evaluate the roundness factor of the silica sand. The roundness factor of the silica sand was observed to be 0.45. The XRD spectrum of the silica sand confirms the dominant presence of SiO_2 phase in the abradant (Fig. 4.12(b)). Figure 4.13 illustrates the schematic of the DSRW apparatus used in the present work. Further details of the DSRW apparatus are described in Fig. A-10 (Appendix A).

Load is an important parameter during wear, hence three-body abrasive wear tests were carried out under different loads using DSRW apparatus without recycling the abrasives. The specimens were ultrasonically cleaned using acetone and were weighed before and after the test using an electronic weight balance (Make: Mettler Toledo, Model: ML104) with an accuracy of ±0.1 mg. In order to ensure reproducibility of the weight loss, three specimens were tested under each loading condition. The mean value of weight loss of these three specimens was used to calculate the cumulative weight loss and wear rate of the WC-12Co MM and NM microwave clads. The wear rate of the MM and NM clads was calculated from the local gradient of cumulative weight loss versus number of revolutions.

The revolutions were converted into equivalent linear distance to report the wear rate in terms of weight loss per unit sliding distance (mg/m). First 1000 revolutions were not considered for weight loss so as to attain a steady state. Each specimen was abraded for 40 min and the weight loss was calculated after every 5 minutes. Further details of the abrasive wear test are summarised in Table 4.4.

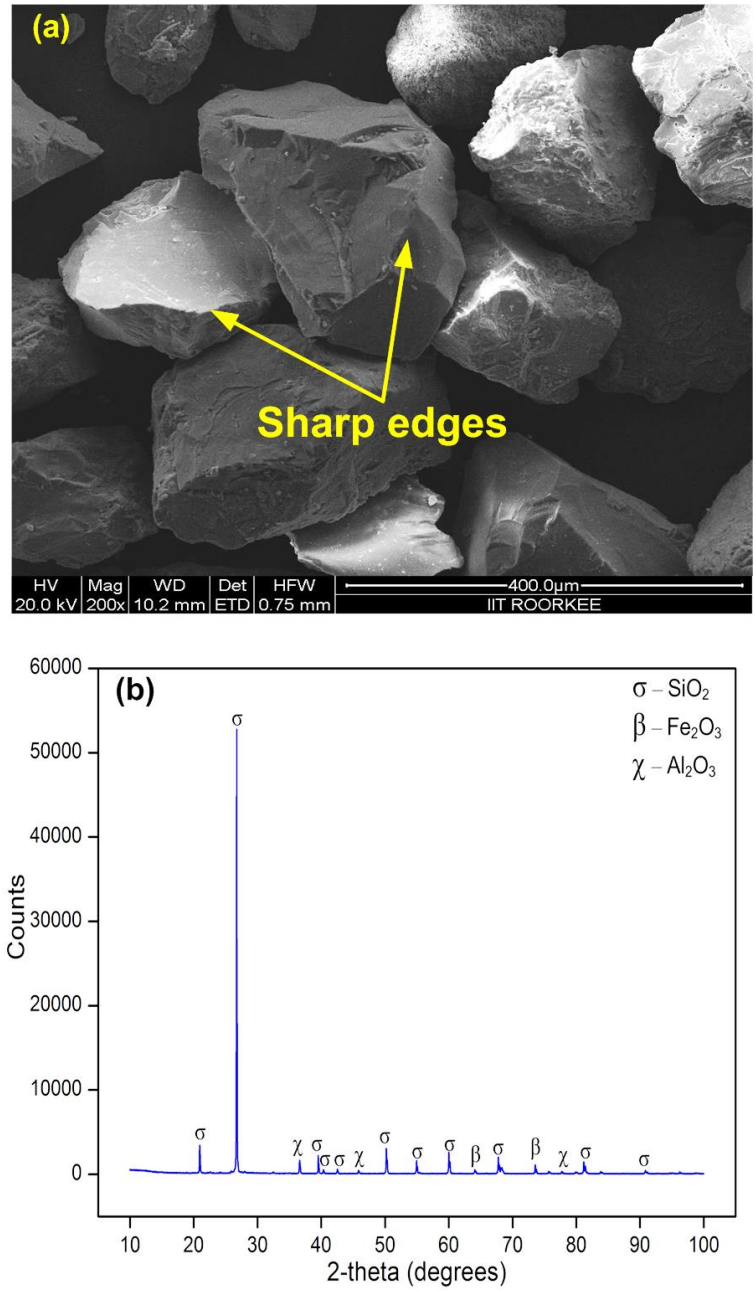

Fig. 4.12- Silica sand (SiO_2) abradant (a) SEM micrograph and (b) XRD spectrum

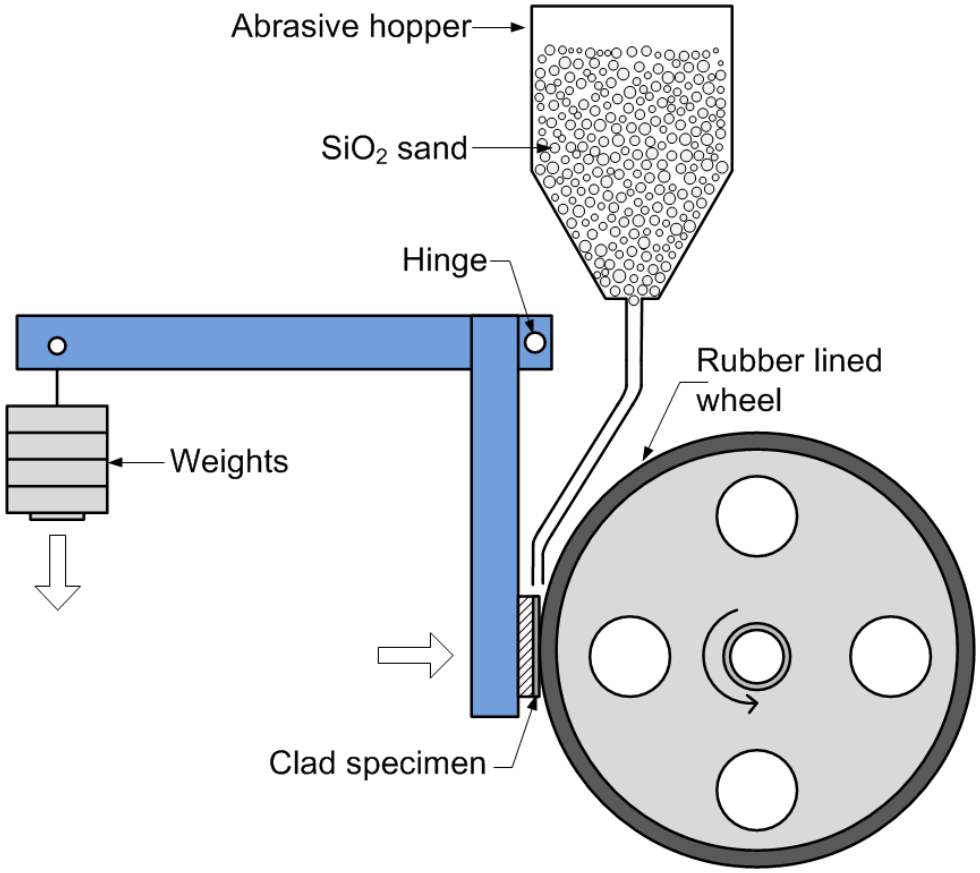

Fig. 4.13- Schematic representation of the dry sand rubber wheel apparatus used for abrasive wear test

Table 4.4- Details of abrasive wear test

Testing parameters	**Value**	**Units**
Scheme	Dry sand rubber wheel test	-
Abradant	Silica sand	-
Abradant particle size	150-355	μm
Abradant feed rate	80±3	g/min
Specimen size	25 ×25 × 7	mm^3
Wheel speed	200±5	RPM
Wheel diameter	240	mm
Normal load	30, 60, 90	N
Total number of revolutions	8000	-
Total linear abrasion	6000	m
Ambient testing temperature	27±3 ºC	ºC
Relative humidity	45±2	%

4.7.3. Solid particle erosion test

The erosive wear behaviour of the WC-12Co MM and NM microwave clads was evaluated using solid particle erosion in an air jet erosion (AJE) test rig (Make: Ducom, Model: TR-470) as per procedure described in ASTM G76 (Fig. 4.13). The SEM micrograph illustrates irregular shaped morphology of the alumina particles (Fig. 4.14(a)). The roundness factor of the alumina particles was observed to be 0.4. Phase analysis of the alumina particles confirmed the presence α-Al_2O_3 as the primary phase along with γ-Al_2O_3 as the secondary phase (Fig. 4.14(b)). The erodent powder was filled in the hopper and fed in the air line through a rotating grooved disc utilized to control the erodent feed rate. A tungsten carbide (WC) nozzle of diameter 1.5 mm was used to force out the air-erodent mixture at high velocity. The erodent jet velocity was measured using a rotating double disc arrangement provided in the AJE test rig. Further details of the AJE apparatus are described in Fig. A-11 (Appendix A).

The test was conducted for 20 min, being interrupted regularly after every 2 min to measure the weight change. Weight loss data after first 2 min was not considered as the AJE test rig was allowed to attain a steady state. The erosive wear test was performed at three impact angles (30°, 60° and 90°). The specimens were ultrasonicated in acetone and were weighed before and after the test using an electronic weight balance (Make: Mettler Toledo, Model: ML104) with an accuracy of ±0.1 mg. Three specimens were tested under each impact angle condition; the mean value of weight loss of these three specimens was further used to calculate the cumulative weight loss and erosion rate in terms of weight loss per unit erosion time (mg/s). The erosion coefficient (ε) was calculated and expressed as the ratio of weight loss from the specimen to the weight of the erodent. Further details of the erosive wear test are presented in Table 4.5.

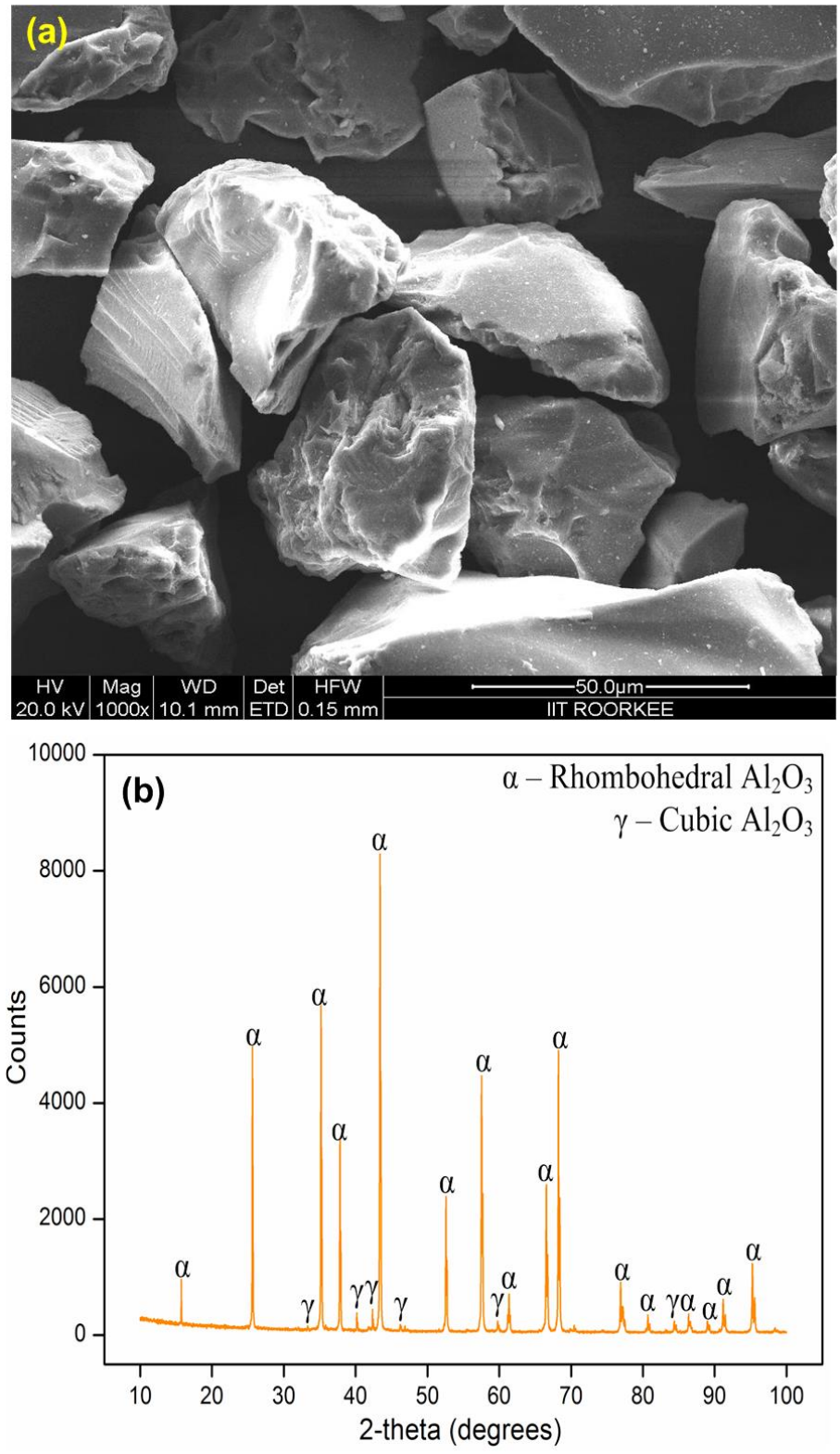

Fig. 4.14- Alumina (Al_2O_3) erodent (a) SEM micrograph and (b) XRD spectrum

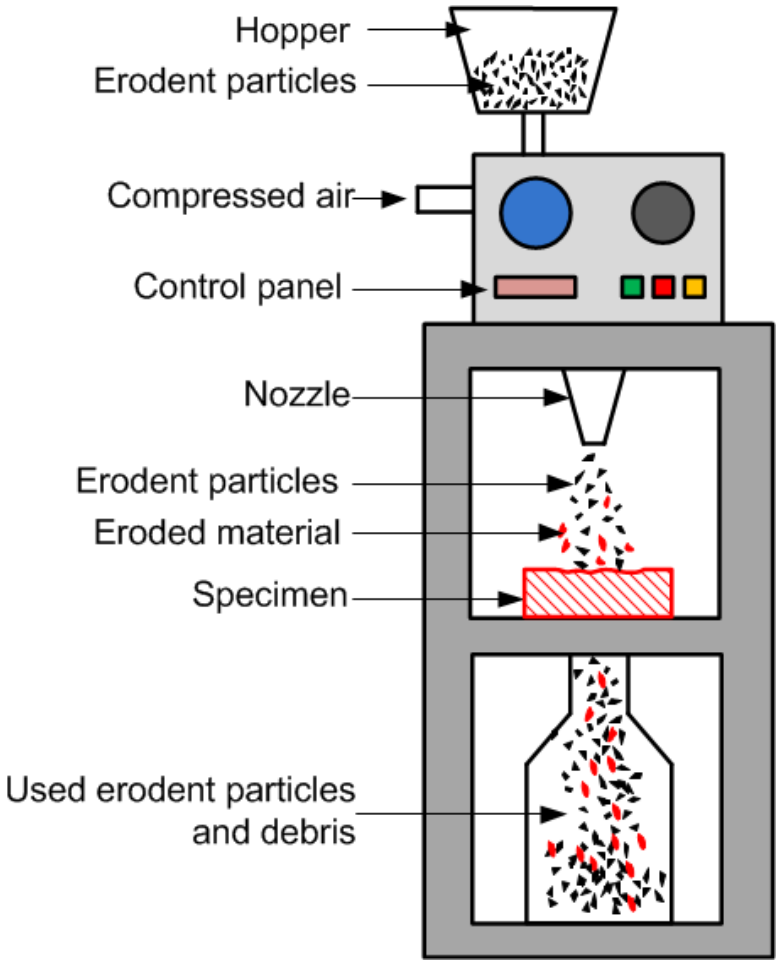

Fig. 4.15- Schematic representation of air jet erosion test rig for erosive wear test

Table 4.5- Details of erosive wear test

Testing parameters	**Value**	**Units**
Scheme	Air jet erosion test	-
Erodent	Alumina	-
Erodent particle size	50±5	µm
Erodent feed rate	5±1	g/min
Erodent velocity	50±3	m/s
Air pressure	1.47±0.19	bar
Specimen size	22 ×22 × 5	mm^3
Specimen to nozzle distance	10	mm
Impact angle	30, 60, 90	degrees
Total erosion time	20	min
Ambient testing temperature	27±3 ºC	ºC
Relative humidity	50±3	%

4.8. SUMMARY

Various characterisations of the austenitic stainless steel (SS-304) substrate and the WC-12Co MM and NM clad powder have been presented in this chapter. A detailed description of the various steps in microwave cladding using MHH has been described. Procedures adopted for metallurgical characterisations using XRD, FE-SEM, EPMA, OM has been briefly discussed. Metallurgical characterisations were carried out in terms of microstructure, phase analysis, elemental composition, and carbide fraction. The relevant mechanical aspects of the clads, viz. microhardness, flexural strength and residual stresses, were evaluated using various techniques. Tribological aspects of the MM and NM WC-12Co microwave clads were evaluated using pin-on-disk tribometer, dry sand rubber wheel apparatus and air jet erosion test rig. Specimens were prepared according to ASTM standards and test conditions were chosen as per the standards adopted and operational constraints of the characterisation facilities.

CHAPTER 5

CHARACTERISATION OF THE CLADS

In the present work, microwave energy has been used as a heat source to develop clads on metallic substrates. Microwave heating is characterised by volumetric heating that results in reduced thermal gradient, less residual stresses and thermal distortion on the target material compared to the material processed through conventional routes. In the present work, MM and NM WC-12Co clads were deposited on bulk SS-304 substrate using microwave cladding technique at 2.45 GHz. The developed clads were characterised for their metallurgical and mechanical aspects using various techniques. The results of various characterisations are discussed in the present chapter.

5.1. METALLURGICAL CHARACTERISATION OF THE CLADS

Metallurgical aspects of the developed clads were characterised through X-ray diffraction, microstructure analysis and measurement of porosity. The characterisation results are discussed with appropriate illustrations in the following sections.

5.1.1. Phase analysis

Various phases present in the WC-12Co MM and NM clads were determined through XRD technique. A typical XRD spectrum of the MM WC-12Co clad is presented in Fig. 5.1(a). The spectrum indicates the presence of W_2C (JCPDS file: 002-1134), corresponding to 2θ values 37.95°, which is attributed to the possible decarburisation of tungsten carbide (WC) from starting powder owing to high temperature during MHH. The decomposition of WC can be represented by the equations 5.1 and 5.2.

$$WC \rightarrow W + C \quad (5.1)$$

$$WC + W \rightarrow W_2C \quad (5.2)$$

The free carbon formed during the chain of reactions will react with atmospheric oxygen to form carbon monoxide (CO), which escapes subsequently during slow cooling of the clad, resulting in less porosity. Formation of carbon monoxide is represented by equation 5.3.

$$2C + O_2 \rightarrow 2CO \quad (5.3)$$

The XRD spectrum illustrates the presence of Co_6W_6C (JCPDS file: 023-0939) corresponding to the 2θ values 22.93˚, 32.66˚, 40.22˚, 42.73˚, 50.34˚, 65.02˚ and 74.08˚. The complex metallic carbide Co_6W_6C exhibits properties like bulk modulus of the irder of 462 GPa, which is higher than WC (approximately, 421 GPa) and diamond (approximately, 444 GPa) (Suetin et al., 2009). Hence, the presence of Co_6W_6C indicates higher toughness of the reinforcing metallic carbides in the MM microwave clads. Presence of the Co_6W_6C can be attributed to the following reaction between WC, Co and O_2 at high temperature (Guilemany et al., 1999).

$$12WC + 12Co + 5O_2 \rightarrow 2Co_6W_6C + 10CO \quad (5.4)$$

The presence of η-phase (Co_3W_3C, JCPDS file: 027-1125), corresponding to 2θ = 46.61˚, may be attributed to diffusion of Co into the WC particles, or WC particles may re-precipitate or decarburise into W and C at high temperature during MHH. Either of these phenomena may result in formation of Co_3W_3C. Formation of Co_3W_3C can be represented by following possible reaction (Guilemany et al., 1999).

$$3WC + 3Co + O_2 \rightarrow Co_3W_3C + 2CO \quad (5.5)$$

Formation of Co_7W_6 (JCPDS file: 002-1091) intermetallic, corresponding to 2θ = 37.95˚ and 44.51˚, occurs due to the reaction between Co_3W_3C and CO. The possible reaction can be represented by the following reaction (Babutina et al., 2004).

$$2Co_3W_3C + 2CO \rightarrow Co_7W_6 + 2C \quad (5.6)$$

Presence of complex carbide Fe_6W_6C (JCPDS file: 023-1127), corresponding to 2θ values 43.36˚ and 59.94˚, may be attributed to the formation of localised convective currents in the melt-pool of the molten powder layer and thin layer of the substrate that causes mixing of the elements in the clad layer. The formation of Fe_6W_6C can be explained by the following possible reaction.

$$6Fe\ (substrate) + 6W + C \rightarrow Fe_6W_6C \quad (5.7)$$

The complex carbide Fe_6W_6C is known for its high microhardness (approximately, 15.6 GPa) (Suetin et al., 2009).

The XRD spectrum of the NM WC-12Co microwave clad in Fig. 5.1(b) shows presence of WC (JCPDS file no. 002-1053, 2θ: 31.44°), W_2C (JCPDS file no. 002-1134, 2θ: 40.24°), predominantly Co_6W_6C (JCPDS file no. 023-0939) corresponding to the 2θ values of 35.65° and 43.33°, Co_7W_6 (JCPDS file no. 002-1091, 2θ: 50.18°) and $Co_3W_9C_4$ (JCPDS file no. 006-0616, 2θ: 73.98°). The WC (a = 4.18 Å) has a simple hexagonal structure with AAA type of metal atom packing due to introduction of carbon planes. Formation of W_2C (a = 2.98 Å and c = 4.71 Å) occurs due to partial decomposition of the WC phase due peritectic reactions occurring at high temperature during the cladding according to the reaction in equation 5.1 and 5.2.

Free carbon reacts with atmospheric oxygen to form CO, which slowly escapes during subsequent solidification of the microwave clad. This leads to formation of crack free clads as illustrated in Fig. 6. The Co_6W_6C, complex metallic carbide, exhibits properties like bulk modulus of the order of 462 GPa which is higher than that of WC (approximately 421 GPa) (Suetin et al., 2009). Accordingly the nanostructured clads are expected to exhibit high hardness. Formation of Co_6W_6C can be attributed to the following reaction between WC, Co and O_2 occurring at high temperature during MHH as shown in equation 5.4 (Guilemany et al., 1999). Further, it is interesting to note that the full width at half maximum (FWHM) of the Co_6W_6C phase in the MM clad (2θ: 42.93°) was observed to be 0.2057, while in the NM clad (2θ: 43.03°) it was observed to be 0.2991. This indicates that size of the Co_6W_6C phase reduces in the NM clad, which is an indicative of improved mechanical and tribological properties of the NM clads. Presence of Co_7W_6 in the microwave clads is attributed to the occurrence of the following reaction between WC and Co during MHH (Babutina et al., 2004) as shown in equation 5.6.

Highly reactive C, formed as per equation 5.1, reacts with Co and W to form $Co_3W_9C_4$ complex metallic carbide according to the following reaction (Gupta and Sharma, 2012).

$$9W + 3Co + 4C \rightarrow Co_3W_9C_4 \quad (5.8)$$

The constituting phases of the nanostructured WC-12Co microwave clad were further analysed using peak intensities of respective phases detected in the XRD spectrum

of the developed clad using normalised intensity ratio (NIR) method (Gupta and Sharma, 2011a; Peelamedu et al., 2002). The NIR of phase-1 is given according to equation 5.9.

$$NIR_1 = \frac{I_1 - I_{back}}{I_1 + I_2 + I_3 + I_4 + I_5 - 5I_{back}} \quad (5.9)$$

Here I_1, I_2, I_3, I_4 and I_5 are the intensities of the 1st, 2nd, 3rd, 4th and 5th phase respectively, and I_{back} is the background intensity. Similar calculations were carried out in order to determine the NIR of other constituting phases. The major peak of a particular phase was considered to determine its NIR value. The NIR does not indicate the exact amount of phases present in the developed clad, but it provides a relative representation of the various phases present in the developed clad. Calculated values of NIR for various phases in MM and NM WC-12Co microwave clads are given Table 5.1 and Table 5.2, respectively. It is clear from the relative phase intensities of various phases in the MM and NM WC-12Co clads, that most of the WC and Co was transformed to Co_6W_6C and Co_7W_6 (49.30% and 16.89% respectively) in the NM clad, while they only 41.03% and 1.92% in MM clads. Presence of such phases is indicative of high hardness of the WC-12Co NM clads.

Table 5.1- Relative intensities of various phases in the WC-12Co MM microwave clads

S.No.	**Phase**	**I_1**	**I_2**	**I_3**	**I_4**	**I_5**	**I_6**	**I_{back}**	**NIR (%)**
1	WC	2650	-	-	-	-	-	2100	7.05
2	W_2C	-	2800	-	-	-	-	2100	8.97
3	Co_6W_6C	-	-	5300	-	-	-	2100	41.03
4	Co_7W_6	-	-	-	2250	-	-	2100	1.92
5	Co_3W_3C	-	-	-	-	2700	-	2100	7.69
6	Fe_6W_6C	-	-	-	-	-	4700	2100	33.33
Total									**100**

Table 5.2- Relative intensities of various phases in the WC-12Co NM microwave clads

S.No.	**Phase**	**I_1**	**I_2**	**I_3**	**I_4**	**I_5**	**I_{back}**	**NIR (%)**
1	WC	2200	-	-	-	-	2000	2.82
2	W_2C	-	2700	-	-	-	2000	9.86
3	Co_6W_6C	-	-	5500	-	-	2000	49.30
4	Co_7W_6	-	-	-	3500	-	2000	21.13
5	$Co_3W_9C_7$	-	-	-	-	3200	2000	16.89
Total								**100**

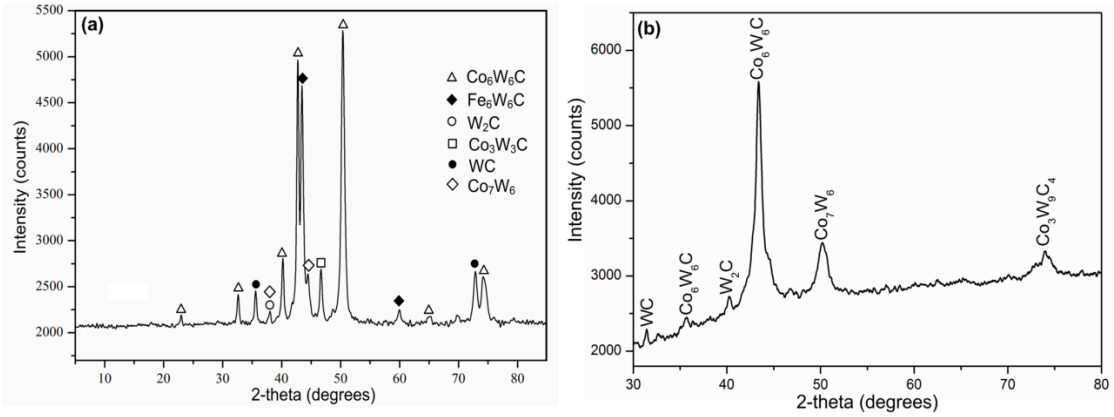

Fig. 5.1- Typical XRD spectra of (a) MM and (b) NM WC-12Co microwave clads

5.1.2. Microstructural characterisation

Quantitative microstructural characterisation involves evaluation of carbide grain size, carbide contiguity, and carbide volume. The microstructural aspects influences various properties of the clads like wear resistance, strength, hardness etc. Microstructural characterisation helps to analyse the effect of the microstructure on various properties of the microwave induced clads. Accordingly, a few studies on microstructures of the developed MM and NM clads were carried out.

5.1.2.1. Microstructure of MM WC-12Co microwave clad

The microstructure of typical transverse section of MM WC-12Co microwave clad is shown in Fig. 5.2. The microwave induced WC-12Co MM clad with an approximate thickness of 1 mm illustrates excellent metallurgical bonding with the substrate (Fig. 5.2(a)). The WC-12Co MM clad was observed to be free from interfacial cracking and visible porosity, in spite of significant differences in the thermo-mechanical properties of the clad powder and substrate material. This is attributed to the uniform heating characteristics of the MHH technique that results in low thermal gradient in the clad. As the clad powder particles start absorbing microwave radiation, the temperature of the powder rises, which consequently causes them to melt. This molten powder layer causes melting of a very thin layer of SS-304 substrate owing to its poor thermal conductivity (16.2 W/m K (Sweet et al., 1987)). The occurrence of inverse thermal

gradient is a common phenomenon associated with microwave heating (Thostenson and Chou, 1999). This causes localised convective currents in the melt pool that results in the formation of a wavy interface as illustrated in Fig. 5.2(a). These localised convective currents lead to the melting of a thin interfacing layer (approximately of 10-20 µm) of the SS-304 and cause the observed wavy interface. Consequently, this leads to intermixing and the diffusion of the elements between the substrate and the clad powder in the vicinity of the interface.

A magnified image of the MM clad is presented in Fig. 5.2(b), which reveals uniformly distributed white coloured skeleton structured metallic carbides in the grey coloured metallic matrix. In the WC-Co system, the eutectic forms at approximately 1320 °C (Upadhyaya, 1999). The Co binder melts during microwave exposure and spreads over the surfaces and/or diffuses into the interfaces between carbide particles. As the temperature increases further, it dissolves the carbides from adjacent particle surfaces. The WC is precipitated on the surfaces of some undissolved carbide thus leading to grain growth. This molten powder layer of the powder particles leads to melting of a very thin layer of the substrate. This leads to nucleation of austenite (γ) that grows at the boundary of the liquid solution along with impoverished tungsten and carbon (Taran et al., 1972). Austenite thus forms binary carbides of tungsten and iron ($(W, Fe)_6C$) having skeleton like structure as shown in Fig. 5.2(c) (Taran et al., 1972). As per the WC-Co binary phase diagram of WC (~55%), the microstructure consists of hypereutectic structure (WC + γ(WC)) (Fernandes and Senos, 2011); here WC is the primary phase and γ(WC) is the eutectic structure. The outline of the eutectic colony repeats itself due to strong influence of the carbide on nucleation and growth of the eutectic colony. The carbides grow between branches of austenitic cell and continuous cooperative growth of two eutectic crystals is characterised by the alterations as the branches develop. This leads to cooperative growth of the eutectic with growth in layers alternate with intergrowth. Cobalt (Co) flow in the carbide matrix occurs well below the eutectic temperature, thus it reduces the surface energy. It was found enhanced inter diffusion occurs at closed packed boundaries formed in Co-rich regions leading to segregation of carbide particles (Taran et al., 1972). Coalescence of contacting grains occurs during solidification phase where there is low misorientation angles between the grains. The WC particles form a continuous skeleton structure as the structure cannot readjust on solidification and contraction. Similar

skeleton-like structures of metallic carbides have also been reported in microwave cladding of WC10Co2Ni powders (Gupta and Sharma, 2012).

Complex tungsten based carbides remain uniformly distributed in the Co based matrix that provides toughness to the clad while acting as reinforcement in the metal-based matrix (grey coloured). Several authors had reported presence of un-melted and un-dissolved carbide particles that were present locally in the regions close to the interface attributable to heat loss to the substrate through conduction (Taha-al et al., 2009; Vreeling et al., 2002). However, no such evidence could be observed in the microstructure of the microwave developed clads owing to volumetric heating nature of MHH and presence of localised currents in the melt-pool of the molten powder layer. Moreover, heat loss to the substrate is minimal owing to its poor thermal conductivity.

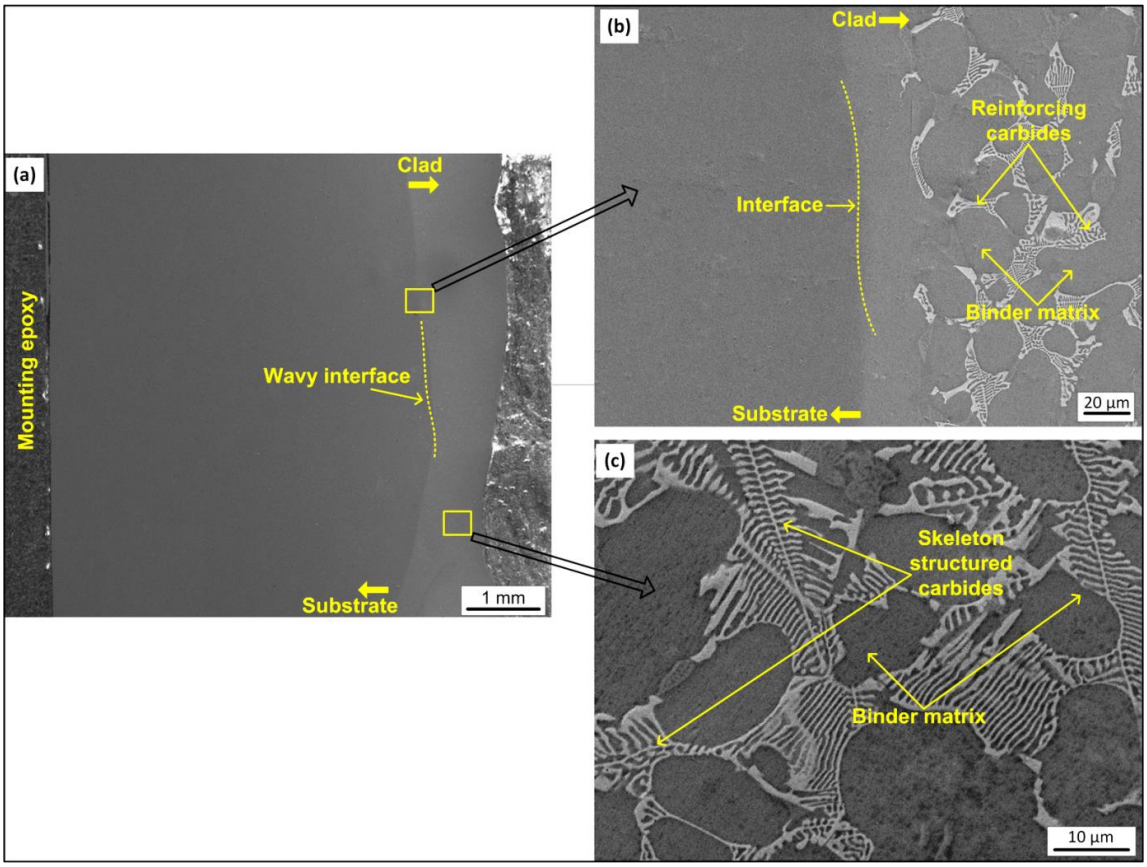

Fig. 5.2- A typical SEM micrographs of (a) transverse section of the MM clad, (b) magnified view of the interface and (c) clad layer illustrating skeleton structured carbides

5.1.2.2. Microstructure of NM WC-12Co microwave clad

A typical SEM micrograph of the NM WC-12Co clad is shown in Fig. 5.3(a). The NM clad with an average thickness of 1 mm was observed to be free from any interfacial cracking. This is attributed to the uniform heating and low thermal gradient characteristics associated with MHH technique. The interface of the NM clads is a fading boundary towards the substrate indicating an ideal clad. However, the wavy nature of the interface as observed in Fig. 5.3(a) can be attributed to the localised convective currents in the melt pool as discussed earlier.

The magnified view of the NM clad is presented in Fig. 5.3(b) and (c). The NM clad exhibits a characteristically different microstructure compared to the MM clad. The microstructure of the NM clads reveals the presence of eutectics of nanocarbides enclosed in a continuous carbide network. The typical microstructure of the NM WC-12Co microwave clad consists of both grey and white phases corresponding to the regions of lower and higher atomic weight. The volumetric heating characteristic of microwaves results in low thermal gradient, which is critical in development of uniform microstructure of the clad. However, regions close to the carbide network were perhaps depleted of the carbide phase owing to the diffusion. Once the temperature of the nanostructured particles reaches beyond the WC-Co eutectic temperature, during MHH, the WC particles get dissolved in the molten Co up to its saturation limit. The unmelted WC particles act as the favourable nucleation sites and subsequently lead to the development of a carbide network. The nanocarbides precipitate in the Co matrix due to their reduced solubility and reduced diffusion coefficient with decreasing temperature during cooling, below the eutectic temperature (Breval et al., 2005). On heating above the WC-Co eutectic point, the core of the WC particles gets dissolved in the molten Co particles. After Co melts, shrinkage and intimate contact between the WC grains takes place, and as the molten Co becomes saturated, formation of W-based phases gets initiated. The unmelted WC particles act as the favourable nucleation sites and subsequent increase in the W-based phases leads to the development of a carbide network (Fig. 5.3(b)). On cooling below the eutectic temperature, the precipitation of the nanocarbides occurs in the Co matrix due to reduced solubility and reduced diffusion coefficient of W with decreasing temperature (Breval et al., 2005). The nanocarbides eutectics improved the distribution of the carbides owing to their high surface area that enhanced the wettability of the other nanocarbide particles. Hence, a consistently

uniform distribution of the carbide particles could be evidenced in the clad microstructure (Fig. 5.3(b) and (c)). Further, the decarburisation of the nanostructured WC-12Co powder was minimised due to uniform volumetric heating characteristics of MHH, which prevented extensive dissolution of the WC into liquid Co. The regions of Co are of 1 µm or less. The eutectics of nanocarbides are formed due to their reduced solubility and diffusion coefficient with reduced temperature.

Further, it is observed that there are differences in the morphologies of the phases in the MM and NM clads. This is explained by the fact that both clads were developed using different processing conditions (microwave power and exposure times were different as required by the processes). Thus, it is likely that the temperatures of the melt-pools were different during processing which would affect the subsequent solidification process and corresponding microstructures.

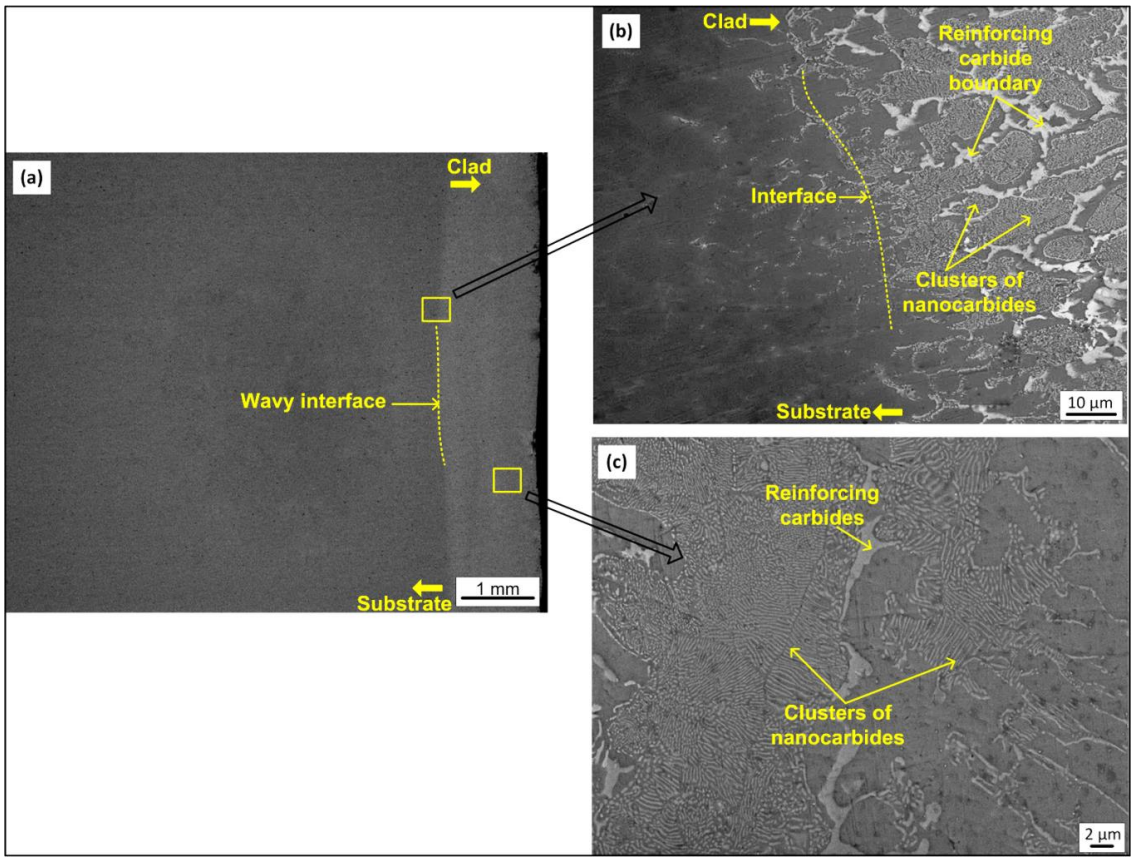

Fig. 5.3- Typical SEM micrographs of (a) transverse section of the NM clad, (b) magnified view of the interface and (c) clad layer illustrating clusters of nanocarbides

5.1.2.3. Elemental analysis of the MM and NM WC-12Co clads

In order to ascertain the elemental composition of the different phases in the microstructure of the MM microwave clads, an EDS study was carried out at different locations and the corresponding results are presented in Fig. 5.4. As evident from the clad microstructure presented at Fig. 5.4(a), three different phases in the microstructure can be observed – white, light grey and grey, marked as 1, 2 and 3, respectively. Point 1 indicates the skeleton structured carbide in the clad matrix appearing as reinforcement, while points 2 and 3 indicate the locations in the clad matrix. The X-ray elemental composition at point 1 (Fig. 5.4(b)) indicates that the white phase is dominated by the presence of W and C with contributions of approximately 78% and 18%, respectively. The interdendritic skeleton like eutectic structures were mainly WC-based eutectic phases in the form of M_6C type carbides (Co_6W_6C and Co_3W_3C). These skeleton structured eutectics act as reinforcement in the clad layer. The X-ray composition study at point 2 (light grey phase) in the clad matrix indicates presence of mainly Fe, W, Co (Fig. 5.4(b)). It was also observed that the Co and Fe contents were higher in the primary dendritic region compared to the interdendritic eutectic structure. As the M_6C carbides get crystallised, the melt pool gets depleted of W and C. Consequently, the darker regions are observed near the eutectics, which were Fe and Co-rich phases. On the other hand, the point 3 (grey phase) in the clad matrix indicates the presence of major alloying elements like Fe, Co (Fig. 5.4(c)). This can be attributed to dilution caused by the localised convective currents in the melt-pool in the layer of molten clad powder. This confirms that the clad consists of relatively tough matrix (Fe-Co based) as compared to the hard skeleton structured reinforcements (W based carbides). Hence, the well distributed hard metallic carbides act as reinforcements in the tough metallic matrix that are expected to provide higher wear resistance to the WC-12Co clads.

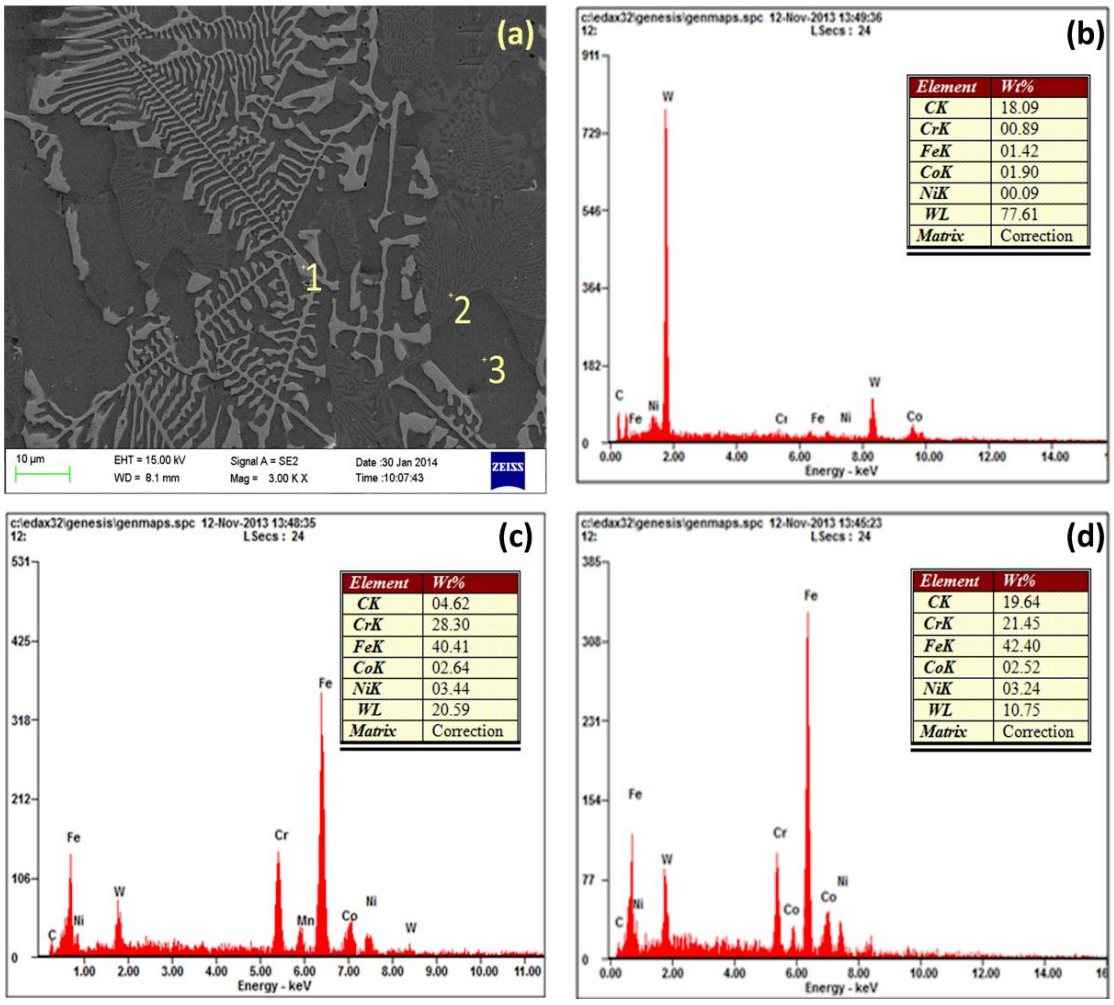

Fig. 5.4- Typical EDS analysis of the WC-12Co cermet microwave clad: (a) secondary electron image showing location of EDS analysis, (b) typical EDS spectrum of clad reinforcement (point 1), (c) typical EDS spectrum of the light grey phase in clad matrix (point 2), (d) typical EDS spectrum of grey phase in clad matrix (point 3)

In order to ascertain the elemental composition of the various phases present in the NM WC-12Co microwave clad, EDS analysis was carried out at various representative locations as shown in Fig. 5.5(a). Point 1 on the white solid boundary mainly consists of W with contributions of approximately 52 % as shown in Fig. 5.5(b). The elemental analysis at point 2 on the eutectics of nanocarbides, on the other hand, indicates dominant presence of Fe and W with contributions of approximately 39% and 35%, respectively as illustrated in Fig. 5.5(c). Consequently, as indicated in the SEM micrograph in Fig. 5.5(a), it was confirmed that that nanostructured size of WC grains is retained in the microwave induced clad. During microwave exposure, as the temperature rises it results in melting of Co, subsequently WC gets dissolved in the molten Co as the temperature would rise. The liquid

Co at 1275 °C will have homogenous concentration of W and C; C was removed primarily by reaction with melt pool through oxygen diffusion in molten particles that will lead to formation of CO. However, removal of C locally from the melt will further cause dissolution of WC grains to establish a local equilibrium (Stewart et al., 2000). Upon solidifying, the diffusion coefficients of W and C drop significantly, which pushes W and C to diffuse towards WC boundary and precipitate on the boundary. Slow cooling in microwave cladding results in C precipitating out of the Co region at 850 °C while W becomes immobile. The EDS analysis at point 3 (Fig. 5.5(a)) confirms dominant presence of Fe (approximately 64%) in the WC depleted region as shown in Fig. 5.5(d). Higher percentage of Fe, Cr, Co can also be attributed to the localised convective currents in the melt pool that cause mixing of the elements between the clad powder and the substrate as discussed earlier. Thus, the microstructural observation of the developed microwave clad reveals that the nanostructured WC grains were uniformly distributed within the WC boundary in a colonised pattern. Grain growth of nanocarbides was suppressed due to relatively short processing time and uniform heating characteristics of MHH.

The result of X-ray elemental mapping in Fig. 5.6 analysis shows the presence of tungsten (W) in the MM and NM clad. The location of X-ray elemental mapping is shown in MM and NM WC-12Co clad in Fig. 5.6 (a) and (b), respectively. It was observed from the elemental mapping that the W is distributed mainly on the skeleton structured carbides in the MM clad (Fig. 5.6 (c)). However, the distribution of W in the NM clad is more or less uniform in the clad (Fig. 5.6 (d)).

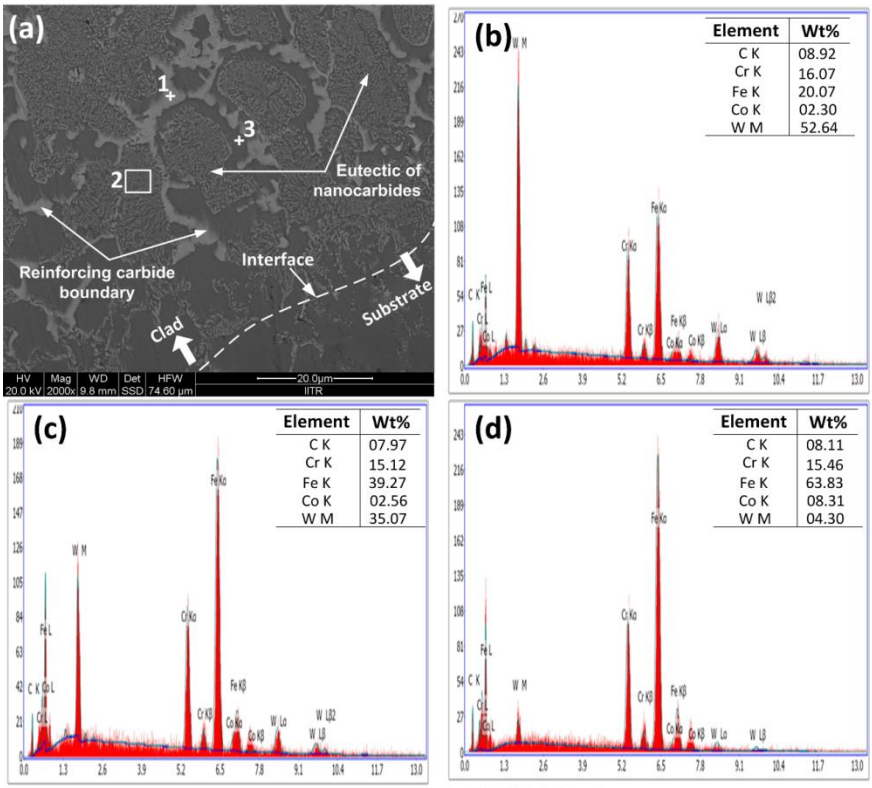

Fig. 5.5- Typical EDS analysis of the nanostructured WC-12Co microwave clad: (a) BSE micrograph showing location of EDS analysis, typical EDS spectra of (b) carbide boundary (point 1, (c) nanocarbide grains (point 2), and (d) carbide depleted zone (point 3)

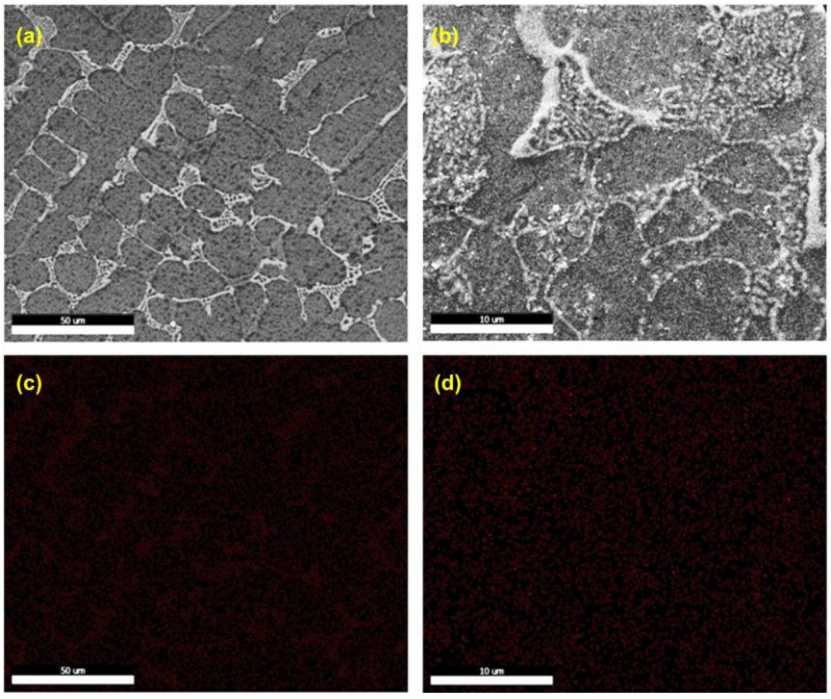

Fig. 5.6- X-ray elemental mapping of WC-12Co microwave clads (a) SEM micrograph of MM clad (scanned area), (b) SEM micrograph of NM clad, (c) elemental distribution of W in MM clad and (d) elemental distribution of W in NM clad

The average volume fraction of the carbides in the MM and NM microwave clads was evaluated using an image analysis tool (ImageJ, Version: 1.46). The image analysis was carried out at five different locations in the clad layer. The SEM images of the selected locations were converted to binary images (grey scale, 8 bit) and the upper and lower threshold values were set in the range of 0 to 170. The representative binary images of the MM and NM clad are shown in Fig. 5.7(a) and (b), respectively. The NM clads were found to exhibit approximately 48% higher carbide volume fraction as compared to the MM clad for a given image area. This is good agreement with results of the X-ray elemental mapping (Fig. 5.6). Hence, the uniformly distributed nanocarbides tend to enhance the hardness and wear resistance in the NM clad.

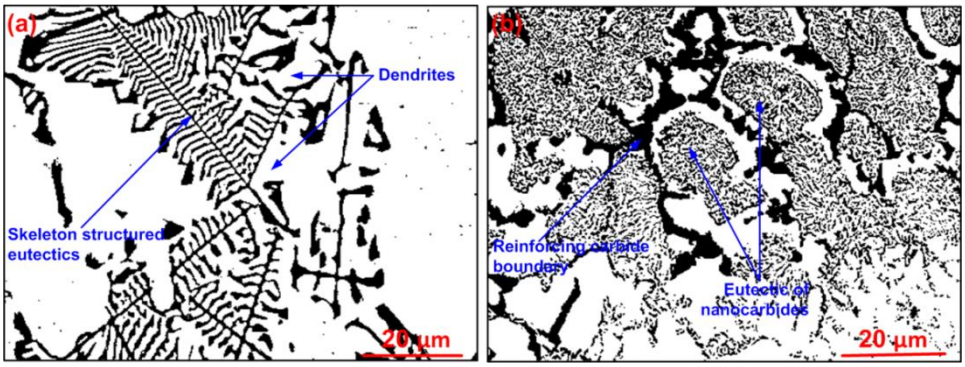

Fig. 5.7- Typical binary images of (a) MM and (b) NM WC-12Co microwave clad

5.1.3. Porosity analysis

The presence of porosity tends to decrease tribological performance of the developed clads in particular applications that involve spalling, abrasion, surface fatigue or dislodgement. Thus, it underlines the importance of assessment of porosity. The porosity assessment of the microwave clads was carried out using image analysis software tool (Dewinter Material plus, version 4.2) as per ASTM B276 standard by analysing 10 areas. The average porosity in the developed clads, calculated over 10 measurements and was observed to be less than 1%. The porosity assessment results of three sample sets, each for MM and NM clad are shown in Fig. 5.8. The observed porosity is found to be lower than the porosity of clads developed through other popular cladding processes like laser cladding (Gäumann et al., 1999). Low value of porosity is attributed to low thermal

gradient setup in the microwave cladding process, which consequently results in low solidification rate.

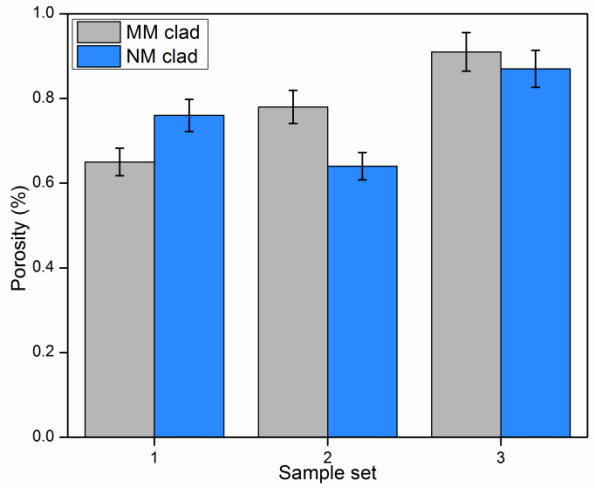

Fig. 5.8- Porosity analysis of WC-12Co MM and NM microwave clads

5.2. MECHANICAL CHRACTERISATION OF THE CLADS

The mechanical characterisations of the WC-12Co MM and NM microwave clads were carried out in terms of microhardness, flexural strength and residual stresses. A Vicker's microindentation test was carried out in order to assess the microhardness of the clads as per the procedure described in section 4.6.1. The fractographs of the flexural specimens were evaluated using SEM, while the residual stresses were evaluated using '$\sin^2\psi$' method.

5.2.1. Microhardness assessment

Various factors influencing the tribological characteristics of the clads include microstructure, carbide grain size as well as the microhardness. In general, higher microhardness and uniformly distributed nanocarbides enhance the wear resistance of a clad layer. The microhardness of the MM and NM clads was evaluated using a Vicker's microhardness tester and correlated with its wear behaviour. The microhardness distribution across the transverse sections of the MM and NM WC-12Co microwave clad are presented in Fig. 5.9. The microhardness values for the MM microwave clad were in the range of 764 to 1625 HV, while the microhardness values for the NM microwave clad were observed between 1053 to 2240 HV. The mean microhardness for the NM microwave clad (1563±53 HV) was about 37% higher than that of the MM microwave clad (1138±90

HV). As the WC grain size reduces to nanometer range, the mean free path of Co matrix is reduced, which results in increased hardness according to the Hall-Petch relationship (equation 5.10) (He and Schoenung, 2002; Jia and Fischer, 1997; Li and Yang, 2013).

$$H(d)=H_o+K/d^{1/2} \qquad (5.10)$$

here, H is the hardness, H_o and K are experimental constants and d is the grain size. This increase in hardness leads to improved wear resistance. The representative indentation geometries on the MM and NM WC-12Co clad layer are presented in Fig. 5.10(a) and (b), respectively. Higher microhardness in the NM clads could also be attributed to the presence of well distributed clusters of nanocarbides as shown in Fig. 5.10(b). These clusters of nanocarbides prevent the plastic deformation of the nearby region due to the decreased mean free path under the load of the indenter. The lower standard deviation of the microhardness distribution of the NM WC-12Co microwave clads also confirms relatively uniform microhardness across the clad layer. Higher volume fraction of the carbides also confirms higher hardness in the NM clad layer. Typical indentation morphologies at interface in the MM and NM clad are shown in Fig. 5.10 (c) and (d), respectively.

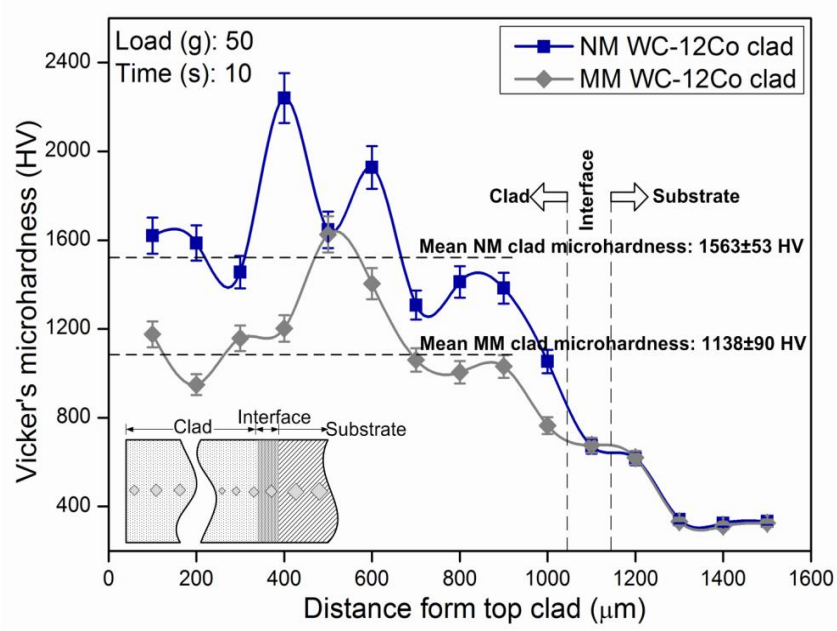

Fig. 5.9- Vickers's microhardness profile across the transverse section of MM and NM WC-12Co microwave clad

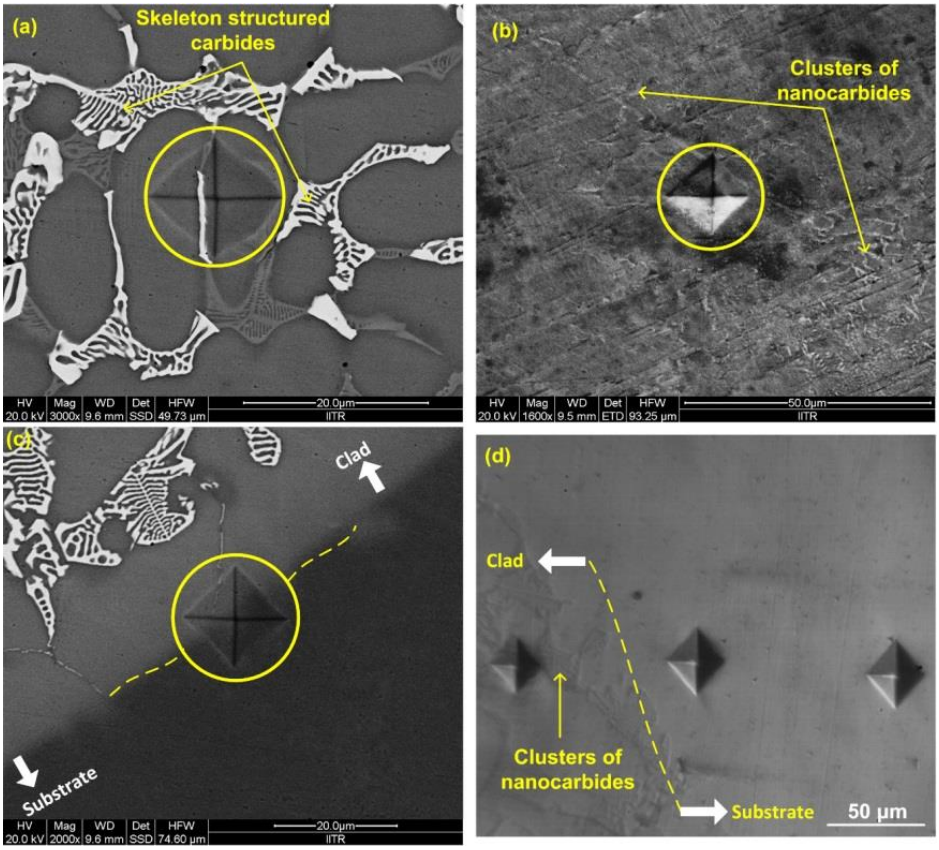

Fig. 5.10- Typical morphologies of Vicker's indentation on (a) clad layer of MM, (b) clad layer of NM, (c) interface of MM clad and (d) interface of NM clad

The contour plot shown in Fig. 5.11 illustrates the variation in the Vicker's microhardness across the clad cross-section. Variation in the microhardness depends on the underlying microstructure. Fig. 5.11(a) reveals presence of high hardness zones (red colour) in MM WC-12Co microwave clad that were attributed to the presence of skeleton carbides present in the clad layer. However, in NM WC-12Co microwave clads, zones with relatively higher hardness were correlated to the clusters of nanocarbides present in the NM clad. The observations from the microhardness contour plots supports the microstructural observation of the MM and NM clads as detailed in section 5.1.2. The presence of nanocarbides and the interconnected carbide network in the NM clad layer acts as the reinforcement. Further analysis of the contour plots reveals relatively more dilution of the substrate in of NM WC-12Co microwave clad (Fig. 5.11(b)). However, this dilution zone is confined to the region of around 10-20 µm at the interface as discussed in section 5.1.2.2. The superior microhardness of the NM WC-12Co clads allows them to endure heavier loads and exhibit increased wear resistance.

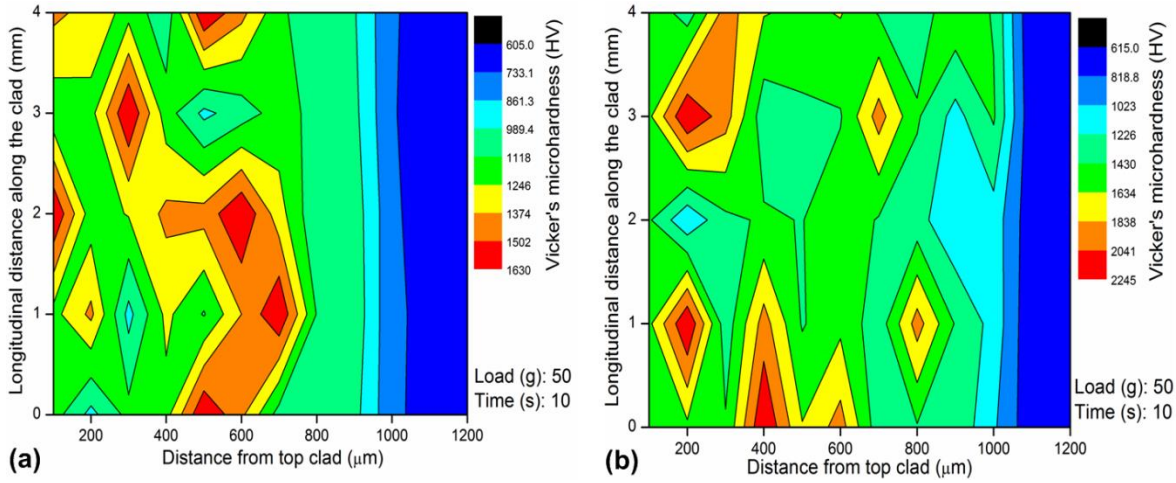

Fig. 5.11- Contour plots of Vicker's microhardness across the clad cross-section (a) MM and (b) NM WC-12Co microwave clad

5.2.2. Flexural strength characterisation

Flexural strength test is an effective way to evaluate the interfacial strength of the clad-substrate interface. The interfacial strength of the WC-12Co MM and NM clads was evaluated through a three-point bend test on a UTM (Make: Instron, Model: 5982) as per the procedure described in Section 4.6.2. A set of three specimens were tested each for MM and NM clad. Typical load displacement curves for the WC-12Co MM and NM microwave clad are shown in Fig. 5.12. The average values along with standard deviation of the maximum load, displacements, deformation indices and maximum flexural strengths are presented in Table. 5.3.

5.2.2.1. Flexural strength characteristics

The flexural strength of the NM clad was approximately 14% higher than the MM clad, and the displacement in the NM clad was observed approximately 50% higher than the MM clads. The nature of the load-displacement curve of the WC-12Co MM was different from the NM clad due to the influence of contiguity of the carbide particles on the mechanical properties of the NM WC-12Co clads. The displacement in the MM clad increased almost linearly up to 2 kN and the load-displacement characteristic displayed a characteristic staircase profile up to 'A' (Fig. 5.12). In this phase, the metallic matrix of the MM clad behaved in an elastic manner. Beyond 'A', the clad underwent plastic deformation

beyond the lower transition load and a further increase in load initiated microcracks at the clad surface. As the load increased further, microcracks on the hard carbide reinforcement grew and propagated into the adjacent regions (up to point 'B'). The crack initiation and propagation helped to release the induced stresses during microwave cladding. As the applied load reached a critical value (point 'C'), further plastic deformation occurred and the microcracks propagated to reach the clad-substrate interface. At this stage, the clad failed and the applied load was transferred the SS-304 substrate.

The NM WC-12Co clads exhibited a uniform load-displacement curve up to point 'D', which resembled elastic-like behaviour of metallic material. This is attributed to the reasonably uniform microstructure that got developed in the microwave induced clads. Up to D, the relatively ductile metallic matrix of the clad deformed elastically under the applied load as indicated by the slope of the curve (slope of stage 'OD' = 5.49). Minute kinks on the load-displacement characteristics (zoomed view, Fig. 5.12) were attributed to the formation of microcracks on the clad face, which released some of the induced stresses (Fig. 5.12). The nanocarbides fractured and decohered, while the matrix yielded under tension during the flexural test. Beyond point 'D', the slope of the curve reduced (1.64) compared to the stage 'OD' and on further loading beyond 'E', the NM clad exhibited a classical plastic behaviour.

Reduced occurrence of kinks in the stage 'DE' is visible in Fig. 5.12. The NM clad exhibits such behaviour up to 1.4 kN load with a corresponding displacement of 0.5 mm ('DE', Stage 2). Stage 2 of the load - displacement curve, which does not reveal classic yielding zone, was interpreted as the transition of the load bearing from the metallic matrix to the clusters of hard carbide particles. Stage 3 (stage 'EF') of the load displacement curve indicated that the NM clad can withstand higher applied load owing to the eutectics of nanocarbides, which arrest the crack front. However, as the unit nanocarbides fail, as indicated by the minute kinks in the deformation characteristics (stage ‘DE’), the load is now being gradually transferred to the relatively ductile matrix. As the proportion of the nanocarbides (eutectics) in the matrix is higher, the NM clads could bear higher applied load compared to the failure load of the MM clads (up to point ‘F’). The NM clads exhibited a typical progressive deformation curve while further opening of the matrix cracks as indicated by the reduced slope of the curve (slope = 0.70). The clad however fails as the main cracks get propagated to the clad-substrate interface. The mechanism is further

explained in the following section with suitable evidences and illustrations. The failure of the clad was confirmed by the sudden drop in load (point 'F'). In the present work, the flexural strength of the microwave induced clads was observed to be approximately nine times higher compared to the WC-12Co laser clads (Paul et al., 2007).

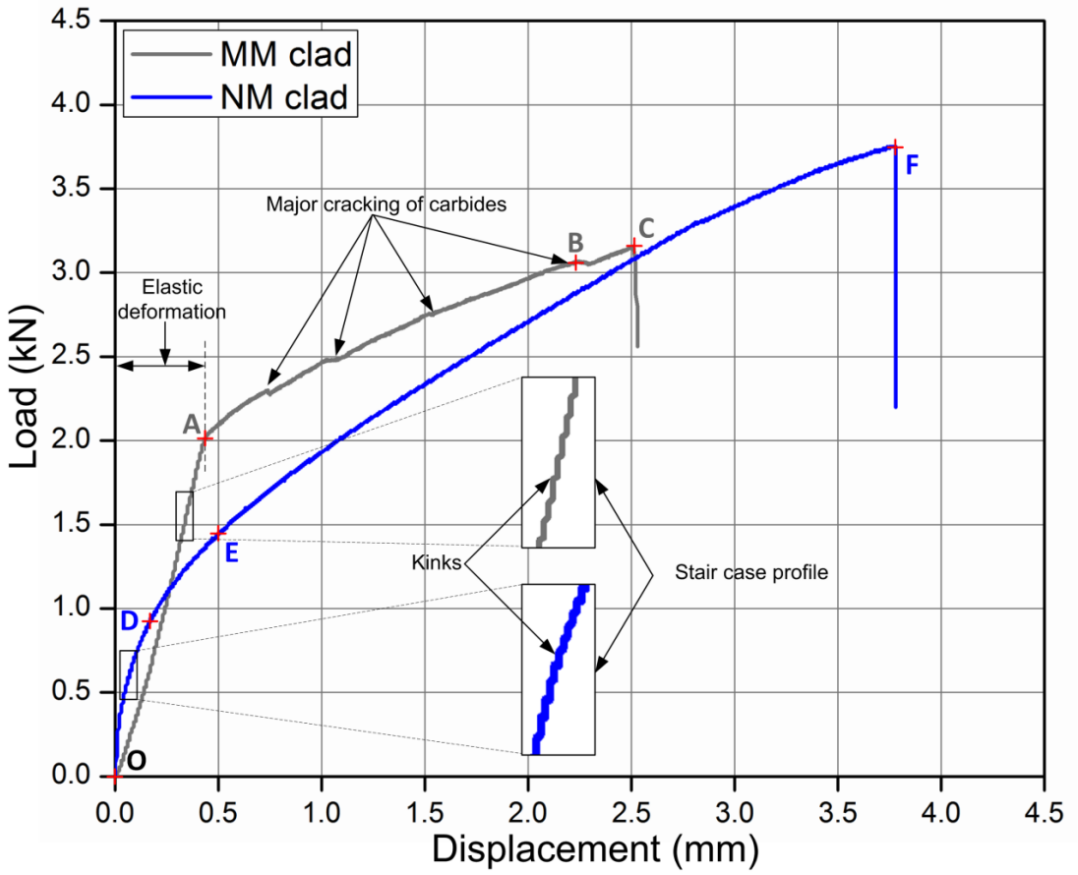

Fig. 5.12- Flexural characteristics of WC-12Co MM and NM microwave clad

Deformation Index (DI) is a useful parameter to analyse the flexural behaviour of coatings/claddings (Sharma and Gupta, 2012). The WC-12Co clads were further analysed in terms of DI using equation 5.11 (Sharma, 2002).

$$DI = \frac{\Delta\delta}{\Delta P}, \text{ mm } N^{-1} \qquad (5.11)$$

where:

$\Delta\delta$ = corresponding change in flexural displacement (mm), and

ΔP = ±10% change in load at 50% of the rupture load P (N).

The DI provides a close indication of the deformation behaviour of the clad substrate system. The computed DIs for the MM and NM clads are shown in Table 5.3 and low DI values of MM clad indicate relatively higher stiffness, attributed to the presence of hard skeleton structured carbides in the clad layer. The higher DI value of NM clad agrees with the higher ductility shown in the side view of the NM clad (Fig. 5.13(d)). The higher DI value of the NM clad is also an indicative of higher flexural strength as indicated by the load displacement curve (Fig. 5.12).

Table 5.3- Flexural strength values of WC-12Co MM and NM microwave clads

S.No.	**Maximum load (kN)**	**Maximum displacement (mm)**	**Maximum flexural strength (MPa)**	**Deformation Index (mm N^{-1})**
MM Clad	3.15	2.53	587±22	1.90×10^{-4}
NM Clad	3.70	3.78	671±28	1.10×10^{-3}

5.2.2.2. Fractographic analysis

Typical photographs of fractured MM and NM WC-12Co microwave clads are shown in Fig. 5.13. The top views of the clad surface show major cracks on the fractured clad layer during loading (Fig. 5.13 (a) and (b)). A single major crack was observed on the fractured MM clad, however, a few flexural cracks parallel to the width of the samples were observed on the fractured NM clad. These cracks are formed under loading as the consequence of load being transferred to the nearby clad region once the main crack was formed. This was attributed to the uniform distribution of the clusters of nanocarbides in the tough binder matrix (Fig. 5.3). The fractured clad layer is shown in the side-view of the MM clad in Fig. 5.13(c). It is evident from the Fig. 5.13(c) that the MM clad layer got partially decohered from the metallic substrate. The metallurgical bonding in the microwave clads prevented the clad layer from getting peeled-off. However, no such observation could be made from the NM clad in Fig. 5.13(d). The NM clad deformed more than the MM clad which agreed with the load displacement characteristics as shown in Fig. 5.12.

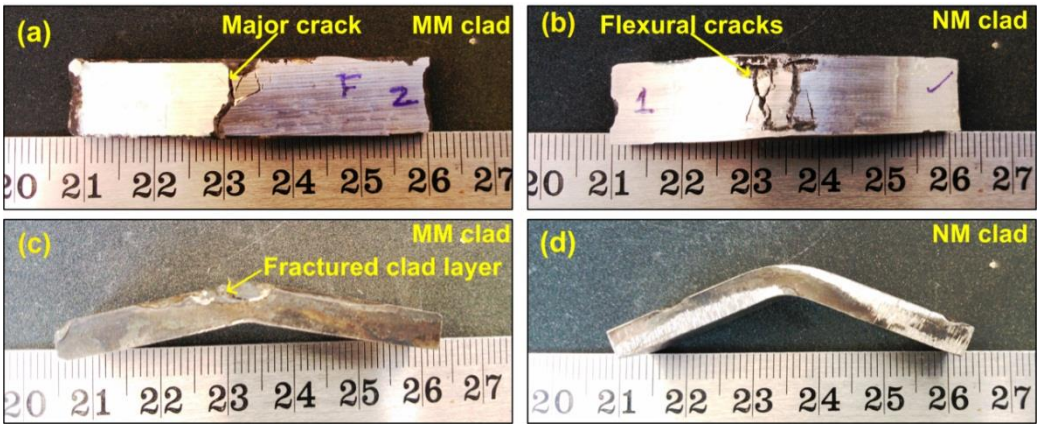

Fig. 5.13- Photographs of fractured specimens after flexural strength test: (a) top view of MM clad, (b) top view of NM clad, (c) side view of MM clad and (d) side view of MM clad

Fractographic analysis of the fractured samples were carried out using SEM to assess the mode of fracture. Typical SEM fractographs of the MM WC-12Co clads after three-point flexural tests are shown in Fig. 5.14. It was observed that loading causes main as well secondary cracking on the clads (Fig. 5.14 (a)). The multidirectional growth of crack was attributed to a multi-phase material system in WC-12Co cermet cladding. It was found in the XRD analysis (section 5.1.1.) that the MM clad consisted of the reinforcement phase mostly in the form of hard carbides (Co_6W_6C, Co_7W_6) uniformly embedded in the relatively soft matrix consisting of mainly Fe-Co. The Co_6W_6C phase exhibits properties like high bulk modulus (~ 462 GPa) which is higher than that of WC (~ 421 GPa, Suetin et al., 2009). It was confirmed earlier (as presented in section 5.1.1), that higher percentage of the Co_6W_6C phase was observed in the NM clads. This indicates higher toughness of the reinforcing nanocarbides in the NM clads.

As a result, of continued loading, high rate of plastic strain is developed in the clads as well as in the clad interface, with the propagation of cracks into the clad surface. The rigid skeleton like carbide constrained the plastic deformation of the metallic binder phase in a very narrow region adjacent to the crack. The relatively soft binder suffered ductile tearing as the crack from the carbide phase entered the binder; the ductile tear ridges in the metallic matrix are shown in Fig. 5.14(b). The cracks nucleated on the outer clad surface during loading get propagated, as it continues to be under tension. While propagating, the microcracks encountered the hard and brittle reinforcement of skeleton structured carbides, which had higher cracking resistance. This results in 'staircase' profile

as observed in the load deformation curve ('OA', Fig. 5.12). However, as the applied load is increased, the cracks tend to propagate laterally to the top face of the clad (Fig. 5.15). At this stage, the hard phase bears the load as it undergoes plastic deformation (stage 'AB', Fig. 5.12). The corresponding mechanism is illustrated in Fig. 5.16 (stage 'OA'). As the load increases beyond the rupture strength of the skeleton carbides, the reinforcement fails and the crack propagates. The nucleated microcracks then meet and lead to main cracks as shown in the stage 'AB' in Fig. 5.16. This phenomenon was also observed in the load displacement curve through the presence of kinks in the stage 'AB' (Fig. 5.12). Consequently, the relatively ductile matrix experiences straining during the loading, which eventually failed on further loading (stage 'BC', Fig. 5.16). The matrix suffered ductile shear deformation as shown in Fig. 5.14(c). A few cracked skeleton-structured carbides are shown in Fig. 5.14(d). The clad layer did not peel off at the end of loading cycle, which indicates good adhesion between the clad and substrate. The fractographic analysis of the fractured specimens indicated both ductile and brittle failure mode owing to the presence of hard and brittle reinforcement uniformly embedded in a ductile metallic matrix in the MM WC-12Co microwave clads.

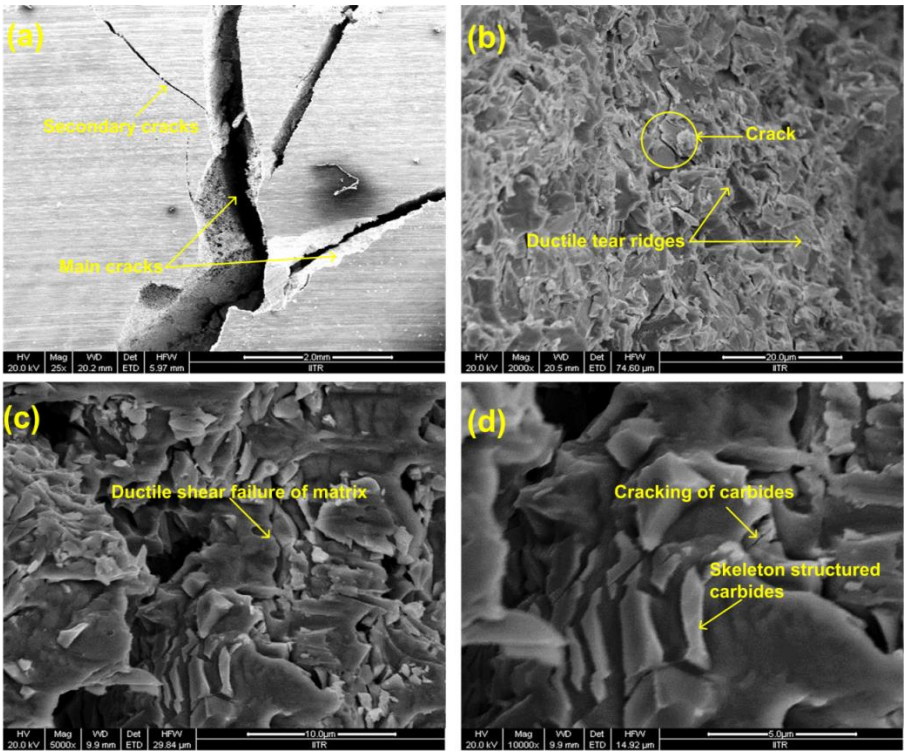

Fig. 5.14- Typical SEM fractographs of the MM clads in three-point flexural test: (a) fractured surface topography illustrating primary and secondary cracks, (b) ductile tear ridges in metallic matrix, (c) failure of matrix, and (d) crack initiation site at skeleton structured carbides

The flexural main cracks parallel to the width of the NM clad are shown in Fig. 5.15(a). The fractured surfaces of the NM clad were characterised by ductile tear ridges of the deformed matrix as shown in Fig. 5.15(b). A closer inspection revealed mixed mode of fracture of the nanometric WC-12Co clads (Fig. 5.15(c)). A large number of nanocarbides can be observed inside the ductile tear ridges. The initiation of microcracks was greatly influenced by the presence and nature of reinforcing carbide particles. However, resistance to cracking is significantly improved if the reinforcing particles are well bonded to the matrix. In general, nanometric particles are more resistant to cracking (Gleiter, 2000). As the load increases, decohesion of the ductile matrix begins with cracks initiated, although the presence of the reinforcing nanocarbides arrest the crack propagation as observed in Fig. 5.15(c). The presence of nanometric carbide phases reduced the slip distance and correspondingly the number of dislocations that could be sustained were reduced (Fig. 5.16). Since decohesion energy of the nanocarbides is higher than the interfacial energy of the carbide matrix interface; therefore, nanocarbides tend to restrict crack propagation. The cracks were resisted more often in the NM clads than in the MM clad owing to uniform distribution of the finer nanocarbides in the matrix. The propagating crack tips encounter the nanocarbides more frequently owing to their higher volume fraction in the NM clads, which then loose energy before getting deflected. The cracks thus get weakened every time they encounter nanocarbide as illustrated in Fig. 5.16. The continuously strained matrix offers resistance to the applied load as indicated by the ‘stage EF’; this stops the secondary cracking and hence decohesion of the matrix of the nanometric WC-12Co clads as schematically illustrated in Fig. 5.16. The NM clads, thus, exhibited a more ductile characteristic as shown in Fig. 5.12. The microvoids promote the dislocation by increasing the free surfaces in the bulk and inducing local strain concentrations (Gleiter, 2000). The presence of some microvoids can be identified at higher magnification (Fig. 5.15(d)), which were the result of decohesion of the clad matrix while failing (Fig. 5.16). The nucleated microcracks in the strained clad microstructure got gradually merged to form main cracks in the proximity to the line of action of the load. As the loading was continued, the main cracks get widened. However, as the clad failed, the nearby clad started bearing the applied load before failing in the similar way, giving rise to the observed parallel cracks a situation almost similar to comb cracking (Fig. 5.13(b) and stage 'EF', Fig. 5.16).

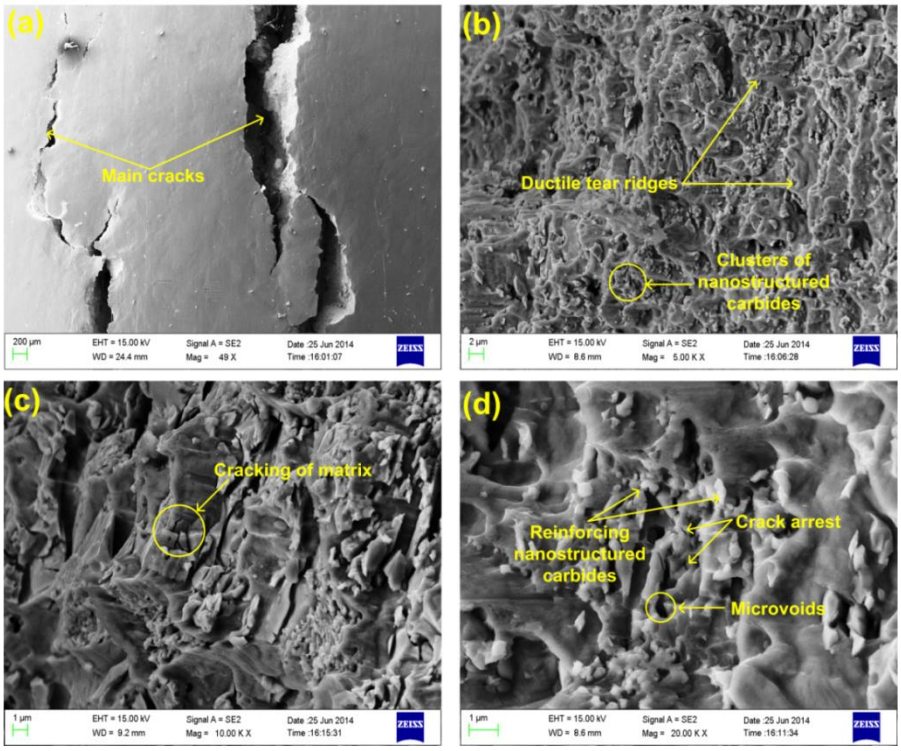

Fig. 5.15- Typical SEM fractographs of the NM clads in three-point flexural test: (a) fractured surface topography, (b) ductile tear ridges on the fractured surface, (c) secondary crack arrest, and (d) microvoids

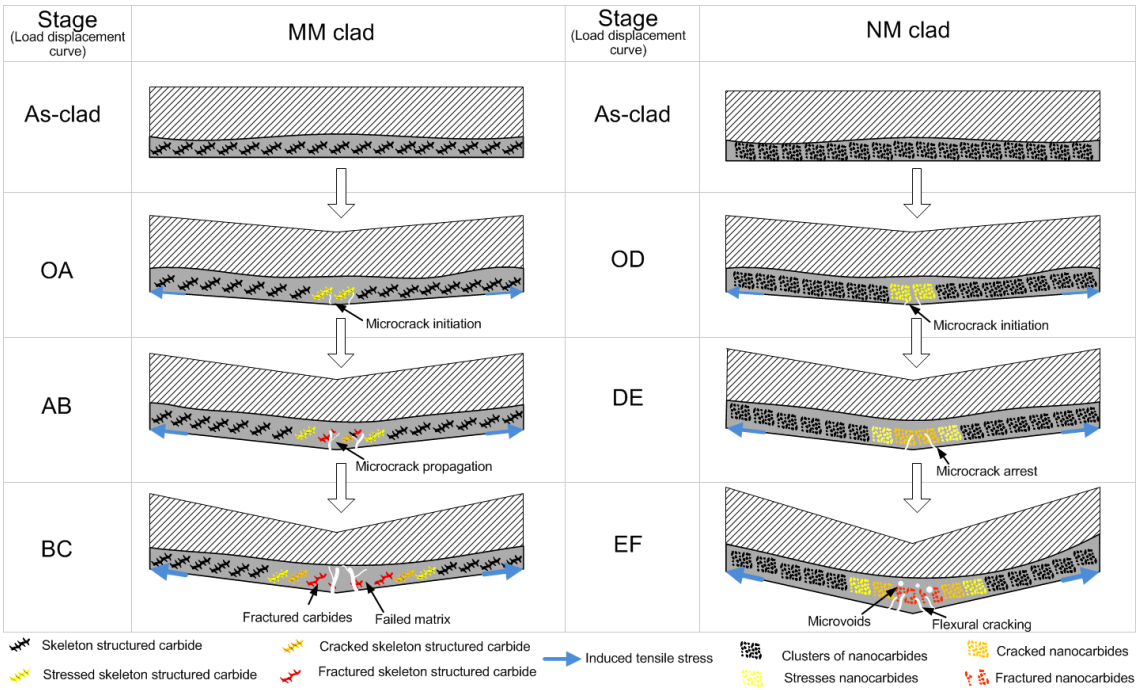

Fig. 5.16- Schematic illustration of flexural behaviour of MM and NM WC-12Co microwave clads

5.2.3. Evaluation of residual stresses

The thermal cycle during microwave cladding results in generation of residual stresses in the clad layer. Evaluation of residual stresses is necessary as the engineering components are often subjected to mechanical and thermal loading. Further the adhesion or the interfacial strength between the clad and the substrate is greatly influenced by presence of residual stresses (Lyphout et al., 2008). Presence of stresses leads to delamination and in worst case, spalling of the clad layer. Further, the presence of compressive stresses at the interface inhibits the formation of through thickness cracks, improves adhesion and fatigue life of the component (Lyphout et al., 2008). The X-ray diffraction technique is a proven method for assessment of residual stresses. The method is based on elastic deformation within the polycrystalline material. The stresses cause change in the lattice spacing (*d*), which are used as internal stain gauges. The stresses are calculated as per the procedure described in section 4.6.3. Various factor affecting the residual stresses are illustrated in Fig. 5.17.

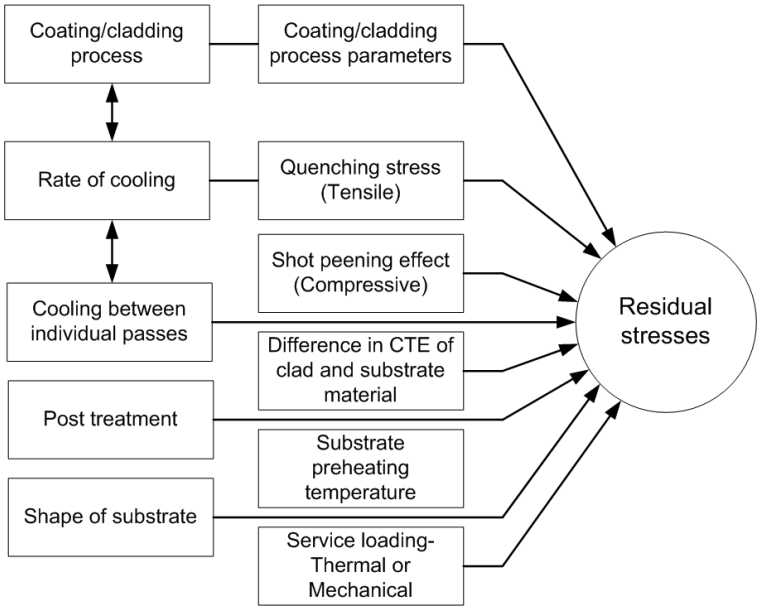

Fig. 5.17- Various factors affecting residual stresses (adapted from Ahmed and Hadfield, 1997)

The surface residual stresses in the MM and NM WC-12Co coatings were evaluated using '$\sin^2\psi$' method using XRD technique. The experiments address the nature and magnitude of the stresses induced in the MM and NM WC-12Co microwave clads. Since the microwave clads are multiphase, the surface residual stresses determined by X-ray diffraction are only concerned with WC phase, since the WC based phases are

dominant in the MM and NM microwave clads. The plot illustrating the $\sin^2\psi$ and lattice spacing (*d*) is shown in Fig. 5.18. The value of Young's modulus (*E*) and Poisson's ratio (*v*) was considered as 563±2 MPa (Bonny et al., 2010) and 0.25 (Santana et al., 2008), respectively. Table 5.4 presents the values of slope of the plot shown in Fig. 5.18 to calculate the residual stresses as per equation 4.2. Three specimens were tested each for MM and NM clads to ensure repeatability of the residual stress values.

Table 5.4- Residual stress values of WC-12Co MM and NM microwave clads

S.No.	Slope	Magnitude of residual stress (MPa)	Nature of residual stress
MM Clad	-0.11262	-50.72±4	Compressive
NM Clad	-0.18819	-84.76±3	Compressive

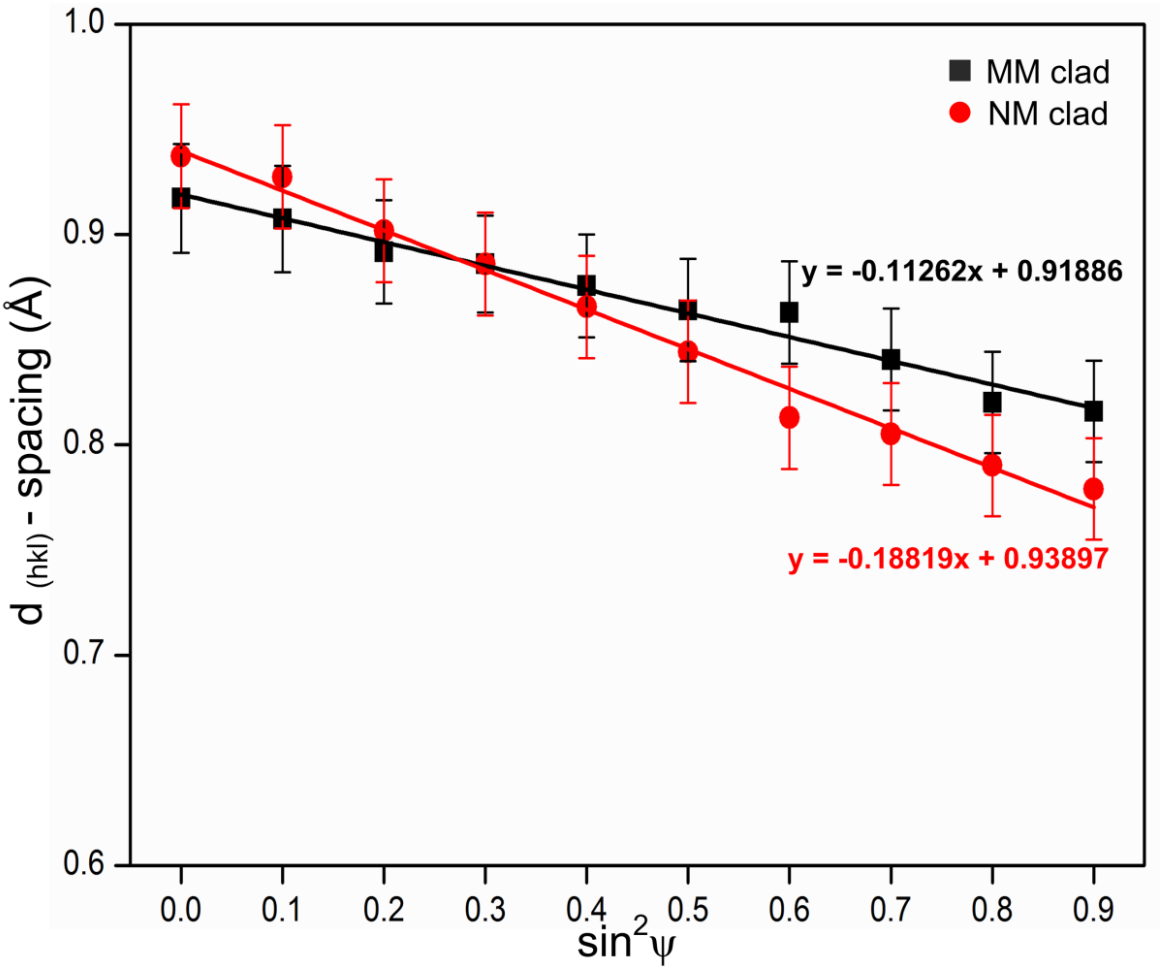

Fig. 5.18- Linear dependency of d-spacing versus $\sin^2\psi$

The relationship between the $\sin^2\psi$ and lattice spacing (d) is shown in Fig. 5.18. The nature of the residual stresses in the MM and NM clads was compressive, and the average residual stress in the NM clads was approximately 68% higher than the MM clad. During microwave exposure, the powder particles get melted on the substrate (SS-304). The molten powder layer causes a thin layer of the SS-304 substrate to melt. The clad powder consisted of predominantly WC as the reinforcement phase and Co as a binder, but the coefficient of thermal expansion (CTE) for Co (13×10^{-6} K^{-1}, Cverna, 2002) is about three times the CTE of WC (4.8×10^{-6} K^{-1}, Kurlov and Gursev, 2013). Owing to the inelastic behaviour of the hard WC based skeleton structure, its contraction is constrained in the clad layer. This leads to generation of micro stresses at the interface of the reinforcement and metallic matrix. Also, during the thermal cycle of the microwave cladding process, initially the SS-304 substrate (CTE: 17×10^{-6} K^{-1}, Cverna, 2002) is at room temperature, but its temperatures rises due to heat conduction and convection from the molten clad powder layer. The heated substrate and clad layer attains ambient atmospheric temperature during cooling. The substrate and clad layer contract (depending on their CTE values), and leads to the generation of residual stresses.

The presence of nanocarbides in the NM clad (Fig. 5.3) provides more interfacial area with Co binder than the skeleton like carbide structure in the MM clad. Consequently, in the NM clad the regions of micro stress generation were more than the MM clad, giving higher compressive residual stresses. The presence of higher compressive residual stresses is considered beneficial for wear resistance, especially during erosive wear applications. It was reported that the WC-12Co laser clads exhibit tensile residual stresses (magnitude of the order of 200 MPa), which caused cracking of the clad layer (Lee et al., 2015). This is attributed to the high thermal gradient associated with the laser cladding process. However, uniform heating and low thermal gradient in microwave cladding lead to development of compressive residual stresses. Therefore, no interfacial cracking was observed in the microwave clads (Fig. 5.2 and 5.3). Absence of interfacial cracking in microwave clads was also reported earlier, and it is now possible to explain one of the reasons.

The observed residual stresses (Table 5.4) can be explained with the help of the schematic diagram shown in Fig. 5.19. The nature of the residual stresses in the clad layer (as-clad specimens) was observed to be compressive (Fig. 5.19(a)). This is contrary to the nature of residual stresses (tensile) in laser clads (Lee et al., 2015). This is indicative of the

solidification of the entire clad layer following the melting of the pre-placed powder layer and localised intermixing at the interface (approximately 10-20 μm thick, Fig. 5.2 and 5.3). In laser cladding, in general, clad thickness gets developed in a layer by layer manner, hence the solidification of each layer takes place separately. The observed higher residual stress values in the NM clad are also supported by the measured higher flexural strength of the NM clads (Fig. 5.12). As the clads are subjected to tensile loading during the flexural test, the initial loading is used to overcome the residual stresses (compressive in nature) of the material (as-clad) as illustrated in Fig. 5.19(b). Thus, higher energy is required to deform (and to rupture) the NM clad layer, which has higher residual stresses compared to the MM clad (Table 5.4).

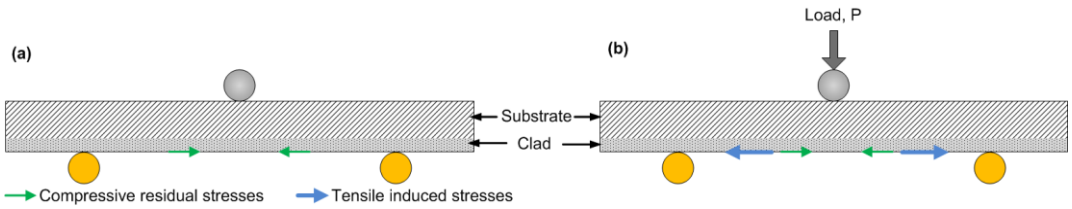

Fig. 5.19- Schematic illustration of stress in clads (a) before loading (as-clad) and (b) during loading

5.3. SUMMARY

The results and detailed discussion pertaining to metallurgical and mechanical characterisations of the MM and NM WC-12Co microwave clads is presented. The phase analysis of the MM and NM WC-12Co microwave clads revealed presence of Co_6W_6C and Co_7W_6. The microstructure of the MM WC–12Co microwave clads contains uniformly distributed skeleton structured eutectics (carbides) distributed in the Fe-Co based dendritic matrix, while the NM WC–12Co consists of uniformly distributed eutectic regions of nanocarbides in the clad layer. The average Vicker's microhardness of the NM WC–12Co clad is 1564±53 HV, which is about 37% higher as compared to its MM counterpart (1138±90 HV). The flexural strength of the NM clad was observed to be approximately 14% higher as compared to the MM clad. The residual stresses in the MM and NM clads were evaluated using '$\sin^2\psi$' method through XRD. The nature of residual stresses was observed to be compressive, while the NM clads exhibited approximately 68% higher compressive stresses than the MM clads.

CHAPTER 6

TRIBOLOGICAL EVALUATION OF THE CLADS

Wear is an unavoidable phenomenon in many industrial applications such as rock drilling, ore crushers, earth-moving equipment, dies in powder metallurgy, extruders etc. Therefore, high wear resistance is desirable in the materials used in such applications. Austenitic stainless steel (SS-304) is a widely used engineering material attributed to its low cost and excellent corrosion resistance. However, severe sub-surface wear due to plastic deformation limits its use in potential wear applications.

The WC-Co based materials are extensively used to combat various modes of wear in several industrial components, even at moderately elevated temperatures (up to 400 °C). In general, hardness and wear resistance of the WC–Co based cermets increases with the decrease of carbide particle size and increased volume fraction of the carbides. Reduced carbide particle size reduces the mean free path of the binder phase, resulting in greater constraints and higher hardness. Consequently, there has been a lot of interest in wear resistant nanostructured WC–Co based overlays. In the present work, two WC-12Co powders, with particle size in the micrometric (MM) and nanometric (NM) range were used to develop clads on austenitic stainless steel (SS-304) using microwave cladding technique. The tribological performance of the MM and NM WC-12Co clads were evaluated using dry sliding wear, three-body abrasive wear and solid particle erosive wear. The results of various tribological characterisations are discussed with suitable illustrations in the present chapter.

6.1. DRY SLIDING WEAR

Sliding is characterised by relative motion between two smooth solid surfaces in contact under load. High local pressure between the contacting asperities results in plastic deformation of the contacting asperities, adhesion and consequently formation of junctions locally. Repetitive sliding between the contacting surfaces causes rupture of these junctions and frequently transfer of material from one surface to the other. Material loss occurs in the form of small particles, which are usually transferred to the other surface or get dislodged from the candidate surface. Sliding is one of the most common types of tribocontact experienced by the functional surfaces of the engineering components like machine tool slides, gears and cutting tools etc. Adhesion, abrasion, tribochemical reaction and surface

fatigue may occur during sliding contact. Different physical processes during sliding wear are well documented. Adhesion leads to formation of welded junction with clean mating counter surface; on the other hand, in abrasion, removal of material occurs due to the presence of hard particles on the counter surfaces. In tribochemical reaction, loose wear particles are formed on the surfaces that consequently act as abrasives. Applications of sliding wear in engineering components have resulted in extensive research in this area (Deuis and Subramanian 2000; Landheer and Zaat 1974; Lovell et al., 2000; Yoffe 2001; Chelliah and Kailas, 2009; Menezes and Kailas, 2009). In the present study, dry sliding wear performance of the MM and NM clads was investigated using a pin-on-disc tribometer as per ASTM G-99 standard in unlubricated conditions. The wear and friction results were correlated with the SEM micrographs of the worn surfaces.

6.1.1. Comparison of MM WC-12Co microwave clad with SS-304 substrate

In the present work, the tribological behaviour of MM WC-12Co microwave clad was investigated using a pin-on-disc arrangement (Fig. 4.10) against an EN-31 counter surface in unlubricated condition as per conditions presented in Table 6.1. Normal contact load was varied in order to investigate its effect on the concomitant sliding wear and friction behaviour of the MM clads and were compared vis-à-vis the SS-304 substrate. The results are discussed with suitable illustrations in the following sections. Various parameters for the wear tests were selected on the basis of the literature review. However, the limitation of the operating parameters of the test setup was considered while selecting the test parameters.

Table 6.1- Details of sliding wear tests

Parameters	**Values**
Test setup and standard	Pin-on-disc, ASTM G-99
Wear pin	(a) WC-12Co microwave clad (b) SS- 304 stainless steel substrate
Initial roughness	R_a = 0.15 µm (based on literature)
Sliding distance	1000 m
Counter disc	Material: EN-31, Hardness: 65 HRC, Diameter: 60 mm
Sliding speed	1 m/s
Normal load	10, 20, 30 N
Lubrication condition	Dry
Temperature	28±2 °C (average room temperature)
Relative humidity	55±4 % (as per average ambient conditions)

6.1.1.1. Wear rate

Dry sliding wear behaviour of the WC-12Co microwave clad and SS-304 substrate was analysed using a pin-on-disc tribometer. Typical wear rate characteristics of WC-12Co microwave clad and SS-304 substrate are presented in Fig. 6.1. It can be observed that during the initial run-in-wear period both, microwave clad and substrate, exhibit high wear rate attributed to the occurrence of run-in-wear phase during which the mating surfaces attain compatibility with each other. The wear rate of WC-12Co microwave clad reduces significantly beyond 400 m and a steady wear zone can be identified as illustrated in Fig. 6.1. A possible explanation of reducing wear rate was formation of a tribofilm by extrusion of the Co binder phase, which protects the surface from further damage followed by removal of WC based carbides. However, the wear rate exhibits a higher value with increase in normal contact load due to increased pressure at the mating surfaces. This results in more binder removal and fragmentation of the carbides. Reduction in wear rate can also be an indicative of better mechanical stability of the surfaces owing to the superior metallurgical bonding during microwave cladding. The reducing wear rate after the run-in-phase may be attributed to the enhanced load bearing capacity of the embedded carbide grains retained on the sliding face of the microwave induced clad and their ability to reduce binder-to-binder contact during sliding. Removal of some carbide grains cause formation of small cavities on the surface (Fig. 6.2(a) and (b)). This happens due to occurrence of surface and sub-surface microcracks that eventually propagate, crushing and detachment of the carbide structure. As the sliding continued, there was rise in temperature at the mating surfaces; hence a thin tribo-oxide layer was formed (Fig. 6.2(c) and 6.2(f)). The tribo-oxide layer being harder than the mating surface matrix material protects the sliding elements against wear. Further, friction between the surfaces and hence the wear reduced with the formation of oxide layer. Presence of oxygen in the EDS spectra (insets Fig. 6.2(d)) indicates the formation of oxides of Cr and Fe, which are characteristically wear resistant.

The wear rate of SS-304 stainless steel substrate was high during the run-in-phase and gradually reduces as seen by settling in tendency of the wear rate characteristics in Fig. 6.1. The wear in SS-304 substrate was due to plastic deformation due to surface and sub-surface deformation, formation of debris, material transfer and reaction due to environment. At higher normal load (30 N) the SS-304 substrate surfaces suffer severe plastic deformation and adhesion (Fig. 6.3(c)), consequently, the wear rate rises. It is

observed form the data that at 10 N the WC-12Co microwave clad exhibit approximately 64% less wear rate than the SS-304 substrate, while at 20 N and 30 N, the wear rates were 59% and 78% less than the SS-304, respectively.

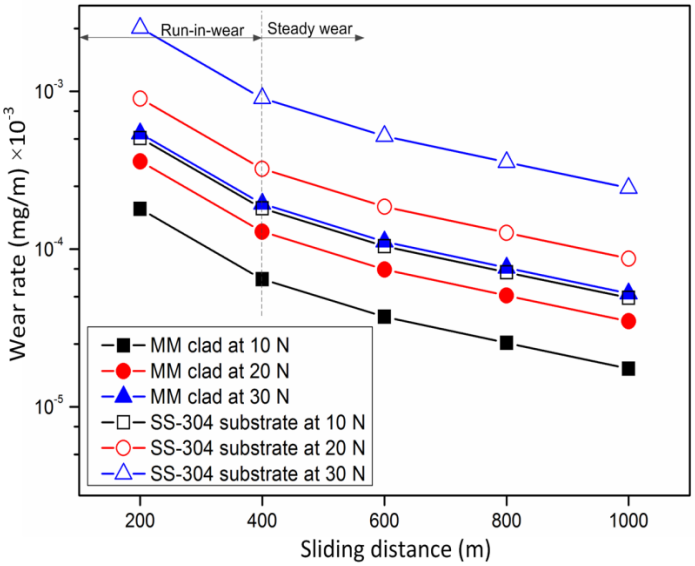

Fig. 6.1- Typical wear rate characteristics of MM WC-12Co microwave clad and SS-304 stainless steel

6.1.1.2. Analysis of the worn surfaces

After the wear testing, the worn surfaces of WC-12Co microwave clad and SS-304 stainless steel were examined using SEM. The worn surfaces of WC-12Co clad at different normal loads are illustrated in Fig. 6.4. Material pullout, debonding of carbide particles, smearing of oxide film and crushing of carbide particles are the main mechanisms of wear in WC-12Co microwave clads. At low normal load (10 N), mild wear in terms of material pull out can be observed from the micrographs as illustrated in Fig. 6.2(a). The carbide reinforcement was well embedded in the tough (Co) binder and remains intact; hence at low load some de-bonding of carbide grains was confirmed through EDS analysis as shown in Fig. 6.2(d). However at medium normal load (20 N), carbide pullout and pitting can be observed (Fig. 6.2(b) and (e)). Since the WC-12Co clads are relatively hard and at medium loads fatigue induced de-bonding results in carbide pullout (Fig. 6.2(b)). Due to carbide pullout small pits are formed on the worn clad faces. Also due to increased normal load, more surface irregularities are in contact with the counter surface, hence the worn surface exhibits loose debris from the counter surface.

Loss material from the binder (Co) occurs mainly due to smearing of oxide layer that is clearly visible in Fig. 6.2(b). However, tungsten carbide (WC) can be clearly seen acting as reinforcement as white skeleton structured carbides. Further increase in normal load causes crushing of carbide particles as observed from Fig. 6.2(c). At higher normal loads, the adhesion junctions may either break in steel or cermet, which results in material transfer or wear from both mating surfaces. Crushing of carbide particles leads to detachment of the carbide grains from the surface. The cyclic load causes occurrence and development of cracks in the binder phase and detachment from the weakest structural element that was between carbide or matrix phase. Due to higher normal load, the smearing of the oxide layer and material transfer from the counter surface can be observed in Fig. 6.2(c) and 6.2(f).

Fig. 6.3 reveals that adhesion, abrasion and plastic deformation were responsible for the wear of SS-304 stainless steel. The typical characteristics of adhesive wear are smearing of surface asperities, spalling of the worn surface (Fig. 6.3(a), plate-like debris (Fig. 6.3(a)) and lumps of material (steel). All are well established phenomena for sliding wear of austenitic stainless steel against various materials (Li and Bell, 2004). Presumptively, the initial high wear rate of SS-304 was attributed to the gradually increased contact area and increased adhesion. It was understood that at the commencement of wear, a two-body wear mechanism occurred between the SS-304 stainless steel substrate and the EN-31 counter surface. But the strong adhesion between SS-304 stainless steel with EN-31 counter surface would change the wear mechanism from two-body to three-body contact with the wear debris present between the mating surfaces as the normal load was further increased. Further, adhesion between the materials attached between the counter disc and the worn SS-304 surface would detach more material from the substrate, resulting in more material transfer and generation of wear debris. The transferred material or wear debris (particles) would then be plastically deformed and compacted by the rubbing action between the SS-304 stainless steel surface and the counter surface, producing the plate-like wear debris. The highly work hardened wear particles wedged between the loaded mating surfaces and moved along with the wear pin results in the characteristic parallel abrasive grooves on the relatively soft austenitic stainless steel surface as seen in Fig. 6.3(a) and (b). The combined action of high normal load (30 N), strong adhesion, abrasion and severe plastic deformation leads to the increased material loss from the SS-304 stainless steel surface (Fig. 6.3(c)). However, as

the sliding continues past 400 m, change in contact area, accumulation of wear debris in the deep wear tracks and work hardening of materials on the wear track during sliding could have resulted decreased wear rate of SS-304 stainless steel (Fig. 6.1).

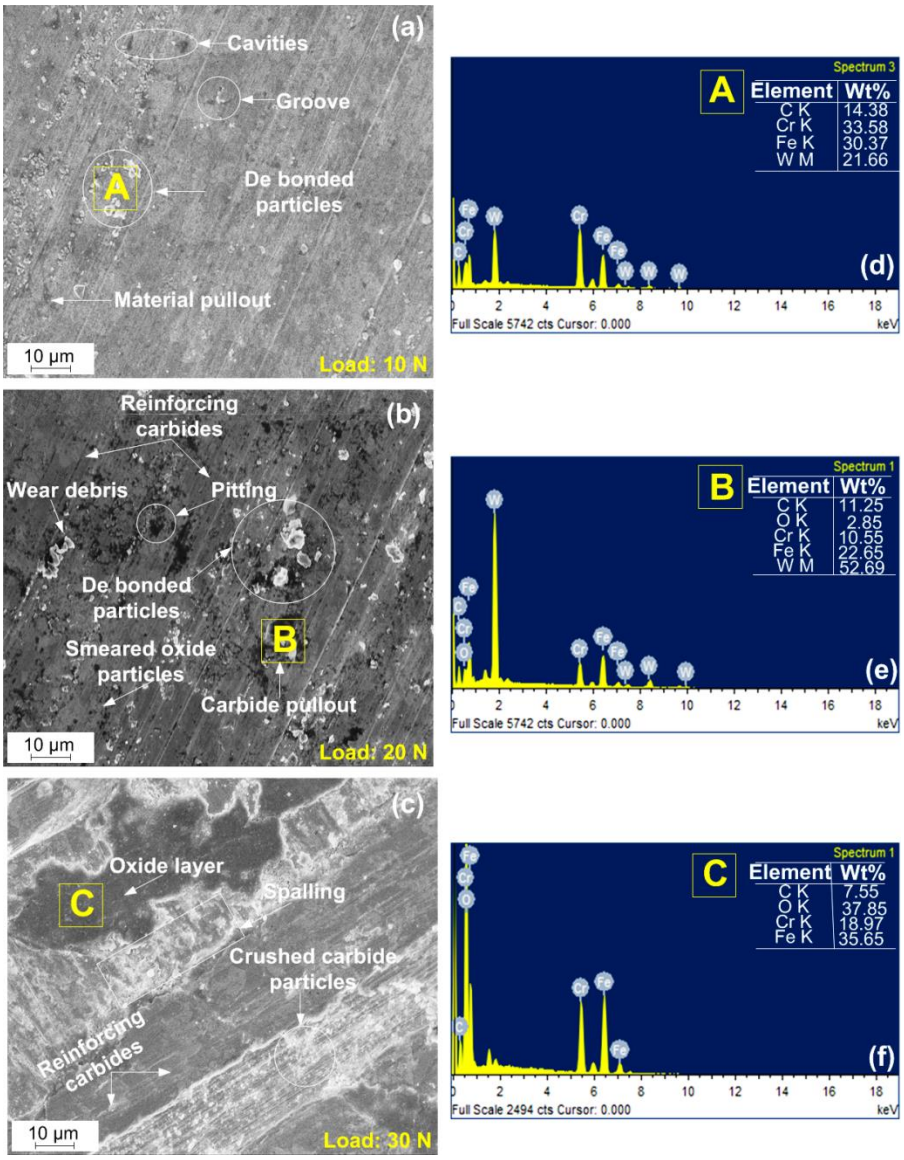

Fig. 6.2- Typical SEM images of (a)–(c) worn WC-12Co clad surfaces and (d)–(f) EDS spectrum at marked location

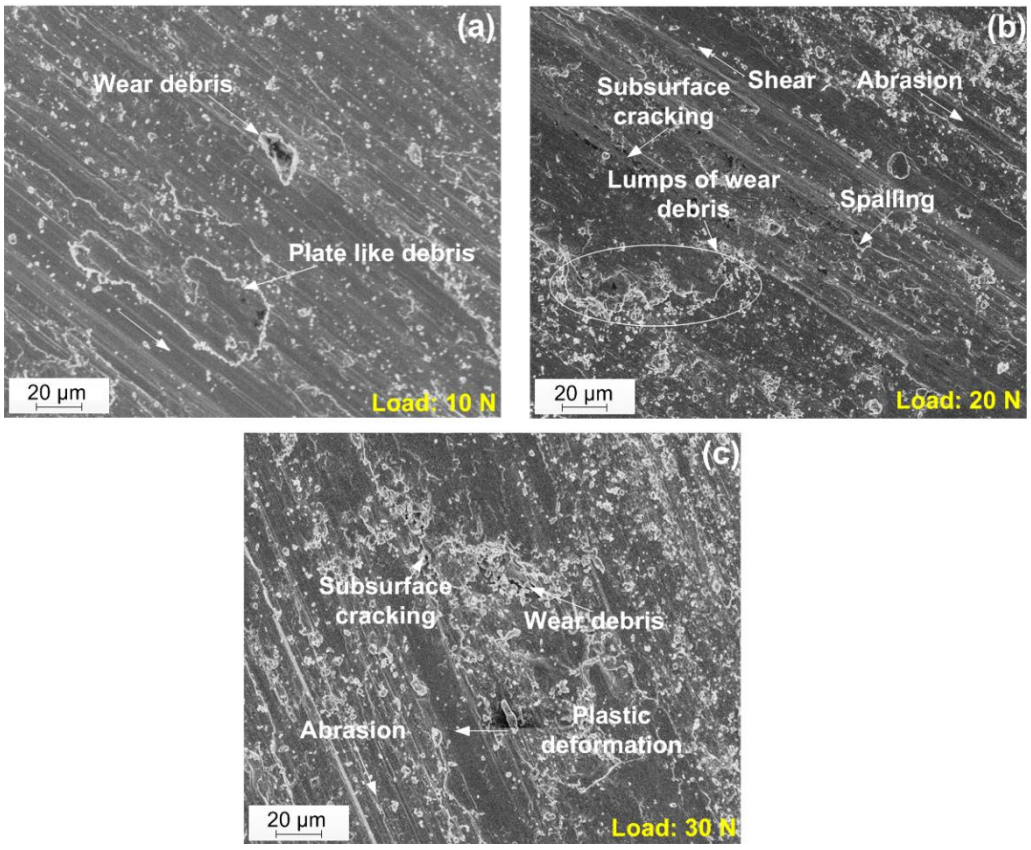

Fig. 6.3- Typical SEM micrographs of the worn surface of SS-304 stainless steel at different normal loads (sliding velocity 1 m/s and sliding distance 1000 m)

6.1.1.3. Pressure-velocity-time (p-v-t) characteristics

A p-v-t analysis on the wear data was carried out in order to analyse the combined effect of the operating variables (pressure, velocity, time) on wear and to determine the optimal operating conditions. Typical p-v-t characteristics of WC-12Co microwave clad and SS-304 substrate at different operating normal loads (0.1, 0.2 and 0.3 MPa) are presented in Fig. 6.4 (a) and (b), respectively. It can be observed from Fig. 6.4(a) that the microwave WC-12Co clads exhibit steady wear until a p-v-t value of 200 MPa.m. In case of higher pressure (0.3 MPa), wear changes to unsteady zone beyond 200 MPa.m. However, in case of SS-304 substrate wear was steady in case of 0.1 MPa, but with the increase in normal load, wear becomes higher and tends to become unsteady as can be seen from Fig. 6.4(b). Wear of more than 425 µm can be considered unsteady in case of SS-304 substrate as at 0.2 MPa wear rises abruptly (Fig. 6.4(b)). Hence, it can be concluded from the p-v-t analysis that the WC-12Co microwave clads exhibit better wear performance under various operating conditions investigated.

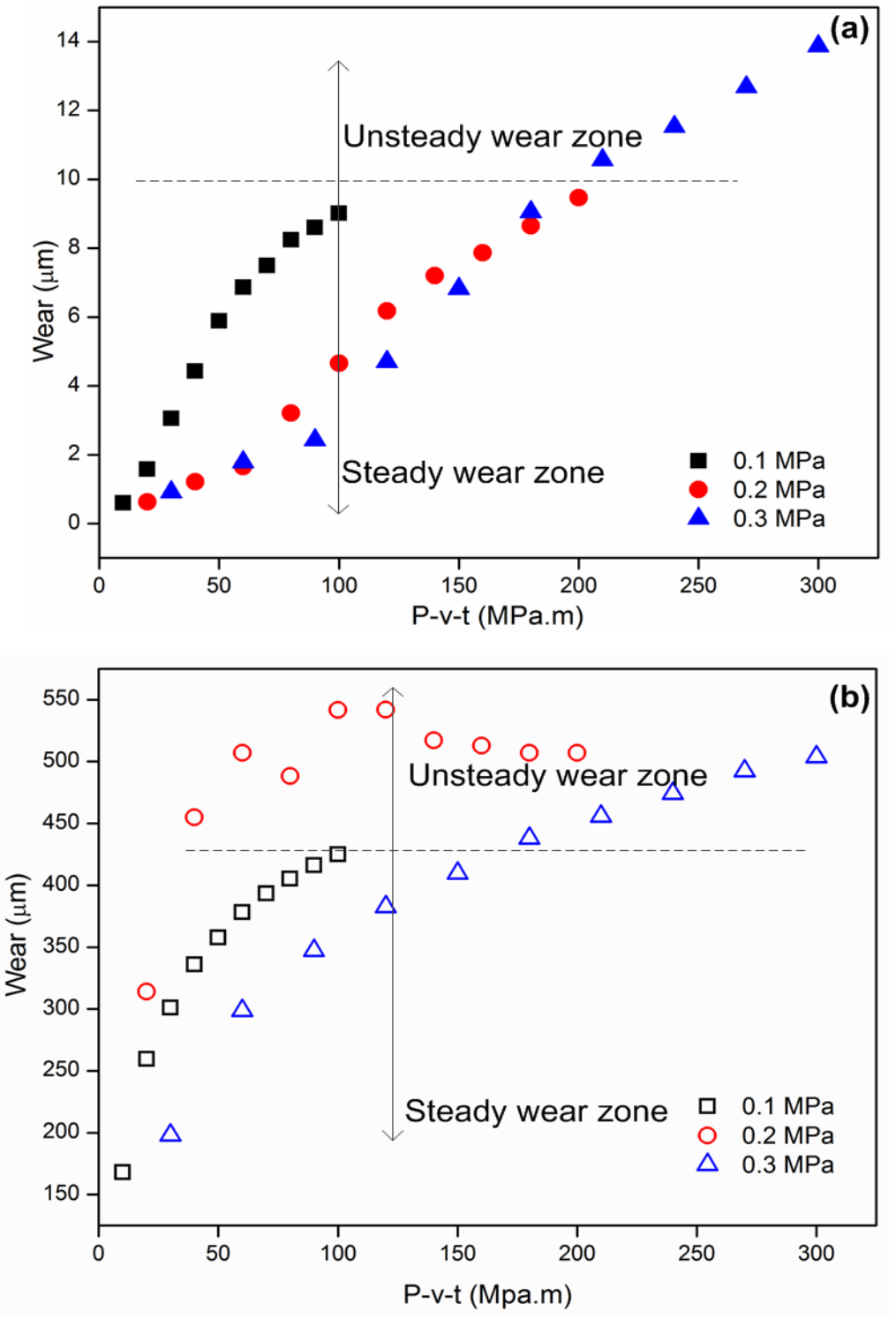

Fig. 6.4- Influence of p-v-t on sliding wear of (a) WC-12Co microwave clad and (b) SS-304 stainless steel

6.1.1.4. Friction characteristics

During the wear test, normal contact force (F_n) and friction force (F_f) were continuously monitored in real time; accordingly friction coefficient (μ) was determined as the ratio of F_f and F_n. Typical friction characteristics of WC-12Co microwave clad and SS-304 stainless steel are shown in Fig. 6.5. A significant observation is that the friction coefficient increases with increase in normal load, which was attributed to the tendency of increased plastic deformation and ploughing effects at higher normal loads. It can be observed from Fig. 6.5(a) that the friction coefficient in case of WC-12Co was lower than SS-304 stainless steel substrate under all normal loading conditions. An initial run-in-wear phase can be identified in the in Fig. 6.5(a) during which the friction coefficient rises rapidly and gradually a steady state was reached after about 400 m of sliding. This can be attributed to the burnishing wear process during the initial stage of sliding that establishes a compatibility with the mating surface by removing the surface asperities. As the sliding proceeds further, the wear track becomes smoother and the mating interface attains a steady state value although friction coefficient remains dependent of the normal load value. Higher coefficient friction was monitored with the increase in normal load. The friction characteristics of SS-304 stainless steel (substrate) are illustrated in Fig. 6.5(b). It is observed that fairly high value of friction coefficient exists in case of SS-304 substrate. The fluctuations observed in friction coefficient can be attributed to the rupture of a tribological layer of the mating SS-304 stainless steel substrate, which continues with sliding distance (Kagnaya et al., 2009). However, a small region where the value of coefficient of friction remains independent of the load was observed. This region can be termed as 'optimal sliding zone'. The spalling of the SS-304 substrate due to sliding causes loss of material from the mating surface. The observed higher friction as indicated by the undulations (Fig. 6.5(b) is an indicative of the 'stick-slip' kind of contact at the interface at relatively higher temperature at 30 N. The 'stick-slip' phenomena results because of unsteady sliding resulting from varying friction force in combination with the elasticity of the mechanical system (Van De Velde and De Baets, 1998). The decrease in the friction coefficient is because of the increased acceleration due to the increased normal distance between the rubbing surfaces due to the asperity interlocking. Due to increased normal contact, the true metal-to-metal contact decreases hence the friction force decreases. The friction force remains constant for some time and increases again because of the growth of

the real contact area resulting from the normal approach of the rubbing surfaces. Further, due to the dry sliding conditions in the present work, the tribo-oxide film breaks due to the wear, which leads to enhanced adhesion between the contact surfaces. A rise in temperature is quite natural with the increasing sliding distance. The adhesion friction also results in shearing of the contacting asperity junctions on continued sliding. At higher normal load, the contacting pressure becomes large enough to plastically deform all the asperities on the relatively soft surface of SS-304 substrate.

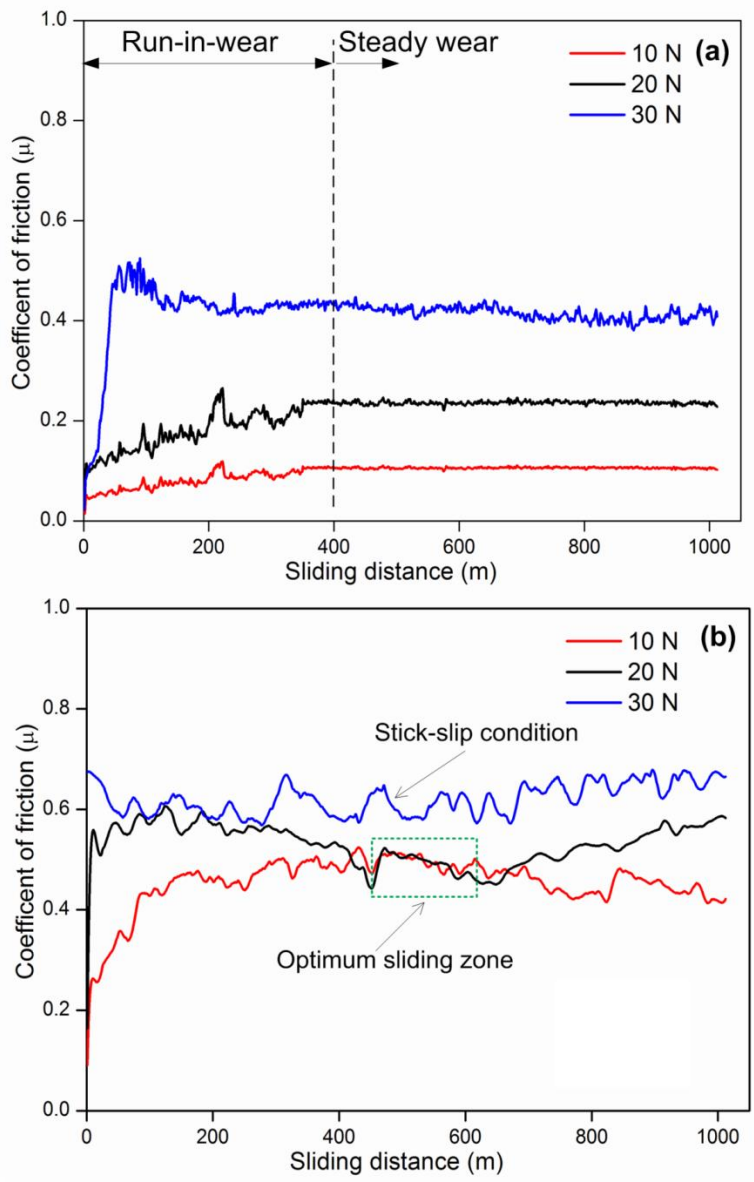

Fig. 6.5- Typical friction characteristics of (a) WC-12Co microwave clad and (b) SS- 304 stainless steel

6.1.1.5. Analysis of wear debris

The wear debris collected from pin-on-disk sliding wear tests were diverse in shape, morphology and size. Fig. 6.6 shows the wear debris generated at 30 N after sliding for 1000 m at 1 m/s. Fig. 6.6(a) illustrates the wear debris generated form WC-12Co microwave clad, which was in the form of small powdered agglomerates, which are an indicative of low wear rate. The EDS spectrum of the debris, as illustrated in Fig. 6.6(b), indicates that the fine wear debris was highly enriched in Fe and O with only trace amount of W and C. Therefore, these are probably the complex iron oxide particles that were formed due to material transfer from the counter surface (EN-31). This indicates better stability of the WC-12Co microwave clads. Presence of smeared oxide layer reduces direct metallic contact hence reduces the wear rate as sliding continues. Hence, a steady wear zone beyond 400 m could be identified in Fig. 6.1.

Irregular flake like debris was generated due to plastic deformation of the SS-304 substrate surface, as shown in Fig. 6.6(c), is indicates higher wear rate. The EDS spectrum of the wear debris confirms that occurrence of oxidation on the worn surfaces of the SS-304 substrate due to higher sliding load and friction heat. These oxide particles formed at high load were fractured and comminuted as sliding continued. Higher Fe percentage in the EDS spectrum (Fig. 6.6(d)) indicates that materials loss occurs from SS-304 substrate. The wear debris was highly enriched in Fe and O and was identified as the iron oxides, which were primarily transferred from the substrate surface that was oxidized during sliding wear. These smeared oxides surface layers would have played the positive roles in reducing material removal rate from both of friction pairs because their presence on the contact surface prevented the contacting surface from direct metallic contact as indicated by the reduced wear rate in Fig. 6.1.

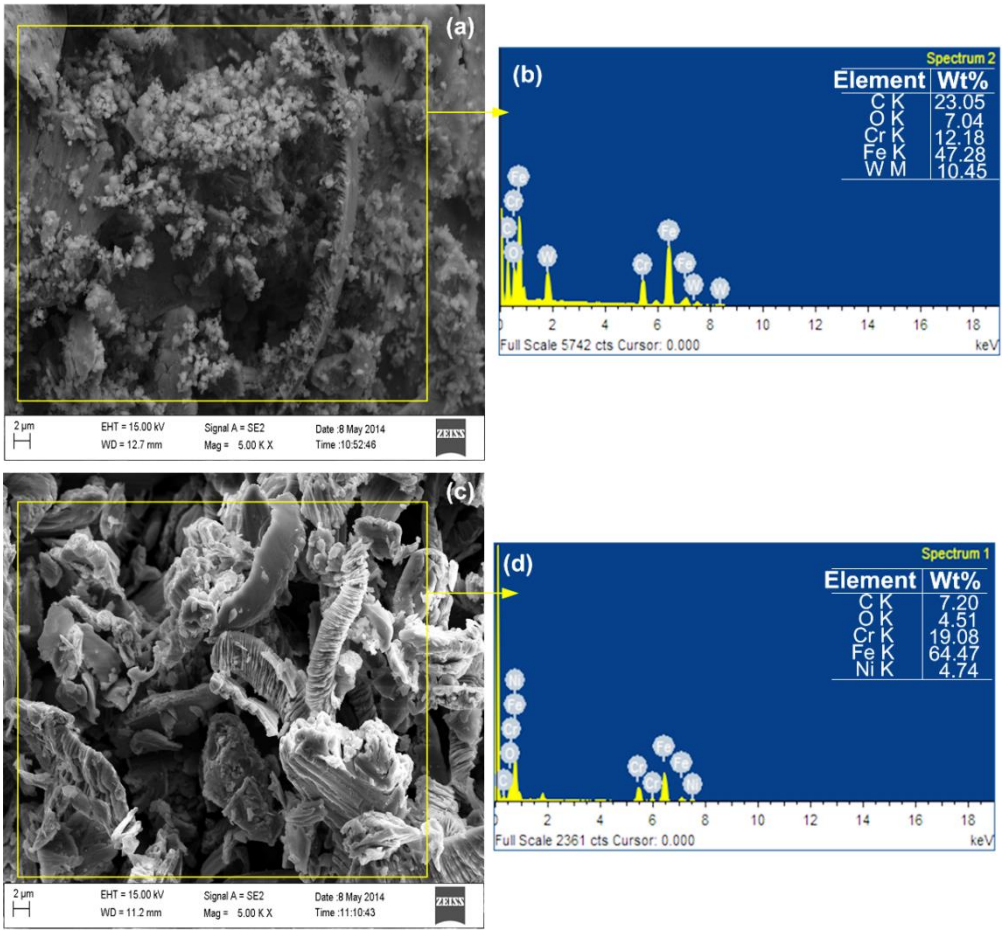

Fig. 6.6- (a) SEM micrograph of wear debris and (b) EDS spectrum of MM WC-12Co microwave clad; (c) SEM micrograph of wear debris and (d) EDS spectrum of SS-304 substrate

6.1.2. Comparison of MM and NM WC-12Co microwave clad

The tribological behaviour of MM and NM WC-12Co microwave clad was investigated using a pin-on-disk arrangement (Fig. 4.10) against an EN-31 counter surface in unlubricated condition as per conditions presented in Table 4.3 (Chapter 4). Normal contact load was varied in order to investigate its effect on the concomitant sliding wear and friction behaviour of the MM and NM microwave clads. The tribological behaviour of the MM clads was compared vis-à-vis the NM microwave clads. Analysis of wear was carried out in terms of wear rate and cumulative weight loss**.** The results are discussed with suitable illustrations in the following sections. Worn wear pins were analysed using SEM for identifying the wear mechanisms. A 3-D optical surface profilometer (Make: Veeco Wyko, Model: 1100NT) was used to characterise the surface profiles of the worn surfaces.

6.1.2.1. Wear rate and cumulative weight loss characteristics

Dry sliding wear performance of MM and NM WC-12Co microwave clad was evaluated using a pin-on-disk tribometer. Grain size is an important factor influencing the wear performance of the WC-12Co clads. In sliding type of tribocontact, normal load on the mating surfaces plays an important role. Hence, the sliding wear tests were carried out by varying the normal load to assess the load sensitivity of the microwave clads. The wear rate characteristics of the MM and NM microwave clads are presented in Fig. 6.7 and the cumulative weight loss characteristics are illustrated in Fig. 6.8. It is observed from Fig. 6.7 that initially both MM and NM WC-12Co microwave clads exhibit high wear rate attributed to the run-in wear phase during which the rough surface asperities are removed. Beyond 2000 m of sliding distance, the wear rate reduces due smoothening of the wear tracks; accordingly, this zone can be termed as 'steady wear zone'. On the other hand, with increased normal load, the wear rate shows an increasing trend due to the increased pressure on the mating surfaces, which results in binder removal and fragmentation of the carbide grains. But the presence of the nanocarbides clusters in the NM WC-12Co microwave clad provide enhanced reinforcement and hardness as compared to the MM WC-12Co microwave clad. Hence, the NM WC-12Co microwave clad effectively resists wear of the mating surfaces.

Improved wear resistance of the NM clad is attributed to reduced abrasion and increased obstruction to crack propagation. Grain boundaries in NM microwave clad are more in number than in the MM microwave clad, hence it impedes the slip which ultimately hampers the crack propagation. The cumulative weight loss characteristics of the MM and NM WC-12Co clads, as shown in Fig. 6.8, reveals that the weight loss in NM microwave clads is almost 72%, 54% and 46% less than the MM WC-12Co clad for normal loads of 10 N, 20 N and 30 N, respectively, for a sliding distance of 5000 m.

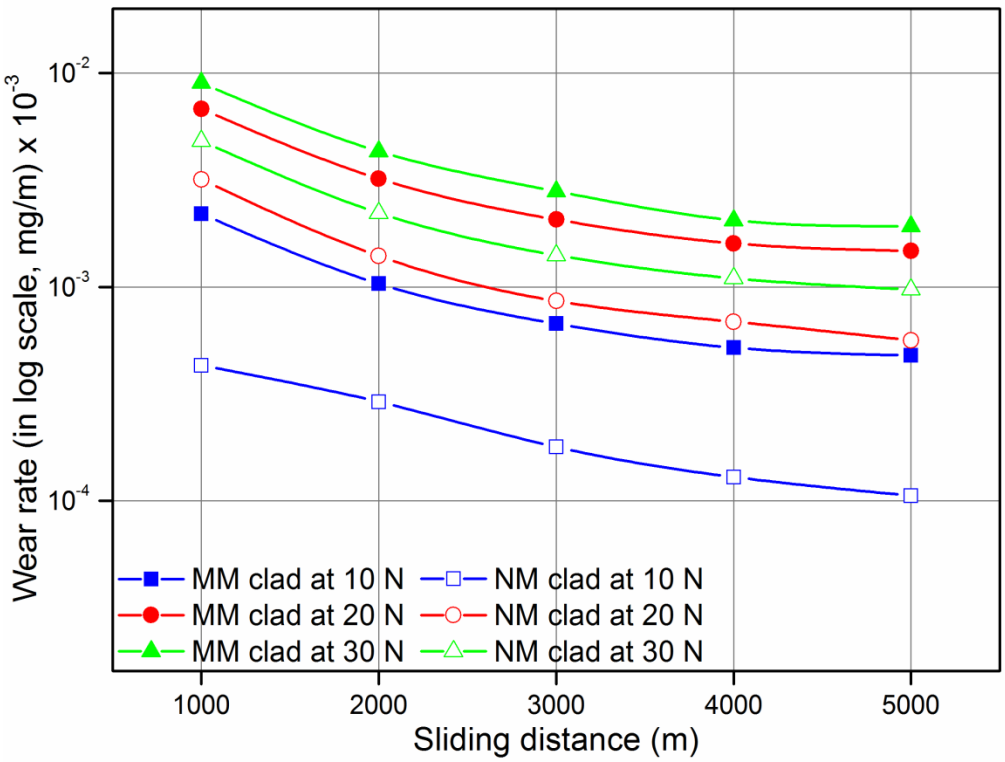

Fig. 6.7- Wear rate of MM and NM clads as a function of normal load

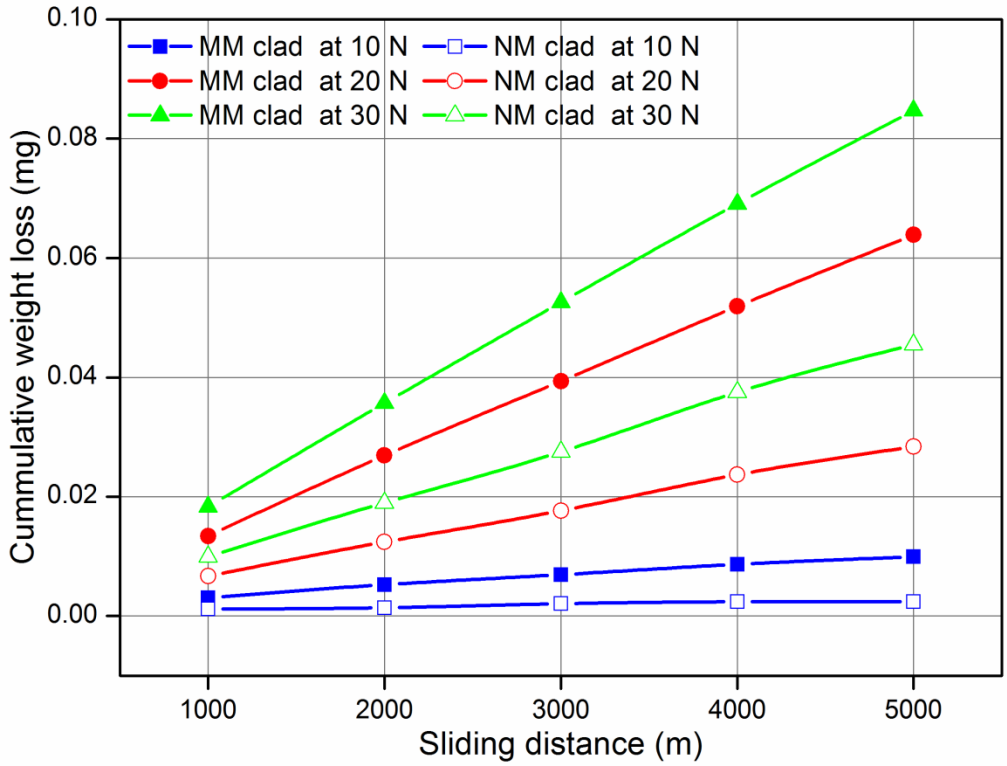

Fig. 6.8- Cumulative weight loss of MM and NM clads as a function of normal load

6.1.2.2. Friction characteristics

The experimental and predicted coefficient of friction (μ) of the MM and NM WC-12Co microwave clads during sliding under various normal loads is shown in Fig. 6.9. It is observed that the NM microwave clad exhibited a lower value of μ compared to the MM clad under various loading conditions. Presences of uniformly distributed nanocarbides in NM clad reduce the direct binder contact with the counter surface. In the MM clad, the metallic binder present in the skeleton structured carbides gets ploughed and plastically deformed that increases the μ value. Initially the high value of friction force is a result of ploughing of surface asperities. The μ value increases rapidly due to the increase in number of wear particles entrapped between the mating surfaces. The deformation of the asperities continues and the adhesion affect continues to increase due to larger clean interfacial areas. The entrapped wear particles between the surfaces cause ploughing and scratching. Since the relatively hard reinforcing carbides get dislodged, they penetrate both the surfaces and thus prevent slippage between the surfaces, hence resulting in maximum friction. As the sliding continues, the number of wear particles entrapped between the surfaces become equal to the number of particles leaving the interface. The contribution to friction force from adhesion remains constant while the delamination creates new surfaces with rough asperities. On further sliding, as the asperities get removed, a mirror like smooth surface is created. The asperities get deformed and the wear track gets smoothened, consequently the friction coefficient exhibits a reducing trend as the entrapped wear particles cannot anchor so easily a polished surface (Fig. 6.9). The value of the friction force is dependent on the phenomena of adhesion between the contacting surfaces.

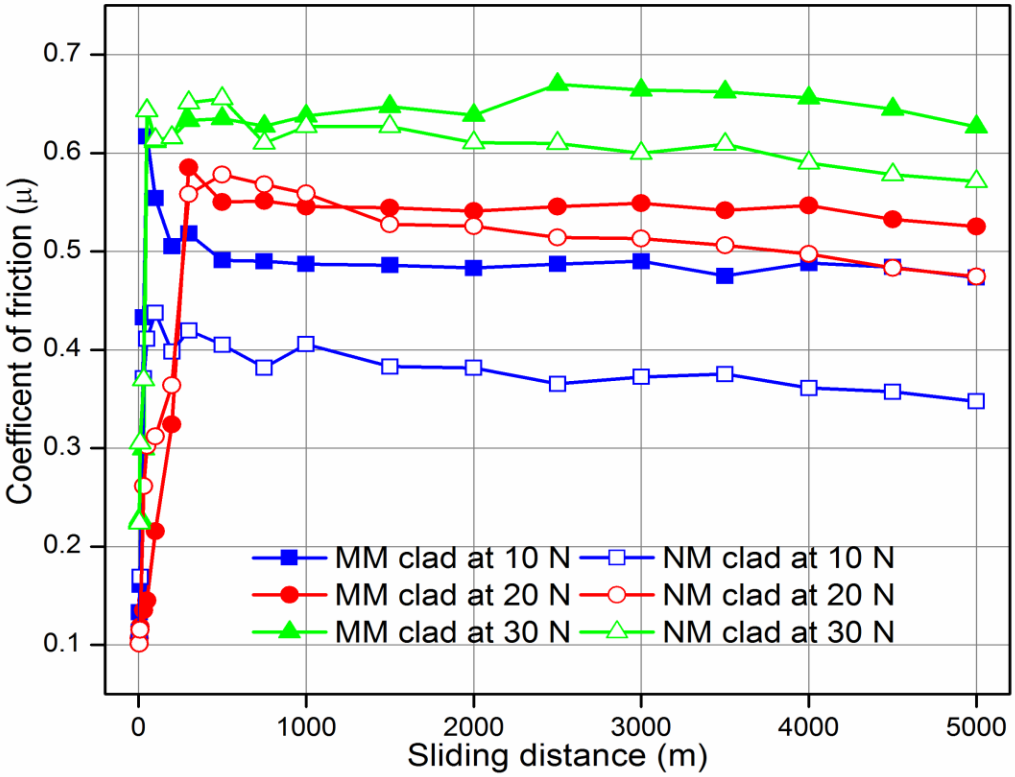

Fig. 6.9- Coefficient of friction of MM and NM clads as a function of normal load

At higher normal load, more frictional heat is generated between the contacting surfaces, owing to which the initial interface temperature rises rapidly. Hence, an unstable oxide film is formed which grows further and reaches a critical thickness. The presence of tribo-oxide film was confirmed by EDS at the marked location in Fig. 6.10 (a) and (b). The chemical analysis of the debris in the MM clad indicates significant amount of Fe, O, Cr and Ni with lean presence of C, Co and W. As the sliding continues, the developed oxide film gets smeared and the hard skeleton structured carbides continue to scratch the wear pin. Further, as the wear pin continues to rub against the counter disc along with the hard oxide debris, the skeleton structured reinforcement gets fractured. The fractured carbides tend to scratch the soft metallic matrix. In case of the NM clad, a continuous tribo-oxide film was not formed as shown in Fig. 6.10(c). The EDS analysis at location 'B' indicates the presence of W also (Fig. 6.10(d)). As the normal load was increased, the relatively ductile matrix got smeared. This caused the dislodgement of relatively hard WC-based carbide phases that caused abrasion on the MM clad surface. In case of the NM clad, the wear particles are made up aggregation of comparatively smaller fragments.

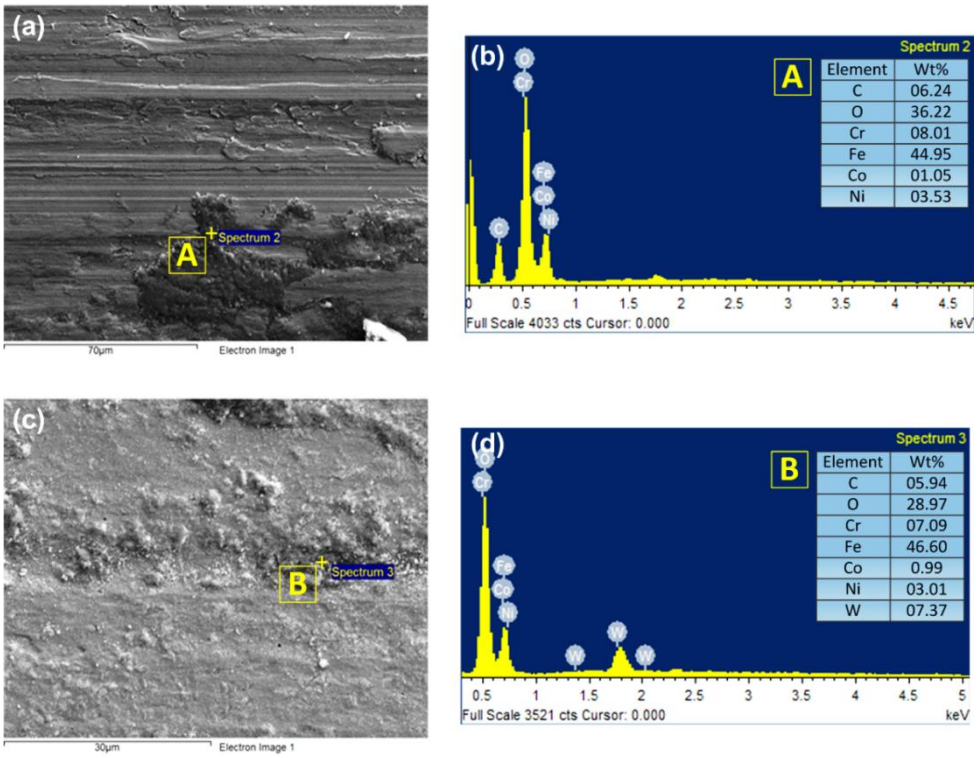

Fig. 6.10- (a) Typical SEM images worn of WC-12Co MM clad surfaces, (b) EDS spectrum at ' A', (c) typical SEM images worn of WC-12Co NM clad surfaces and (d) EDS spectrum at ' B', Load: 30 N

6.1.2.3. SEM analysis of the worn surfaces

In order to understand the wear mechanisms, the worn surfaces of the MM and NM WC-12Co microwave clad were analysed using SEM. Fig. 6.11 (a-c) and (d-f) illustrate the worn surfaces of the MM and NM WC-12Co microwave clads, respectively, at various normal loads. At low loads, mild wear in the form of adhesion and abrasion could be observed in MM microwave clad (Fig. 6.11(a)). Magnified view of the wear track in the inset shows the extrusion of the metallic binder (Inset: Fig. 6.11(a)). However, relatively smooth wear tracks and less material loss from the mating surfaces could be evidenced in NM WC-12Co microwave clad (Fig. 6.11(d)). Shallow wear grooves are indicative of low wear in the NM microwave clad (Inset: Fig 6.11(d)). At medium load (20 N), the worn surface of the MM clad exhibits evidence of carbide pullout. Carbide pullout can be confirmed by the presence of pits on the worn surfaces as shown in Fig. 6.11(b). Shallow pits are presented in the magnified view of the wear track in the inset in Fig. 6.11(b). In Fig. 6.11(e) it is evident that under identical loading conditions, NM microwave

suffered less material loss as revealed from the shallow wear tracks. The presence of the discontinuous ploughing marks, mild abrasion and microcutting could also be observed in Fig. 6.11(e). At higher load (30 N), material transfer occurs between the clad face and the counter surface. The SEM micrographs in Fig. 6.11(c) and (f) show the worn surfaces of the MM and NM microwave clad, respectively at a normal load of 30 N. It was observed that the MM WC-12Co microwave clad suffered severe material loss due to ploughing of the metallic matrix. Under high load, fragmentation of carbide grains occurs and the fractured grains act as abrasives and cause three-body abrasion. Severe ploughing of the MM clad results from extensive scratching by the fractured carbide grains and generation of large sized wear debris. De-bonded carbide particles also caused microcutting on the clad face (Inset: Fig. 6.11(c)). The wear grooves of the NM WC-12Co clad were observed to be shallow. Material loss took place due to plastic deformation and fatigue because of repeated action of the slider (Fig. 6.11(f)). Increased wear resistance of the NM WC-12Co microwave clad could be attributed to the presence of the clusters of nanocarbides which leads to higher hardness and enhanced reinforcement of the clad. Evidences of plastic deformation and delamination due to shear stress could also be observed from Fig. 6.11(f) (Inset). Plastic deformation occurs on the mating surfaces owing to severe sliding. The presence of grain boundaries, second phase particles causes obstructions to slipping which increases stress concentration (Chen et al., 2009). In the NM WC-12Co microwave clad, the radius of the stress field is similar to the radius of the reinforcing nanocarbides. Consequently, there is a uniform deformation, which results in low cracking and low material loss in the NM microwave clad. Hence, it can be concluded that the wear mechanisms of the MM and NM clad are quite different. Under high load, the binder in MM clads is selectively removed and then the applied normal load is transferred to the carbide grains causing fragmentation and pitting on the clad surface. However, the NM WC-12Co clad undergoes plastic deformation and wear on microscale, thus forming a smooth surface. Scratches exhibited on the worn surfaces of the NM clads are similar to that of a hard material. The uniformly distributed nanocarbides in the NM clad layer contribute effectively to reduce the removal of the ductile binder, hence decrease in material loss is observed in various loading conditions. Similar observations were reported earlier for WC-Co based coatings processed through other routes (Di Girolamo et al., 2013; Jia and Fischer, 1996; Stewart et al., 1999; Wang et al., 2012; Zhu et al., 2001).

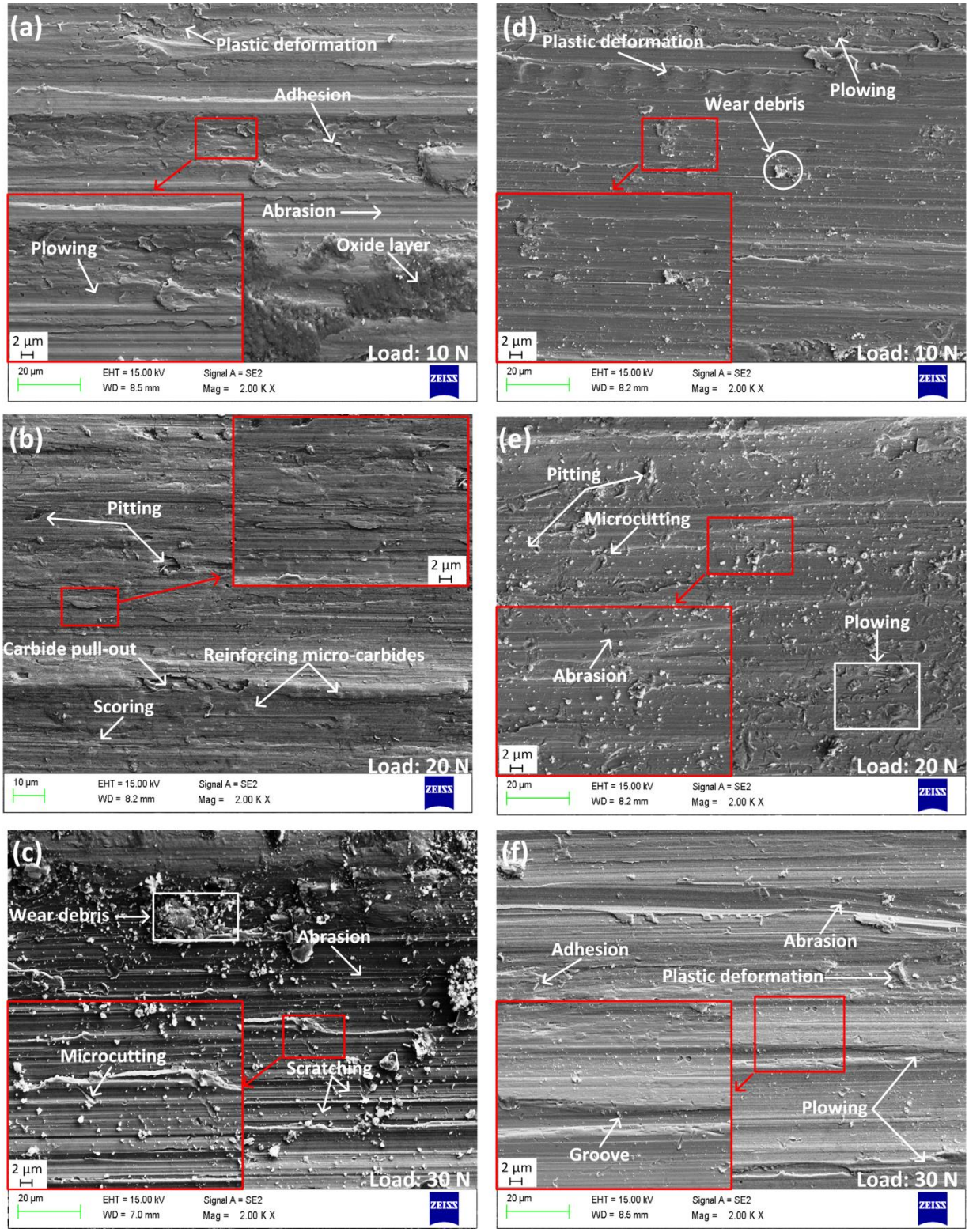

Fig. 6.11- Typical SEM micrographs of worn surfaces at various normal loads (a-c) MM microwave clad and (d-f) NM microwave clad

In order to analyse the wear process and understand the wear mechanisms of the WC-12Co MM and NM microwave clads, 3D surface profiles of the worn surfaces are presented in Fig. 6.12. The R_a values of the worn surfaces at various loads are summarised in Table 6.3. At low loads, shallow discontinuous grooves are evident on the worn surface of the MM WC-12Co microwave clad (Fig. 6.12 (a)). However, the NM clads exhibit a relatively smooth surface profile at the same load (Fig. 6.12 (b)). The R_a value of the NM clads was observed to be 1.83 times lower compared to the MM clads. At medium normal load (20 N), the grooves become continuous on the worn surface of the MM clad, however the NM clad exhibits shallow grooves. The R_a value of the NM clad was observed to be 0.68 times less than the MM clad at medium load (Table 6.3). At higher normal load, it was observed that the grooves on the MM worn surfaces become deep and continuous. However, the surface morphology of the NM clads was observed to be uniform as compared to the MM clads. At high normal loads, the MM clad asperity tip contacts exceed the plasticity limit of the material resulting in higher levels of plastic deformation of metallic matrix and sub-micron scale cracking of the WC phase due to fragmentation or grain pullout. It can be observed from Fig. 6.12 (c) and (f) that the occurrence of the grooves was reduced in the NM clad. This is attributed to higher average microhardness and better stability of the NM. The R_a values of the NM clad were reduced by 1.12 times as compared to the MM clad (Table 6.2).

Table 6.2- Observed R_a values at various normal loads

Load (N)	**R_a (µm)**		**Decrease for NM clad**
	MM	**NM**	
10	12.06	04.24	64.8%
20	17.11	10.14	40.7%
30	25.12	11.83	52.9%

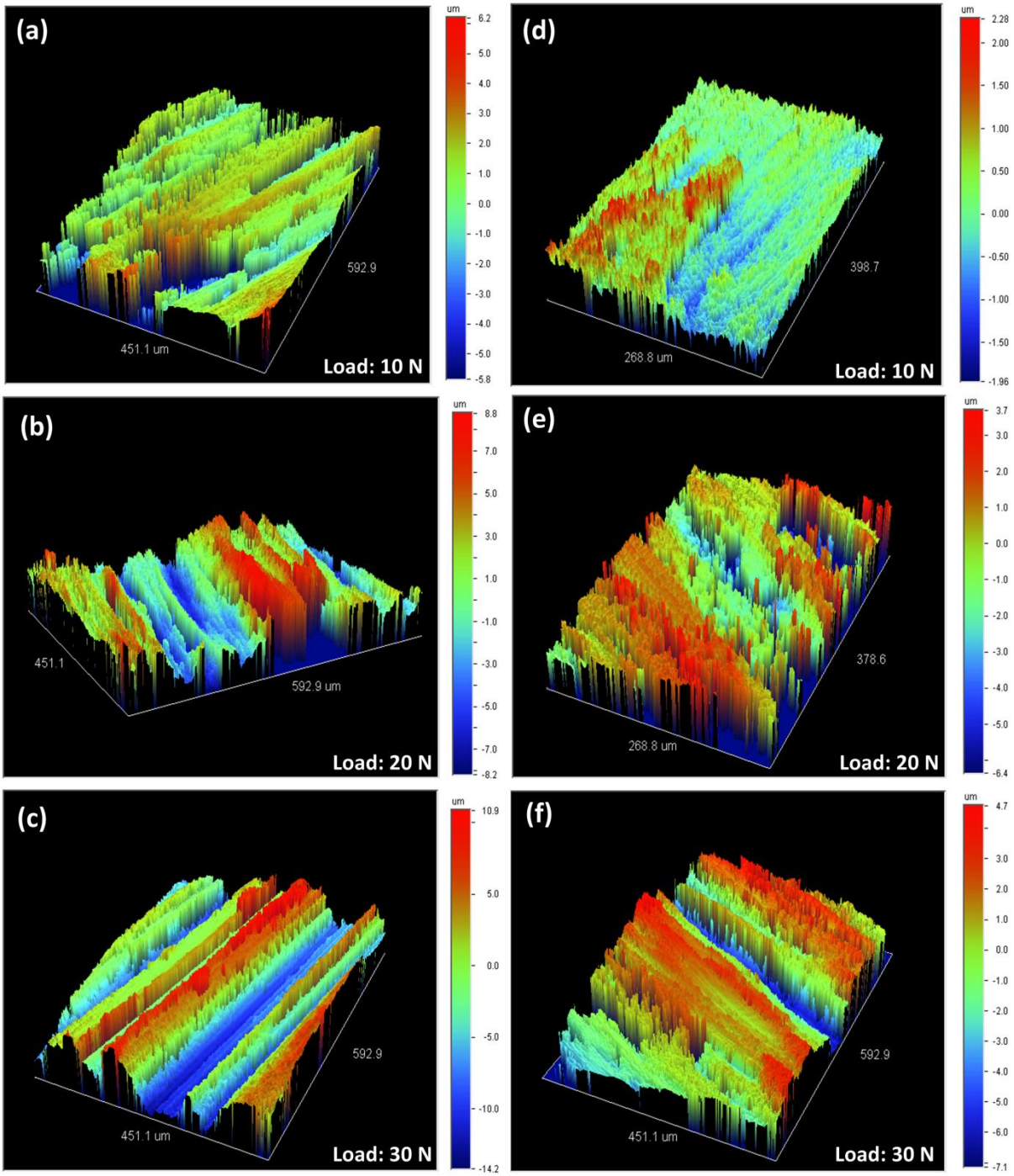

Fig. 6.12- 3D surface profiles of the worn surfaces: (a-c) MM microwave clad and (d-f) NM microwave clad

6.1.3. Prediction of tribological behaviour of MM and NM WC-12Co microwave clads through artificial neural network (ANN)

Artificial neural network (ANN) is a powerful computing algorithm that imitates the biological neuron network through a non-linear regression model. It is used to model and analyse and model complex non-linear processes. The ANN model is trained using the data; once trained, the network is able to identify, characterise and extract patterns within the data. A few ANN elements that influence the performance of the network are training function, input data, number of hidden layers and number of neurons. A well-trained network predicts the wear loss with reasonably good accuracy with the experimental data.

Accordingly, in the present work an ANN model has been developed to predict the wear rate and friction coefficient of the MM and NM WC-12Co microwave clads. While developing the ANN model, transfer function and number of neurons in the hidden layer were varied to optimise the ANN model. The size of the reinforcing carbide effects the wear performance of the clads, therefore the nature of reinforcement (conventional or nanostructured) was chosen as one of the input parameter for the ANN model. Further, sliding distance and normal load were also have been chosen as the input variables to the ANN network. Wear rate and coefficient of friction (μ) was then predicted using the optimised ANN model. The predicted values showed a good agreement with the experimental values. The ANN model was developed using MATLAB Neural Network toolbox (version: 7.10.0.499) on Dell XPS laptop powered by Core-i3 processor.

The neural network modelling of wear rate and friction coefficient of WC-12Co microwave clad needs an appropriate architecture of the neural network in order to represent a functional relation between the inputs and outputs of the network. A neural network consists of three layers of neurons, an input layer, a hidden layer and an output layer. The neurons of the networks are connected by weights. Each input to a neuron represents the output of a neuron from the previous layer. The input to the network must be scaled in the efficient working range of the network. The outputs are produced using data from the input layer and processing through the hidden layer, bias and the activation function. The output depends on the input variables and values of the weights. A general output (y) can be mathematically written as:

$$y = \varphi\left(\sum_{i=1}^{n} \omega_i x_i + b\right) \tag{6.1}$$

Here ω denotes the vector of weights, x is the vector of inputs, b is the bias and φ is the activation function. In the present ANN model, one of the most commonly used training algorithms, back propagation (BP), has been used owing to its reliability and simplicity (Cetinel, 2012; Zhang et al., 2003). The BP algorithm was originally developed using the gradient descent algorithm to train multi-layered neural networks. The popularity of BP algorithm is attributed to its advantages like ability to store patterns, acquire complex nonlinear mapping and parallel computing structured (Rashed and Mahmoud, 2009). The ANN network consists of an input layer, one hidden layer and an output layer. The input variables for the network were selected as nature of reinforcement (conventional or nanostructured), normal load and sliding distance. Conventional reinforcement refers to the presence of skeleton structured carbides in MM clads, while in NM it is the clusters of nanocarbides. The conventional and nanostructured reinforcement was coded as 1 and 2 respectively for the ANN model. The experimental data was collected systematically followed by a series of attempts to optimise the neural network. The ANN model was trained using Levenberg-Marquardt ('trainlm') training algorithm. The 'trainlm' training algorithm has the best performance when training is repeated on the same dataset. During training, the ANN model compares the predicted output and input data, and adjusts the 'weight' and 'bias' of the neurons to achieve close results. The adaptation process is dependent on the training algorithm of the ANN model. The developed model displayed minimum error in about 35 epochs. Epochs are the number of times the ANN model has adjusted to achieve close predicted results. The purpose of retaining the network is to teach the network the relation between the inputs and outputs and get the results with lowest possible error. The training process is computer intensive and involves searching an optimum nonlinear relationship between inputs and outputs. The transfer function and number of neurons in the hidden layer were chosen to optimise the neural network. The MATLAB ANN toolbox is equipped with three transfer functions: tan-sigmoid, log-sigmoid and pure linear. Pure linear function generates any numerical values ranging from integers, fractions etc., while the tan-sigmoid and log-sigmoid functions generate values between 0 and 1. A sigmoid is mathematical function having a 'S' shape. The log-sigmoid takes the any input value in between plus and minus infinity and gives output in the range of 0 to 1. The tan-sigmoid is bipolar sigmoid function whose output is in the range of -1 to +1. Both of these functions are trained using BP algorithm because part of these is differentiable. In the present work both, tan-sigmoid and log-sigmoid performed better

than the pure linear function. Accordingly, the tan-sigmoid and log-sigmoid were chosen to optimise the network architecture. Different configurations and number of neurons on the hidden layer provide different performance of the neural network. Therefore, in the present work the number of neurons in the hidden layer was also chosen as parameter to be optimised. The range of the values of the chosen network parameters are presented in Table 6.3. The model was trained and tested to predict the wear rate of the MM and NM WC-12Co microwave clads. A total of 600 data points were converted into MATLAB matrix files and were used to train the developed ANN model. The accuracy of the developed ANN model increases with retraining as the model adjusts itself for higher accuracy. Fig. 6.13 describes the procedure adopted in order to optimise the neural network architecture. The architecture of the ANN model is illustrated in Fig. 6.14. When the set of input patterns, and the set of desired output patterns are provided, the neural network is trained to compute the ideal patterns. The predictive performance of the neural networks was evaluated on the basis of mean square error (MSE). To avoid the over fitting problem, the model was validated using 60 data points which were independent of the training data.

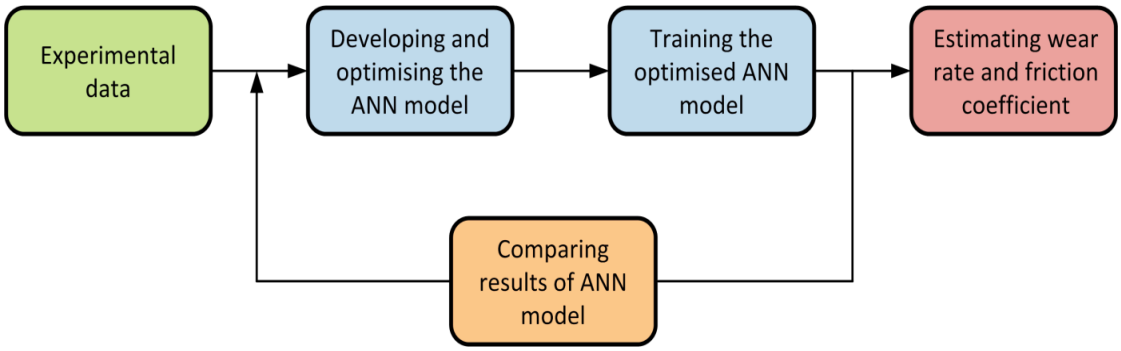

Fig. 6.13- Flow chart for developing the ANN model

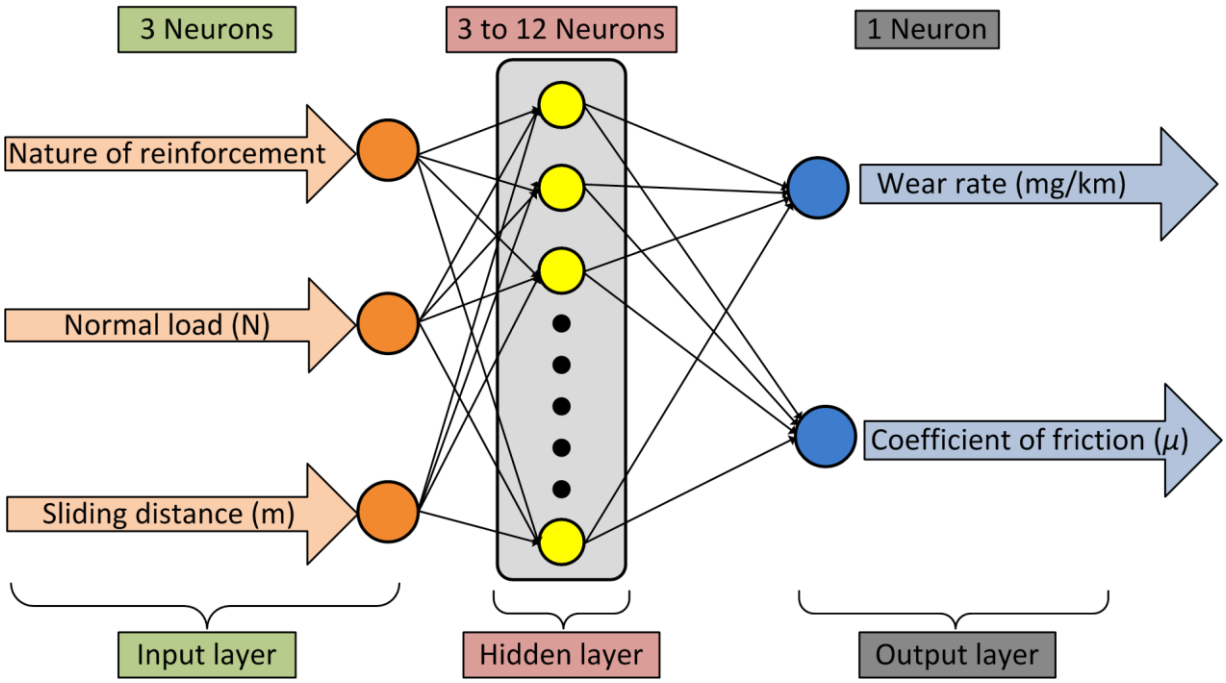

Fig. 6.14- Architecture of the developed ANN model

Table 6.3- Parametric details used for optimising the ANN model

Parameters	**Values**
Training algorithms	Levenberg-Marquardt (trainlm)
Transfer functions	tan-sigmoid and log-sigmoid
Number of neurons in the hidden layer	3 to 12
Maximum number of epochs	500

A number of architectures on the ANN were attempted and MSE were computed using two transfer functions (log-sigmoid and tan-sigmoid). Different architectures (3-[N]-1) provided different performances. Here '3' is the number of inputs, 'N' is the number of neurons in the hidden layer and '1' is the number of output of the ANN model. The number of neurons in the hidden layer was also varied. The ANN models were trained up to 500 epochs using the training data. The MSEs corresponding to different architectures of the network have been presented in Figure 4. It is observed that in the present work, as the number of neurons was increased the performance of the ANN model improved (Fig. 6.15). However, beyond eight neurons in the hidden layer, the MSE increased in case of both the transfer functions. As per the input data of the network, it seems eight neurons were sufficient to perform the computational task. It appears that for the given patterns,

more than eight neurons will tend to increase the neuron population without getting them involved in the computation; this creates an apparent idleness among the neuron population and their efficiency decreases, which is reflected in increase in MSE (Fig. 6.15). Hence it can be concluded that the ANN model with tan-sigmoid transfer function and architecture of 3-[8]-1 showed the best performance. Consequently, 3-[8]-1 tan-sigmoid ANN architecture was chosen to predict the wear rate of the WC-12Co MM and NM microwave clads. The accuracy of the selected ANN model was further improved through retraining.

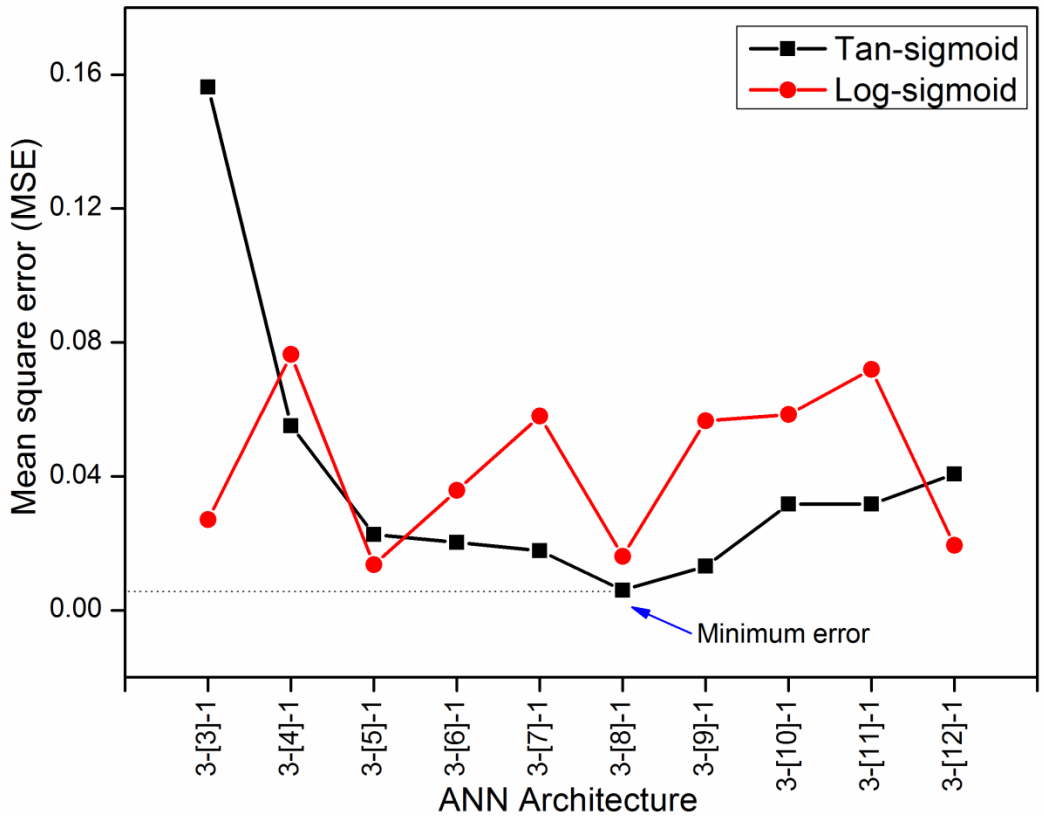

Fig. 6.15- Performance of the ANN model after 500 epochs

The predicted and experimental wear rates of MM and NM WC-12Co microwave clad are shown in Fig. 6.16. A good correlation between the experimental and the ANN predicted values under various loading conditions are illustrated by higher values of correlation coefficient (R^2) in Fig. 6.16. It was observed that during the initial run-in-wear period, both MM and NM clads exhibited high wear rate attributed to removal of the asperity peaks through shearing during which the mating surfaces achieve compatibility with each other. However, higher wear resistance of the NM clads compared to the MM

clads is observed. This is attributed to the higher volume fraction and nanostructured size of the reinforcing carbides in NM clads. This improved wear resistance is due to reduced abrasion and increased obstruction to crack propagation. Higher number of grain boundaries in NM microwave clad impedes the slip, which ultimately confines the crack propagation in the clad layer. However increased loads results increased pressure on the mating surfaces, which leads to higher material loss from the mating surfaces (Fig. 6.16 (a)and (b)). It can be observed that the ANN predicted values of wear rate follow the same trend as the experimental values for both MM and NM clads under various loading conditions. This can be confirmed as R^2 values of the experimental and predicted wear rate is fairly close to one in all the loading conditions Fig. 6.16 (a) and (b).

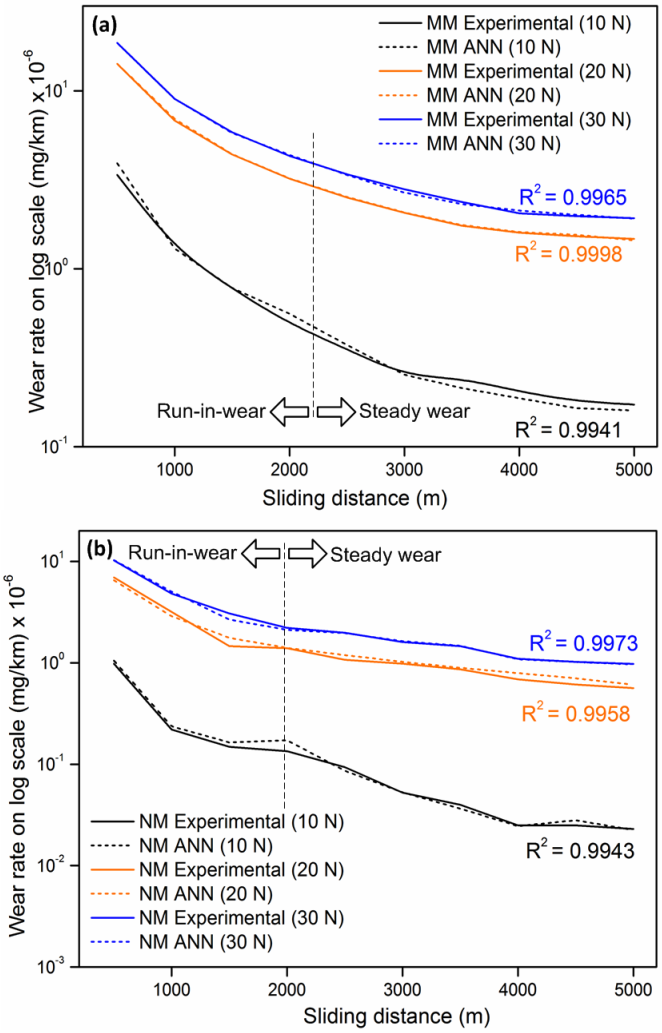

Fig. 6.16- Predictive and experimental wear rate results as a function of normal load for (a) MM and (b) NM WC-12Co microwave clads, ANN model: 3-[8]-1

The experimental and predicted coefficient of friction (μ) of the MM and NM WC-12Co microwave clads during sliding under various normal load values is shown in Fig. 6.17. It is observed that the NM microwave clad exhibited a lower value of μ as compared to the MM clad under various loading conditions. Presences of uniformly distributed nanocarbides in NM clad reduce the direct binder contact with the counter surface. In the MM clad, the metallic binder present in between the skeleton structured carbides gets ploughed and plastically deformed that increases the μ value. As the sliding continues, the wear track gets smoothen, consequently the friction coefficient exhibits a slight reducing trend (Fig. 6.17 (a), (b) and (c)). The ANN predicted values of μ for the MM and NM clads is in good agreement in with experimental values. This close agreement between the experimental and predicted values of wear rate and friction coefficient implies that the ANN model can be successfully used to predict the tribological properties of the MM and NM WC-12Co microwave clads. The ANN model can be used to predict the influence of the nature of reinforcement, normal load and sliding distance of the wear rate of the WC-12Co microwave clads.

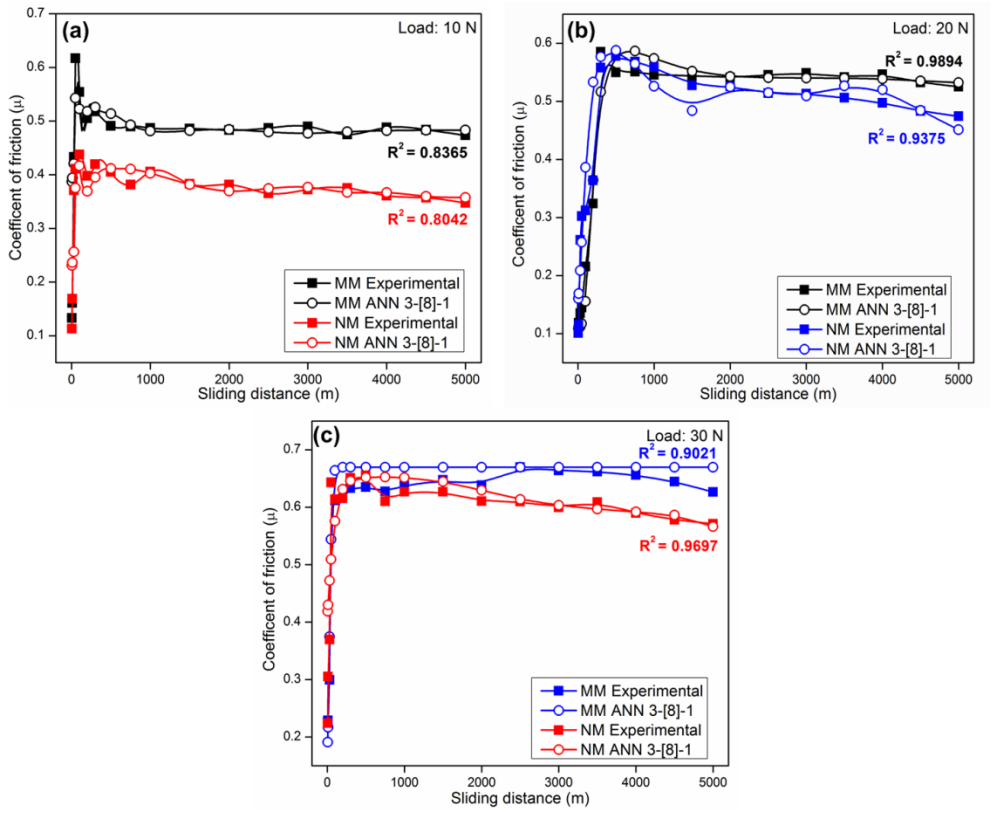

Fig. 6.17- Predictive and experimental coefficient of friction results as a function of normal load for MM and NM WC-12Co microwave clads at (a) 10 N, (b) 20 N and (c) 30 N, ANN model: 3-[8]-1

6.2. ABRASIVE WEAR

In abrasive wear, displacement of material is caused by the presence of hard particles present in between or embedded in one or both of the two surfaces in relative motion, or by the presence of hard protuberances on one or both of the relatively moving surfaces. Abrasive wear can occur in two types, two-body abrasive wear and three-body abrasive wear. Two-body abrasive wear is caused by hard protuberances on the counter surface, while in three-body abrasive wear hard particles are free to roll and slide between the two surfaces. Chutes, hydraulic systems with dirt, extruders, rock crushers, dies in powder metallurgy are some of the tribosystems in which abrasive wear is predominant. In three-body abrasion, abrasive particles act as interfacial elements between the solid body and counterbody. Worms of extruders processing plastics with enclosed abrasive fillers and jaw crushers are among those worn due to three-body abrasion. The magnitude of wear is smaller in three body abrasive wear test as compared to two-body abrasive wear test due to variation in angle of attack of the abrasives. Free rolling or sliding particles cause little wear loss (Zum Gahr, 1987).

6.2.1. Wear rate

The results of the abrasive wear test of the MM and NM WC-12Co microwave clads are presented in Fig. 6.18. The inset in Fig. 6.18 (a) schematically illustrates the approximate depth of abrasive wear with respect to the clad thickness. The depths of wear (in μm) were estimated as : 9.11 (at 30 N), 14.26 (at 60 N), 18.75 (at 90 N) and 4.01 (at 30 N), 6.35 (at 60 N) and 12.48 (90 N) for the MM and NM clads, respectively. In general, the cumulative weight loss of the NM clads was observed to be less than the MM clads (Fig. 6.18 (a)). The average cumulative weight loss of NM clads was reduced by approximately two times at 30 N and 60 N and by 1.4 times at 90 N. However, it was also observed that increased load results in higher material loss. The wear rate characteristics indicate that MM and NM WC-12Co clads exhibit high wear rate during the initial run-in period, after which the wear rate exhibits a reducing trend as shown in Fig. 6.18 (b). Clearly, there is an asymptotic trend, particularly beyond 2100 m of abrasion barring the characteristic of MM clad at 90 N load. This a known phenomenon in almost all classical wear cases that as the mating surfaces attain compatibility following the run-in-phase, the wear rate reduces. However, considering the severe interaction between the mating abradant and the clad

surface (30-90 N) and the presence of Co-based metallic matrix in the clad, possible effect of strain hardening of the clad was anticipated. The increased subsurface hardness of the clad (worn surfaces) indicates the same and perhaps can be correlated to have contributed towards the observed reduction in the wear rate. The abrasive wear resistance of the WC-Co cermets is given by the following relation (Wayne et al., 1990).

$$R \propto \frac{K_{IC}^{\frac{3}{8}} H^{\frac{1}{2}}}{D} \tag{6.2}$$

where, R is the abrasive wear resistance, K_{IC} and H are the fracture toughness and hardness of the cermet and D is the carbide grain size. Consequently, NM WC-12Co clads exhibit higher abrasive wear resistance as compared to the MM clads. The abrasive wear coefficient (k) for the MM and NM clads was calculated using Archard's Equation (equation 6.3). The computed values of the abrasive wear coefficient (k) corresponding to the applied load are shown in Table 6.4.

$$Q = \frac{kW}{H} \tag{6.3}$$

Here, Q is the wear rate, k is the abrasive wear coefficient, H is the indentation hardness of the material and W is the load applied. It can be observed from Table 6.4 that the abrasive wear coefficient of the NM clads is less than the MM clads under identical loading conditions. The trend can be attributed to the higher hardness of the cluster of nanocarbides as evidenced in the microstructure of the clads. Similar trends of wear were observed for thermally sprayed WC-Co coatings (Shipway and Hogg, 2005). Further, as the volume percent of the nanocarbides is relatively higher, the load gets distributed uniformly.

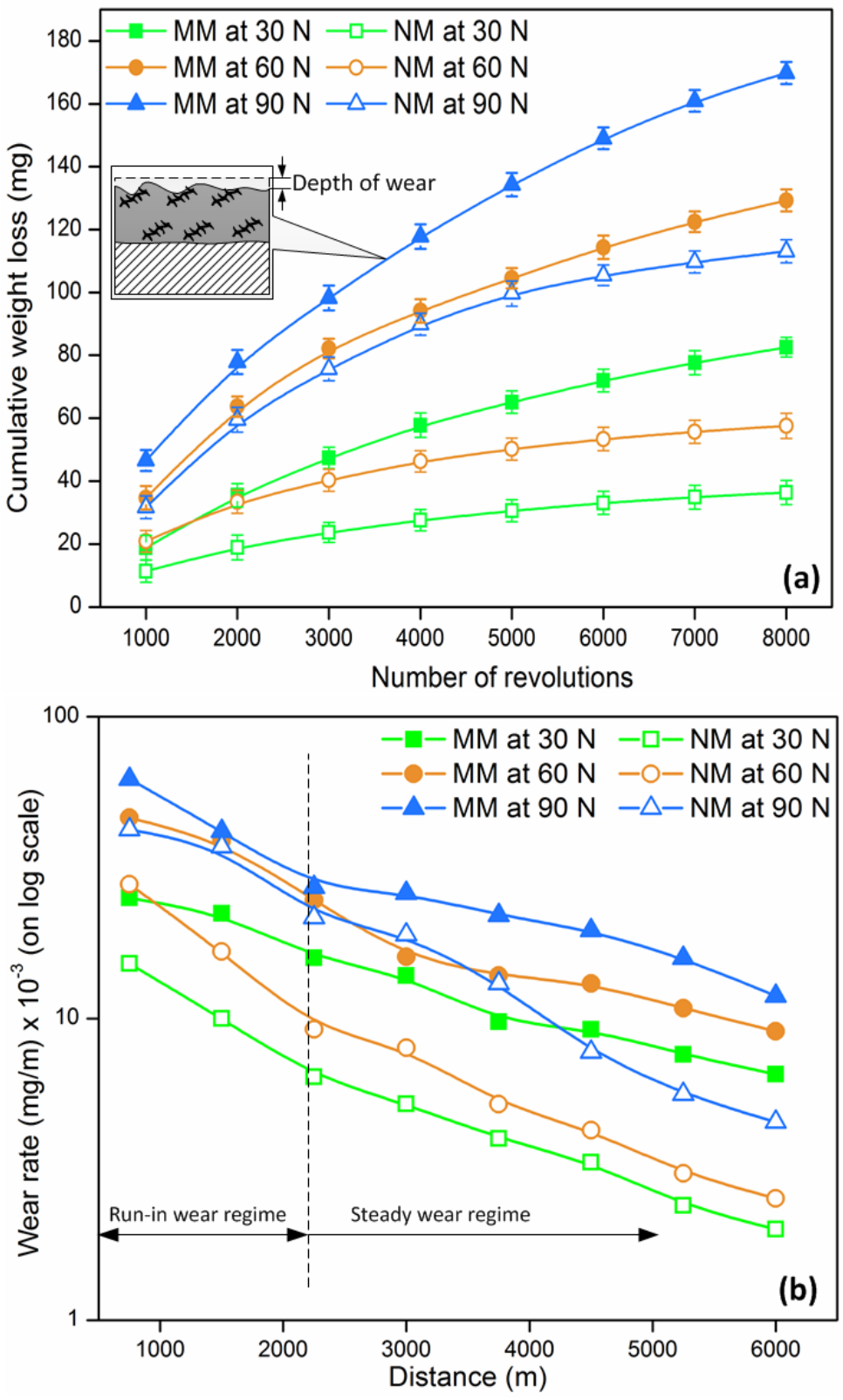

Fig. 6.18- Abrasive wear characteristics (a) cumulative weight loss, and (b) wear rate, Inset: schematic illustration of the depth of abrasive wear

Table 6.4- Abrasive wear coefficient (*k*) as a function of applied load

Load (N)	**Abrasive Wear coefficient (*k*)**	
	MM	NM
30	0.522	0.316
60	0.409	0.250
90	0.358	0.328

6.2.2. Analysis of worn surfaces through SEM

Typical SEM micrographs illustrating worn surfaces of the MM and NM WC-12Co microwave clads during three-body abrasion are illustrated in Fig. 6.19. Relative motion between the loose abradants and specimen surface produced scratches on the surface. At 30 N, the worn surfaces of the MM clad exhibits partial ploughing along with the continuous grooves (Fig. 6.19(a)). The ploughing of the relatively soft matrix displaces the material binding the reinforcing carbides thus causing carbide pullout. However, the worn surface of the NM clad exhibits discontinuous grooves along with signature of microcutting (Fig. 6.19(d)). This substantiates the reason of low material loss from the NM clads. At medium load of 60 N, continuous grooves along evidence of microcutting can be observed on the MM WC-12Co clads (Fig. 6.19(b)). However, the depth of the groove was reduced on the skeleton structured carbides as compared to areas devoid of carbide. On the other hand, discontinuous grooves were evident on the worn surface of NM clad even at 60 N (Fig. 6.19(e)). At 90 N, higher material loss from the MM clad can be substantiated due to severe carbide pullout, microcracking and microcutting as shown in Fig. 6.19(c). This can be attributed to the initiation and propagation of the cracks on the binder due cyclic load during the abrasive wear test. The worn surface of the NM clad exhibits mild scratching, ploughing and pitting, thus leading to low material loss (Fig. 6.19(f)). During the abrasive wear test, normal cyclic and tangential forces cause displacement of the reinforcing carbides. This displacement caused removal of the extruded binder between the carbide particles. Higher the mean free path, higher is the displacement of the binder matrix. Hence, removal of the binder matrix caused fracture or pullout of the carbides. Thus, it was observed that abrasive wear response of the clads can be correlated with the size and distribution of the reinforcing carbide phase.

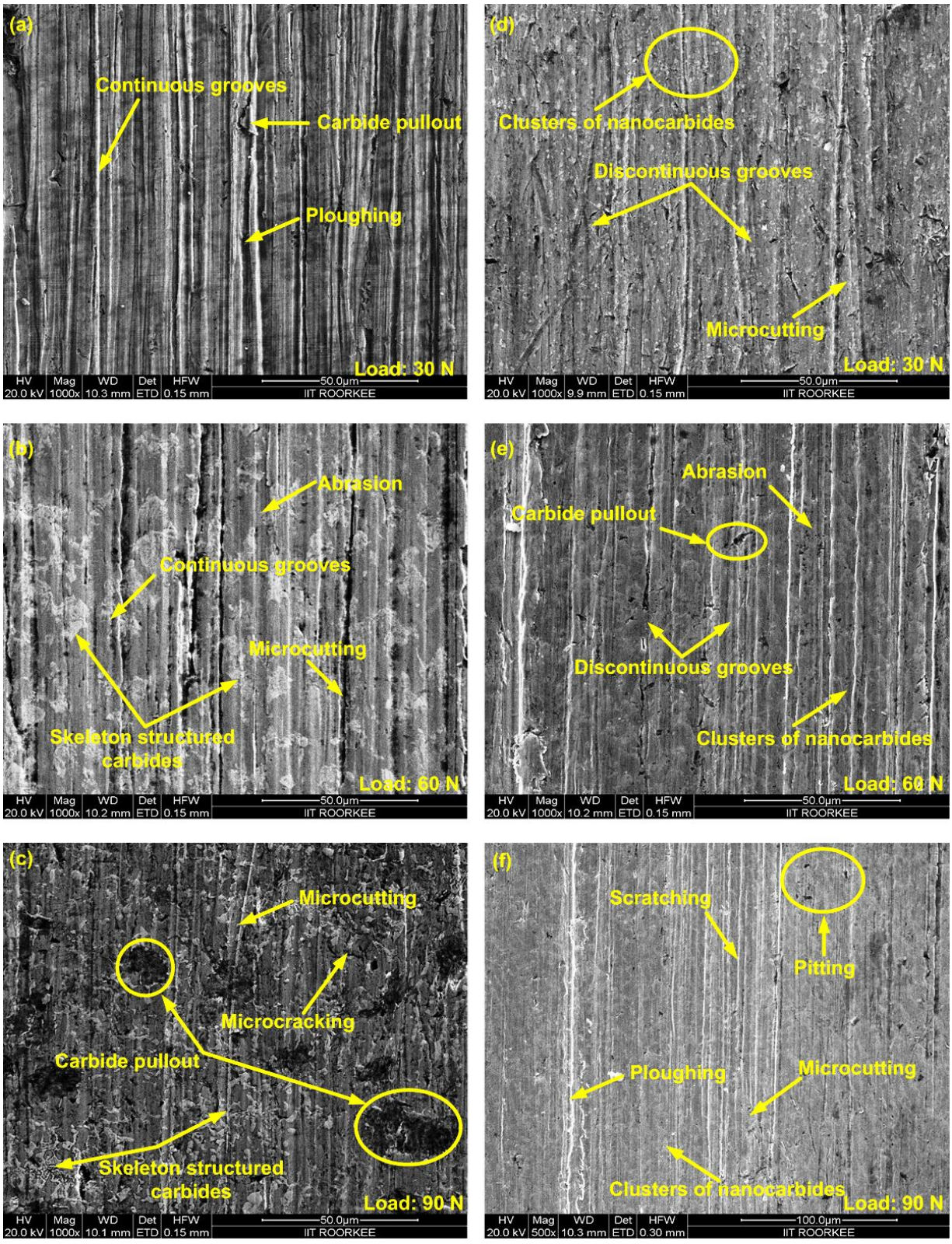

Fig. 6.19- Typical SEM micrographs of worn surfaces after abrasive wear test (a-c) MM and (d-f) NM WC-12Co

6.2.3. Mechanism of abrasive wear

Fig. 6.20 schematically illustrates the difference between the abrasive behaviour of the MM and NM WC-12Co clad on the basis of the size and distribution of the reinforcing carbide and the morphology of the grooves. Finely dispersed reinforcing carbides cause increase in the flow stress of the matrix that leads to enhanced wear resistance. Clusters of reinforcing nanocarbides reduce the interparticle spacing in the relatively soft matrix, leading to higher wear resistance. In MM clads, due to the reduced carbide volume fraction, the abradant preferentially causes wear on the relatively soft matrix. This exposes the relatively larger skeleton structured carbides to applied load, as the carbides are more vulnerable to fracture they fail, resulting in carbide pullout as evidenced in Fig. 6.19(c). On the other hand, higher volume fraction of the carbide in NM clads results in short mean free path, which contributes in enhancing the abrasive wear resistance.

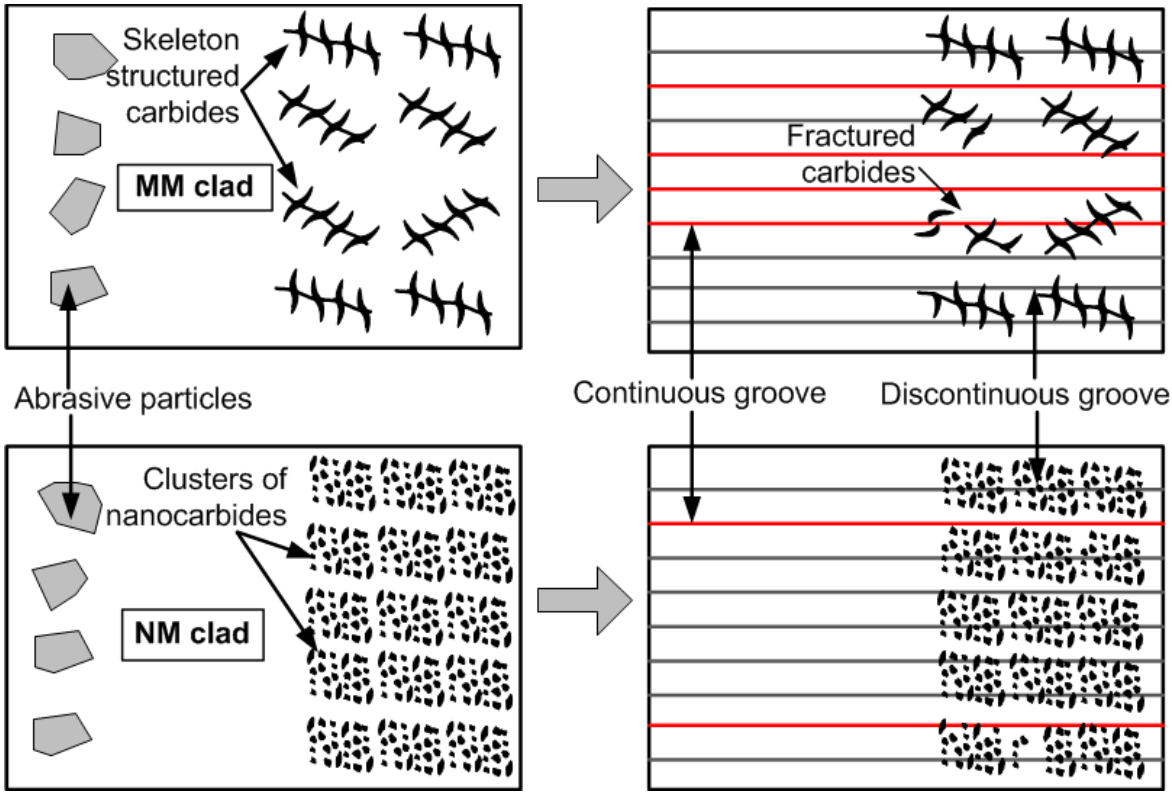

Fig. 6.20- Schematic representation of abrasive wear behaviour of the MM and NM WC-12Co microwave clads

6.2.4. Analysis of abrasive wear through subsurface

In order to understand the abrasive wear mechanisms of the MM and NM clads, cross-sections of the selected worn specimens were analysed using SEM. Strain hardening was quantified by evaluating the microhardness in the subsurface region of the worn specimens. Fig. 6.21 presents the cross-sections of the abraded specimens of MM and NM clads at 90 N. Well-defined grooves presented in Fig. 6.21(a) confirms microcutting of the clad surface by the abrasive particles. However, presence of matrix cracking revealed partially work hardened matrix and removal of the brittle carbides, which eventually contribute to high material loss due to abrasion. It was observed that during abrasion under high load, mostly removal of the binder matrix occurred. This led to the fracture and subsequent removal of carbide structure. Work hardening of the surface due to abrasive action of the abradant under influence of high load leads to development of radial cracks in the MM clad as shown in Fig. 6.21(a). As the surface of the specimen gets work hardened to some extent, its hardness and brittleness tend to increase. Consequently, on continued abrasion under high load, the skeleton carbide structure and the binder matrix get removed in large parts. However, presence of clusters of nanocarbides resulted in low free mean path, which led to higher hardness and low material loss. Presence of hairline subsurface cracks with no evidence of radial or lateral cracks was observed in the NM clads (Fig. 6.21(b)). This confirms that the presence of clusters of nanocarbides enhanced the abrasive wear resistance of the NM WC-12Co clads.

The subsurface hardness distributions on the abraded (at 90 N) MM and NM clad is illustrated in Fig. 6.22. It can be observed that the subsurface of MM and NM clad gets strain hardened during abrasion. This stain hardening tends to reduce the wear rate as the abrasion is continued as indicated in the abrasive wear rate characteristics in Fig. 6.18(b). The hardness across the depth of the subsurface was evaluated at load of 50 g. The hardness value at locations 20-30 μm beneath the subsurface layer appears to be a little higher compared to the hardness at other locations.

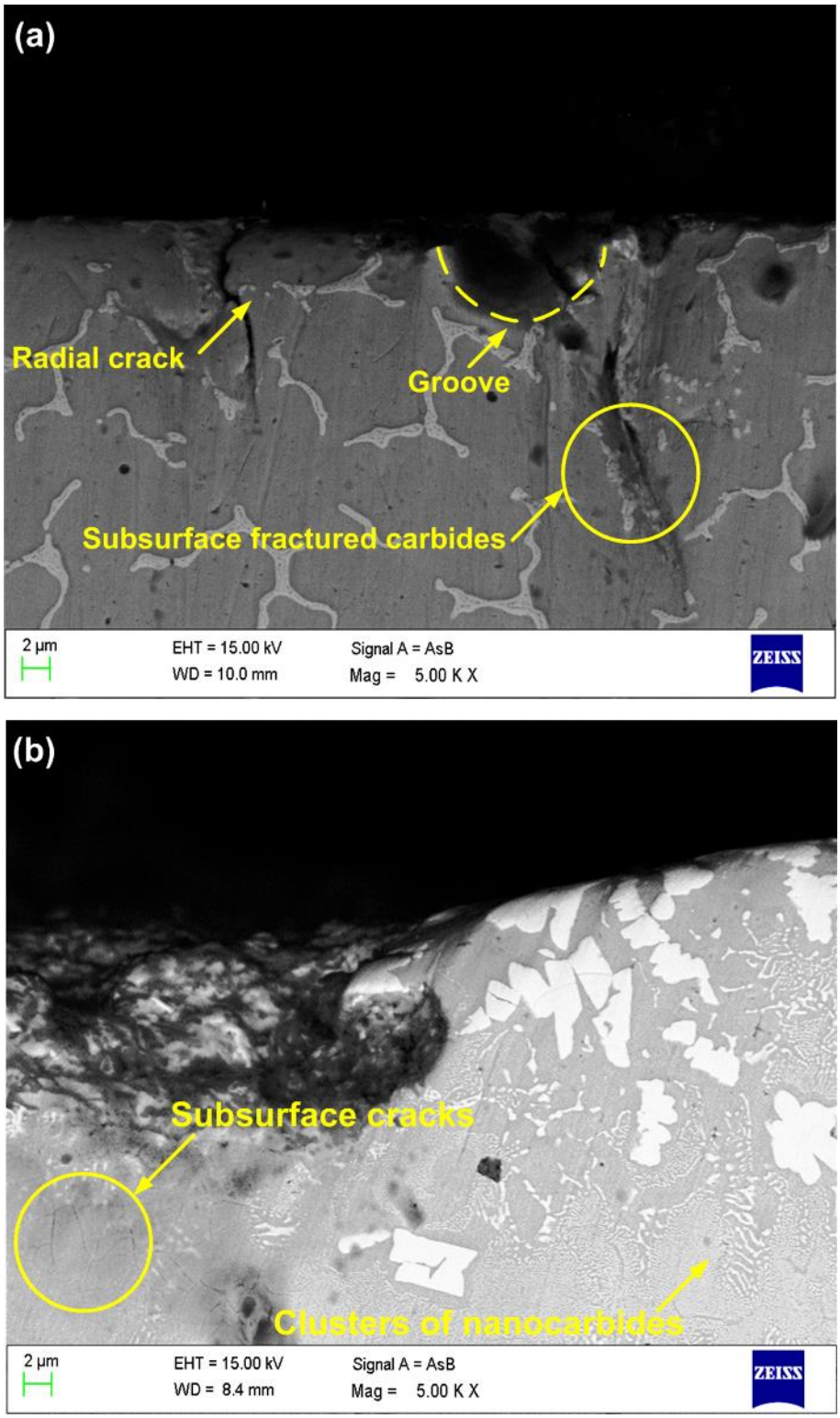

Fig. 6.21- Transverse section of (a) MM and (b) NM WC-12Co microwave clad after abrasive wear, normal load: 90 N

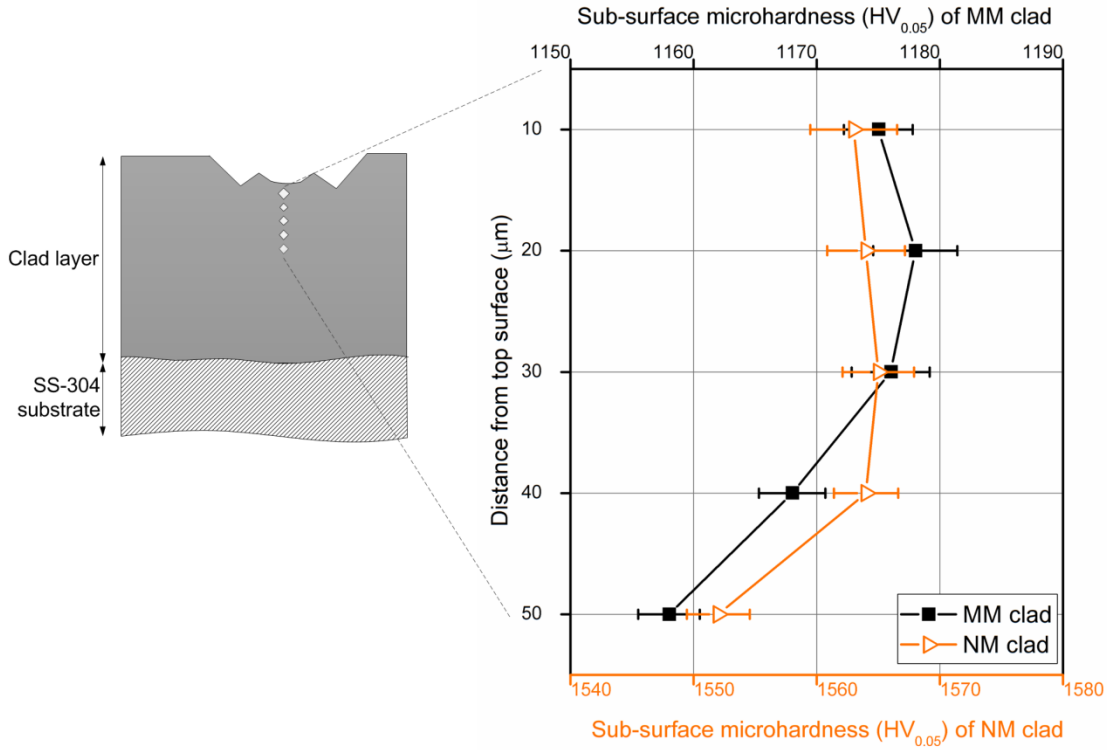

Fig. 6.22- Subsurface hardness distribution of the MM and NM WC-12Co microwave clads after abrasive wear test at 90 N

6.3. SOLID PARTICLE EROSIVE WEAR

Erosion is a result of simultaneous occurrence of a number of complex material removal phenomena. Therefore, identification and characterisation of these phenomena is a challenging task. In the present study, attempts were made to understand the response of the WC-12Co MM and NM microwave clads to solid particle erosion. Solid particle erosion is common in applications like helicopter rotor blades, wind turbines, power generation gas turbines as well as aircraft windshields, fuselage and engines etc.

6.3.1. Wear rate

Fig. 6.23(a) presents the cumulative weight loss of the clads with respect to exposure time, whereas variation in the erosion rate (mg/s) with testing time is plotted in Fig 6.23(b). Approximate depth of erosive wear with respect to the clad thickness is schematically illustrated in Fig. 6.23 (a, inset). It was observed that as the impact angle increased the material loss from both MM and NM clad increases. This can be attributed to

the dominant presence of hard and brittle WC phase in the clad; conventionally, such materials are known to exhibit maximum material loss due to erosion at normal incidence. However, it can also be observed that the NM clads exhibited superior erosive wear resistance as compared to the MM clads at various impact angles. At lower impact angles (30°), material loss mainly took place due to the cutting action of the erodent particles. But at a higher impact angle (90°), material loss in clads occurred due to plastic deformation of the binder matrix and fracture of the carbides. The depths of erosive wear (in μm) were observed as: 4.73 (at 30°), 5.37 (at 60°), 6.02 (at 90°) for MM clads and 1.28 (at 30°), 1.80 (at 60°) and 4.88 (90°) for the NM clads, respectively.

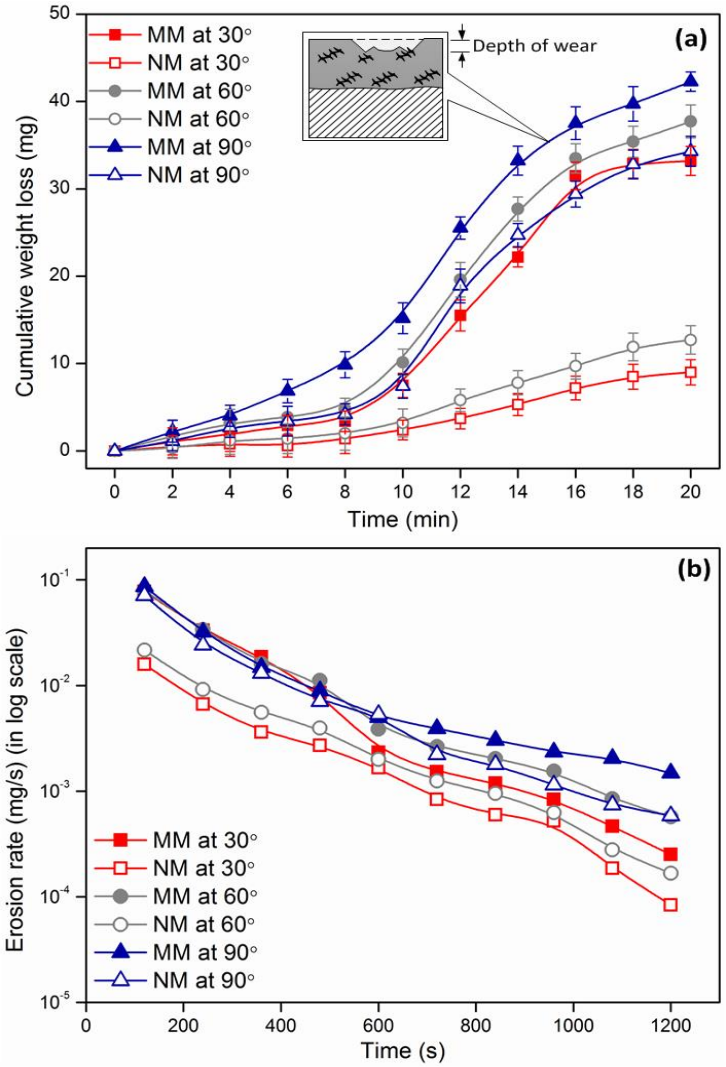

Fig. 6.23- Erosive wear characteristics: (a) cumulative weight loss and (b) wear rate. Inset: schematic illustration of the depth of erosive wear

The erosion rate of NM clads was reduced by 4.4, 3.3 and 1.25 times at 30°, 60° and 90° respectively. The severity of erosion in the MM and NM WC-12Co microwave clads was assessed using the erosion coefficient, ε. The erosion coefficient (ε) is defined as the ratio of the mass of the material removed to the mass of the erodent particles striking the surface. Fig. 6.24 illustrates the erosion coefficient (ε) of the MM and NM clads as a function of the impact angle. The NM clad exhibited lower erosion coefficient at various impact angles. This is attributed to the increased hardness, lower mean free path and higher carbide volume fraction in the NM clads.

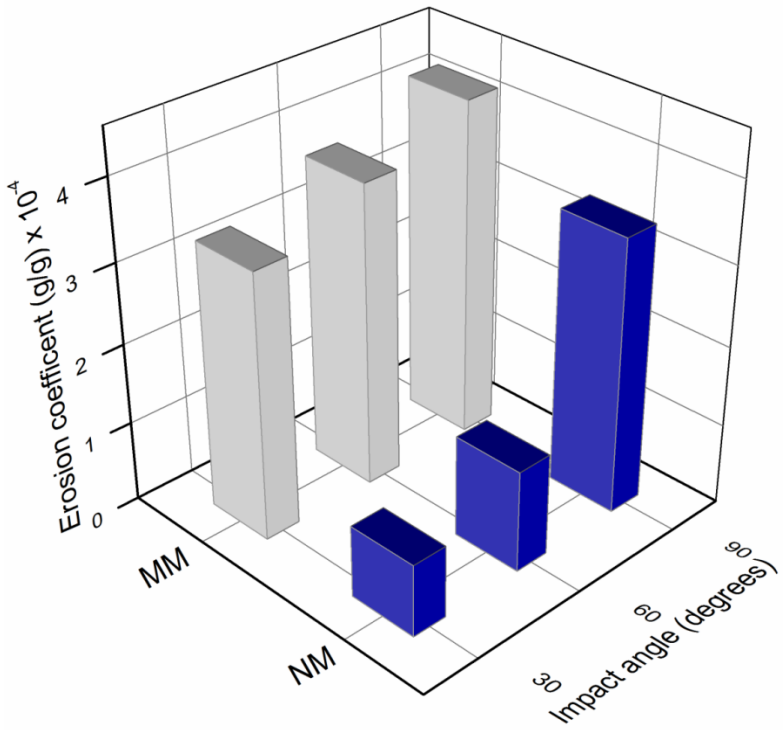

Fig. 6.24- Erosion coefficient of the MM and NM WC–12Co microwave clads as the function of impact angle

6.3.2. Erosion wear model

It was found that the impact angle and the time of erosion are the two significant parameters, which influence the amount of eroded material (weight loss). Accordingly, experimental data were used to develop a regression model to estimate the cumulative weight loss *(CWL)*. The *CWL* can be estimated as a function of erosion time (t) and impact angle (θ) as shown in equation 6.4.

$$CWL = f\ (t, \theta) \tag{6.4}$$

Considering the second order relationship, the equation 6.4 can be further written as equation 6.5.

$$CWL = A \times t + B \times \theta + C \times t^2 + D \times \theta^2 + E \times t \times \theta + F \tag{6.5}$$

where, A, B, C, D, E ,F are the coefficients to be determined. In order to establish the correlation between the solid particle erosion wear parameters, erosion time (t) and impact angle (θ) and the response i.e. cumulative weight loss (CWL), a second order regression model was developed using statistical software MINITAB (version 16.1.1). From the experimental data, 40% of the data was used to develop the model. The obtained regression equation is as follows:

$$CWL = -0.878288 + 0.481813 \times t - 3.30027 \times \theta + 0.0629089 \times t^2 + 0.422024 \times t \times \theta + 2.22558 \times \theta^2 \tag{6.6}$$

where, t is the erosion time in min and θ is the impact angle in radians.

The magnitude of the coefficients suggests the weightage of each predictor variables. From equation 6.6 it is observed that impact angle is major governing factor for the cumulative weight loss. This may be associated to the fact that as the impact angle approach orthogonal, the relative values of the normal components of the kinetic energy of the erodents get transferred to the target material. As the impact energy of the erodents exceeds the elastic strain energy of the clad layer, plastic deformation takes place. Penetration of the erodents leads to the developments of cracks and eventually loss of material. Low value of the coefficient for time of erosion indicates less effect on the cumulative weight loss of the specimens.

In order to examine the validity of the developed regression model, the remaining experimental values (60%) were compared with the predicted values. The predicted values are closely matching with the experimental values as shown in Fig. 6.25. A good fit of the developed regression model is substantiated by the high value of correlation coefficient (R^2= 0.9567) with a standard deviation of 3.34.

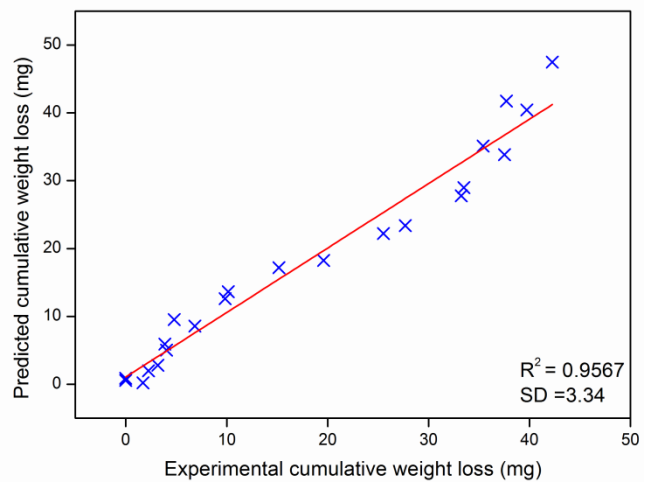

Fig. 6.25- Measured and regression predicted cumulative weight loss values

6.3.3. Analysis of worn surfaces through SEM

In order to understand the erosive wear mechanism of the MM and NM clads, the worn top surfaces of the clad were studied using SEM. Fig. 6.26 presents the worn top surfaces of the MM and NM clads at various impact angles. At low angle impact (30°), the vertical component of the kinetic energy caused the erodents to penetrate the clad surface, while the horizontal component of the kinetic energy caused the erodent to plough and cut the surface. Several ploughing marks can be observed on the worn surface of MM clad in Fig. 6.26(a). The erodent cause cutting and ploughing of the relatively soft binder matrix around the skeleton structured carbides. This caused carbide pullout leading to material loss. However, occurrence of microcutting and ploughing was reduced in the case of the NM clads (Fig. 6.26(d)), owing to the lower mean free path due to higher carbide fraction in the clads. The vertical component of the kinetic energy caused fracture of the carbides and contributed to the erosion. At an impact angle of 60°, the vertical component of the kinetic energy caused more material removal due to cracking, carbide fracture and plastic deformation of the matrix (Fig. 6.26(b)). On the other hand, it was observed that cracking of the carbide was suppressed in the NM clads (Fig. 6.26(e)). This can be attributed to low mean free path and higher hardness of the NM clads. At normal impact (90°), formation of platelets on the binder matrix is evidenced in the MM clad as shown in Fig. 6.26(c) and (f). Formation of platelets is a result of the combined action of plastic deformation and fatigue phenomena due to repeated impact of the erodents. Lip formation at the craters indicates strain hardening of the binder matrix. Removal of the binder and fracture of the carbides

resulted in material loss due to brittle mode. However, cracking was suppressed in the NM clads owing to the presence of nanocarbides having a low mean free path. Thus, a change in the material removal mechanism was observed as the impact angle changes from acute to normal.

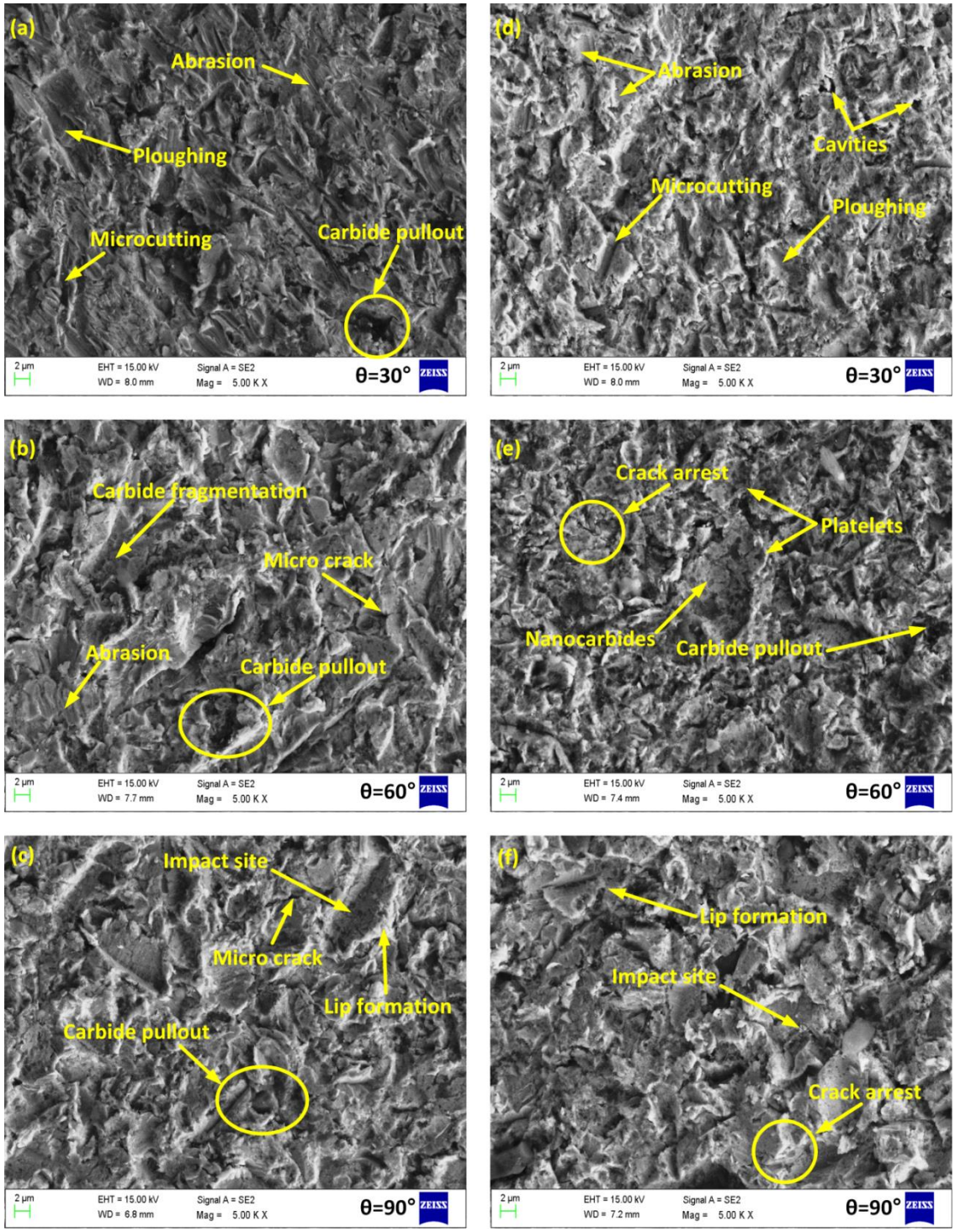

Fig. 6.26- Typical SEM micrographs of worn surfaces after erosive wear test: (a–c) MM and (d–f) NM WC–12Co clad

6.3.4. Mechanism of erosive wear

Further, even though the mechanism of material loss was brittle fracture of the carbide structure, but material around the point of contact of the impact site was plastically deformed. The extent of material removal due to impacting particles was more severe when the direction of the erodents was normal to the surface as shown in the erosive wear characteristics in Fig. 6.23. Hence, the mechanism of material loss due to erosive wear test at 90° can be explained by a series of events as schematically illustrated in Fig. 6.27. It was observed that during orthogonal impact, the carbide structure fractured due to the impact of the high speed erodents. Repetitive impact leads to plastic deformation and localised work hardening of the binder matrix. Continued impact caused removal of fractured carbide particles, which further exposes the relatively soft binder matrix to the erodents. In MM clads, removal of the binder matrix took place due to the plastic deformation of the exposed surface. The cracks propagated in the binder matrix due to higher free mean path in the MM clad. This caused material loss as illustrated in Fig. 6.27. However, low mean free path and higher carbide fraction in the NM clads suppressed further cracking. Hence, NM clad exhibit higher erosive wear resistance under normal impact angle.

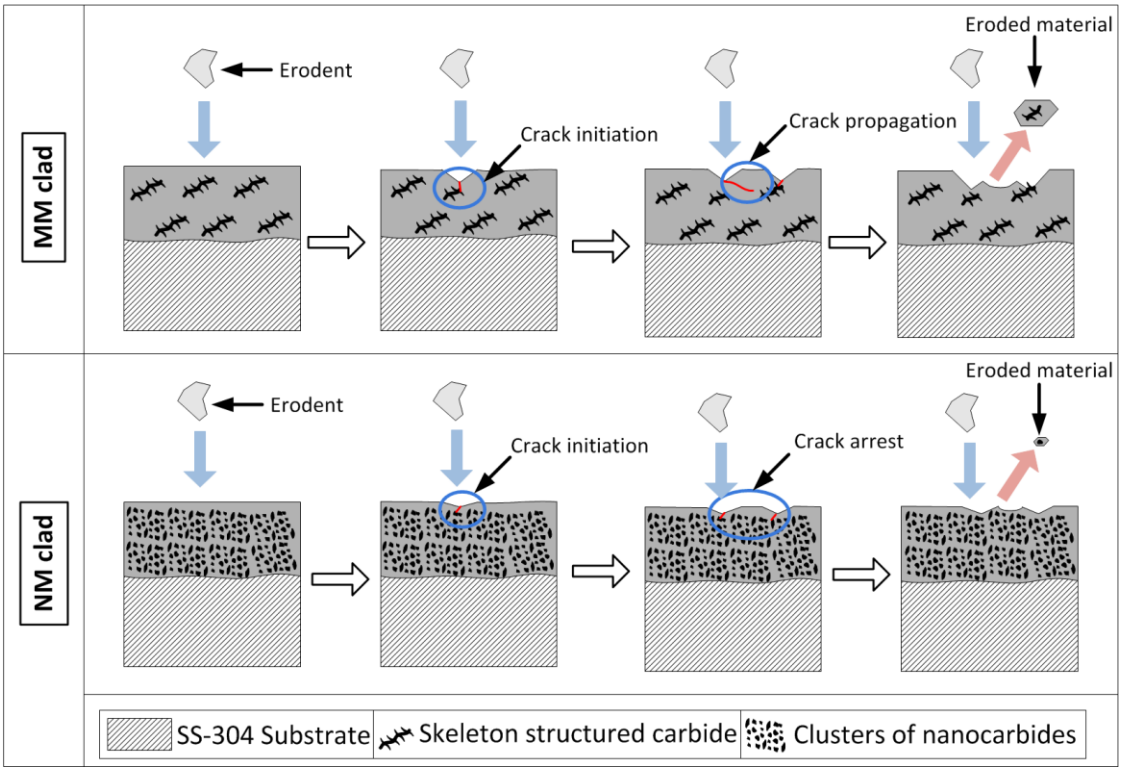

Fig. 6.27- Schematic representation of material removal mechanism during erosive wear in MM and NM WC–12Co microwave clads at normal impact

6.3.5. Analysis of erosive wear through the subsurface

In erosion, the erodents make single dynamic contact with specimen surface and partially transfer their kinetic energy onto the surface. Typical transverse sections of MM and NM WC-12Co microwave clad after erosive wear test (20 mins) are shown in Fig. 6.28. The clad surfaces get work-hardened due to repetitive impacts of the erodent. As the stress increased beyond the critical value, the removal of material takes place due to fatigue phenomenon. Formation of lateral and radial cracks occurred in the subsurface of the material that led to material loss due to the intersection of these cracks. Several cracks parallel to the clad surface could also be observed in the skeleton structured carbides in the MM clads. Highly localised stresses in the work hardened subsurface layer also lead to splitting of skeleton structured carbides. Consequently, fractured carbides can be identified in the cross-section of the MM clad as shown in Fig. 6.28(a). However, in the NM clad, a uniformly distributed network of the nano carbides tends to arrest crack propagation. The extent of material removal can also be approximated by the size of the impact site in the MM and NM clad. Crack arrest due the presence of more uniformly distributed nanocarbides can be identified in the NM clad as shown in Fig. 6.28(b). This can be correlated with lower free mean path due to the higher carbide volume fraction in the NM clads. Onset of platelet formation and flaking can also be identified in both MM and NM clads.

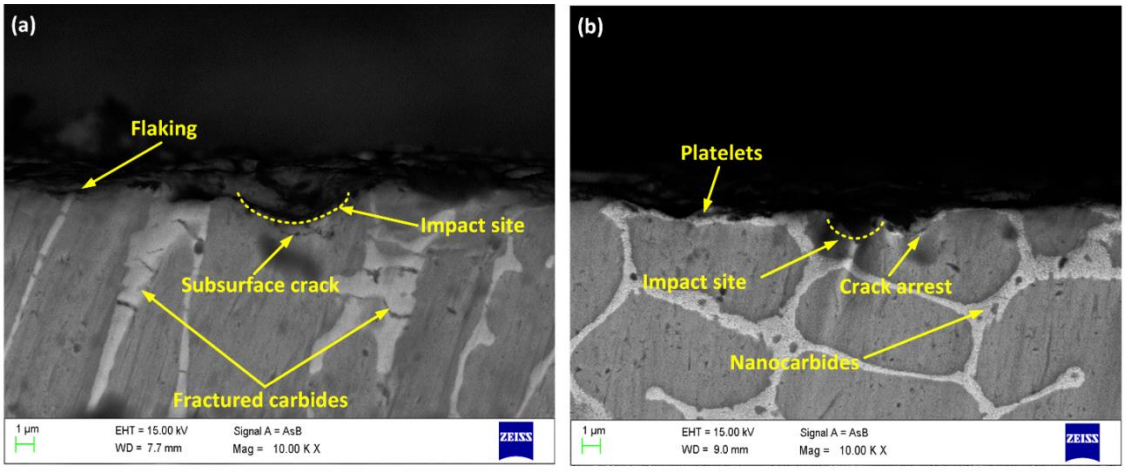

Fig. 6.28- Transverse section of (a) MM and (b) NM WC–12Co microwave clad after erosive wear (impact angle: 90°)

The hardness across the depth of the subsurface was evaluated at load of 50 g. The hardness value 20-30 µm beneath the subsurface layer appears to be a little higher as compared to the hardness at other locations (Fig. 6.29). This is attributed to the possible work-hardening of the eroded surface due to plastic deformation caused by repetitive impact of the erodents. The indentations on the matrix were considered to ascertain possible work hardening, rather than the indentations on the carbides.

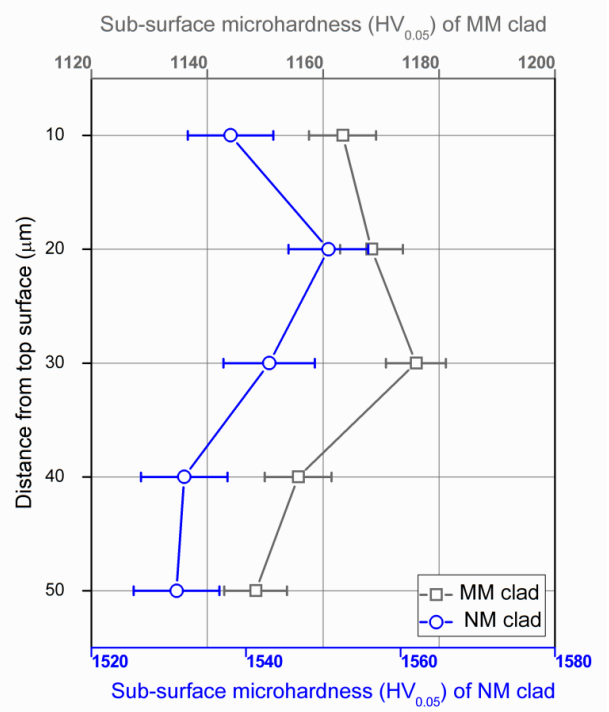

Fig. 6.29- Subsurface hardness distribution of the MM and NM WC–12Co microwave clads after erosive wear test at 90°

6.4. SUMMARY

The tribological aspects of MM and NM WC-12Co microwave clads were discussed with suitable illustrations. The wear rate of the MM clads was reduced by 67% compared to the SS-304 substrate for a sliding distance of 1000 m. The mechanisms of material removal were studied on worn surfaces of MM WC-12Co clads and SS-304 substrate. For a sliding distance of 5000 m, the average mass loss of NM clad was 54% less as compared with the MM clad. This was attributed to uniform distribution of the nanocarbides in the NM clad layer, which lead to increased hardness. The abrasive and erosive wear mass loss for NM clads was reduced to 0.6 times and 0.3 times, respectively.

Mechanisms of abrasive and erosive wear for MM and NM clads have discussed were found to be extrusion of binder and carbide fracture, respectively. Details on subsurface wear analysis have also been presented.

CHAPTER 7
CONCLUSIONS AND SCOPE FOR FUTURE WORK

Developing wear resistant surfaces through microwave cladding on bulk metallic substrates is a challenging task as metals reflect microwaves at room temperature. A state-of-the-art literature review indicates that nanomaterials offer improved mechanical and tribological properties of the engineered surfaces. However, application of nanomaterials to develop wear resistant surfaces using microwaves has not been attempted. In the present work, WC-12Co powder in micrometric and nanometric sizes were used to develop approximately 1 mm thick clads on austenitic stainless steel (SS-304) using microwave cladding technique. The microwave clads were characterised and compared in terms of metallurgical, mechanical and tribological aspects. Finite element (FE) study through COMSOL Multiphysics software was explored to investigate the principles of microwave cladding process. The following sections conclude the major findings and summarise the contributions of the present work; scopes for future work have also been indicated.

7.1. CONCLUSIONS

7.1.1. General conclusions

1. It is possible to develop nanometric clads on bulk metallic substrates using microwave energy at 2.45 GHz.
2. Materials, such as ceramics, whose loss tangent is low at room temperature, require hybrid heating to elevate the temperature beyond its critical temperature, so as to increase the loss tangent. The materials then get directly heated (coupled) with microwave radiation and consequently get melted.
3. The increase in the loss tangent is also closely related to the increase in the skin depth, which is a critical parameter to achieve microwave coupling of materials.
4. Lower values of microwave power and exposure time are required to develop the nanometric WC-12Co based clads compared to the micrometric clads owing to the higher surface area and better microwave absorption of the nanometric powder.
5. The development of nanometric clads needs less power (1.1 kW) and less exposure time (510 s), compared to the micrometric clads (1.4 kW and 600 s, respectively).

6. A thin interfacing layer of the substrate (10-15 μm) also gets melted at the powder-substrate interface. The localised convective currents in the melt pool resulted in dilution of the substrate and interdiffusion of the elements across the interface.
7. The microwave clads are free from interfacial and solidification cracking owing to the volumetric heating and low thermal gradient during microwave cladding.
8. The average porosity in the microwave clads was less than 1% in both the clads.

7.1.2. Simulation of microwave cladding

1. The simulated results largely agree with the experimentally obtained temperature data.
2. The temperature of the clad layer is well higher than the temperature of the susceptor layer, which is in agreement with the inverse heating phenomena associated with microwave heating.
3. The microwave energy gets concentrated at the corners of the hybrid heating arrangement due to the formation of hot spots.
4. The electric field distribution in the applicator cavity is non-uniform, but higher electric field intensity occurs within the clad layer. This implies that the electric field component has major influence on the heating of the WC-12Co clad powder.
5. The distribution of the resistive losses is the maximum in the clad layer. This confirms that the clad layer gets heated up due to the incident microwave radiation subsequent to the pre-heating through the conventional modes up to the critical temperature.
6. The non-uniform distribution of the resistive losses leads to inverse thermal gradient in the molten clad layer. This inverse thermal gradient leads to the occurrence of convective currents in the clad layer, which results in the formation of wavy interface.

7.1.3. Characterisation of the clads

1. Microwave clads are characterised by partial diffusion of the substrate owing to localised currents in the melt-pool. Clads are developed due to metallurgical bonding of the overlay clad powder with partial melting of the substrate interface layer.

2. The intermetallic carbides such as WC, W_2C, Co_6W_6C, Co_7W_6 and $Co_3W_9C_4$ were formed during the clad formation. The Co_6W_6C phase, which contributes to higher wear resistance, is higher in the NM clad compared to the MM clad.
3. The microstructure of the MM WC–12Co microwave clads consists of skeleton structured carbides distributed in the metallic matrix, while the microstructure of the NM WC–12Co consists of uniformly distributed clusters of nanocarbides in the clad layer.
4. The nanocarbides were uniformly distributed in the clad layer in the form of clusters of carbide. However, some carbide particles got diluted in the substrate that caused increased microhardness in the proximity of the interface.
5. The carbide volume fraction in the NM clads was about 48% higher compared to the MM clad.
6. The average Vickers's microhardness of the NM clad (1564±53 HV) was about 1.37 times the microhardness of the MM clad (1138±90 HV). The higher microhardness of the NM WC–12Co microwave clad is attributed the presence of uniformly distributed nanocarbides and increased carbide volume fraction in the clad layer.
7. The average flexural strength of the MM clad was of 587±22 MPa, while the flexural strength of the NM clad is approximately 1.14 times higher (671±28 MPa) than the MM clad. The NM clad exhibited more ductile deformation during flexural loading.
8. The deformation index (DI) of the NM clad is nearly six times higher than the MM clad. The clad DI is a good indicator of the flexural properties; higher DI indicates more ductile-like deformation characteristics.
9. The flexural loading in the MM clads caused cracking of the skeleton, while the matrix underwent ductile shear deformation.
10. The matrix of the NM clads exhibits ductile tear ridges, while the uniformly distributed nanocarbides restricted the crack propagation. This enabled the NM clad layer to withstand higher fracture loads.
11. The nature of residual stresses was compressive for both, MM and NM clads. The magnitude of residual stresses in NM clad was approximately 1.68 times higher than the MM clads.
12. The higher residual compressive stresses influence the flexural properties of the microwave clad; the flexural strength increases with the magnitude of the residual stresses in the clad layer.

7.1.4. Tribological characteristics of the clads

1. The MM WC-12Co microwave clads exhibits an approximately 67% lower wear rate than the SS-304 substrate under various loading conditions.
2. In WC-12Co microwave clads, wear occurs mainly due to pullout of the carbide phases from the metallic matrix and extrusion of the binder as the normal load increases. Strong adhesion, abrasion and severe plastic deformation are the main causes of material loss in the case of SS-304 substrate.
3. The friction coefficient of the WC-12Co clad rises rapidly during the first 200 m and then gets stabilized beyond 400 m. The friction coefficient was reduced by 56% for the MM WC-12Co microwave clad compared to the SS-304 substrate under various loading conditions.
4. The low friction coefficient in WC-12Co clads is due to the high hardness and burnishing action during the wear process. The relatively higher value of friction coefficient in SS-304 is due to rupture and regeneration phenomena of the tribo-oxide layer on the surface.
5. The wear debris of WC-12Co microwave clad was observed to be in the form of small agglomerated particles enriched in Fe and O, indicating better stability of the clads, whereas irregular flake-shaped wear debris were produced in the case of SS-304 substrate.
6. The NM WC–12Co microwave clad exhibits higher wear resistance than the MM clads. The average weight loss for the NM microwave clad is 54% less compared to the MM microwave clad.
7. The enhanced sliding wear resistance of the NM microwave clads is attributed to the uniform distribution of the nanocarbides and enhanced microhardness of the clad layer.
8. The MM clads suffer removal of the binder and fragmentation of the carbide grain during sliding; while the NM clads undergo plastic deformation on microscale.
9. Fragmented and pulled out carbides in the MM clad act as the third body leading to a three-body abrasion. The nanocarbides in NM clads, on the other hand, remain well distributed in the matrix that results in reduced abrasion.
10. Higher load bearing ability of the nanocarbides in the NM clads reduces crushing of carbides.

11. The abrasive wear of NM clad is approximately 1.6 times less compared to the MM clad. Uniformly distributed nanocarbides increase the flow stress, hence the wear resistance of the NM clads gets enhanced.
12. Material removal in abrasive wear took place due to the extrusion of the binder that leads to fracture or pullout of the carbides. The presence of clusters of nanocarbides in the NM clads results in a low free mean path, which leads to higher hardness and low wear.
13. Material loss due to erosive wear was approximately one third for the NM clad compared to the MM clad. This is attributed to the low mean binder path and higher carbide volume fraction in the NM clads.
14. At low impact angles, material gets removed by microcutting of the relatively soft binder, followed by the loosening and carbide pullout. However, at high impact angles, material loss took place due to fatigue induced carbide fracture as a result of repetitive impacts of the erodents.
15. Removal of the matrix through flaking, carbide fracture and pullout were the main wear mechanisms during erosive wear. However, the presence of clusters of nanocarbides having a low mean free path effectively arrests cracking, which contributes to reduced wear.

7.2. MAJOR CONTRIBUTIONS OF THE PRESENT WORK

1. Microwave cladding of nanomaterials on bulk metallic substrates at 2.45 GHz has been successfully demonstrated.
2. Structure-property correlations in MM and NM clad have been explained through various metallurgical, mechanical and tribological evaluations.
3. Contributed to the knowledge repository of microwave cladding in terms of simulation data, experimental data, wear mechanism of micrometric and nanometric clads.

7.3. SCOPE FOR FUTURE WORK

The present investigation opens up several opportunities for future work. Some of the scopes can be summarised as follows:

1. Cladding trials can be carried out in single mode applicator and results can be compared with that of the multimode applicator.

2. Trials can be carried out at higher available frequency, such as 30 GHz and higher power (such as 3.0 and 6.0 kW), and results can be compared.
3. Simulation studies can be attempted with more realistic assumptions, such as dynamic changes in the properties of the material during exposure.
4. Material variations in terms of the substrate as well as the overlay can be explored.

REFERENCES

[1] Acierno, D., Barba, A.A., D'Amore, M., 2004. Heat transfer phenomena during processing materials with microwave energy. Heat Mass Transf. 40, 413–420.

[2] Agrawal, D., 2010. Latest global developments in microwave materials processing. Mater. Res. Innov. 14, 3–8.

[3] Ahmed, R., Hadfield, M., 1997. Experimental measurement of the residual stress field within thermally sprayed rolling elements. Wear 209, 84–95.

[4] Aliofkhazraei, M., 2011. Nanocoatings: Size Effect in Nanostructured Films. Springer-Verlag Berlin Heidelberg. Berlin, Germany.

[5] Almen, J.O., 1950. Mechanical Wear, in: Burwell, J.T. (Ed.), American Society for Metals. pp. 229–288.

[6] Al-Mutairi, S., Hashmi, M.S.J., Yilbas, B.S., Stokes, J., 2015. Microstructural characterization of HVOF/plasma thermal spray of micro/nano WC–12%Co powders. Surf. Coat. Technol. 264, 175–186.

[7] Alpert, Y., Jerby, E., 1999. Coupled thermal-electromagnetic model for microwave heating of temprature-dependent dielectric media. IEEE Trans. Plasma Sci. 27, 555–562.

[8] Andersson, J., Erck, R.A., Erdemir, A., 2003. Friction of diamond-like carbon films in different atmospheres. Wear 254, 1070–1075.

[9] Arabi Jeshvaghani, R., Shamanian, M., Jaberzadeh, M., 2011. Enhancement of wear resistance of ductile iron surface alloyed by stellite 6. Mater. Des. 32, 2028–2033.

[10] Aravindan, S., Ramkumar, J., Krishnamurthy, R., 2000. Microwave joining of Al_2O_3 and SiC with glass interlayer. Microwave, Theory and Application in Materials Processing, V Second World Congress on Microwave and Radio Frequency Processing Ceramic Transactions, 3, 289–294.

[11] Aravindan, S., Krishnamurthy, R., 1999. Joining of ceramic composites by microwave heating. Mater. Lett. 38, 245–249.

[12] Axen, N., Jacobson, S., 1994, A model for the abrasive wear resistance of multiphase materials, Wear 174, 187–199.

[13] Ayappa, K.G., Davis, H.T., Crapiste, G., Davis, E.A., Gordon, J., 1991. Microwave heating: an evaluation of power formulations. Chem. Eng. Sci. 46, 1005–1016.

[14] Babutina, T.E., Uvarova, I. V., Konchakovskaya, L.D., Kuz'menko, L.N., Kuz, L.N., 2004. Theory, production technology, and properties of powders and fibers preparation of hard alloy WC and WC−Co mixtures with reduction and carbidizing treatment of oxidized tungsten containing scrap. Powder Metall. Met. Ceram. 43, 111–116.

[15] Bajpai, P.K., Singh, I., Madaan, J., 2012. Joining of natural fiber reinforced composites using microwave energy: Experimental and finite element study. Mater. Des. 35, 596–602.

[16] Bansal, A., Sharma, A.K., Kumar, P., Das, S., 2014. Characterization of bulk stainless steel joints developed through microwave hybrid heating. Mater. Charact. 91, 34–41.

[17] Bansal, A., Sharma, A.K., Kumar, P., Das, S., 2015. Structure–property correlations in microwave joining of Inconel 718. JOM 67, 2087–2098.

[18] Bartkowski, D., Młynarczak, A., Piasecki, A., Dudziak, B., Gościański, M., Bartkowska, A., 2015. Microstructure, microhardness and corrosion resistance of Stellite-6 coatings reinforced with WC particles using laser cladding. Opt. Laser Technol. 68, 191–201.

[19] Bendeich, P., Alam, N., Brandt, M., Carr, D., Short, K., Blevins, R., Curfs, C., Kirstein, O., Atkinson, G., Holden, T., Rogge, R., 2006. Residual stress measurements in laser clad repaired low pressure turbine blades for the power industry. Mater. Sci. Eng. A 437, 70–74.

[20] Beste, U., Hammerström, L., Engqvist, H., Rimlinger, S., Jacobson, S., 2001. Particle erosion of cemented carbides with low Co content, Wear 250, 809–817.

[21] Bhushan, B., 1999. Principles and Applications in Tribology. John Wiley and Sons, New York, U.S.A.

[22] Bilecka, I., Niederberger, M., 2010. Microwave chemistry for inorganic nanomaterials synthesis. Nanoscale 2, 1358–1374.

[23] Blau, P.J. (Ed.), 1992. ASM Handbook Volume 18: Friction, Lubrication, and Wear Technology. ASM International, U.S.A.

[24] Blau, P.J., 1997. Fifty years of research on the wear of metals. Tribol. Int. 30, 321–331.

[25] Boccaccini, A.R., Veronesi, P., Leonelli, C., 2001. Microwave processing of glass matrix composites containing controlled isolated porosity. J. Eur. Ceram. Soc. 21, 1073–1080.

[26] Bonny, K., Baets, P. De, Perez, Y., Vleugels, J., Lauwers, B., 2010. Friction and wear characteristics of WC–Co cemented carbides in dry reciprocating sliding contact. Wear 268, 1504–1517.

[27] Borneman, K.L., Saylor, M.D., 2008. Microwave process for forming a coating. US20080138533 A1.

[28] Bowden, F.P., Tabor, D., 2001. Friction and Lubrication of Solids, Oxford University Press. New York, U.S.A.

[29] Breval, E., Cheng, J.P., Agrawal, D.K., Gigl, P., Dennis, M., Roy, R., Papworth, A. J., 2005. Comparison between microwave and conventional sintering of WC/Co composites. Mater. Sci. Eng. A 391, 285–295.

[30] Brosnan, K.H., Messing, G.L., Agrawal, D.K., 2003. Microwave sintering of alumina at 2.45 GHz. J. Am. Ceram. Soc. 12, 1307–1312.

[31] Buchelnikov, V.D., Louzguine-Luzgin, D.V., Anzulevich, A.P., Bychkov, I.V., Yoshikawa, N., Sato, M., Inoue, A., 2008. Modeling of microwave heating of metallic powders. Phys. B Condens. Matter 403, 4053–4058.

[32] Burnell-Gray, J.S., Datta, P.K. (Eds.), 1996. Surface Engineering Casebook: Solutions to Corrosion and Wear-related Failures. Woodhead Publishing Limited, Cambridge, U.K.

[33] Buytoz, S., Ulutan, M., Yildirim, M.M., 2005. Dry sliding wear behavior of TIG welding clad WC composite coatings. Appl. Surf. Sci. 252, 1313–1323.

[34] Cammarota, G.P., Casagrande, A., Poli, G., Veronesi, P., 2009. Ni–Al–Ti coatings obtained by microwave assisted SHS: Effect of annealing on microstructural and mechanical properties. Surf. Coat. Technol. 203, 1429–1437.

[35] Carton, J.-F., Vannes, A.-B., Vincent, L., 1995. Basis of a coating choice methodology in fretting. Wear 185, 47–57.

[36] Cetinel, H., 2012. The artificial neural network based prediction of friction properties of Al_2O_3-TiO_2 coatings. Ind. Lubr. Tribol. 64, 288–293.

[37] Chandrakanth, R.G., Rajkumar, K., Aravindan, S., 2009. Fabrication of copper–TiC–graphite hybrid metal matrix composites through microwave processing. Int. J. Adv. Manuf. Technol. 48, 645–653.

[38] Chaudhry, V., Kailas, S.V., 2015. Damage mechanisms in stainless steel and chromium carbide coatings under controlled environment fretting conditions, Wear 334, 75–81.

[39] Chelliah, N., Kailas, S.V., 2009. Synergy between tribo-oxidation and strain rate response on governing the dry sliding wear behavior of titanium,Wear 266, 704–712.

[40] Chen, H., Gou, G., Tu, M., Liu, Y., 2009. Research on the friction and wear behavior at elevated temperature of plasma-sprayed nanostructured WC-Co coatings. J. Mater. Eng. Perform. 19, 1–6.

[41] Chen, H., Xu, C., Zhou, Q., Hutchings, I.M., Shipway, P.H., Liu, J., 2005. Micro-scale abrasive wear behaviour of HVOF sprayed and laser-remelted conventional and nanostructured WC–Co coatings. Wear 258, 333–338.

[42] Cheng, F.T., Lo, K.H., Man, H.C., 2003. NiTi cladding on stainless steel by TIG

surfacing process. Surf. Coat. Technol. 172, 308–315.

[43] Cheng, J., Agrawal, D., Zhang, Y., Roy, R., 2001. Microwave reactive sintering to fully transparent aluminum oxynitride (ALON) ceramics. J. Mater. Sci. Lett. 20, 77–79.

[44] Chiu, K.Y., Cheng, F.T., Man, H.C., 2005. A preliminary study of cladding steel with NiTi by microwave-assisted brazing. Mater. Sci. Eng. A 407, 273–281.

[45] Cho, T.Y., Yoon, J.H., Kim, K.S., Song, K.O., Joo, Y.K., Fang, W., Zhang, S.H., Youn, S.J., Chun, H.G., Hwang, S.Y., 2008. A study on HVOF coatings of micron and nano WC–Co powders. Surf. Coat. Technol. 202, 5556–5559.

[46] Clark, D.E., Folz, D.C., West, J.K., 2000. Processing materials with microwave energy. Mater. Sci. Eng. A 287, 153–158.

[47] Clark, D.E., Sutton, W.H., 1996. Microwave processing. Annu. Rev. Mater. Sci. 26, 299–331.

[48] Clemens, J., Saltielt, C., 1996. Numerical modeling of materials processing in microwave furnaces. Int. J. Heat Mass Transf. 39, 1665–1675.

[49] Cullity, B.D., Stock, S.R., 2001. Elements of X-Ray Diffraction, 3rd ed. Prentice Hall. Massachusetts, U.S.A.

[50] Cverna, F. (Ed.), 2002. ASM ready reference: Thermal properties of metals. ASM International, U.S.A.

[51] D'Oliveira, A.S.C., Vilar, R., Feder, C., 2002. High temperature behaviour of plasma transferred arc and laser Co-based alloy coatings. Appl. Surf. Sci. 201, 154–160.

[52] Das, S., Mukhopadhyay, A.K., Datta, S., Basu, D., 2010. Evaluation of microwave processed glass–ceramic coating on nimonic superalloy substrate. Ceram. Int. 36, 1125–1130.

[53] Das, S., Mukhopadhyay, A.K., Datta, S., Das, G.C., Basu, D., 2008. Hard glass-ceramic coating by microwave processing. J. Eur. Ceram. Soc. 28, 729–738.

[54] Demirskyi, D., Ragulya, A., Agrawal, D., 2011. Initial stage sintering of binderless tungsten carbide powder under microwave radiation. Ceram. Int. 37, 505–512.

[55] Deng, H., Shi, H., Tsuruoka, S., 2010. Influence of coating thickness and temperature on mechanical properties of steel deposited with Co-based alloy hardfacing coating. Surf. Coat. Technol. 204, 3927–3934.

[56] Deuis, R.L., Subramanian, C., 2000. Dry sliding wear behaviour at ambient and elevated temperatures of plasma transferred arc deposited aluminium composite coatings. Mater. Sci. Technol. 16, 209–219.

[57] Deuis, R.L., Yellup, J.M., Subramanian, C., 1998. Metal-matrix composite coatings by PTA surfacing. Compos. Sci. Technol. 58, 299–309.

[58] Di Girolamo, G., Marra, F., Pilloni, L., Pulci, G., Tirillò, J., Valente, T., 2013. Microstructure and wear behavior of plasma-sprayed nanostructured WC-Co coatings. Int. J. Appl. Ceram. Technol. 10, 60–71.

[59] Dikhtyar, V., Jerby, E., 2006. Fireball ejection from a molten hot spot to air by localized microwaves. Phys. Rev. Lett. 96, 045002.

[60] Dinda, G.P., Dasgupta, A.K., Mazumder, J., 2009. Laser aided direct metal deposition of Inconel 625 superalloy: Microstructural evolution and thermal stability. Mater. Sci. Eng. A 509, 98–104.

[61] Dowson, D., 1998. History of Tribology. Professional Engineering Publishing, London, U.K.

[62] Duan, Y., Sorescu, D.C., Johnson, J.K., 2006. Finite elements approach to microwave sintering of oxide materials, in: COMSOL Users Conference. Boston, U.S.A.

[63] Dunaevsky, V.V., 1997. Friction and wear equations. In: Tribology Data Handbook. CRC Press, New York, U.S.A.

[64] Eyre, T.S., 1976. Wear characteristics of metals. Tribol. Int. 9, 203–212.

[65] Fang, C.Y., Randal, C.A., Lanagan, M.T., Agrawal, D.K., 2008. Microwave processing of electroceramic materials and devices. J. Electroceramics 22, 125–130.

[66] Farag, S., Sobhy, A., Akyel, C., Doucet, J., Chaouki, J., 2012. Temperature profile prediction within selected materials heated by microwaves at 2.45GHz. Appl. Therm. Eng. 36, 360–369.

[67] Farahmand, P., Liu, S., Zhang, Z., Kovacevic, R., 2014. Laser cladding assisted by induction heating of Ni–WC composite enhanced by nano-WC and La_2O_3. Ceram. Int. 40, 15421–15438.

[68] Fernandes, C.M., Senos, A.M.R., 2011. Cemented carbide phase diagrams: A review. Int. J. Refract. Met. Hard Mater. 29, 405–418.

[69] Fida Hassan, S., Al-Qutub, A.M., Tun, K.S., Gupta, M., 2014. Study of wear mechanisms of a novel magnesium based hybrid nanocomposite. J. Tribol. 137, 011601.

[70] Fisher, J., Woo, S., Bai, K., Han, I., Lee, K., Hong, K., Seo, D., 2003. Microwave reaction bonding of silicon nitride using an inverse temperature gradient and ZrO_2 and Al_2O_3 sintering additives. J. Eur. Ceram. Soc. 23, 791–799.

[71] Frenk, A., Kurz, W., 1993. High speed laser cladding: solidification conditions and microstructure of a cobalt-based alloy. Mater. Sci. Eng. A 173, 339–342.

[72] Gäumann, M., Henry, S., Cléton, F., Wagnière, J.-D., Kurz, W., 1999. Epitaxial laser metal forming: analysis of microstructure formation. Mater. Sci. Eng. A 271, 232–241.

[73] Gell, M., 1995. Application opportunities for nanostructured materials and coatings.

Mater. Sci. Eng. A 204, 246–251.

[74] Gholipour, A., Shamanian, M., Ashrafizadeh, F., 2011. Microstructure and wear behavior of stellite 6 cladding on 17-4 PH stainless steel. J. Alloys Compd. 509, 4905–4909.

[75] Gleiter, H., 1989. Nanocyrstalline Materials. Prog. Mater. Sci. 33, 223–315.

[76] Gleiter, H., 1995. Nanostructured materials: state of the art and perspectives. Nanostructured Mater. 6, 3–14.

[77] Gleiter, H., 2000. Nanostructured materials: basic concepts and microstructure. Acta Mater. 48, 1–29.

[78] Grewal, H.S., Agrawal, A., Singh, H., 2013a. Slurry erosion performance of Ni–Al_2O_3 based composite coatings, Tribol. Int. 66, 296–306.

[79] Grewal, H.S., Singh, H., Agrawal, A., 2013b. Microstructural and mechanical characterization of thermal sprayed nickel–alumina composite coatings. Surf. Coat. Technol. 216, 78–92.

[80] Grewal, H.S., Singh, H., Agrawal, A., 2013c. Understanding Liquid Impingement erosion behaviour of nickel–alumina based thermal spray coatings, Wear 301, 424– 433.

[81] Guilemany, J.M., de Paco, J.M., Miguel, J.R., Nutting, J., 1999. Characterization of the W_2C phase formed during the high velocity oxygen fuel spraying of a WC + 12 pct Co powder. Metall. Mater. Trans. A 30, 1913–1921.

[82] Guo, C., Chen, J., Zhou, J., Zhao, J., Wang, L., Yu, Y., Zhou, H., 2011. Effects of WC–Ni content on microstructure and wear resistance of laser cladding Ni-based alloys coating. Surf. Coat. Technol. 206, 2064–2071.

[83] Guoqing, C., Xuesong, F., Yanhui, W., Shan, L., Wenlong, Z., 2013. Microstructure and wear properties of nickel-based surfacing deposited by plasma transferred arc welding. Surf. Coat. Technol. 228, S276–S282.

[84] Gupta, D., 2012. Microwave Cladding of Metal-Based Materials and their Characterisation. IIT Roorkee, Roorkee, India.

[85] Gupta, D., Paul, C.P., Gandhi, B.K., Gupta, S.R., Nath, A.K., 2008. Wear behavior of laser clad surfaces of Cr_3C_2, WC and Mo on austenitic AISI 304L steel. J. Laser Appl. 20, 140.

[86] Gupta, D., Sharma, A.K., 2011a. Development and microstructural characterization of microwave cladding on austenitic stainless steel. Surf. Coat. Technol. 205, 5147–5155.

[87] Gupta, D., Sharma, A.K., 2011b. Investigation on sliding wear performance of WC10Co2Ni cladding developed through microwave irradiation. Wear 271, 1642–1650.

[88] Gupta, D., Sharma, A.K., 2012. Microstructural characterization of cermet cladding

developed through microwave irradiation. J. Mater. Eng. Perform. 21, 2165–2172.

[89] Gupta, D., Sharma, A.K., 2014. Microwave cladding: A new approach in surface engineering. J. Manuf. Process. 16, 176–182.

[90] Gupta, D., Bhovi, P.M., Sharma, A.K., Dutta, S., 2012. Development and characterization of microwave composite cladding. J. Manuf. Process., 14, 243–249.

[91] Gupta, M., Wong, W.L.E., 2005. Enhancing overall mechanical performance of metallic materials using two-directional microwave assisted rapid sintering. Scr. Mater. 52, 479–483.

[92] Gupta, N., Midha, V., Balakotahia, V., Economou, D.J., 1999. Bifurcation analysis of thermal runaway in microwave heating of ceramics. J. Electrochem. Soc. 146, 4659–4665.

[93] Hasan, M., Stokes, J., Looney, L., Hashmi, M.S.J., 2008, Effect of spray parameters on residual stress build-up of HVOF sprayed aluminium/tool-steel functionally graded coatings. Surf. Coat. Technol. 202, 4006–4010.

[94] He, J., Schoenung, J.M., 2002. A review on nanostructured WC – Co coatings. Surf. Coat. Technol. 157, 72–79.

[95] Heidary, D.S.B., Madadi, F., Shamanian, M., 2015. Study of the microstructures and abrasive characteristics of Mo-Fe-C hardfacing alloys fabricated by gas tungsten arc welding. Tribol. Trans. 58, 225–230.

[96] Hill, J.M., Jennings, M.J., 1993. Formulation of model equations for heating by microwave radiation. Appl. Math. Model. 17, 369–379.

[97] Hjörnhede, A., Nylund, A., 2004. Adhesion testing of thermally sprayed and laser deposited coatings. Surf. Coat. Technol. 184, 208–218.

[98] Hogmark, S., Jacobson, S., Larsson, M., 2000. Design and evaluation of tribological coatings. Wear 246, 20–33.

[99] Holmberg, K., Matthews, A., 2009. Coatings Tribology- Properties, Mechanisms, Techniques and Applications in Surface Engineering, Second. ed. Elsevier Science Ltd., Oxford, U.K..

[100] Holubar, P., Jilek, M., Sima, M., 2000. Present and possible future applications of superhard nanocomposite coatings. Surf. Coat. Technol. 133-134, 145–151.

[101] Hutchings, I.M., 1992. Tribology, Friction and Wear of Engineering Materials. Arnold, London, U.K.

[102] Hwang, D.H., Zum Gahr, K.H., 2003. Transition from static to kinetic friction of unlubricated or oil lubricated steel/steel, steel/ceramic and ceramic/ceramic pairs. Wear 255, 365–375.

[103] Ion, J., 2005. Laser Processing of Engineering Materials: Principles, Procedure and Industrial Application. Butterworth-Heinemann, Norfolk, Great Britain.

[104] Iskander, M.F., Smith, R.L., Andrade, A.O.M., Kimrey, H., Wal, L.M., 1994. FDTD simulation of microwave sintering of ceramics in multimode cavities. IEEE Trans. Microw. Theory Tech. 42, 793–800.

[105] Jia, K., Fischer, T.E., 1996. Abrasion resistance of nanostructured and conventional cemented carbides. Wear 200, 206–214.

[106] Jia, K., Fischer, T.E., 1997. Sliding wear of conventional and nanostructured cemented carbides. Wear 203-204, 310–318.

[107] Jones, D.A., Lelyveld, T.P., Mavrofidis, S.D., Kingman, S.W., Miles, N.J., 2002. Microwave heating applications in environmental engineering-A review. Resour. Conserv. Recycl. 34, 75–90.

[108] Kagnaya, T., Boher, C., Lambert, L., Lazard, M., Cutard, T., 2009. Wear mechanisms of WC–Co cutting tools from high-speed tribological tests. Wear 267, 890–897.

[109] Karthikeyan, S., Vijayaraghavan, L., Madhavan, S., Almeida, A., 2016. Study on the mechanical properties of heat-treated electroless NiP coatings reinforced with Al_2O_3 nano particles. Metall. Mater. Trans. A 47, 2223– 2231.

[110] Kathuria, Y.P.U., 2000. Some aspects of laser surface cladding in the turbine industry. Surf. Coat. Technol. 132, 262–269.

[111] Kaushal, S., Sirohi, V., Gupta, D., Bhowmick, H., Singh, S., 2015. Processing and characterization of composite cladding through microwave heating on martensitic steel. Proc. Inst. Mech. Eng. Part L J. Mater. Des. Appl. 0, 1–7. doi:10.1177/1464420715616139

[112] Kim, D.E., Suh, N.P., 1991. On microscopic mechanisms of friction and wear. Wear 149, 199–208.

[113] Ku, H., Siores, E., Taube, A., Ball, J.A.R., 2002. Productivity improvement through the use of industrial microwave technologies. Comput. Ind. Eng. 42, 281–290.

[114] Kurlov, A.S., Gursev, A.I., 2013. Tungsten Carbides: Structure, Properties and Application in Hardmetals. Springer, London, U.K.

[115] Landheer, D., De Gee, A.W.J., 1991. Adhesion, friction and wear. MRS Bull. 10, 36–40.

[116] Landheer, D., Zaat, J.H., 1974. The mechanism of metal transfer in sliding friction. Wear 27, 129–145.

[117] Lee, C., Park, H., Yoo, J., Lee, C., Woo, W., Park, S., 2015. Residual stress and

crack initiation in laser clad composite layer with Co-based alloy and WC+NiCr. Appl. Surf. Sci. 345, 286–294.

[118] Leonelli, C., Veronesi, P., Denti, L., Gatto, A., Iuliano, L., 2007. Microwave assisted sintering of green metal parts. J. Mater. Process. Technol. 5, 489–496.

[119] Li, C.J.C.X., Yang, G.J., Gao, P.H., Ma, J., Wang, Y.Y., Li, C.J.C.X., 2007. Characterization of nanostructured WC-Co deposited by cold spraying. J. Therm. Spray Technol. 16, 1011–1020.

[120] Li, C.J., Yang, G.J., 2013. Relationships between feedstock structure, particle parameter, coating deposition, microstructure and properties for thermally sprayed conventional and nanostructured WC–Co. Int. J. Refract. Met. Hard Mater. 39, 2–17.

[121] Li, C.X., Bell, T., 2004. Sliding wear properties of active screen plasma nitrided 316 austenitic stainless steel. Wear 256, 1144–1152.

[122] Liljas, M., 1995. Development of superaustenitic stainless steels. Weld. World 36, 55–63.

[123] Lin, C.M., Chang, C.M., Chen, J.H., Hsieh, C.C., Wu, W., 2010. Microstructure and wear characteristics of high-carbon Cr-based alloy claddings formed by gas tungsten arc welding (GTAW). Surf. Coat. Technol. 205, 2590–2596.

[124] Lin, Y.C., Cho, Y.H., 2009. Elucidating the microstructural and tribological characteristics of NiCrAlCoCu and NiCrAlCoMo multicomponent alloy clad layers synthesized in situ. Surf. Coat. Technol. 203, 1694–1701.

[125] Lin, Y.C., Wang, S.W., 2003. Wear behavior of ceramic powder cladding on an S50C steel surface. Tribol. Int. 36, 1–9.

[126] Lin, Y.C., Wang, S.W., 2004. Microstructure of TiC–W cladding on steel in nanoscale. Wear 256, 720–725.

[127] Link, G., Feher, L., Thumm, M., Ritzhaupt-Kleissl, H.J., Bohme, R., Weisenburger, A., 1999. Sintering of advanced ceramics using a 30-GHz, 10-kW, CW industrial gyrotron. IEEE Trans. Plasma Sci. 27, 547–554.

[128] Lippold, J.C., Kotecki, D.J., 2005. Welding Metallurgy and Weldability of Stainless Steels. Wiley-Interscience, New Jersey, U.S.A.

[129] Liu, C., Sheen, D., 2008. Analysis and control of the thermal runaway of ceramic slab under microwave heating. Sci. China Ser. E Technol. Sci. 51, 2233–2241.

[130] Liu, S.L., Zheng, X.P., Geng, G.Q., 2010. Influence of nano-WC–12Co powder addition in WC–10Co–4Cr AC-HVAF sprayed coatings on wear and erosion behaviour. Wear 269, 362–367.

[131] Liyanage, T., Fisher, G., Gerlich, A.P., 2012. Microstructures and abrasive wear

performance of PTAW deposited Ni–WC overlays using different Ni-alloy chemistries. Wear 274-275, 345–354.

[132] Liyanage, T., Fisher, G., Gerlich, A.P., 2010. Influence of alloy chemistry on microstructure and properties in NiCrBSi overlay coatings deposited by plasma transferred arc welding (PTAW). Surf. Coat. Technol. 205, 759–765.

[133] Lovell, M.R., Deng, Z., Khonsari, M.M., 2000. Experimental characterization of sliding friction: crossing from deformation to plowing contact. J. Tribol. 122, 856–863.

[134] Luo, J., Hunyar, C., Feher, L., Link, G., Thumm, M., Pozzo, P., 2004. Potential advantages for millimeter-wave heating of powdered metals. Int. J. Infrared Millimeter Waves 25, 1271–1283.

[135] Lyphout, C., Nylén, P., Manescu, A., Pirling, T., 2008. Residual stresses distribution through thick HVOF sprayed Inconel 718 coatings. J. Therm. Spray Technol. 17, 915–923.

[136] Ma, C.H., Huang, J.H., Chen, H., 2002. Residual stress measurement in textured thin film by grazing-incidence X-ray diffraction. Thin Solid Films 418, 73–78.

[137] Madadi, F., Shamanian, M., Ashrafizadeh, F., 2011. Effect of pulse current on microstructure and wear resistance of Stellite6/tungsten carbide claddings produced by tungsten inert gas process. Surf. Coat. Technol. 205, 4320–4328.

[138] Marland, S., Merchant, A., Rowson, N., 2001. Dielectric properties of coal. Fuel 80, 1839–1849.

[139] Marple, B.R., Lima, R.S., 2005. Process temperature/velocity-hardness-wear relationships for high-velocity oxyfuel sprayed nanostructured and conventional cermet coatings. J. Therm. Spray Technol. 14, 67–76.

[140] Martin, P.M., 2011. Introduction to Surface Engineering and Functionally Engineered Materials, 1st ed. Wiley-Scrivener, New Jersey, U.S.A.

[141] Mendez, P.F., Barnes, N., Bell, K., Borle, S.D., Gajapathi, S.S., Guest, S.D., Izadi, H., Gol, A.K., Wood, G., 2014. Welding processes for wear resistant overlays. J. Manuf. Process. 16, 4–25.

[142] Menezes, P.L., Kailas, S.V., 2009. Influence of surface texture and roughness parameters on friction and transfer layer formation during sliding of aluminium pin on steel plate. Wear 267, 1534–1549.

[143] Metaxas, A.C., 1991. Microwave heating. Power Eng. J. 5, 237–247.

[144] Michálek, M., Sedláček, J., Parchoviansky, M., Michálková, M., Galusek, D., 2014. Mechanical properties and electrical conductivity of alumina/MWCNT and alumina/zirconia/MWCNT composites. Ceram. Int. 40, 1289–1295.

[145] Minay, E.J., Boccaccini A.R., Veronesi P., Cannillo V., Leonelli, C., 2004. Processing of novel glass matrix composites by microwave heating. J. Mater. Process. Technol. 155–156, 1749–1755.

[146] Mishra, R.R., Sharma, A.K., 2016. Microwave-material interaction phenomena: heating mechanisms, challenges and opportunities in material processing. Compos. Part A Appl. Sci. Manuf. 81, 78–97.

[147] Molleda, F., Mora, J., Molleda, F.J., Mora, E., Carrillo, E., Mellor, B.G., 2006. A study of the solid – liquid interface in cobalt base alloy (Stellite) coatings deposited by fusion welding (TIG). Mater. Charact. 57, 227–231.

[148] Mondal, A., Shukla, A., Upadhyaya, A., Agrawal, D., 2010. Effect of porosity and particle size on microwave heating of copper. Sci. Sinter. 42, 169–182.

[149] Musil, J., 2000. Hard and superhard nanocomposite coatings. Surf. Coat. Technol. 125, 322–330.

[150] O'Quigley, D.G.F., Luyckx, S., James, M.N., 1997. An empirical ranking of a wide range of WC-Co grades in terms of their abrasion resistance measured by the ASTM standard B 611-85 test. Int. J. Refract. Met. Hard Mater. 15, 73–79.

[151] Oghbaei, M., Mirzaee, O., 2010. Microwave versus conventional sintering: A review of fundamentals, advantages and applications. J. Alloys Compd. 494, 175–189.

[152] Pathania, A., Singh, S., Gupta, D., Jain, V., 2015. Development and analysis of tribological behavior of microwave processed EWAC+20% WC10Co2Ni composite cladding on mild steel substrate. J. Manuf. Process. 20, 79–87.

[153] Paul, C.P., Alemohammad, H., Toyserkani, E., Khajepour, A., Corbin, S., 2007. Cladding of WC–12 Co on low carbon steel using a pulsed Nd:YAG laser. Mater. Sci. Eng. A 464, 170–176.

[154] Paul, C.P., Mishra, S.K., Tiwari, P., Kukreja, L.M., 2013. Solid-particle erosion behaviour of WC/Ni composite clad layers with different contents of WC particles. Opt. Laser Technol. 50, 155–162.

[155] Peelamedu, R.D., Roy, R., Agrawal, D.K., 2002. Microwave-induced reaction sintering of $NiAl_2O_4$. Mater. Lett. 55, 234–240.

[156] Peng, D.X., Kang, Y., 2015. Wear behavior of ceramic powder and solid lubricant cladding on carbon steel surface. Tribol. Trans. 58, 177–185.

[157] Plaut, R.L., Herrera, C., Escriba, D.M., Rios, P.R., Padilha, A.F., 2007. A short review on wrought austenitic stainless steels at high temperatures: processing, microstructure, properties and performance. Mater. Res. 10, 453–460.

[158] Plaza-González, P., Monzó-Cabrera, J., Catalá-Civera, J.M., Sánchez-Hernández, D.,

2004. New approach for the prediction of the electric field distribution in multimode microwave-heating applicators with mode stirrers. IEEE Trans. Magn. 40, 1672–1678.

[159] Qiao, Y., Fischer, T.E., Dent, A., 2003. The effects of fuel chemistry and feedstock powder structure on the mechanical and tribological properties of HVOF thermal-sprayed WC–Co coatings with very fine structures. Surf. Coat. Technol. 172, 24–41.

[160] Rabinowicz, E., 1967. Variation of friction and wear of solid lubricant films with film thickness. ASLE Trans. 10, 1–9.

[161] Rabinowicz, E., 1995. Friction and Wear of Materials. Wiley-Interscience. New York, U.S.A.

[162] Rajakumar, S., Vijayaraghavan, L., Mayuram, M.M., Krishnamurthy, R., 2010. Flexural characteristics of D-gun sprayed functionally graded alumina and alumina-zirconia ceramic composites coatings, Int. J. Mater. Eng. Innov. 1, 398–416.

[163] Rajkumar, K., Aravindan, S., 2009. Microwave sintering of copper-graphite composites. J. Mater. Process. Technol. 209, 5601–5605.

[164] Rajkumar, K., Aravindan, S., 2011. Tribological performance of microwave sintered copper–TiC–graphite hybrid composites. Tribol. Int. 44, 347–358.

[165] Ramkumar, J., Aravindan, S., Malhotra, S.K., Krishnamurthy, R., 2002. Enhancing the metallurgical properties of WC insert (K-20) cutting tool through microwave treatment. Mater. Lett. 53, 200–204.

[166] Ramkumar, J., Malhotra, S.K., Krishnamurthy, R., 2005. Effect of microwave treatment of WC inserts for drilling of GFRP composites. Mach. Sci. Technol. 9, 263–269.

[167] Rashed, F.S., Mahmoud, T.S., 2009. Prediction of wear behaviour of A356/SiC_p MMCs using neural networks. Tribol. Int. 42, 642–648.

[168] Rattanadecho, P., Klinbun, W., 2011. Theoretical analysis of microwave heating of dielectric materials filled in a rectangular waveguide with various resonator distances. J. Heat Transfer 133, 1–10.

[169] Ravnikar, D., Dahotre, N.B., Grum, J., 2013. Laser coating of aluminum alloy EN AW 6082-T651 with TiB_2 and TiC: microstructure and mechanical properties. Appl. Surf. Sci. 282, 914–922.

[170] Reidenbach, F., 1994. Surface Engineering, ASM Handbook, Volume 5, 10th ed. ASM International.

[171] Riedel, H., Svoboda, J., 2006. Simulation of microwave sintering with advanced sintering models, in: Advances in Microwave and Radio Frequency Processing. pp.

210–216.

[172] Rigney, D.A., 1997. Comments on the sliding wear of metals. Tribol. Int. 30, 361–367.

[173] Rigney, D.A., Hirth, J.P., 1979. Plastic deformation and sliding friction of metals. Wear 53, 345–370.

[174] Rödiger, K., Dreyer, K., Gerdes, T., Willert-Porada, M., 1998. Microwave sintering of hardmetals. Int. J. Refract. Met. Hard Mater. 16, 409–416.

[175] Roger, J.M., 1998. Engineer's Handbook of Industrial Microwave Heating. The Institution of Engineering and Technology, London, U.K.

[176] Roy, R., Agrawal, D., Cheng, J., Gedevanishvili, S., 1999. Full sintering of powdered-metal bodies in a microwave field. Nature 399, 668–670.

[177] Rybakov, K.I., Olevsky, E.A., Krikun, E.V., 2013. Microwave sintering: Fundamentals and modeling. J. Am. Ceram. Soc. 96, 1003–1020.

[178] Salvi, D., Boldor, D., Ortego, J., Aita, G.M., Sabliov, C.M., 2010. Numerical modeling of continuous flow microwave heating: a critical comparison of COMSOL and ANSYS. J. Microw. Power Electromagn. Energy 44, 187–197.

[179] Santana, Y.Y., Renault, P.O., Sebastiani, M., La Barbera, J.G., Lesage, J., Bemporad, E., Le Bourhis, E., Puchi-Cabrera, E.S., Staia, M.H., 2008. Characterization and residual stresses of WC–Co thermally sprayed coatings. Surf. Coat. Technol. 202, 4560–4565.

[180] Santos, T., Costa, L.C., Valente, M., Monteiro, J., Sousa, J., 2010. 3D Electromagnetic Field Simulation in Microwave Ovens: A tool to control thermal runaway, in: Proceedings of the COMSOL Conference. Paris, France, 3–7.

[181] Santos, T., Valente, M.A., Monteiro, J., Sousa, J., Costa, L.C., 2011. Electromagnetic and thermal history during microwave heating. Appl. Therm. Eng. 31, 3255–3261.

[182] Sharma, A.K., 2002. Microwave Glazing of Plasma Sprayed Ceramic Composite Coatings and their Characterisation. IIT Madras, Chennai, India.

[183] Sharma, A.K., Aravindhan, S., Krishnamurthy, R., 2001. Microwave glazing of alumina – titania ceramic composite coatings. Mater. Lett. 50, 295–301.

[184] Sharma, A.K., Gupta, D., 2010. A Method of Cladding/Coating of Metallic and Non-metallic Powders on Metallic Substrates by Microwave Irradiation. 527/Del/2010.

[185] Sharma, A.K., Gupta, D., 2012. On microstructure and flexural strength of metal-ceramic composite cladding developed through microwave heating. Appl. Surf. Sci. 258, 5583–5592.

[186] Sharma, A.K., Krishnamurthy, R., 2002. Microwave processing of sprayed alumina

composite for enhanced performance. J. Eur. Ceram. Soc. 22, 2849–2860.

[187] Shipway, P.H., Hogg, J.J., 2005. Dependence of microscale abrasion mechanisms of WC-Co hardmetals on abrasive type. Wear 259, 44–51.

[188] Shipway, P.H., McCartney, D.G., Sudaprasert, T., 2005. Sliding wear behaviour of conventional and nanostructured HVOF sprayed WC-Co coatings. Wear 259, 820–827.

[189] Shukla, A.K., Mondal, A., Upadhyaya, A., 2010. Numerical modeling of microwave heating. Sci. Sinter. 42, 99–124.

[190] Siegel, R.W., 1993. Nanostructured materials - mind over matter. Nanostructured Mater. 3, 1–18.

[191] Singh, R., Kumar, M., Kumar, D., Mishra, S.K., 2012. Erosion and corrosion behavior of laser cladded stainless steels with tungsten carbide. J. Mater. Eng. Perform. 21, 2274–2282.

[192] Singh, S., Gupta, D., Jain, V., 2015a. Recent applications of microwaves in materials joining and surface coatings. Proc. Inst. Mech. Eng. Part B J. Eng. Manuf. doi:10.1177/0954405414560778.

[193] Singh, S., Gupta, D., Jain, V., Sharma, A.K., 2015b. Microwave processing of materials and applications in manufacturing industries: A review. Mater. Manuf. Process. 30, 1–29.

[194] So, H., Chen, C.T., Chen, Y.A., 1996. Wear behaviours of laser-clad stellite alloy 6. Wear 192, 78–84.

[195] Srinath, M.S., Murthy, P.S., Sharma, A.K., Kumar, P., Kartikeyan, M.V., 2012. Simulation and analysis of microwave heating while joining bulk copper. Int. J. Eng. Sci. Technol. 4, 152–158.

[196] Srinath, M.S., Sharma, A.K., Kumar, P., 2011a. A new approach to joining of bulk copper using microwave energy. Mater. Des. 32, 2685–2694.

[197] Srinath, M.S., Sharma, A.K., Kumar, P., 2011b. Investigation on microstructural and mechanical properties of microwave processed dissimilar joints. J. Manuf. Process. 13, 141–146.

[198] Stachowiak, G.W. (Ed.), 2005. Wear-Materials, Mechanisms and Practice, 1st ed. Wiley, West Sussex, England.

[199] Stewart, D., Shipway, P.H., McCartney, D., 2000. Microstructural evolution in thermally sprayed WC–Co coatings: comparison between nanocomposite and conventional starting powders. Acta Mater. 48, 1593–1604.

[200] Stewart, D.A., Shipway, P.H., McCartney, D.G., 1999. Abrasive wear behaviour of conventional and nanocomposite HVOF-sprayed WC–Co coatings. Wear 225–229, 789–

798.

[201] St-Georges, L., 2007. Development and characterization of composite Ni–Cr+WC laser cladding. Wear 263, 562–566.

[202] Stokes, J., Looney, L., 2004. Residual stress in HVOF thermally sprayed thick deposits. Surf. Coat. Technol. 177, 18–23.

[203] Stokes, J., Looney, L., 2009. FEA of residual stress during HVOF thermal spraying. J. Mater. Eng. Perform. 18, 21–25.

[204] Sudha, C., Shankar, P., Rao, R.V.S., Thirumurugesan, R., Vijayalakshmi, M., Raj, B., 2008. Microchemical and microstructural studies in a PTA weld overlay of Ni–Cr–Si–B alloy on AISI 304L stainless steel. Surf. Coat. Technol. 202, 2103–2112.

[205] Suetin, D.V., Shein, I.R., Ivanovskii, A.L.Ã., 2009. Structural, electronic and magnetic properties of η carbides (Fe_3W_3C, Fe_6W_6C, Co_3W_3C and Co_6W_6C) from first principles calculations. Phys. B Phys. Condens. Matter 404, 3544–3549.

[206] Suh, N.P., Sin, H.C., 1981. The genesis of friction. Wear 69, 91–114.

[207] Sun, Y., Bell, T., 2002. Dry sliding wear resistance of low temperature plasma carburised austenitic stainless steel. Wear 253, 689–693.

[208] Sunil, B.R., Sivaprahasam, D., Subasri, R., 2010. Microwave sintering of nanocrystalline WC-12Co: Challenges and perspectives. Int. J. Refract. Met. Hard Mater. 28, 180–186.

[209] Sweet, J.N., Roth, E.P., Moss, M., 1987. Thermal conductivity of Inconel 718 and 304 stainless steel. Int. J. Thermophys. 8, 593–606.

[210] Tada, S., Echigo, R., Yoshida, H., 1998. Numerical analysis of electromagnetic wave in a partially loaded microwave applicator. Int. J. Heat Mass Transf. 41, 709–718.

[211] Taha-al, Z.Y., Hashmi, M.S., Yilbas, B.S., 2009. Effect of WC on the residual stress in the laser treated HVOF coating. J. Mater. Process. Technol. 9, 3172–3181.

[212] Takadoum, J. (Ed.), 2010. Nanomaterials and Surface Engineering. Wiley-ISTE, London, U.K.

[213] Taran, Y.N., Ivanov, L.I., Moshkevich, L.D., 1972. Morphology of the eutectic in Fe-W-C alloys. Met. Sci. Heat Treat. 14, 3–5.

[214] Thostenson, E.T., Chou, T.-W., 1999. Microwave processing: fundamentals and applications. Compos. Part A Appl. Sci. Manuf. 30, 1055–1071.

[215] Tun, K.S., Gupta, M., 2009. Development of magnesium/(yttria+nickel) hybrid nanocomposites using hybrid microwave sintering: Microstructure and tensile properties. J. Alloys Compd. 487, 76–82.

[216] Tun, K.S., Gupta, M., Srivatsan, T.S., 2010. Investigating influence of hybrid (yttria

+ copper) nanoparticulate reinforcements on microstructural development and tensile response of magnesium. Mater. Sci. Technol. 26, 87–94.

[217] Upadhyaya, G.S., 1999. Cemented Tungsten Carbides: Production, Properties and Testing (Materials Science and Process Technology). Noyes Publications, New Jersey, U.S.A.

[218] Vaidhyanathan, B., Agrawal, D.K., Shrout, T.R., Fang, Y., 2000. Microwave synthesis and sintering of $Ba(Mg_{1/3}Ta_{2/3})O_3$. Mater. Lett. 42, 207–211.

[219] Van De Velde, F., De Baets, P., 1998. The relation between friction force and relative speed during the slip-phase of a stick-slip cycle. Wear 219, 220–226.

[220] VaradaRajan, Y.S., Vijayaraghavan, L., Krishnamurthy, R., Bhanuprasad, V.V., 2006, Performance enhancement through microwave irradiation of K20 carbide tool machining Al/SiC metal matrix composite, J. Mater. Process. Technol. 173, 185–193.

[221] Vaz, R.H., Pereira, J.M.C., Ervilha, A.R., Pereira, J.C.F., 2014. Simulation and uncertainty quantification in high temperature microwave heating. Appl. Therm. Eng. 70, 1025–1039.

[222] Veronesi, P., Leonelli, C., Pellacani, G.C., Boccaccini, A.R., 2003. Unique microstructure of glass-metal composites obtained by microwave assisted heat-treatments. J. Therm. Anal. Calorim. 72, 1141–1149.

[223] Vijayakumar, K., Sharma, A.K., Mayuram, M.M., Krishnamurthy, R., 2002. Response of plasma-sprayed alumina – titania ceramic composite to high-frequency impact loading. Mater. Lett. 54, 403–413.

[224] Vreeling, J.A., Ocelík, V., De Hosson, J.T.M., 2002. Ti–6Al–4V strengthened by laser melt injection of WC_p particles. Acta Mater. 50, 4913–4924.

[225] Wang, Q., Chen, Z., Li, L., Yang, G., 2012. The parameters optimization and abrasion wear mechanism of liquid fuel HVOF sprayed bimodal WC – 12Co coating. Surf. Coat. Technol. 206, 2233–2241.

[226] Wang, X.H., Song, S.L., Zou, Z.D., Qu, S.Y., 2006. Fabricating TiC particles reinforced Fe-based composite coatings produced by GTAW multi-layers melting process. Mater. Sci. Eng. A 441, 60–67.

[227] Wayne, F., Baldonia, J.G., Buljana, S.-T., 1990. Abrasion and erosion of WC-Co with controlled microstructures. Tribol. Trans. 33, 611–617.

[228] Wong, W., Gupta, M., 2007. Development of Mg/Cu nanocomposites using microwave assisted rapid sintering. Compos. Sci. Technol. 67, 1541–1552.

[229] Wong, W.L.E., Karthik, S., Gupta, M., 2005. Development of hybrid Mg/Al_2O_3 composites with improved properties using microwave assisted rapid sintering route.

J. Mater. Sci. 40, 3395–3402.

[230] Xie, G., Suzuki, M., Louzguine-Luzgin, D.V., Li, S., Tanaka, M., Sato, M., Inoue, A., 2009. Analysis of electromagnetic field distributions in a 915 MHz single-mode microwave applicator. Prog. Electromagn. Res. 89, 135–148.

[231] Xu, G., Kutsuna, M., Liu, Z., Katsusige, Y., 2006a. Comparison between diode laser and TIG cladding of Co-based alloys on the SUS403 stainless steel. Surf. Coat. Technol. 201, 1138–1144.

[232] Xu, G., Kutsuna, M., Liu, Z., Sun, L., 2006b. Characteristic behaviours of clad layer by a multi-layer laser cladding with powder mixture of Stellite-6 and tungsten carbide. Surf. Coat. Technol. 201, 3385–3392.

[233] Yakovlev, A., Bertrand, P., Smurov, I., 2004. Wear-resistant coatings with engineered structure by laser cladding. Tribol. Lett. 17, 705–708.

[234] Yang, Q., Senda, T., Ohmori, A., 2003. Effect of carbide grain size on microstructure and sliding wear behavior of HVOF-sprayed WC–12% Co coatings. Wear 254, 23–34.

[235] Yang, Y., Man, H.C., 2000. Microstructure evolution of laser clad layers of W-C-Co alloy powders. Surf. Coat. Technol. 132, 130–136.

[236] Yi-du, H., Bai-quan, L., He, L., Hua-ming, D., Chuan-jie, Z., Hao, Y., 2016. Three-dimensional simulation of microwave heating coal sample with varying parameters. Appl. Therm. Eng. 93, 1145–1154.

[237] Yoffe, E.H., 2001. Sliding without wear. Wear 249, 601–605.

[238] Zafar, S., Bansal, A., Sharma, A.K., Arora, N., Ramesh, C.S., 2014. Dry erosion wear performance of Inconel 718 microwave clad. Surf. Eng. 30, 852–859.

[239] Zafar, S., Sharma, A.K., Arora, N., 2013. Development and microstructural characterisation of Inconel cladding on stainless steel through microwave irradiation. J. Mech. Eng. 3, 9–16.

[240] Zhang, H., Shi, Y., Kutsuna, M., Xu, G.J., 2010. Laser cladding of Colmonoy 6 powder on AISI316L austenitic stainless steel. Nucl. Eng. Des. 240, 2691–2696.

[241] Zhang, S., Sun, D., Fu, Y., Du, H., 2003. Recent advances of superhard nanocomposite coatings: A review. Surf. Coat. Technol. 167, 113–119.

[242] Zhang, Z., Barkoula, N.M., Karger-Kocsis, J., Friedrich, K., 2003. Artificial neural network predictions on erosive wear of polymers. Wear 255, 708–713.

[243] Zhao, X.Q., Zhou, H.D., Chen, J.M., 2006. Comparative study of the friction and wear behavior of plasma sprayed conventional and nanostructured WC–12%Co coatings on stainless steel. Mater. Sci. Eng. A. 431, 290–297.

[244] Zhenda, C., Chewh, L.I.M.L., Mingh, Q., Chen, Z., Lim, L.C., Qian, M., 1996. Laser

cladding of WC - Ni composite. J. Mater. Process. Technol. 62, 321–323.

[245] Zhong, M., Liu, W., 2010. Laser surface cladding: The state of the art and challenges. Proc. Inst. Mech. Eng. Part C J. Mech. Eng. Sci. 224, 1041–1060.

[246] Zhong, M., Liu, W., Yao, K., Goussain, J.C., Mayer, C., Becker, A., 2002. Microstructural evolution in high power laser cladding of Stellite 6+WC layers. Surf. Coat. Technol. 157, 128–137.

[247] Zhou, S., Dai, X., Zheng, H., 2011. Analytical modeling and experimental investigation of laser induction hybrid rapid cladding for Ni-based WC composite coatings. Opt. Laser Technol. 43, 613–621.

[248] Zhou, S., Huang, Y., Zeng, X., Hu, Q., 2008a. Microstructure characteristics of Ni-based WC composite coatings by laser induction hybrid rapid cladding. Mater. Sci. Eng. A 480, 564–572.

[249] Zhou, S., Zeng, X., Hu, Q., Huang, Y., 2008b. Analysis of crack behavior for Ni-based WC composite coatings by laser cladding and crack-free realization. Appl. Surf. Sci. 255, 1646–1653.

[250] Zhu, S., Fahrenholtz, W.G., Hilmas, G.E., Zhang, S.C., Yadlowsky, E.J., Keitz, M.D., 2008. Microwave sintering of a ZrB_2–B_4C particulate ceramic composite. Compos. Part A Appl. Sci. Manuf. 39, 449–453.

[251] Zhu, Y.C., Yukimura, K., Ding, C.X., Zhang, P.Y., 2001. Tribological properties of nanostructured and conventional WC-Co coatings deposited by plasma spraying. Thin Solid Films 388, 277–282.

[252] Zum Gahr, K.H., 1987. Microstructure and Wear of Materials (Tribology Series). Elsevier Science Ltd. New York, U.S.A.

APPENDIX-A

- Model: D8 Advance
- Make: Bruker AXS Instruments
- Radiation: Cu-Kα
- Scan rate: 0.5 to 1° min^{-}1
- Scan range: 5° to 120°

Fig. A-1- A typical view of the X-ray diffractometer

- Model: Ultra Plus
- Make: Carl Ziess
- Operating voltage: 2-25 kV
- Magnification: 25× to 1000000×
- Gun: Field Emission Gun

Fig. A-2- A typical view of the scanning electron microscope

- Model: SX100
- Make: Cameca
- Accelerating Voltage: 0.2 to 40 kV
- Beam Current: 10^{-5} to 10^{-12} A
- Beam Diameter: 0.6 µm at 15 kV and 100 nA
- WDS: 4 No. WDS with crystal LiF, PET, TAP
- Electron Gun: Tungsten filament
- Magnification: 150× to 400,000×

Fig. A-3- A typical view of the electron probe micro analyser

- Model: LT-23B
- Make: Dewinter
- Magnification:50 ×, 100 ×, 200 ×, 500 ×
- Display: Large field
- Interface: With USB Digital camera and Image Analysis Software (Dewinter Material Plus, Version 4.2)

Fig. A-4- A typical view of the optical microscope

- Model: Economet VH–1 MD
- Make: Chennai Metco
- Indenter: Vicker's
- Test load: 10-1000 gf
- Dwell time: 10-30 s
- Min measuring unit: 0.05 µm
- Hardness measuring range: 5-2500 HV
- Test microscope magnification: 400× (Measuring), 100× (Observation)
- Data Output: LCD screen display

Fig. A-5- A view of the typical microhardness tester

- Model: 5982
- Make: Instron
- Maximum capacity: 100 kN
- Load measurement accuracy: +/- 0.5% of reading down to 1/1000 of load cell capacity
- Strain rate: Speed range of 0.00005 to 1016 mm/min.
- Operating condition: tensile and compression

Fig. A-6- A view of the universal testing machine

- Model: Baincut LSS
- Make: Chennai Metco
- Maximum speed: 240 RPM
- Blade thickness: 500 µm

Fig. A-7- A view of the low speed diamond saw

- Model: WUC- 4L
- Make: Wensar
- Capacity: 3 liters
- Ultrasonic frequency: 33± 3 kHz
- Tank material: Stainless steel tank
- Ultrasonic wattage: 100 W
- Power supply: 200 V, 50 Hz, Single phase

Fig. A-8- A typical view of the ultrasonic cleaner

- Model: TR-201LE-M8
- Make: Ducom
- Counter disc: EN-31 (hardness: 65 HRC)
- Load range: upto 200 N
- Maximum speed: 2000 RPM
- Compound wear measurement: 0-1200 µm

Fig. A-9- A typical view of the pin-on-disc tribometer

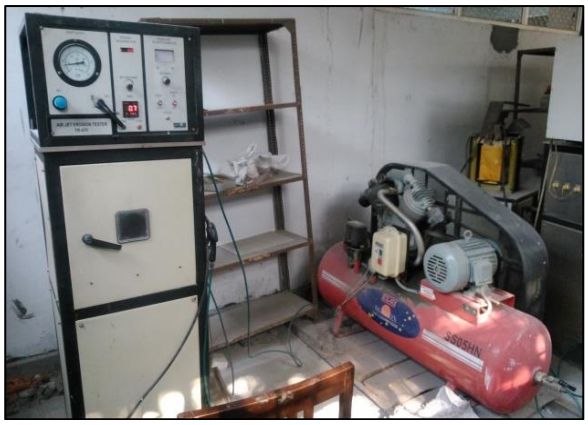

- Model: TR-470
- Make: Ducom
- Nozzle diameter: 1.5 mm
- Particle velocity: 30 -100 m/s
- Erodent feed rate: 0.5-5 g/min
- Angle of impingement: 30°, 45°, 60° and 90°
- Sample to nozzle distance: 10 mm

Fig. A-10- A typical view of the solid particle erosion test rig

- Wheel diameter: 240 mm
- Rubber material: Chlorobutyl rubber
- Maximum speed: 350 RPM
- Speed control: Variable
- Maximum load: 150 N
- Motor drive power: 0.7 kW (1 HP)
- Abradant feed rate: 50-150 g/min

Fig. A-11- A typical view of the three-body abrasion test rig

- Make: Veeco Wyko
- Model: NT1100
- Light: Tungsten halogen lamp
- Objectives: 5×, 20× and 50×
- Field of view: 0.5, 1.0, 1.5
- Display: TFT mointor to locate the field of interest and fringes

Fig. A-12- A typical view of the 3D surface optical profilometer

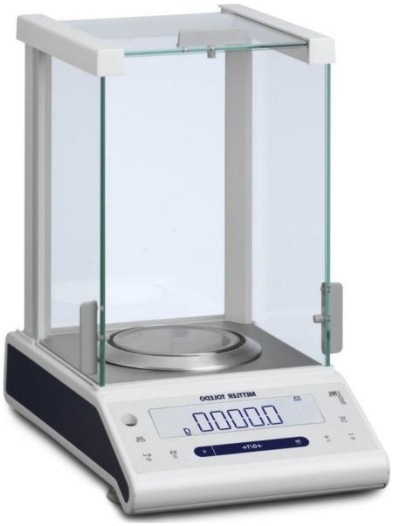

- Make: Mettler Toledo
- Model: ML104
- Maximum capacity: 120 g
- Readout accuracy: 0.0001 g
- Display: Blacklit display

Fig. A-13- A typical view of the weighing balance

VISIBLE OUTPUTS

[A] JOURNALS

1. **Sunny Zafar** and Apurbba Kumar Sharma, Investigations on Flexural Performance and Residual Stresses in Nanometric WC-12Co Microwave Clads, **Surface and Coatings Technology**, Elsevier, 291, 2016, 413-422. **(IF: 2.0, 5-year IF: 2.374)**.
2. **Sunny Zafar** and Apurbba Kumar Sharma, Structure-Property Correlations In Nanostructured WC-12Co Microwave Clad, **Applied Surface Science,** Elsevier, 370, 2016, 92-101. **(IF: 2.711, 5-year IF: 2.735)**.
3. **Sunny Zafar** and Apurbba Kumar Sharma, Abrasive and Erosive Wear Behaviour of Nanometric WC-12Co Microwave Clads, **Wear,** Elsevier, 346-347, 2016, 29-45. **(IF: 1.913, 5-year IF: 2.109)**.
4. **Sunny Zafar** and Apurbba Kumar Sharma, Dry Sliding Wear Performance of Nanostructured WC-12Co deposited through Microwave Cladding**, Tribology International,** Elsevier, 91, 2015, 14-22. **(IF: 2.12, 5-year IF: 2.094).**
5. **Sunny Zafar** and Apurbba Kumar Sharma, On Friction and Wear Behaviour of WC-12Co Microwave Clad, **Tribology Transactions**, Taylor and Francis, 58, 2015, 584-591. **(IF: 1.349).**
6. **Sunny Zafar** and Apurbba Kumar Sharma, Development and Characterisations of WC–12Co Microwave Clad, **Materials Characterization**, Elsevier, 96, 2014, 241-248. **(IF: 1.925, 5-year IF: 2.2).**
7. **Sunny Zafar** and Apurbba Kumar Sharma, Prediction of Tribological Behaviour of WC-12Co Nanostructured Microwave Clad through ANN, **Tribology Online**, Japanese Society of Tribologists, 11, 2016, 333-340.
8. **Sunny Zafar** and Apurbba Kumar Sharma**,** Microstructure and Wear Performance of Heat Treated WC-12Co Microwave Clad, **Vacuum**, Elsevier, (Revision submitted) **(IF: 1.858, 5-year IF: 1.647).**

[B] CONFERENCES

1. **Sunny Zafar** and Apurbba Kumar Sharma, Response of Nanometric WC-12Co Microwave Clads to Abrasive Wear, Proceedings of **29th International Conference on Surface Modification Technologies, Technical University of Denmark, Copenhagen, Denmark**, June 2015.
2. **Sunny Zafar** and Apurbba Kumar Sharma, An ANN Approach for Prediction of Wear Behaviour of WC-12Co Nanostructured Microwave Clad, **Proceedings of International Tribology Conference-2015, Tokyo University of Science, Tokyo, Japan**, September 2015.
3. **Sunny Zafar** and Apurbba Kumar Sharma, Influence of Post Clad Heat Treatment of WC based Composite Microwave Clad, **Proceedings of Processing and Fabrications of Advanced Materials: XXIII, Indian Institute of Technology Roorkee, India**, December 2014.
4. **Sunny Zafar** and Apurbba Kumar Sharma, FE Simulation of Microwave Heating of Characteristically Different Materials, Proceedings of **International Conference on Latest Developments in Material, Manufacturing and Quality Control**, **Giani Zail Singh College of Engineering & Technology, Bathinda, Punjab, India,** February 2016.